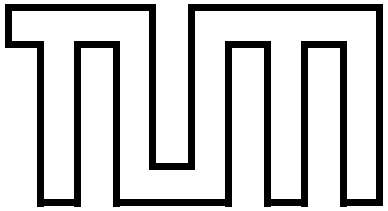

Fakultät für Physik
der Technischen Universität München

Max-Planck-Institut für Biochemie
Abteilung für Molekulare Strukturbiologie

Electron Cryo-Tomography Studies of Mammalian Neurons

Shoh Michael Asano

Vollständiger Abdruck der von der Fakultät für Physik
der Technischen Universität München
zur Erlangung des akademischen Grades eines
Doktors der Naturwissenschaften (Dr. rer. nat.)
genehmigten Dissertation.

Vorsitzender:		Univ.-Prof. Dr. M. Zacharias
Prüfer der Dissertation:	1.	Hon.-Prof. Dr. W. Baumeister
	2.	Univ.-Prof. Dr. M. Rief
	3.	Prof. Dr. B. Koster (Universität Leiden, Niederlande) (nur schriftliche Beurteilung)

Die Dissertation wurde am 23.03.2015 an der Technischen Universität München eingereicht und durch die Fakultät für Physik am 03.06.2015 angenommen.

Table of Contents

Abstract

More than hundred years have passed since Santiago Ramón y Cajal has published his pioneering analysis of the function and development of the central nervous system and created awe-inspiring drawings of neurons and their dendritic networks in the end of the 19th century, marking the beginning of modern neuroscience doctrine [1]. In his remarkable studies he proposed that the transmission of information in neurons takes place uni-directionally at the sites of contact between the small membranous protrusions of the neurons. This tight cellular junction, the synapse, as it was christened by Charles Scott Sherrington in 1897, was first visualised in high resolution by means of transmission electron microscopy (TEM) by Edward George Gray in 1959 [2].

Structural imaging methods, such as TEM, complement the modern advanced light microscopy techniques, and in combination with biochemistry and bioengineering, lend fundamental insights into the function of synapses, by providing the ultrastructural details necessary for a more mechanistic understanding. One of the enlightening discoveries enabled by TEM in the neuronal field, was the discovery of synaptic vesicles (SVs) inside synapses [3] - essentially the carrier of the smallest unit of information. Even today, the majority of ultrastructural studies are performed with a similar conventional TEM approach, using chemically fixed and artificially stained samples. These fixation processes, however, produce substantial imaging artifacts, limiting its use for low resolution studies.

With new developments in preparational techniques, transmission electron cryo-microscopy (cryo-TEM) allows for recording of biological samples in their native environment without chemical fixation, enabling precise and quantitative analyses [4]. Combined with electron tomography [5], electron cryo-tomography (ECT) has further revolutionized the electron microscopy (EM) field by providing means for an undisturbed and artifact-free three-dimensional reconstruction of the extra- and intracellular environment. Owing to the recent developments of electron direct detection device cameras and novel electron phase plate designs, ECT is on the road of becoming one of the mainstream technologies in the area of structural biology nowadays.

Due to the capability of imaging delicate structures in a close-to-native state, ECT was chosen as the primary characterisation method for the functional and ultrastructural studies of neurons, presented in the scope of this thesis. Namely, one of the main questions approached in this work was the fragile and obscure protein homeostasis involved in complex neuronal signal propagation and processing. In this respect, we investigated how a defect in this protein homeostasis was affecting SV exocytosis. Moreover, a light uncaging based approach to record these transient events, such as SV exocytosis, was taken by means of time-resolved ECT. A particular attention was drawn later to the essential ubiquitin-proteasome system (UPS), which allows for marking and disposing of unnecessary or misfolded proteins by means of the 26S proteasome complex.

The first study discussed in this thesis (chapter 3), employed ECT for studying the role of the protein RIM1α in synapses, which is vital for maintaining the probability of neurotransmitter release through its various interactions with other

crucial synaptic proteins. The study was focusing on the comparison of morphological features in synapses of RIM1α-deficient and wildtype mice. Based on the ECT results, we succeeded in linking the significant ultrastructural alterations displayed in RIM1α-deficient mice with a functional deficit. Additionally, by applying a proteasome inhibitor to the altered synapses, both ultrastructural and functional defects could be fully recovered. These findings allowed for the formulation of a SV exocytosis initiation model, substantiating the importance of RIM1α.

In the next study, fluorescent microscopy (FM) was used to record cultured and transfected rat hippocampal neurons, which genetically expressed novel fluorescent Ca^{2+} sensors (chapter 4). The application of light uncaging methods on these neurons allowed us to directly invoke and observe postsynaptic activity. Furthermore, total internal reflection fluorescence microscopy (TIRFM) was used to quantitatively describe the activity and characterize the novel Ca^{2+} indicators. This study served as the proof-of-concept investigation for the subsequent implementation of a modified light stimulation setup into the ECT workflow described in the following chapters 5 and 6.

Chapter 5 covered the applicability of the modifications to the vitrification devices, or cryo-plungers, that enabled imaging transient events at millisecond timescales. The modified cryo-plungers employed ultraviolet (UV) light-based stimulation of synapses and allowed for extremely precise and controllable time-resolutions ranging from 10 ms to 120 ms. Moreover, chapter 6 demonstrated the capability of the modified cryo-plungers with biological samples. Stimulated synapses prepared with this setup presented distinct morphological features and enabled direct visualization of highly transient synaptic events.

The final study in chapter 7 examined 26S proteasomes that could be detected *in situ* in cultured neurons. These 26S proteasomes could be individually classified in two assembly states and two distinct conformations. We succeeded in identifying whether a particular 26S proteasome was idle or processing a substrate, and demonstrated that under normal conditions, the capacity of 26S proteasomal degradation is far underused. Together with the nanometer precision and accurate orientation information obtained, a first molecular census of single 26S proteasomes inside the neuron could be taken. Incorporating both the 26S proteasome and neurons in a cellular context in a coherent ultrastructural *in situ* study is highly attractive, as defects in the UPS were linked to several neurodegenerative diseases.

Summarized, the studies presented in this thesis provide novel insights into the mechanism of synaptic transmission by elucidating the role of the important synaptic protein RIM1α in SV exocytosis. To supplement this, we were able to directly visualize highly transient events, such as SV exocytosis or clathrin mediated endocytosis (CME) from UV light stimulated synapses on a tailor-made setup. Finally, we succeeded in localizing and describing individual 26S proteasomes *in situ* inside intact neurons for the first time, indubitably heralding the start into the field of “visual proteomics” in neurons based on the cellular ECT.

1. Transmission Electron Microscopy

1.1 Electron - Specimen Interactions

Electrons can interact with the sample in two ways, by either elastic, or inelastic scattering. A very idealized schematic of an electron energy loss spectrum after scattering is demonstrated in figure 1.1. In biological materials, where elements with a low atomic number (Z) predominate, inelastic scattering occurs more frequently than the elastic one. The basic concepts behind the interactions of the electrons with the sample and the final image formation are evaluated in this chapter.

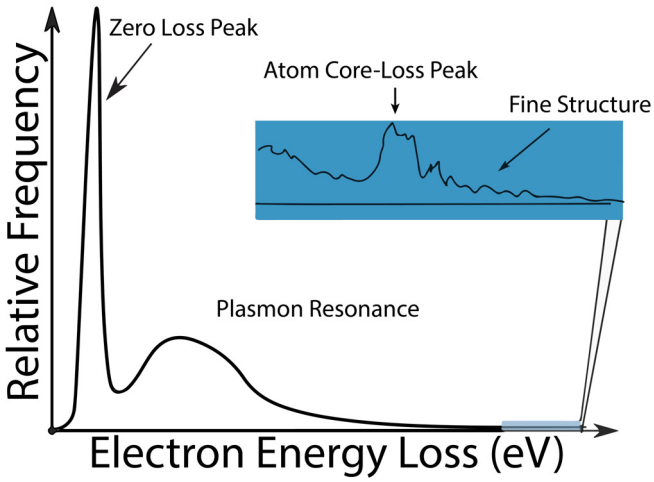

Figure 1.1: The idealized spectrum shows the energy distribution of the electron after scattering with a material. The zero loss peak represents the energy width of the electron source as well as elastic scattering events. Every electron beyond this peak has been scattered inelastically. Ionization events are displayed on the far right side of the spectrum and is enlarged in the blue inset. Slightly modified from [6] with permission.

Elastic Scattering

Elastic scattering of electrons occurs at the Coulomb potential of the nuclei in the sample. This Coulomb potential is proportional to Z and is therefore relatively weak in biological samples, and furthermore also gets attenuated exponentially due to screening by the surrounding electron shell. We can describe this potential by the Wentzel approximation for light atoms [7]:

$$V(r) = \frac{Ze}{4\pi\epsilon_0 r} e^{-\frac{r}{\kappa}} \tag{1.1}$$

where the fraction describes the potential of a atom with the atomic number Z in the distance r and e the electron charge. The screening radius can be estimated from the Fermi model of the atom: $\kappa = 0.885 \cdot r_b Z^{-\frac{1}{3}}$ with Bohr radius r_b. If we now assume the first Born approximation of weak phase objects in our mostly low Z environment [7], we can get the differential cross section:

$$\frac{d\sigma}{d\Omega} = (\frac{m}{2\pi\hbar^2})^2 |V(q)|^2 \tag{1.2}$$

with $\hbar$ the reduced Planck constant, m the electron mass and $V(q)$ the Fourier transform of the potential:

$$V(q) = \int V(r) e^{-iqr} d^3r \tag{1.3}$$

Now we integrate the differential cross section (equation (1.2)) over the whole angular area $d\sigma = 2\pi sin(\theta) d\theta$ and obtain the total cross section dependent on the de Broglie wavelength (λ) of the electron [7]:

$$\sigma_{el} = 2\pi \int \frac{d\sigma}{d\Omega} sin(\theta) d\theta \propto \lambda^2 Z^{4/3} \tag{1.4}$$

$$\lambda = \frac{h}{p} = \frac{h}{\sqrt{2mE(1 + \frac{E}{2E_0})}} \tag{1.5}$$

The relativistic formula for the de Broglie electron wavelength is used, with h the Planck constant, the momentum p defined by the kinetic energy calculated with the electron charge and the acceleration voltage $E = eU$ and the rest energy $E_0 = mc^2$ given by the electron mass and the velocity of light c. For the acceleration voltage used in this study, we get $\lambda \approx 1.96$ pm. The total cross section obtained here is proportional to the probability of interaction between an electron and a nucleus. The elastically scattered electrons thereby allow for the precise localization of the core potential interaction and constitute the high resolution component data in electron microscopy.

Another important quantity is the mean free path, which describes the average distance between two scattering events. It can be calculated using:

$$\Lambda_{el} = (\sum_i \rho_i \sigma_{el,i} \frac{N_A}{A_i})^{-1} \tag{1.6}$$

Where i is the type of atom, ρ the mass density, N_A is the Avogadro number and A the atomic mass. The same formula applies for inelastic scattering by substituting $\sigma_{el,i}$ with the value of $\sigma_{inel,i}$.

Finally, we can reciprocally add the mean free paths of elastically and inelastically scattered electrons to yield the total mean free path of scattered electrons Λ_{total} [7]:

$$\frac{1}{\Lambda_{total}} = \frac{1}{\Lambda_{el}} + \frac{1}{\Lambda_{inel}} \tag{1.7}$$

The value for the total mean free path is mainly influenced by the inelastic scattering in ice of around $\Lambda_{inel} \approx 175nm$ for 300 keV electrons [8, 9], and ultimately the reason behind the restriction in sample thickness in TEM.

Inelastic Scattering

In the case of inelastic scattering, primary electrons lose significant energy, even when scattered at small angles. This energy is deposited inside the sample causing heating as well as the breaking of ionic and covalent bonds, which may lead to formation of free radicals. Radiolysis of organic compounds may build up pockets of hydrogen gas in the ice which can cause the "bubbling" effect, generating a "boiling" appearance in EM [10]. Furthermore, inelastically scattered electrons only offer poor localization compared to its elastic counterpart. The reason is the non-localized plasmon interaction volume in inelastically scattered electrons, compared to the very confined interaction volume of the screened Coulomb potential (equation (1.1)) in the elastic scattering [11]. Whereas highly scattered electrons are effectively blocked by the objective aperture, the typically low scattering angle makes it difficult to block inelastically scattered electrons. However, if the electron energy loss is considerable, these electrons may be removed by a post column energy filter. By removing inelastically scattered electrons, we record in "zero-loss" imaging, which will be described in more detail in section 1.4. This term is not entirely correct, because electrons with small energy loss (scattered by oscillations of nuclei ("phonons")) are not removed [7]. Altogether, there are three general classes of inelastic scattering events [7]:

- Phonon excitation in molecules only lowers the electron energy by 20 meV - 1 eV and therefore cannot be distinguished in "zero-loss" imaging from the energy spread of the electron source [12].
- Intra- and interband excitations as well as plasmon excitations results in an electron energy loss in the order of few eV.
- The ionization of core electrons results in a substantial electron energy loss, which is dependent on the sample and can be used for electron energy loss spectroscopy (EELS). This class of inelastic scattering occurs with a lower probability (seen in figure 1.1 (highlighted in blue, and displayed enlarged in inset)).

The different interaction mechanisms complicate a general description of the scattering events. By assuming that plasmon excitation is the main contributor, an average inelastic cross section (σ_{inel}) can be approximated [13]:

$$\sigma_{inel} = \frac{1.5 \cdot 10^{-20}}{\beta^2} Z^{1/2} ln(\frac{2}{\theta_E}) \propto Z^{1/2} \tag{1.8}$$

with $\theta_E \approx 13.5eV\frac{Z}{mv^2}$ and the relativistic correction ($\beta = \frac{v}{c}$). The contribution of inelastic (equation (1.8)) compared to elastic scattering (equation (1.2)) is rather high, with the theoretical ratio of around $\frac{\sigma_{inel}}{\sigma_{el}} \approx \frac{26}{Z}$ and the experimental value of about $\frac{\sigma_{inel}}{\sigma_{el}} \approx \frac{20}{Z}$ [7].

1.2 Image Contrast Formation

Image contrast can be defined with the difference in the intensity between two adjacent areas (I_1 and I_2) [14]:

$$C = \frac{I_2 - I_1}{I_1} = \frac{\Delta I}{I_1} \tag{1.9}$$

The two constrast forming mechanisms in EM (phase and amplitude contrast) are briefly described in the following subchapters [7].

1.2.1 Phase Contrast

The electron waves are scattered in the sample and their phases get subsequently shifted. These scattered waves can then (positively or negatively) interfere with the superposition of other waves in the image plane, and producting a phase dependent contrast. Termed phase contrast, this mechanism represents the major contributor of image contrast for our low Z samples. We define a scattered electron wave (Ψ) of the form (inc: incoming, sc: scattered):

$$\Psi_{sc} = \Psi_{inc} e^{i\Phi} \tag{1.10}$$

where Φ is the phase shift produced by the sample. With the simplification $\Phi \ll 1$ (weak scattering object in case of low Z) we can approximate the equation with the first two Taylor coefficients:

$$\Psi_{sc} \approx \Psi_{inc}(1 + i\Phi) \tag{1.11}$$

Two more properties play a crucial role in phase contrast formation: Objective aperture and contrast transfer function (CTF) [14].

The objective aperture cuts off the spatial frequencies beyond a certain value, which is dependent on the radius of the aperture and can described by a simple heaviside function in Fourier space (with wavenumber $k = \frac{2\pi}{\lambda}$, and k_{max} the maximal frequency passed by the aperture) [14–16]. On the other hand, the objective lens specific term can be defined by the CTF [14, 16]:

$$A(k) = \Theta(k - k_{max}) \tag{1.12}$$

$$CTF(k) = 2sin(\frac{\pi}{2}(C_s\lambda^3 k^4 + 2\lambda\Delta z k^2)) \tag{1.13}$$

Wherein C_s is the spherical aberration coefficient and Δz the defocus value. Both equations ((1.12) and (1.13)) combined with the original scattered wave function (equation (1.11)) give us a good approximation of the final wave function [16]:

$$\Psi_{final} = \mathcal{F}^{-1}(A(k) \cdot CTF(k) \cdot \mathcal{F}(\Psi_{sc})) \tag{1.14}$$

where $\mathcal{F}$ is the Fourier transformation and $\mathcal{F}^{-1}$ the inverse transformation operator.

The image itself (the intensity profile) is then calculated by the square of the absolute value [16]:

$$Image_{final} = \left|\Psi_{final}(k)\right|^2 = \Psi_{final}(k) \cdot \Psi^*_{final}(k) \tag{1.15}$$

1.2.2 Amplitude Contrast

Amplitude contrast is caused by removal of elastically scattered electrons by means of the objective aperture. A simplified calculation reveals that the number of electrons passing the objective aperture can be approximated [14] by:

$$n = n_0 e^{-N\sigma_{el}x} \tag{1.16}$$

Where $N = \frac{N_A}{A}$ (with A the atomic mass) and $x = \rho t$ is the mass thickness. The scattering cross-section σ_{el} (equation (1.2)) can be calculated with the scattering amplitude $f(\theta)$ [7]:

$$\sigma_{el}(\alpha) = \int_{\alpha}^{\pi} |f(\theta)|^2 2\pi sin(\theta) d\theta \tag{1.17}$$

where α corresponds to the angle through which an electron can pass the objective aperture. Summarized, this contrast mechanism increases with a smaller aperture radius, higher Z, mass density ρ and thickness t and is also often called mass density, or absorption contrast [14].

1.3 Transmission Electron Microscopy

Microscopy Techniques in Biochemistry

Chemistry in combination with physics gave us an enormous set of techniques to analyze biochemical processes both quantitatively and qualitatively. These techniques can provide cellular insights within a wide range of spatial resolutions. According to Abbe's law of diffraction (equation 1.18), the attainable resolution is proportional to the wavelength (λ) (with NA as the numerical aperture).

$$d = \frac{\lambda}{2NA} \tag{1.18}$$

Light-optical methods of live objects usually have resolutions in the low μm range, with up to the diffraction limit (equation (1.18)) of a few hundred nm in the case of confocal microscopy. The best possible resolution to achieve with FM nowadays is about 6 nm in lateral direction with stimulated emission depletion (STED) [17]. Other notable techniques include stochastic optical reconstruction microscopy (STORM) [18] or photo activated localization microscopy (PALM) [19]. Three pioneers of high resolution light microscopy techniques were awarded the Nobel Prize in Chemistry in 2014. Nonetheless, both the necessity for labeling, as well as the comparatively low resolution in "real" biological samples (up to 40 nm) make these methods unusable in attaining highly detailed structural information.

X-ray diffraction can achieve resolutions of up to a few Angstrom, capable of resolving atomic structures of proteins. Unfortunately, techniques in this class may be used for highly homogeneous protein crystals exclusively, but biomaterial rarely aligns in lattices naturally. Salting and packing effects might furthermore degenerate the quality obtained in the sample [20]. Thus, the fine structure of these measurements can vary from the physiological and working protein. Bigger proteins with higher flexibilities, are most often not feasible for X-ray diffraction since they almost never align in a crystal structure. The same problem applies to analysis of most bound complexes. The field of high resolution spectroscopy methods based on nuclear magnetic resonance alliviates the crystallization problem by using highly purified proteins in solution.

Several imaging techniques use electrons as an illumination source. The negative charge of an electron causes strong interactions with the atomic core, rendering all transmission techniques limited by the specimen thickness (see before in section 1.1 and later discussed in section 1.5). Describing biological samples thicker than $\approx 1\mu m$ with electrons is limited to its surface by scanning electron microscopic (SEM) techniques, initially developed by Von Ardenne in 1938 [21]. Most commonly, secondary electrons emitted by the sample after illumination is detected in SEM, which is used to reproduce the topology of the sample. Elastically backscattered electrons, or emitted X-rays are used in analytical SEM for information about the chemical composition of the specimen.

The internal structure of a sample can be described by using TEM, which was developed in 1931 by Ernst Ruska and Max Knoll [22]. Today even sub-Angstrom resolution is possible in material sciences (high resolution TEM on atoms in silicon) [23], with recent advances to sub-50 pm resolution in scanning transmission microscopy [24].

Biological TEM methods include ECT or single particle analysis (SPA). In SPA, purified samples of proteins can be processed to yield a three-dimensional protein structure from a collection of two-dimensional images. The underlying concept of SPA is very similar to that of tomography, which will be discussed later (section 1.5). The resolution attainable by SPA is dependent on the sample, but sub-nanometer resolution is easily attainable today [25], and (near-)atomic resolutions (≤ 3Å) can be achieved, by either the use of symmetry [26] or by the benefit of modern detectors and algorithms [27].

A prime example of a macroprotein used in both SPA [25, 28–30] and ECT [31, 32] in the department of Prof. Wolfgang Baumeister is the 26S proteasome, a 33 subunit and 2.5 MDa complex responsible for protein degradation. In order to investigate such fragile structure in the nanometer scale, we have to resort to TEM. But the observation in TEM is not limited to only proteins. In cellular ECT, a three dimensional image of the cell or compartments thereof can be recorded and used to elucidate their ultrastructure [33–35]. As this thesis will mainly employ cellular ECT in neuronal structures, the theory behind tomographic image acquisition is described in detail in section 1.5.

1.4 The Electron Microscope

To understand the underlying instrumentation, the main parts of the electron microscope (schematic view shown in figure 1.2) with an imaging system are described in this section.

The path from electron extraction to the camera has to be under high vacuum (up to 10^{-9} Torr) [14] in order to minimize scattering of the electron beam. Therefore, the sample is required to be resistant to evaporation, e.g. by vitrification (see details about sample vitrification in section 1.5) [14].

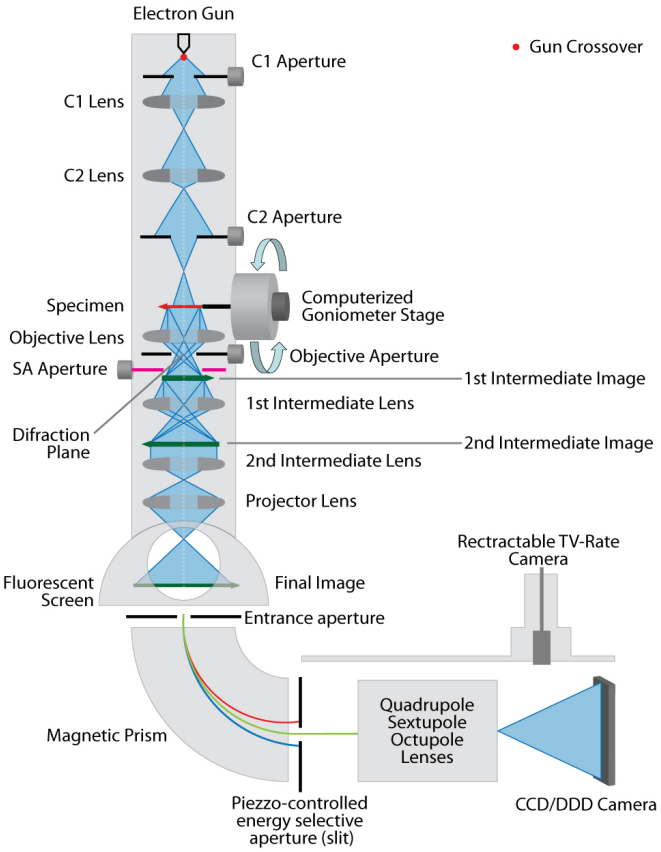

Figure 1.2: Annotated, schematic lens and aperture system of a modern electron microscope, including the image filter and the camera system. The electron beam path is shown in blue. From [36] with permission.

Electron Source

The ideal electron source should have a high brightness and lifetime, low noise, small source size and a very low electron energy spread [14]. To accomodate most of these features, modern electron microscopes are typically equipped with a field emission gun (FEG) as their source of electrons. A Schottky type sharply tipped tungsten crystal is covered by a thin layer of zirconia in order to lower the work function and enable electron extraction at a lower temperature [37]. Electron extraction is performed by applying a

high voltage to the crystal, producing a very strong electric field at the sharp tip. The operating temperature is around 1700K [14, 37]. Again, the main advantages of a FEG include better temporal and spatial coherence, higher current density (brightness), as well as smaller beam diameter than their purely thermionic counterparts. In mathematical terms, the enhanced coherence weakens the exponential attenuation of the CTF and thus increases the attainable resolution [33].

Lens and Aperture System

After the electrons are accelerated and focused onto a small area, the beam enters a series of electromagnetic lenses and metal apertures. We can change the lens strength and subsequently the beam deflection, which in turn is used for magnification and beam focussing [14]. Both condenser lenses C1 and C2 and corresponding apertures (refer to figure 1.2) are used to optimize the illumination of the sample.

The EM grid itself is held in the beam path by either a specimen holder screwed tightly into position (in case of the FEI Tecnai G2), or an automatic grid grapping arm (in case of the FEI Titan Krios).

Below the sample, the objective lens collects both scattered and unscattered electrons and produces an intermediate image at 20-50x magnification [7]. The objective aperture then filters out highly scattered electrons which would otherwise contribute to noise. Subsequently, the projection is further enlarged by diffraction and intermediate lenses, and is either displayed on a phosphor screen or guided to the camera system [14].

Image Filter

In the case of thick biological specimen, inelastically scattered electrons are a major source of noise. Removing these electrons from the final image can be accomplished by an image filter positioned after the column (“post-column filter”). The basic mechanism of this filter can be compared to that of a prism spectrometer [7, 14]: Depending on the energy and thus speed of the incoming electron, it gets more or less deflected by a magnetic field and can be filtered out. In the so-called “Zero-Loss” imaging mode, the energy window is set manually to 20 eV around the average energy of 300 keV, which is sufficiently wide to include the electron energy spread of the FEG, but narrower than the smallest energy loss through single plasmon loss of about 20 eV (see section 1.1) [14]. After filtering out the inelastically scattered electrons, the beam once more passes through a series of lenses leading to an additional magnification of the image.

Types of Cameras

Two types of cameras are currently used for ECT studies. Slow scan charged coupled device (CCD) cameras have been in use since 1986 and became widely popular in the 1990s [38, 39], whereas CMOS-based direct electron detection camera technology only recently matured [40, 41].

In a CCD based camera system, the electron beam hits a scintillator, which is directly

attached and fiber-optically coupled to the camera chip. Depending on its luminescent properties and thickness, a certain number of photons gets emitted per incident electron, also described as the conversion rate [14]. This photon signal is then measured by photon collector tubes which re-convert the light again to electrons using the photoelectric effect. The CCD chip itself is cooled down to about -20 °C to minimize thermal noise (dark current) [39].

The photon cloud produced by the electron impact (described by the modulation transfer function (MTF) [16]), necessitates the physical pixel size of modern CCDs used in ECT to be in the range of $10-20\ \mu m$. While the pixel size should be as big as possible, the amount of pixels should be adequately high to allow for a big and detailed field of view. Technical difficulties such as wafer production and scintillator glueing are limiting the total size of a usable camera chip.

Those restriction were recently lifted with the development of a CMOS-based sensors, enabling direct detection of electrons on the CMOS chip without the need for a scintillator layer, which enables a reduction of the MTF and a smaller physical pixel size [42]. Though direct detection of primary electrons are damaging the sensor over time [43], rad-hardened and additionally back-thinned chips provide a higher resistance to radiation damage by lowering backscattering events drastically, which in turn, subsequently reducing the MTF as well [44]. With the latest direct detectors (e.g. Gatan K2 summit), the camera can deliver up to 400 frames per second - significantly faster than with CCD chips [45] [1]. This allows for fine correction of sample drifting after acquisition *in silico* and ultimately, highly preserving detailed structural features [42].

1.5 Electron Cryo-Tomography

In electron tomography, the sample is tilted inside the electron microscopy column and at each step, a projection image is acquired. These images are then recombined into a three dimensional volume [33].

Radon already described the mathematical principle behind tomography in 1917 [46]. The Radon transform is the integral transform of a known function over straight lines. Radon also included an inverse function in his work which can be used to calculate an unknown function with given Radon transform. In electron tomography, the inverse formula is used to get the *a priori* unknown three-dimensional (3D) density of the object with two-dimensional (2D) projections obtained by the microscope. An example showing a simplified object, its subsequent imaging and reconstruction is displayed in figure 1.3. To illustrate the basic mathematical concept of tomography, the projection-slice theorem in Fourier space [16, 47] can be used (see also figure 1.4):

$$F_2 P_2 I = S_2 F_3 I \tag{1.19}$$

[1] Gatan Homepage http://www.gatan.com/products/tem-imaging-spectroscopy/k2-camera

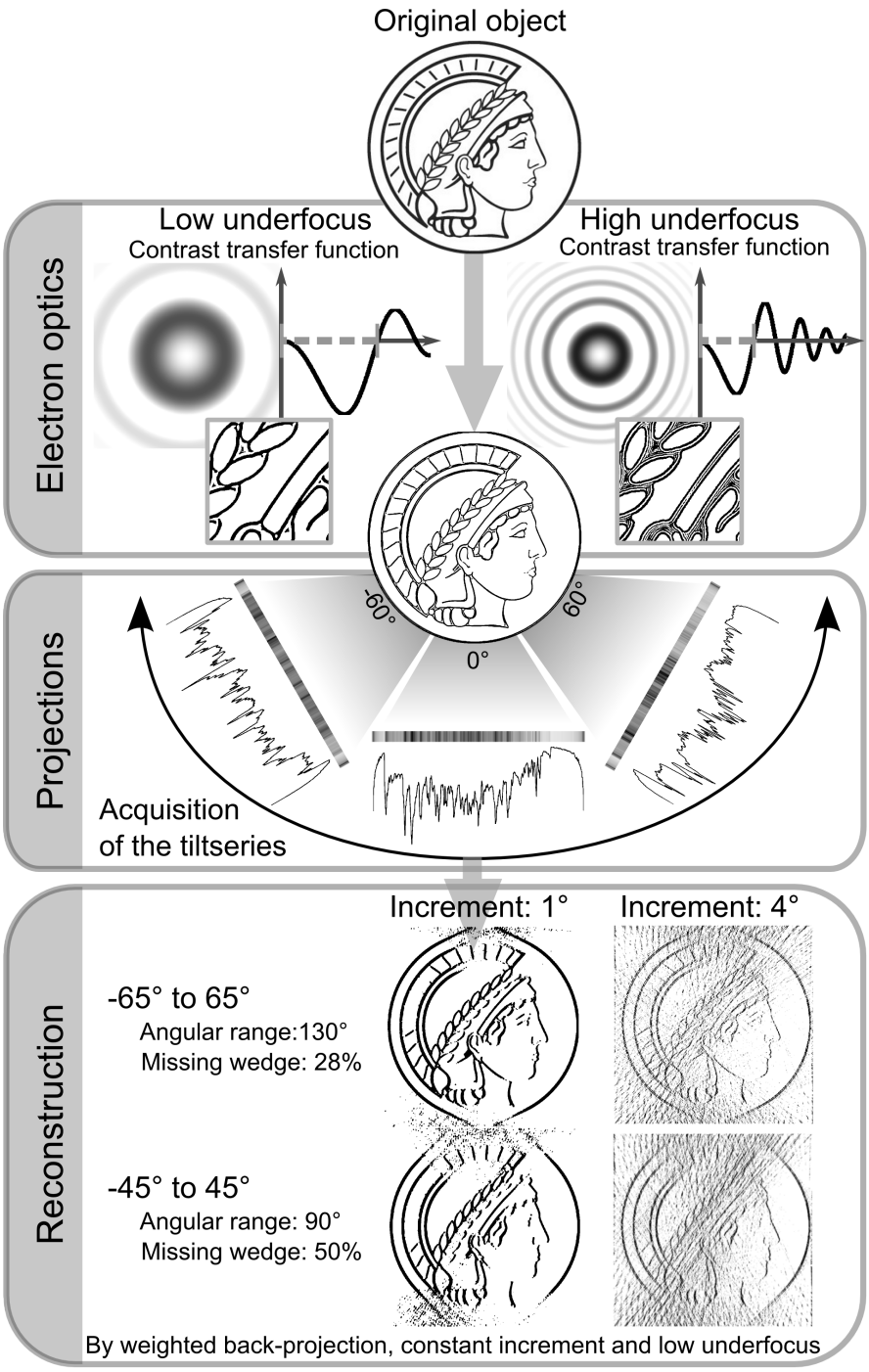

Figure 1.3: Overall tomographic acquisition and reconstruction scheme. The *a priori* unknown object (top, Minerva 2D image) is influenced by the electron optics (top box, CTF, see section 1.13). The object is rotated and projections taken at different degrees (e.g. -60°- +60°, middle box). The one-dimensional projections are shown as both image projections and line graphs. The smaller the angular increment, and higher the total angular range, the better the final quality of the reconstruction (bottom box). Image from [35] with permission.

Where F_2/F_3 is the 2/3 dimensional Fourier transformation operator, P_2 the projection operator (projection of a 3D function onto a 2D area) and S_2 a slice operator (slicing the 3D image into a 2D image). I is the 3D image we want to investigate.

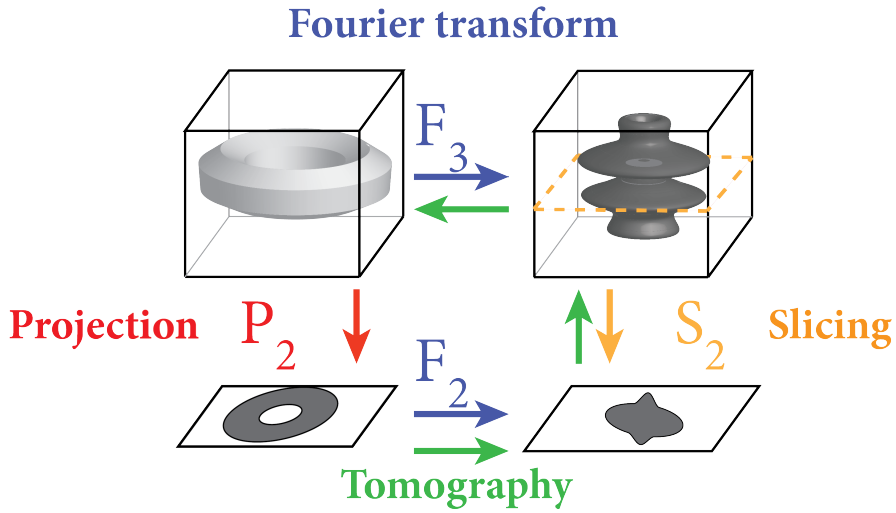

Figure 1.4: A schematic of the projection-slice theorem. A three dimensional density of a torus (top left) can either be Fourier transformed (blue arrow F_3 transformation), and then the central slice of the transformed volume (marked by the orange dotted line, top right) extracted (orange arrow S_2 operator, resulting in bottom right), or first projected (red arrow P_2 transformation, resulting bottom left) and then Fourier transformed (blue arrow F_2 transformation, resulting bottom right), ultimately yielding the same result. Tomography can use the two dimensional projections at given tilt angle values, and reconstruct the *a priori* unknown three dimensional density by the transformation path indicated with green arrows. Modified from [48] with permission.

In tomography, by acquiring projections ($P_2 \cdot I$), one could take the 2D-Fourier transform of these images ($F_2 P_2 \cdot I$) and then calculate the 3D volume by inverse 3D-Fourier transformation of the differently angled slices in Fourier space ($F_3^{-1} S_2^{-1} F_2 P_2 \cdot I$). This way a "perfect" reconstruction of the volume can be made by acquiring projections over the full angular range of tilts (±90°) with infinitesimal small angular steps. Due to mechanical constraints and electron dose considerations, a full tilt is not possible for our specimen.

Crowther showed [49] that the highest isotropic resolution d obtainable is:

$$d = \frac{\pi D}{N} \tag{1.20}$$

This formula only applies to a cylindrical object of thickness D over a single full tilt series (±90°) with constant angular spacing (N number of projections). It does not include any limiting factors like noise or low contrast due to radiation limitation.

According to the dose fractionation theorem [50], a single projection image and a set of images taken at different angles of the same object (tomography) with both the same total electron dose do not differ in signal-to-noise ratio (SNR). It is therefore recommended to take tomograms (if possible) to obtain additional 3D information, however the spatial

distortion is highly anisotropic. The best resolution can be obtained in xy (imaging) plane perpendicular to the beam, while the z-direction is only moderately represented (figure 1.3) [35]. With the specimen holder limitations explained above, there are always projections missing. This leads to an effect called "missing-wedge", because a wedge formed area (corresponding to the high angular tilts) is missing in both -z and z direction in the Fourier space. This also leads to an elongation of the observed structures in z-direction (figure 1.3) [35]. When doing ECT analyses, this particular effect needs special attention, due to its distorting effects. Therefore, special routines accounting for the missing-wedge are used for subtomogram averaging, and/or template matching approaches discussed later (chapter 7).

A method of reducing this effect by combining two orthogonal tilt series ("dual-axis tomography") is described later in section 1.6.1.

Rapid Freezing

To overcome problems arising from chemical fixation, dehydration and staining, the technique of rapid freezing of samples was developed in the early 1980s [51]. Here, the rapid freezing of the sample is the key to achieve amorphous, vitreous ice. In this state, water molecules are arranged randomly [51] and ice crystal formation is prevented, which would otherwise disrupt and damage the sample [52]. Successful vitrification occurs with cooling rates higher than 300000 $\frac{^\circ C}{s}$ and does not damage biological ultrastructures [53].

Sufficiently thin samples (thickness $\leq 20\mu m$ [35]) can be vitrified by means of quickly dropping it into a coolant. Such devices, so-called "cryo-plungers" usually release a rod with the (prepared) EM-grid attached into a small volume of liquid ethane (refer to section 8.1.1 for details). Liquid ethane has a much higher thermal conductivity compared to liquid nitrogen, ensuring a significantly faster heat transfer required for proper vitrification [53, 54]. Furthermore, the Leidenfrost effect is heavily reduced in liquid ethane, which would otherwise cause a formation of a "warm" and insulating gas layer around the sample, and preventing it from reaching the proper freezing rates.

Once frozen, the samples always have to be kept at liquid nitrogen temperature to avoid devitrification and ice crystal formation [54]. The main advantages in using cryo-fixed samples are (in the order of importance):

1. Preservation of structure in a native environment
2. An almost nonexistent evaporation rate
3. No diffusion or movement of the sample
4. Radiation resistance to electrons in cryo conditions is about a factor of (at least) four higher compared to room temperature [55–58]

Radiation Damage

One important parameter for EM image acquisition is the electron dose distribution on the sample, as ionization occurs quickly in high electron doses and leads to structural changes and bubbling effects [59]. Both effects severely alters ultrastructure and cause

alignment errors. To keep the electron dose minimal, searching for suitable areas is done carefully at a much lower magnification in low dose operation mode. Tomographic images are acquired by an automated imaging procedure [12]. In this scheme all important steps (adjusting image shift, focusing, re-centering energy slit and final image acquisition) are done automatically. To lower the electron dose, a position along the tilt axis and outside the recording position is chosen for tracking and focusing [12].

Low Signal-to-Noise Ratio

With increasing ice thickness, the SNR of the sample decreases due to increasing multiple scattering events (see section 1.1). Several approaches can be taken against low SNR in cellular ECT:

1. A well aligned and small objective aperture only passes electrons with a small scattering angle. With this removal of highly scattered electrons, aberration effects are reduced, and therefore spatial resolution is improved [14]. On the other hand, badly aligned or very small apertures can interfere with tomographic acquisition and reduces overall brightness.
2. Using an energy filter to remove inelastically scattered electrons (see section 1.4)
3. Increasing the electron dose attributed to the sample will yield in a higher SNR. Unfortunately, there is an upper limit to this approach as radiation damage (see section 1.5) renders tomographic reconstructions useless for high resolution studies.
4. Using a higher acceleration voltage ensures a higher mean free path length (section 1.1) and thus better sample penetration. This gain diminishes with higher voltages, making 300 kV a practical compromise [16]. Furthermore, a higher voltage enhances radiation damage by inelastically scattered ("knock-on") events, where the electron energy transferred to the atom is beyond its binding energy [16].
5. The thickness of the sample can be modified, albeit tediously, by means of cryo-sectioning [60] or cryo-focussed ion beam (FIB) milling [61]. Several imaging artifacts, including massive compression in cryo-sectioning or gallium ion deposition on the sample in the case of FIB [61] requires careful consideration of these techniques.
6. Using software solutions, such as anisotropic nonlinear diffusion (AND) denoising algorithms can significantly reduce noise levels (see section 8.1.3) after tomogram acquisition, but may cause loss of ultrastructural details.
7. Both the use of electron direct detectors (see section 1.4) and the electron phase plate [62] (see section 1.6.2), can improve the SNR dramatically.
8. Subtomograms of identical proteins can be averaged together to boost the signal and cancel out noise, thus increasing the SNR. The method of subtomogram averaging (see section 1.6.3) is ideally used in studies of identical (e.g. isolated, or highly homogeneous) proteins.

Some of the solutions provided are considered *de facto* standard in ECT, such as a proper objective aperture setting, the use of the highest ultrastructure-preserving electron dose, and the operation of an energy filter. Technical ways to enhance the SNR, namely dual-axis tomography, the use of a phase plate/direct detector camera, as well as subtomogram averaging will be discussed in detail in the next subsections 1.6.1, 1.6.2, and 1.6.3.

1.6 Advanced ECT Methods

1.6.1 Dual Axis Tomography

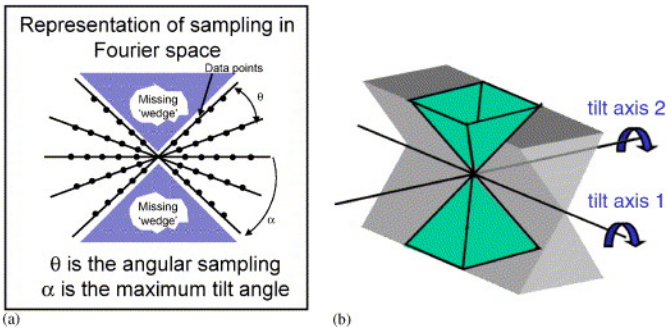

Figure 1.5: Left: Missing wedge geometry in Fourier space for a single tilt acquisition. Right: The missing wedge turns into a "missing pyramid" when using dual axis tomography. Image from [63] with permission.

Dual-axis tilt tomography was developed to decrease the missing wedge effect (explained in section 1.5) by combining two tilt series from two (orthogonal) axis [64–66]. Effectively, the missing wedge would turn into an "missing pyramid" in Fourier space (figure 1.5), improving the isotropic resolution. Due to constraints in the sample holder and geometry, the resolution perpendicular to the imaging plane, still remains to be improved.

Three major problems arise from dual-axis tilt tomographic approaches [66]:

1. Electron dose accumulation on the sample from two tilt series
2. Difficulties in image alignment, as two separate tomograms need to be combined
3. Recording time at least doubles per tomogram

The first two points are also correlated to each other, as dose dependent fiducial movement was demonstrated in vitrified specimen [67, 68].

1.6.2 Phase Plate TEM (PTEM)

In order to enhance phase contrast, a "Zernike-type" phase plate, essentially a continuous carbon layer with around 31 nm thickness with a central hole, can be inserted in the diffraction (back-focal) plane of the electron microscope (figure 1.6 A) [69]. While the unperturbed / unscattered electron beam passes the small (1 μm diameter) hole without

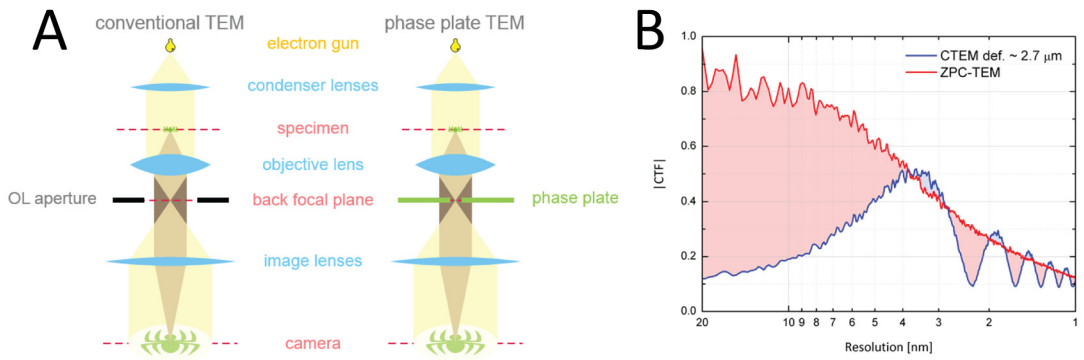

Figure 1.6: A) Schematic beam path in conventional TEM(left) and PTEM (right). Overall, instead of an objective aperture (left, black bar, labelled "OL aperture"), the PTEM has a phase plate (right, green bar, "phase plate") installed at the backfocal plane. Image courtesy of Dr. Radostin Danev. B) Measured CTF curves from conventional TEM (CTEM) with $\Delta z \approx 2.7 \mu m$ defocus (blue curve), and Zernike Phase Contrast TEM (red curve). Especially in the low resolution (low frequency) regime, the PTEM has an increased contrast compared to the conventional TEM. Image courtesy of Dr. Radostin Danev.

interaction, scattered electrons pass though the carbon layer and gain a $-\frac{\pi}{2}$ phase shift at 300 kV acceleration voltage. In the more recent "Volta" phase plate design, the phase difference works exactly opposite by shifting the unscattered primary beam by $+\frac{\pi}{2}$, while not affecting the scattered one [62].

In both phase plate designs, this phase difference results in a major improvement of about a factor of 3-5 in phase contrast [69]. The $\frac{\pi}{2}$ phase change switches the aforementioned CTF *sin* (see equation (1.13)) into a complementary *cos* function, effectively boosting the CTF and similarly the final image (equation (1.2.1)) at low frequencies and low defocus. The difference between PTEM and conventional TEM can be observed in their respective CTF curves (see figure 1.6 B) [69]. The CTF is dependent on the defocus Δz (1.13), resulting in diminishing signal in conventional TEM doing "close to focus" studies at $\Delta z \approx 0 \mu m$. However, this does not apply for PTEM and therefore, low defoci are exclusively used in this operation mode. Summarized, while conventional TEM suffers from loss of contrast near low frequencies (see CTF figure 1.6 B and equation 1.13), PTEM is able to reproduce very detailed images in high contrast using very low defocus (typically $\Delta z \approx -1 \mu m$, or close to focus) [69].

The major differences between the old "Zernike" design [69] and the new Volta phase plate (VPP) [62] are:

- The original Zernike design has a central hole, which need a perfect alignment in every tilt angle. However, the new VPP does not have this hole any longer, making especially automated tomographic acquisitions easier and faster
- In the VPP, the phase shift is affecting the unscattered beams
- In the VPP, the phase change is mainly caused by an electric field, the "Volta" potential - the difference between inner and surface potential of the amorphous carbon film

1.6.3 Subtomogram Averaging

To elucidate the fine structure of reoccuring macroproteins inside tomograms, subtomogram averaging can used for enhancing SNR. The technique requires the similarity of protein complexes within the tomogram, and has been employed and developed for more than 30 years [70–72]. The goal is to average multiple single subtomograms from different orientations, so that both background noise and the missing wedge are removed. Mathematically, we can consider each subtomogram Vol_i as the sum of a signal S_i and noise N_i:

$$Vol_i = S_i + N_i \tag{1.21}$$

We assume the signal to be the same ($S_i = S$, e.g. the same particle), the SNR for one subtomogram is given as:

$$\text{SNR}_{Single} = \frac{< S_i^2 >}{< N_i^2 >} = \frac{< S^2 >}{< N_i^2 >} \tag{1.22}$$

If the particles are aligned, the average volume A_{Av} over N particles is:

$$A_{Av} = \frac{1}{N}\sum_{i=1}^{N}(S_i + N_i) = S + \frac{1}{N}\sum_{i=1}^{N}N_i = S + \overline{N_i} \tag{1.23}$$

The SNR for N subtomogram is then computed as in equation (1.22) with the signal from the average given by equation (1.23):

$$\text{SNR(N)} = \frac{< S_i^2 >}{< \overline{N_i}^2 >} = \frac{< S^2 >}{\frac{1}{N^2} < \sum_{i=1}^{N} N_i >^2} \tag{1.24}$$

The noise is assumed to be uncorrelated, and therefore the divisor in (1.24) can be simplified as following:

$$\frac{1}{N^2} < \sum_{i=1}^{N} N_i >^2 = \frac{1}{N^2}\sum_{i=1}^{N} < N_i^2 > = \frac{1}{N^2} N < N_i^2 > = \frac{1}{N} < N_i^2 > \tag{1.25}$$

Inserting it to the averaged SNR from (1.24) and substituting it with the SNR from a single subtomogram obtained earlier (1.22):

$$\text{SNR(N)} = N\frac{< S^2 >}{< N_i^2 >} = N \cdot \text{SNR}_{Single} \tag{1.26}$$

Summarized, if we assume that the alignment conditions are perfect, the signal of all particles the same, as well as the noise uncorrelated, the SNR of an average increases linearly with the number of particles. However, problems in alignment (e.g. caused by highly noisy images), low number of subtomograms, highly heterogeneous protein conformations and poor rotational sampling reduce this value [73].

2. Introduction to Synapses

2.1 Neurons

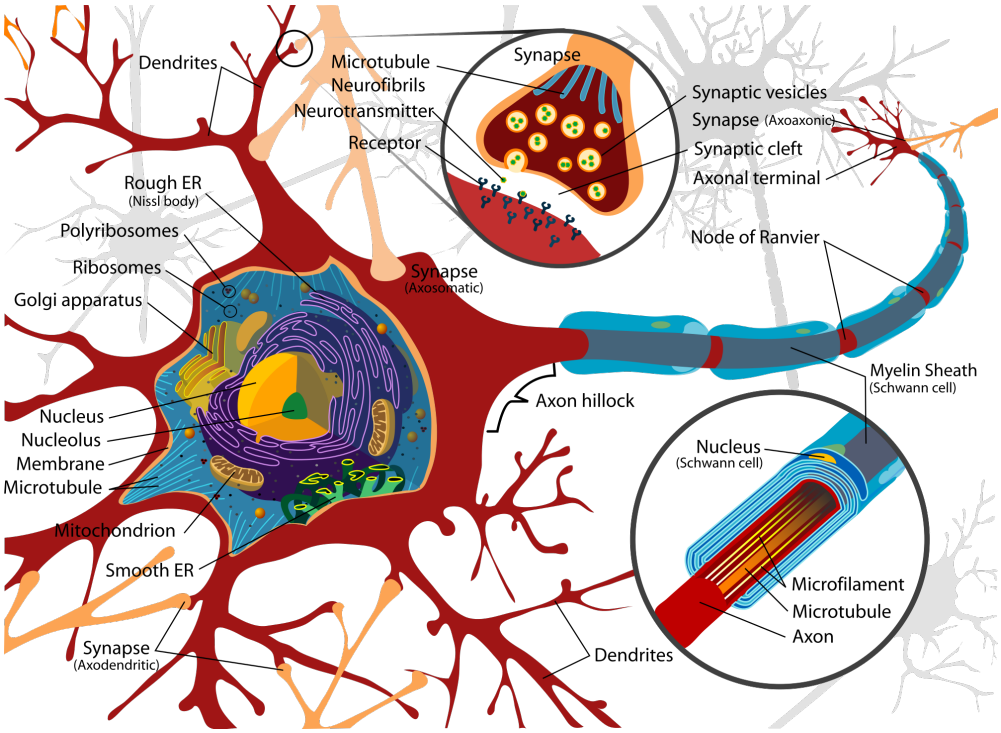

Figure 2.1: Annotated overview of a neuronal cell, with the top center inset displaying a synaptic connection in detail. Bottom inset shows the structure of an axon. From [74].

The nerve cell, or neuron is a specialized cell, and make up the core component of the nervous system. Like any other eukaryotic cell, the neuron has a nucleus, which is surrounded by various other important organelles, such as Golgi apparatus, mitochondria and endoplasmic reticulum (see the annotated overview figure 2.1).

The transmission of an electrical signal between two adjacent neurons takes place at their junction, also termed a synapse. The signal of a neuron is carried by the axon (see the annotated inset in figure 2.1), a long protrusion of the neuron. At the axon terminal, several synapses are established with other neurons. The axonal part of the synapse is also termed the presynapse, as the origin of the signal propagation. The signal is received most commonly by branched extensions of the opposing neuron, called dendrites, where the protrusion from the dendrites forming the synapse are called dendritic spine or postsynapse. Thus, the name of this most common type of synaptic connection is called an axodendritic synapse. This clear distinction of two cellular compartments, the axon and dendrites give rise to the "polarity" of the neurons [75].

2.2 Basic Structure of a Synapse

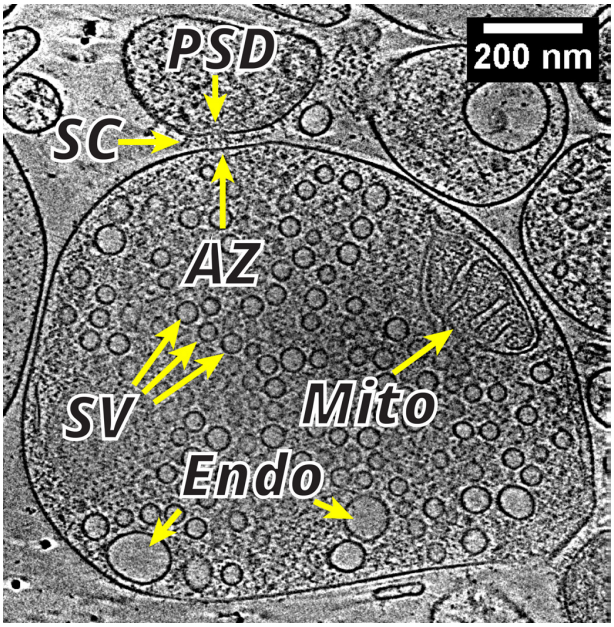

Figure 2.2: Overview slice of a representative synaptosome tomogram displaying several synaptic components (yellow arrows): "PSD": Postsynaptic site with visible PSD; "SC": Synaptic cleft with density variations; "SV": Synaptic vesicles; "Mito": Mitochondria; "Endo": Putative early endosomes. Scalebar: 200 nm

The cellular asymmetry underlying the polarity of the synapse can be easily observed with electron cryo-microscopy, such as in figure 2.2. The cellular terminal on the invoking side, the presynaptic terminal, and the receiving side, the postsynaptic part, can be readily distinguished. In between, the synaptic cleft is located with a width of about 25 nm. The presynaptic part contains multiple SVs around 40 nm in diameter filled with neurotransmitters [76, 77]. As we can see from figures 2.2 and 2.3, the SVs are partly interconnected with each other through short molecular filaments, termed connectors. Docked SVs are directly connected to the presynaptic membrane by a filamentous structure called a tether (figure 2.3). SVs are released at the membrane area called the active zone (AZ), which is directly opposed to the postsynaptic side (figure 2.4). The pre- and postsynaptic terminals are held together by different synaptic adhesion molecules

[78] and this density of proteins can be as well seen in the synaptic cleft in figure 2.2. Several different receptors are residing within the postsynaptic membrane embedded in a complex network of proteins called PSD, equally well resolvable in ECT (figure 2.2).

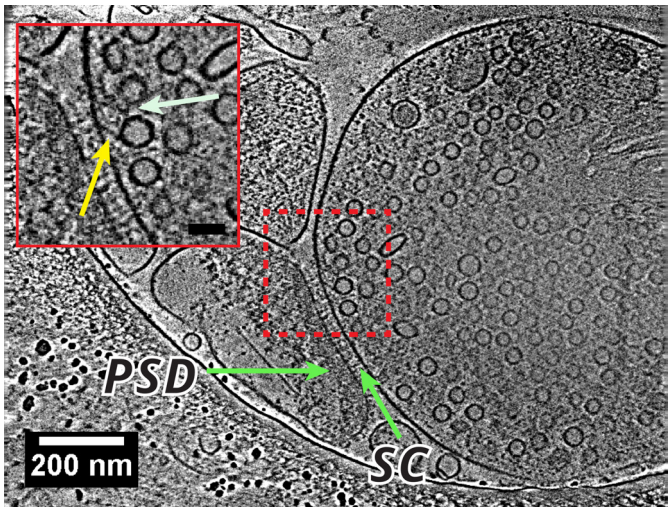

Figure 2.3: Overview slice of a representative synaptosome showing a tether between a SV and the AZ membrane. Postsynaptic density ("PSD"), and synaptic cleft ("SC") are denoted with green arrows. The red dotted rectangle is enlarged in the top left to show the tether (yellow arrow) and connector filament of a tethered SV (light green). Scalebars: 200 nm in the overview, 50 nm in the inset.

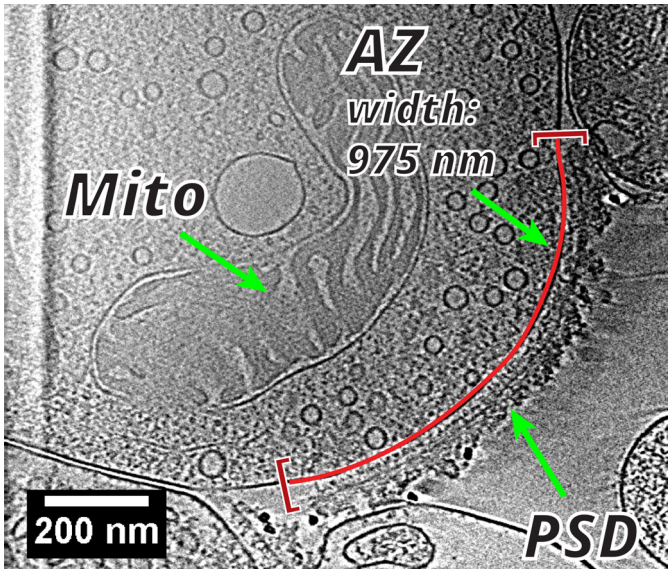

Figure 2.4: Overview slice of a synaptosome showing a wide AZ. The AZ was overlayed with a red line tracing the membrane. The width of the AZ here was almost 1 μm measured between the two brackets (ends of the postsynaptic membrane). Postsynaptic density ("PSD") and mitochondria ("Mito") are denoted with green arrows. Scalebar: 200 nm.

2.2.1 Basic Function of the Presynapse

During synaptic transmission, a sharp membrane potential difference, called an action potential, arrives at the presynapse. This causes a depolarization of the presynaptic terminal and opens voltage-gated Ca^{2+} channels. The subsequent Ca^{2+} influx activates Ca^{2+}-sensitive proteins adhering on the SVs and may induce fusion with the presynaptic membrane by means of SNAREs (proteins mediating membrane fusion). The process continues with the exocytosis of SVs and the subsequent release of neurotransmitters, which then diffuse through the protein network inside the synaptic cleft to the receptors on the postsynaptic side. By binding to receptors, ion channels open and (in case of an excitatory synapse) depolarize the postsynaptic membrane and may cause a postsynaptic potential, which is then further propagated.

SV Recycling Pathway

Two different modes of SV exocytosis are currently in discussion: The first one is the well established "full-collapse" exocytosis mode, in which a SV membrane completely integrates into the AZ membrane after exocytosis and neurotransmitter release. The evidence produced by numerous studies over the period of almost 50 years in different neuron types make this mode the primary model for SV exocytosis [79, 80]. On the other hand, a second mode of "kiss-and-run" exocytosis has been proposed, where the SV only opens up a small pore to the synaptic cleft for neurotransmitter release [81–83]. This membrane fusion between the SV and the AZ is transient, ultimately keeping the composition and identity of the two membranes completely apart. After neurotransmitter release, the SV pinches off the AZ and can be refilled and/or recycled, by various endocytosis mechanisms. It is postulated that both "kiss-and-run" and "full collapse" occur in hippocampal synapses [84].

In order to transfer signals during or after prolonged stimuli, the retrieval of SVs by means of endocytosis is a necessity. There are two different modes of endocytosis, depending on the membrane surface area retrieved. Single SV retrieval through a membrane invagination is performed with the coat-forming protein clathrin [85]. The timescale for the clathrin-mediated SV retrieval to complete is estimated to about a few tens of seconds [85]. In CME, first a small invagination of the membrane is formed by clathrin coat formation, also called a "coated pit" [86]. This coating process is mediated by several adapter proteins like AP2 and AP180 [87]. The affected membrane then buds into the cytosol of the cell and gets pinched off.

Another mode of endocytosis is bulk endocytosis, where membrane surface areas larger than that of a normal SV get pinched off. Some of them seem to accumulate into an "early endosomes" from where final single SVs are retrieved. This event is expected to occur in matter of tens of seconds [88, 89]. However, more recent studies using time-resolved EM showed that ultrafast bulk endocytosis is happening within less than a second after stimulation, with single SV retrieval within only 5-6 seconds after stimulation [90, 91]. This particular endocytosis mechanism appear to be independent of clathrin for the initial membrane retrieval, as also the very fast time-scale suggests [90, 91]. The different exo- and endocytosis mechanisms for SVs are schematically shown in figure 2.5 [85].

Once single SVs are formed, ATPases located on the SV membrane acidify the SV lumen under ATP consumption [92, 93]. Re-uptake of neurotransmitter is performed by transporters using the electrochemical gradient built up [94]. The total time for SV recycling takes 15-20 seconds, as shown ultrastructurally [79] and by FM [95, 96].

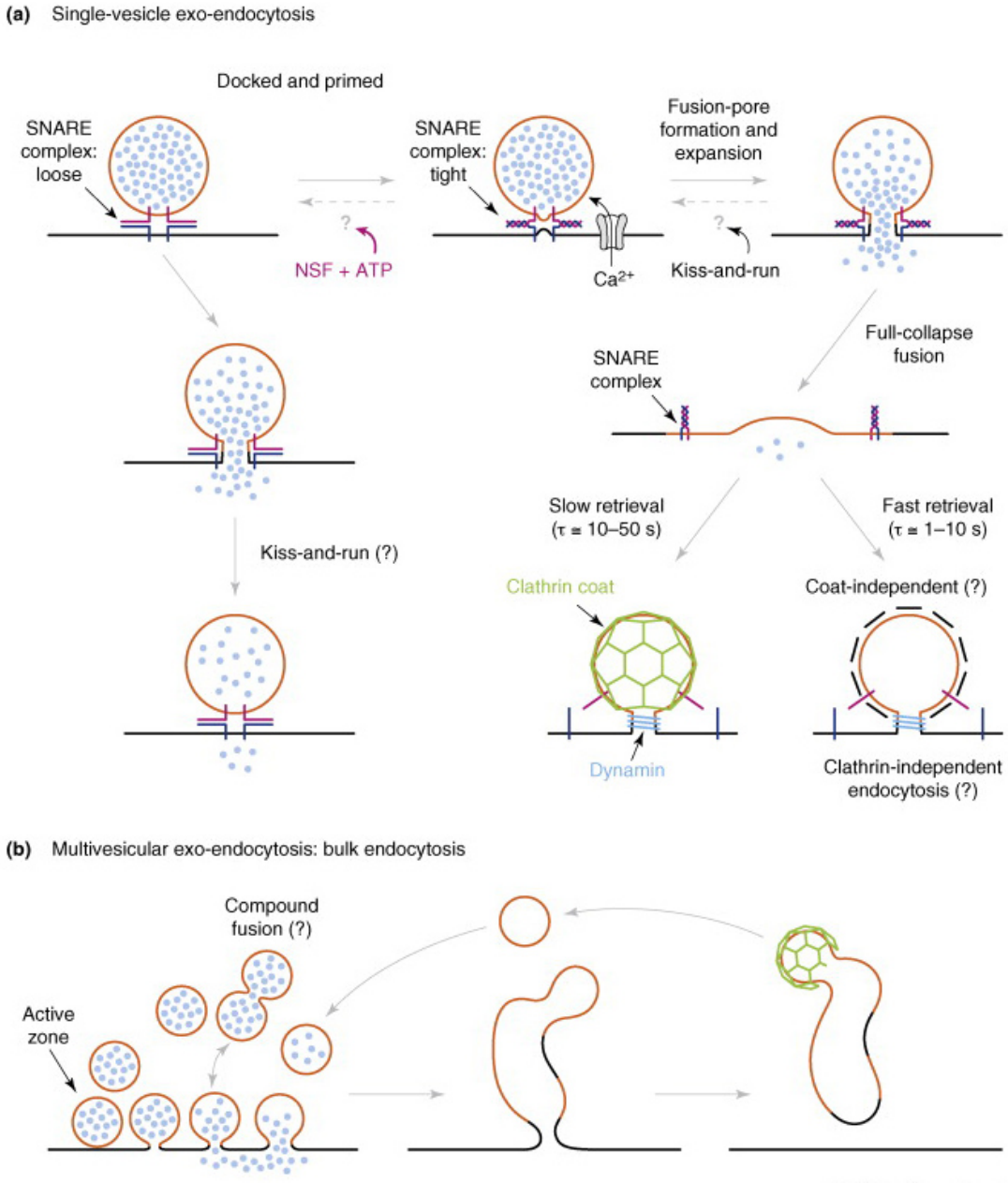

Figure 2.5: Overview of SV exocytosis and endocytosis models in synapses. a) SV demonstrating a kiss-and-run exo- and endocytosis mechanism (left), and a full-collapse fusion with clathrin dependent and independent endocytosis (right). b) Model for bulk endocytosis with intial endosome formation and subsequent CME of single SVs. From [85] with permission.

2.3 UPS in Synapses

The UPS is a cellular regulatory mechanism used to control the protein homeostasis by means of protein degradation [97–99]. This process of protein clearance by the 26S proteasome is described here in brief and a scheme is provided in figure 2.6.

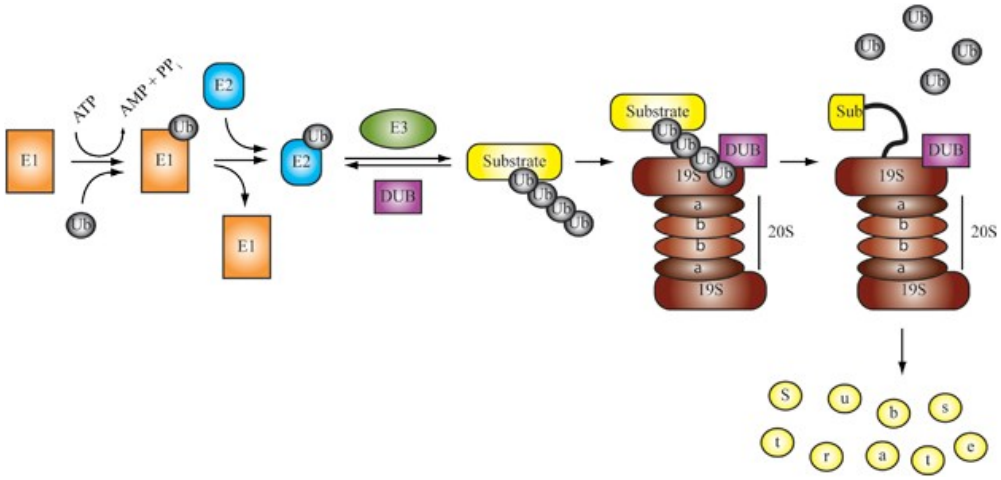

Figure 2.6: A schematic depiction of the UPS pathway. Through a cascade of ligases (E1-E3), ubiquitin (Ub, grey spheres) are attached to the substrate (yellow rounded rectangle). The polyubiquinated substrate is recognized by the 26S proteasome (brown structure), and more specifically, by the 19S RP (top part, labeled "19S"). The substrate is unfolded and passed into the 20S core particle for degradation. Meanwhile, deubiquitinases (purple, labeled "DUB") are cleaving ubiquitins from the substrate to be reused again. Reprinted by permission from Macmillan Publishers Ltd: Cell Death & Differentiation [100], copyright 2009

First, misfolded or otherwise non-functional proteins that are to be degraded (more generally termed "substrates") are identified (figure 2.6) [101]. To initiate ubiquitylation, an E1 ubiquitin-activating enzyme adenylate a single ubiquitin monomer under ATP-consumption. Next, this ubiquitin is transferred to the E2 ubiquitin-conjugating enzyme and subsequently recognized by the E3 ligase. This in turn attaches the ubiquitin to the substrate via a covalent bond. By successive addition of ubiquitins, a polyubiquitin chain is formed at the substrate. This polyubiquitin chain is recognized by the 19S RP subcomplex of the 26S proteasome (which can have either one or two RPs attached) [30, 32]. Subsequently, the substrate is unfolded and guided by the 19S RP into the 20S core particle, where the catalytic sites of the proteasome are located. Once inside the 20S, the unfolded substrate chain is degraded into oligopeptides, whereas the ubiquitin is cleaved and recycled by deubiquitinating enzymes on the 19S RP [102].

In neurons, the UPS was recently shown to play an important role in the postsynapse, regulating synaptic plasticity [103], as well as in the presynapse by adjusting levels of a variety of presynaptic scaffolding proteins [104]. Incubation with protease inhibitor MG-132 prevented the decrease of active synapses and decreasing levels of RIM1 and MUNC13-1 [105] indicating a strong role of the UPS in synapse protein homeostasis. From a therapeutic perspective, a disturbed UPS system is linked to many neurodegenerative disorders, such as Parkinson's, or Alzheimer's disease [106, 107].

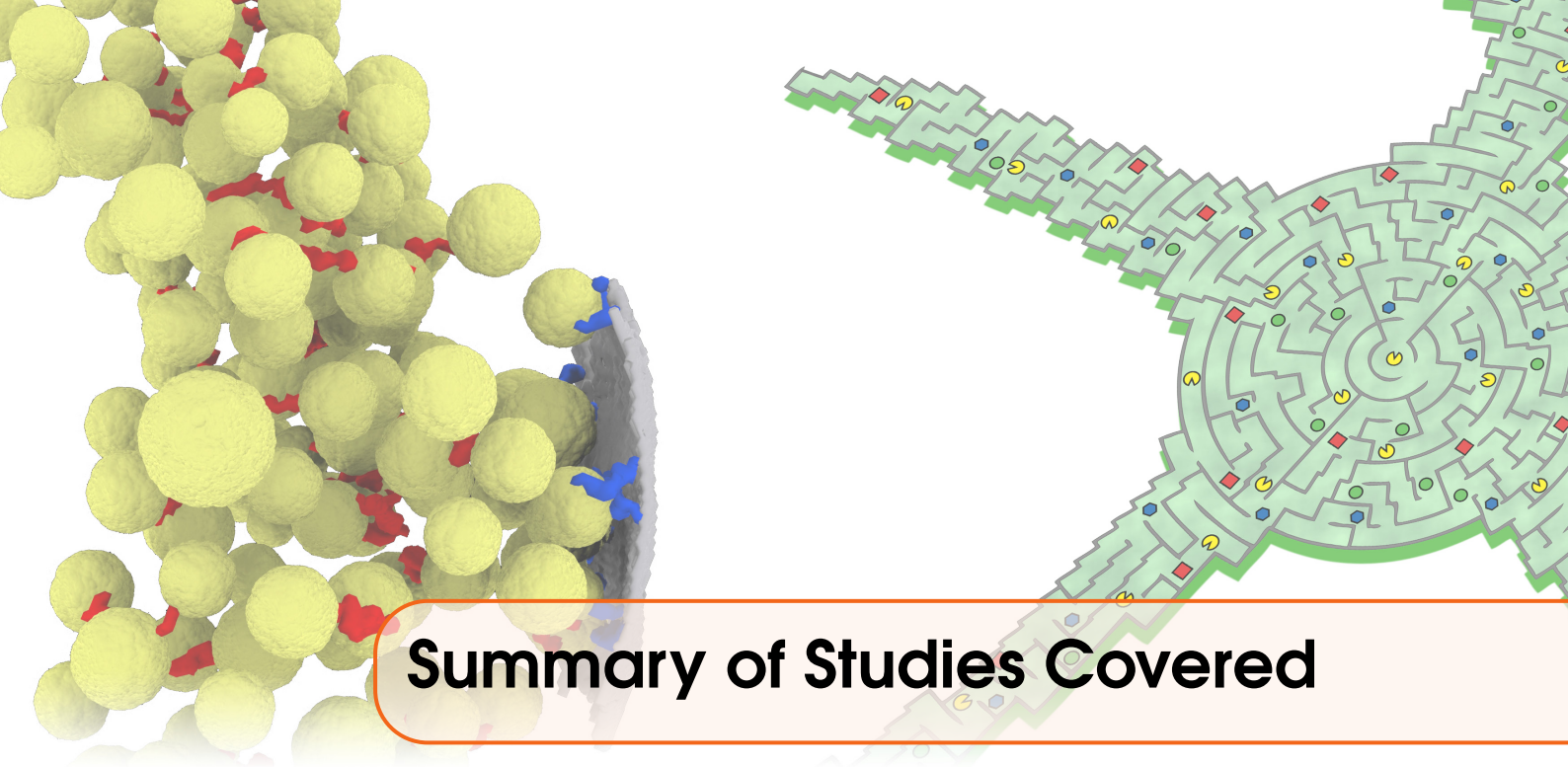

Summary of Studies Covered

This thesis incorporated several ultrastructural studies of neuronal structures by means of ECT. We initially first recorded synapses of SV release deficient mice and validated and improved a model for SV exocytosis [108], based on our findings. However, this study generated several further follow-up questions, such as the ultrastructural identity of SV exocytosis events and its effect on the synaptic morphology, or the characterization of the 26S proteasome in neurons. These issues were further analyzed in each of the chapters.

The Role of RIM1α in Synapses (chapter 3)

The first study shed light on the influence of a crucial AZ protein (RIM1α) on the structure of the synaptic cytomatrix. Previous conventional EM methods failed to detect an ultrastructural defect in RIM1α deficient mice. By employing ECT on synaptosomes extracted from RIM1α deficient mice and comparing the results to wildtype mice, we showed significant changes upon RIM1α deletion in tethering. We were able to correlate the ultrastructural deficits observed in RIM1α deficient mice with the functional deficit observed by electrophysiology. Furthermore, this study examined the effects of proteasome inhibitor on synapse ultrastructure and showed that the deficits observed in RIM1α deficient mice could be reversed upon proteasome inhibition.

TIRFM Studies on Neurons (chapter 4)

This FM study covered the visual identification of postsynaptic responses reported by a novel genetically encoded Ca^{2+} sensors. First, neuronal cultures and calcium-phosphate transfection methods were adapted and qualitative assessments of subsequently transfected cultures were done. So far, FM studies were unable to detect a postsynaptic response reliably with a genetically encoded reporter protein. However, TIRFM on

transfected cultures expressing the novel genetically encoded Ca^{2+} reporters GCaMP6 and GCaMP7 revealed spontaneous Ca^{2+} spikes at individual postsynaptic spines. The data obtained were used to quantitatively characterize the fluorescence kinetics of the Ca^{2+} reporter, as well as the postsynaptic response by means of self-written programs.

Studies of UV-Light Stimulated Synapses (chapters 5 and 6)

A better ultrastructural description of transient events during synaptic stimulation is key for the mechanistic understanding of the SV recycling pathway. Through extensive technical developments and modifications of two different cryo-plungers, we aimed to describe events and morphological changes upon synaptic stimulation by means of UV light uncaging based time-resolved ECT. First, some simulations and experiments confirming the usability of the method were provided, then the modification and the final designs of the cryo-plungers presented. These setups allowed capturing events as shortly as 10 ms after UV light stimulation. Results of the ECT study characterizing synapses stimulated using these modified cryo-plungers are provided, showcasing morphological changes upon short stimulation, as well as snapshots of SV exocytosis.

Characterizing 26S Proteasomes *in Situ* in Intact Neurons (chapter 7)

So far, the 26S proteasome could not be reliably localized and described *in situ* inside cells. The current understanding of this protein complex mainly derives from studies using isolated 26S proteasomes, with only limited applicability within the cellular context. With the latest developments in the camera and phase plate research, we were able to identify single proteins (26S proteasomes) inside cryotomograms of neurons. This study described the 26S proteasome *in situ* within its native neuron environment ultrastructurally. We were able to identify different assembly states and activity statuses by means of subtomogram averaging and classification, demonstrating that the majority of 26S proteasomes only have one RP bound and that most RPs are in fact not processing any substrates under resting conditions. Finally, we were able to map each individual 26S proteasome in its assembly and conformation state inside the cytosol with nanometer precision and exact orientation.

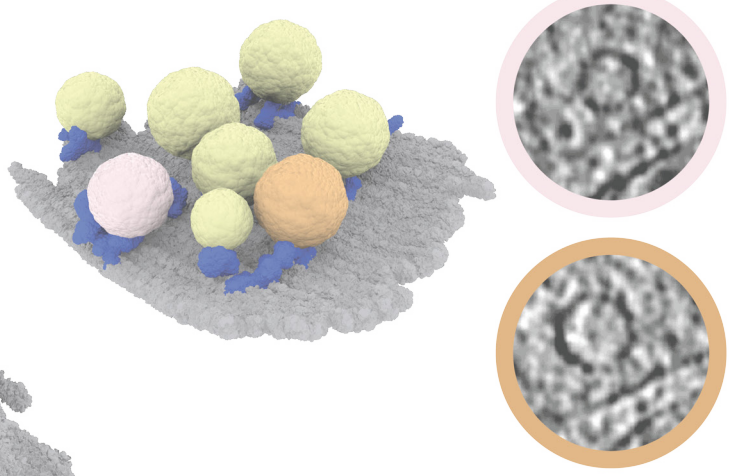

3. The Role of RIM1α in Synapses

3.1 Preface

The study reported here is adapted from the research article "Cryo-electron tomography reveals a critical role of RIM1α in SV tethering" and has been published in the Journal of Cell Biology [109]. The authors were Ruben Fernandez-Busnadiego, Shoh Asano*, Ana-Maria Oprisoreanu, Eri Sakata, Michael Doengi, Zdravko Kochovski, Magdalena Zürner, Valentin Stein, Susanne Schoch, Wolfgang Baumeister, and Vladan Lucic*
*Equal contribution of the two first authors (marked with *)*

The contributions for the work were as following:

Dr. Ruben Fernandez-Busnadiego	Initial preparation, tomogram acquisition and data analyses
Shoh Asano	Preparation, tomogram acquisition and data analyses
Ana-Maria Oprisoreanu	Immunofluorescence microscopy, western blots
Dr. Eri Sakata	Western blots, and proteasome activity assays
Dr. Michael Doengi	Electrophysiology
Zdravko Kochovski	Synaptosomal preparation
Dr. Magdalena Zürner	Provider of RIM mice
Prof. Valentin Stein	Group leader, supervised electrophysiology
Prof. Susanne Schoch	Group leader, supervised RIM mice generation and biochemistry
Prof. Wolfgang Baumeister	Head of department
Dr. Vladan Lucic	Group leader, project design, supervised tomography and data analysis

All authors contributed in the discussion and manuscript generation. Figures were predominately done by the author or by Dr. Ruben Fernandez-Busnadiego. Senior

authors were all participating in the analyses steps.

3.2 Introduction

Neurotransmitter release, the basis of synaptic transmission, takes place via SV fusion at the AZ (see section 2.2.1). The AZ is a specialized part of the presynaptic membrane covered by a dense network of different proteins [110].

While several proteins in the presynaptic cytomatrix have been identified [111], their exact function remain largely elusive. In a recent study [108], our lab has shown that in synaptosomes, the presynaptic cytomatrix is mainly comprised of filaments, which either connect the SV with each other ("connectors") or the AZ ("tethers") (demonstrated in figure 2.3). This study suggested a model in which the SV, after its initial contact with the AZ by one or few tethers, gets closer to the AZ and by gaining additional shorter tethers. The SV is now "structurally primed" and may exhibit SV fusion and exocytosis upon Ca^{2+} influx.

Standing out of the myriad of different synaptic proteins, Rab3-interacting molecules (RIMs) are prime potential candidates for tether formation due to their wide range of interactions with Ca^{2+} channels, SV proteins and many other AZ-enriched proteins (figure 3.1 A) [112]. Recent studies further demonstrated the role of RIM proteins in SV priming, where MUNC13 homodimers are converted into a RIM/MUNC13 heterodimer, which in turn promoted SV priming [113, 114] (figure 3.1, B). Furthermore, RIMs are also necessary to recruit Ca^{2+} channels and contribute to SV priming [115–117] (figure 3.1, B).

In general, proteins at the AZ can be divided into several categories [111]:

1. Proteins involved in SV fusion
2. Cytoskeletal proteins
3. Scaffolding proteins
4. Voltage-gated calcium channels
5. Cell adhesion molecules

RIMs belong to the third group, and are widely considered to play a major role in the membrane trafficking machinery. In vertebrates, four RIM genes have been shown to encode for seven isoforms (RIM1α, RIM2α, RIM1β, RIM2β, RIM2γ, RIM3γ and RIM4γ) [120], with the major isoforms, RIM1α and RIM2α sharing a similar structure [121]. Several *Caenorhabditis elegans* and mice experiments could show the importance of RIM in SV docking, priming and synaptic plasticity [122–124], but both mechanism and ultrastructure accompanying these events remained obscure.

RIM1α mutant mice have been generated [125] and demonstrated reduced priming [126] that might be linked to the decrease of MUNC13-1 observed [125]. These mice were viable and only showed minor behavioral differences. Interestingly, they display no structural abnormalities in brain architecture when imaged with conventional EM [125].

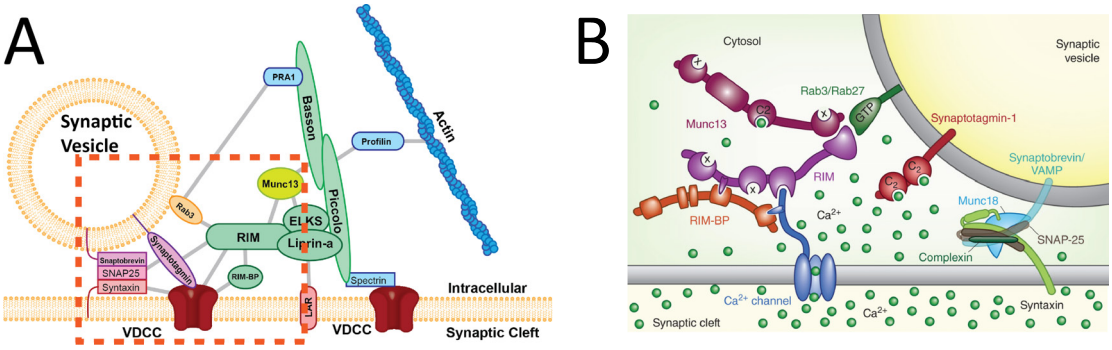

Figure 3.1: A) RIM is depicted inside the green rounded rectangle in the center and forms many interactions in the protein network within the AZ. Most notably are its interactions with the SNARE complex proteins and synaptotagmin (purple) and SV-attached Rab3 (orange). Other important synaptic scaffolding proteins in the AZ are displayed in green. From [118] with permission. B) Interactions of RIM with the SV and AZ. RIM (purple) and MUNC13 (dark purple) form a heterodimer and bind to the SV. Additionally, RIM recruits Ca^{2+} channels (blue) close to the SV and therefore act as part of the docking scaffold between the SV to the AZ membrane. Ca^{2+} ions are shown as green spheres. Reprinted by permission from Macmillan Publishers Ltd: Nature Medicine [119], copyright 2013.

RIM1α-deficient (KO) mice, immunostaining data, as well as western blots were provided by the lab of Prof. Susanne Schoch (University of Bonn). Patch clamp measurements shown additionally were done in the lab of Prof. Valentin Stein (University of Bonn).

3.3 RIM1α KO Study Results

3.3.1 Introduction

The knockout of RIM1α produced a viable phenotype in mice [125], which is necessary in our experiments. Animals were shown to exhibit deficits in synaptic transmission [127], as well as a severe reduction in release probability in excitatory synapses [125]. No structural phenotype was observed in either RIM1α KO or in RIM1α/2α DKO synapses with chemically fixed EM [111, 125]. It is well known that chemical fixation methods employed in conventional EM produces a plethora of artifacts [4, 128, 129], making detection and analysis of fragile structures, such as the presynaptic protein architecture, difficult. We therefore opted to compare the ultrastructure of synaptosomes of RIM1α KO mice with those from wildtype (WT) mice by ECT.

The term synaptosome was first used 1964 by Whittaker [130] to describe nerve terminals torn off from the neuron to form a single, membrane enclosed compartment. Both pre- and postsynaptic terminals could be found frequently next to each other, interconnected with a network of proteins within the synaptic cleft. The synaptosome was a suitable model system for our ECT study, because it was sufficiently thin to be recorded by TEM as well as physiologically very similar to a native synaptic connection. Even after the harsh centrifugation steps, its physiological function is retained for several hours [131].

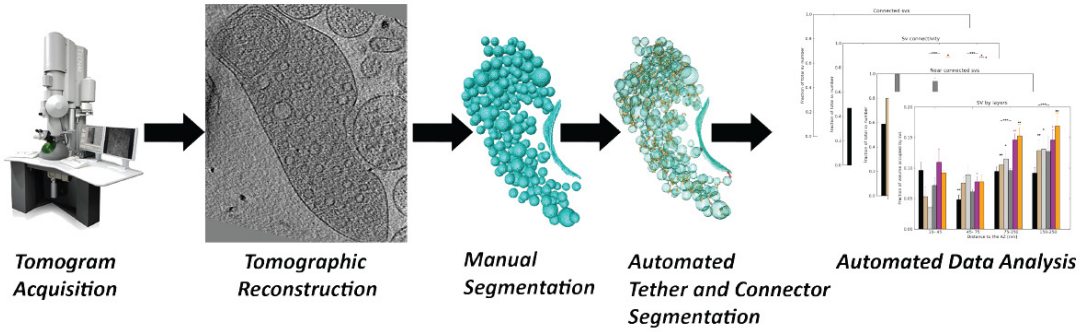

Figure 3.2: Overview of the synaptosomes computational analysis workflow employed in this study and the UV flash stimulation studies later (chapter 6). From left to right: Tomographic acquisition in the electron cryo-microscope. Subsequent tomographic reconstruction, resulting in a tomogram of a synapse (displayed). The manual segmentation of both AZ and SV are followed by the automatic tether and connector detection. Finally, automated data analysis is performed by using the previously segmented dataset.

In this work we quantitatively analyzed synaptosomes (from here on referred to as synapses) of WT and RIM1α KO mice with and without MG132, a potent proteasome inhibitor [132]. Numbers of animals, as well as synapses analyzed are presented in table 3.1, and the general workflow depicted in figure 3.2. 17 tomograms were acquired by the author in this study. Synaptosomes without mitochondria, as well as those with visibly impaired structure (e.g. flat SVs), were not included in the analysis (see section 8.1.4 for details). The analysis was done using an approach developed in our lab [108] allowing for objective detection of small structures such as SV connectors and/or tethers. The necessary segmentations were almost exclusively done by the author, as well as the initial data analysis and statistics on those (details in chapter 8.1.4).

The study only focused on RIM1α KO mice, as RIM1α/2α DKO studies exhibit much higher difficulty in sample preparation due to the postnatal lethality of the mice [111, 133].

Sample	Number of animals	Number of synapses	Total number of vesicles	Total number of tethers	Total number of connectors
WT	2	9	781	134	540
KO-altered	3	4	494	11	673
KO-aligned	3	5	450	60	1079
KO (all)	3	9	944	71	1752
WT + MG132	3	8	835	135	1887
KO + MG132	2	14	1681	160	5662
Total	**8**	**49**	**5185**	**571**	**11593**

Table 3.1: Number of animals, synapses, vesicles, tethers, and connectors used for ECT analysis for each category.

3.3.2 Synaptic Morphology

Both WT and RIM1α KO mice synapses shared a similar general overall morphology with smooth and continuous membranes and a size and thickness of 0.5-1 μm and 300-500 nm, respectively. 100-500 spherical SVs were embedded within the presynaptic cytomatrix of each synapse, which consisted mainly of SV connectors and SV tethers. Mitochondrial membranes looked intact and formed mostly irregularly shaped structures (figure 3.3).

SV concentration

First we compared WT and RIM1α KO synapses in terms of fraction of cytoplasmic volume occupied by SVs ("SV concentration") (figure 3.4). WT synapses (figures 3.3 A, 3.4 A) showed a characteristic SV concentration profile already described previously in rat WT synapses [108], where the SV concentration was high within the proximal zone 0-45nm from the AZ, lower in the intermediate zone 45-75nm away and reaching higher levels for SVs further away in the two distal zones (75-150nm, 150-250nm). When we pooled all WT traces together, the SV concentration in the intermediate zone was indeed significantly lower compared to the proximal and the distal zones ($P<0.05$ and $P<0.01$, t-test, figure 3.4 A).

However, in RIM1α KO synapses ("KO"), we found a severe SV level reduction of around 40% in the proximal zone ($P<0.05$, t-test, figure 3.4 A). Figure 3.5 A shows that this decrease translated into a reduction from 10.7 ± 1.8 in WT to 4.9 ± 1.0 proximal SVs per synapse in KO (mean ± sem and $P<0.05$, t-test).

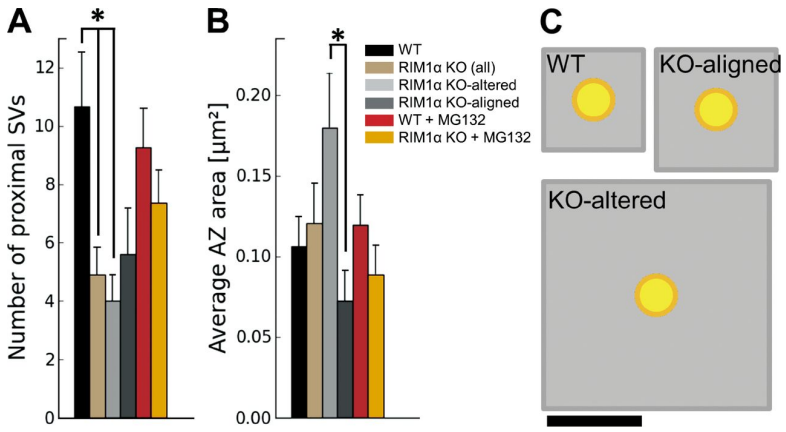

Figure 3.5: The number of proximal SVs per synapse is shown in A, and the average AZ area (in μm^2) in B. A visual comparison of the average AZ area available for one SV is demonstrated in C, where a yellow circle depicts a single SV and the grey area denotes the AZ membrane patch (scalebar: 100nm).

Subclasses in RIM1α KO synapses

Within the heterogenity of the SV concentration in RIM1α KO mice synapses (figures 3.3F, 3.3G), we identified two different subpopulations defined by stark differences in the proximal zone. A subgroup consisting of five out of nine KO synapses exhibited

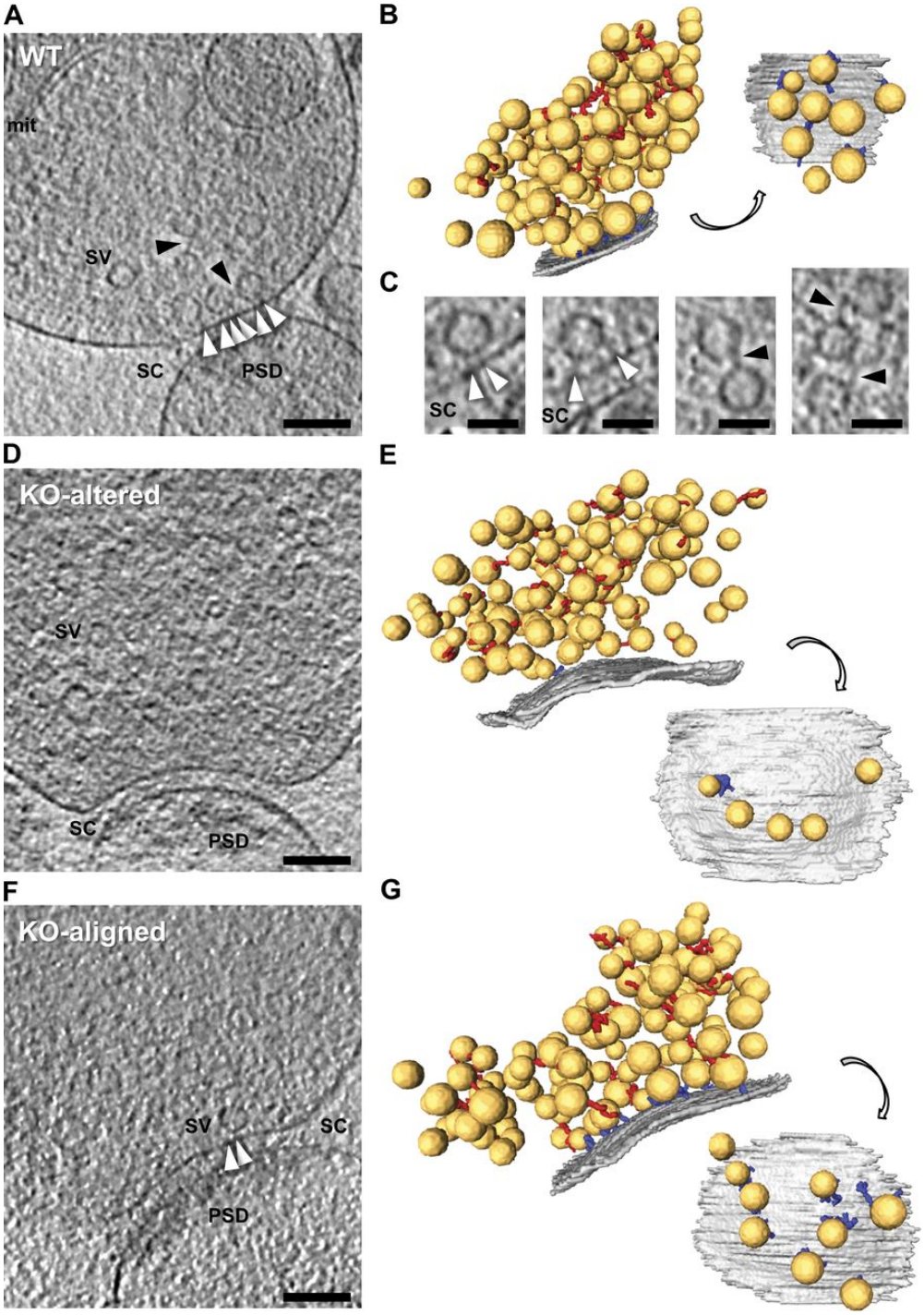

Figure 3.3: Morphology of WT and RIM1α KO mice. Slices of cryo-ET tomograms from WT (A), KO altered (D) and KO aligned (F) and their respective 3D renderings (B, E, G). Connectors (black arrowheads) and tethers (white arrowheads) are demonstrated in the WT case (A) and further magnified in (C). 3D rendering colorscheme: SV (yellow), AZ (grey), connectors (red) and tethers (blue). With mitochondria ("mit"), synaptic vesicles ("SV"), synaptic cleft ("SC"), and postsynaptic density ("PSD"). Scalebars for tomographic slices 100 nm, for magnified image 50 nm.

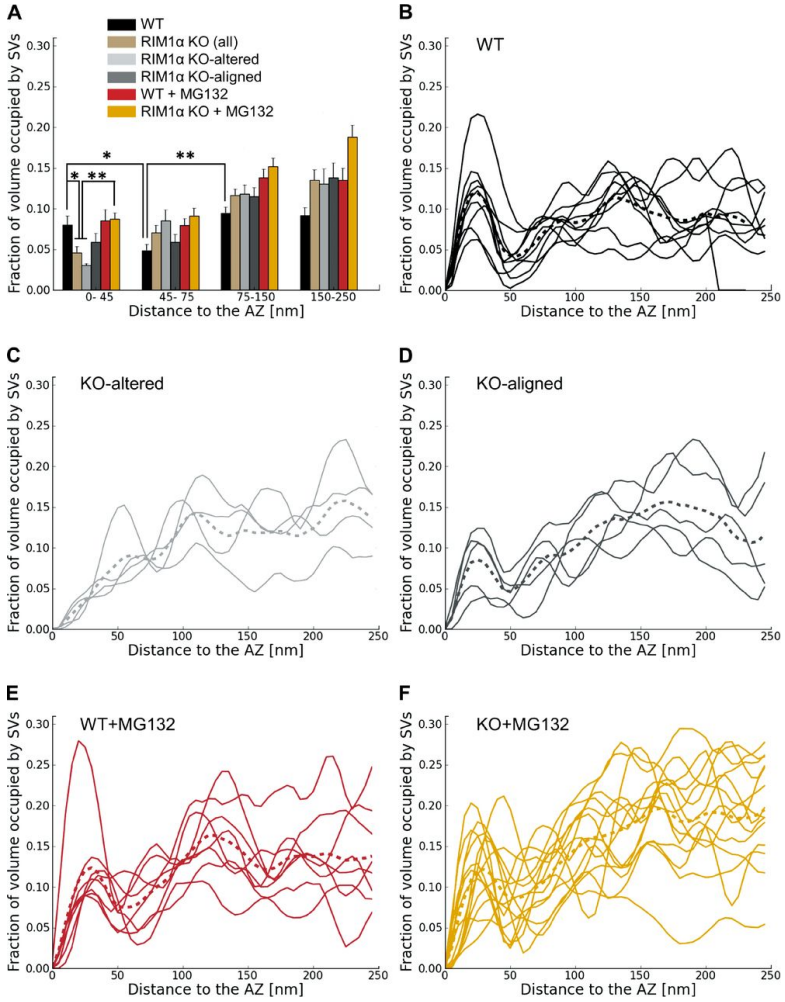

Figure 3.4: SV concentration within 250 nm from the AZ, (A) showing mean and sem of all treatments. The other graphs (B, C, D, E and F) depict the traces of individual synapses within the subgroup.

a similar SV concentration profile compared to WT, which we subsequently termed "KO-aligned". The remaining synapses had a significantly lower SV level compared with WT in the proximal zone ($P<0.05$, t-test) and were referred to as "KO-altered". Additionally, in KO-altered synapses, the difference in proximal SVs was even more pronounced with the number of SVs drop to 4.0 ± 0.9 ($P<0.05$, t-test). Interestingly, both subgroups of synapses were found in every KO mice analyzed.

Active Zone Area

The heterogenity in the KO subgroups could be seen here as well, where KO-altered had a significantly larger average AZ area than KO-aligned synapses ($P<0.05$, t-test, figure 3.5 B). While the difference in average AZ area between WT and KO was not striking, when we calculated the average AZ area per proximal vesicle, we observed a 3-fold increase for all KO terminals (n.s.). Furthermore, when we looked at KO-altered synapses only, a significant 5-fold increase over the WT level could be observed (figure 3.5 C, $P<0.01$, t-test). We used this data to additionally test for correlation between the

number of SVs and the AZ area. While the correlation was intact in the case of WT (Pearson correlation, P<0.01, t-test, table 3.2), it was completely lost in KO synapses (Pearson correlation, P>0.05, t-test, table 3.2). We did not observe any obvious clustering of SVs along the AZ.

Synaptic Vesicle Tethers

In agreement with previous data [108], proximal SVs were mostly connected to the AZ by filaments ("tethers") without any direct membrane contact (figures 3.6 A, 3.6 C and 3.6 F). It was proposed that proximal SVs with multiple small tethers are structurally primed and belong to the readily releasable pool (RRP) group - and ready for exocytosis [108].

While WT synapses had on average 6.4 ± 1.1 SVs tethered per synapse, this number dropped significantly to 1.7 ± 0.9 in KO-altered (mean ± sem, P<0.05, t-test, figure 3.6 A). Due to the larger AZ surface in KO-altered, the average number of tethers per unit AZ surface were also dramatically affected (P<0.01 by t-test, figure 3.6 D). While KO-altered showed no SV with more than two tethers, KO-aligned and WT shared a similar abundance thereof (figure 3.6 C). Subsequently, we calculated the correlation between the distance between SV and AZ and the number of tethers (table 3.3). WT showed an inverse correlation (Pearson correlation, P<0.001, t-test, table 3.3) while that correlation was lost in KO synapses (Pearson correlation, P>0.05, t-test, table 3.3). This became apparent as the tethers were significantly longer (P<0.01 by Kruskal-Wallis test, figures 3.6 E), whereas the fraction of short tethers got reduced (figure 3.6 F, P<0.01 by chi-square test, figure 3.6 E) in KO synapses. Again, the KO-altered subgroup showed an even more drastic effect.

3.3.3 Immunostaining Experiments

Immunostaining preparation and acquisition was done by Ana-Maria Oprisoreanu, and the analysis done by the author.

To quantify the existance of certain proteins in synaptosomes by fluorescence microscopy, we performed immunostaining experiments on synaptosomes from WT and RIM1α KO mice (for details refer to section 8.1.1). Our collaborator tested for the spatial overlap (colocalization) of AZ proteins ELKS, MUNC13, RIM1 and RIM2 with

Condition	Pearson Correlation Coefficient	P (t-test)
WT	0.82	< 0.01
KO	0.07	**> 0.05**
WT+MG132	0.80	< 0.05
KO+MG132	0.76	< 0.01

Table 3.2: Correlation between AZ area and number of proximal vesicles. The KO mice was not showing the typical correlation, as both the correlation coefficient and the statistical significance (marked red) shows. Statistical significances (P values) were determined by t-test (see section 8.1.4 for details).

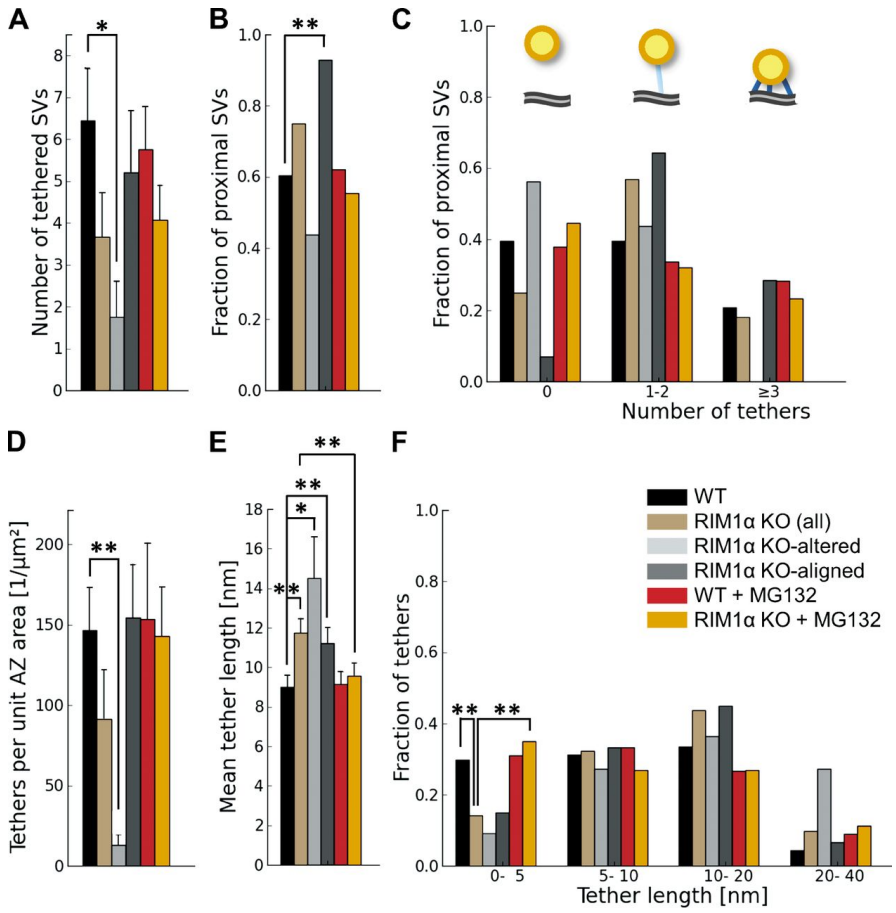

Figure 3.6: Tethering of proximal SVs (within 45 nm from the AZ, as virtually no vesicles were tethered in more distal areas).
Top row: (A) Number of tethered vesicles per synapse, which was strongly reduced in RIM1α KO-altered synapses. (B) Fraction of proximal vesicles tethered to the AZ. (C) Histogram of number of tethers per proximal vesicle. Note that no vesicles with more than two tethers were found in KO-altered synapses. (top) The cartoon represents the bins of the histogram: nontethered vesicles (left), vesicles with one to two tethers (middle), and vesicles with multiple tethers (right). AZ (gray), proximal vesicles (yellow), and tethers (blue) are shown.
Bottom row: (D) Number of tethers per AZ unit area. (E) Tether length. (F) Histogram of tether lengths. Short tether formation was impaired in RIM1α KO synapses. A, B, D, and E show mean values and sem (error bars). B, C, and F show number of occurrences (consequently no error bars are displayed).

Condition	Pearson Correlation Coefficient	P (t-test)
WT	-0.44	< 0.001
KO	-0.28	**> 0.05**
WT+MG132	-0.54	< 0.001
KO+MG132	-0.48	< 0.001

Table 3.3: Correlation between number of tethers per SV and SV distance to the AZ. Again, the KO mice did not display a correlation (marked in red). Statistical significance (P values) was determined by t-test.

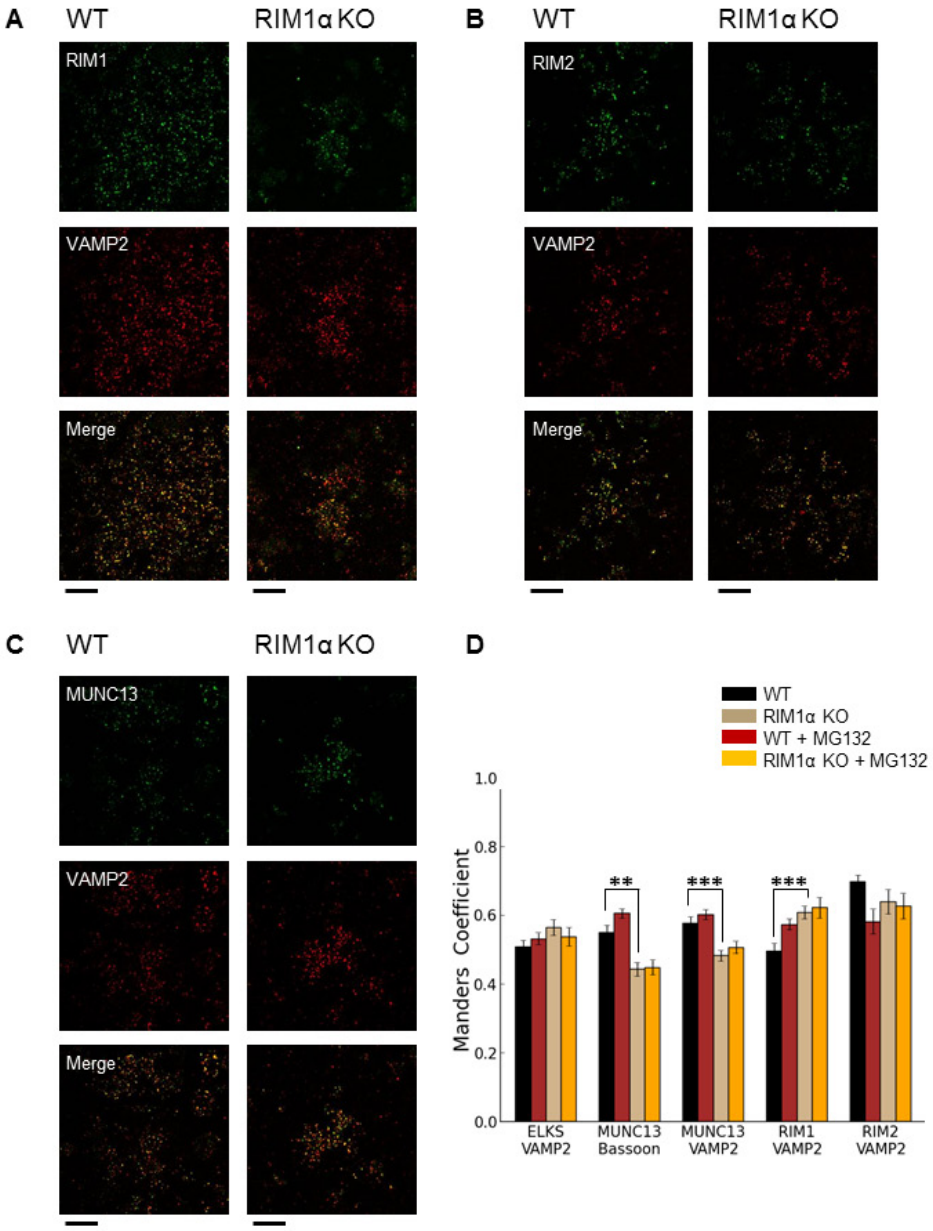

Figure 3.7: Immunostaining for AZ proteins. (A-C) Synaptosomes immobilized on coverslips were immunostained for VAMP2 (red) or Bassoon as presynaptic markers and for AZ proteins (green) including RIM1 (A), RIM2 (B), and MUNC13 (C). (D) Quantification of the fraction of AZ protein staining (ELKS, MUNC13, RIM1, and RIM2) colocalizing with presynaptic marker staining (VAMP2 and Bassoon), as measured by thresholded Manders' coefficients. Plot shows mean values and sem (error bars). Confidence values: $**, P < 0.01; ***, P < 0.001$ (n = 5 WT/ RIM1α KO littermate pairs, 15-20 images per condition). Bars, 20 μm.

presynaptic terminals, marked either by VAMP2 or Bassoon by means of FM. MUNC13 colocalization was significantly weaker in RIM1α KO synapses, confirming the previous

reports [125, 133]. RIM1 localization however increased in RIM1α KO synapses (both P<0.001, t-test, figure 3.7 A, D), which hinted to an upregulation of RIM1β, which was also observed in the western blot analysis. The other proteins tested showed no significant changes in the co-localization.

3.3.4 Proteasome Inhibitor Treatment

It is known that proteasomes are active in freshly extracted synaptosomes [134, 135]. With the widely used protease inhibitor MG132 we investigated the role of the UPS and its possible structural interactions with RIM1α in both WT and RIM1α synaptosomes.

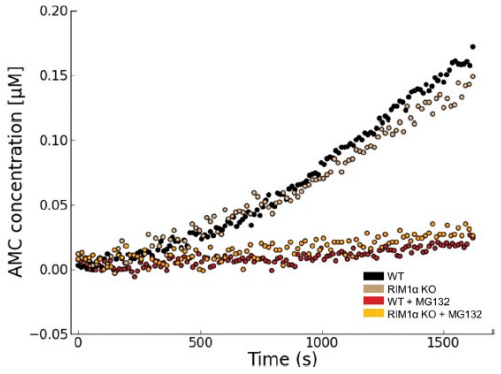

Figure 3.8: Proteasome chymotryptic-like activity in synaptosomes (representative traces), measured as AMC fluorescence resulting from substrate (Suc-LLVY-AMC) degradation. Proteasome activity was largely suppressed by MG132 treatment in both WT and RIM1α KO (n = 3 WT/ RIM1α KO littermate pairs).

A proteasome activity assay from the co-author Dr. Eri Sakata showed protein degradation activities that are actively inhibited by MG132 in both WT and KO littermate pairs (figure 3.8).

The western blot provided by Dr. Eri Sakata and Ana-Maria Oprisoreanu (figure 3.9) showed a downregulation of MUNC13 in KO synapses. Furthermore, a slight upregulation of RIM1β could be detected, while all other presynaptic proteins tested (RIM2, ELKS, Liprin2, Liprin3, Rab3, synaptotagmin1, syntaxin1, SNAP25 and VAMP2) remained unchanged.

Expectedly, KO synapses lacked RIM1α (figure 3.9) and furthermore showed reduced levels of MUNC13 [125, 133]. Upon incubation with MG132, higher concentrations of RIM1α in WT and MUNC13 in WT and KO could be observed.

MG132 Effects on Structure

MG132 incubation did not change the overall morphology of the synapses compared to untreated ones (figure 3.10 A, B, C, D). In general, WT synapses treated with MG132 were very similar to untreated ones in tethering properties. However, the KO synapses treated with MG132 showed predominantly (12 out of 14) WT-like SV concentration

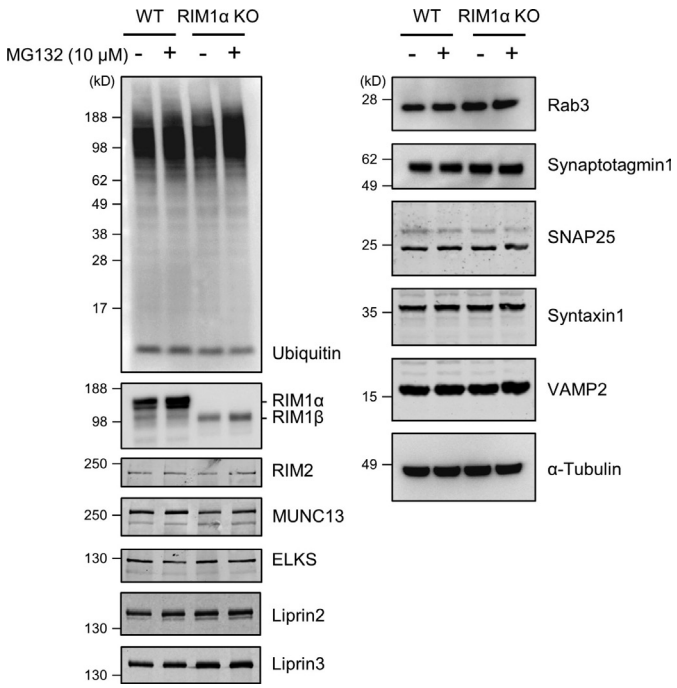

Figure 3.9: The double band detected for RIM1α corresponds to splice variants (see, e.g., Fig. 1 of [133]). MG132 induced an increase in the levels of RIM1α (WT), RIM1β (KO), and MUNC13 (WT and KO) and a smaller increase in RIM2 (KO) but not in other presynaptic proteins.

(figures 3.10, 3.4 A, F). The correlation between the AZ area and number of proximal SV was restored to WT levels as well (Pearson correlation, P<0.01, t-test, table 3.2).

Aforementioned increase in tether length in KO synapses (see subsection 3.3.2), as well as fraction of short tethers were reverted to WT levels upon MG132 incubation (P<0.01 (Kruskal-Wallis test), figure 3.6 E and P<0.01 (t-test), figure 3.6F). Importantly, the correlation between the number of tethers per SV and the SV distance to the AZ was restored to WT levels as well after MG132 treatment (Pearson correlation, P<0.001, t-test, table 3.3). In other criteria, such as number of tethered SV fraction, tethers per SV, and tethers per unit AZ surface, MG132-treated KO synapses were indistinguishable from WT (figure 3.6 B, C, D).

The electrophysiological paired-pulse facilitation (PPF) experiments performed by co-authors Dr. Michael Doengi and Prof. Valentin Stein offered an indicator for SV release probability [136] (figure 3.11). The PPF for MG132 treated KO synapses were very similar to those of WT (figure 3.11). Thus, while untreated KO slices suffered from low release probability (inverse to the PPF ratio value shown in figure 3.11, also previously reported [125]), the value for MG132 treated KO and WT slices appeared to be identical. MG132 did not show any effect when used on WT slices. Therefore the structural and functional deficit of RIM1α deficient synapses can be rescued by MG132.

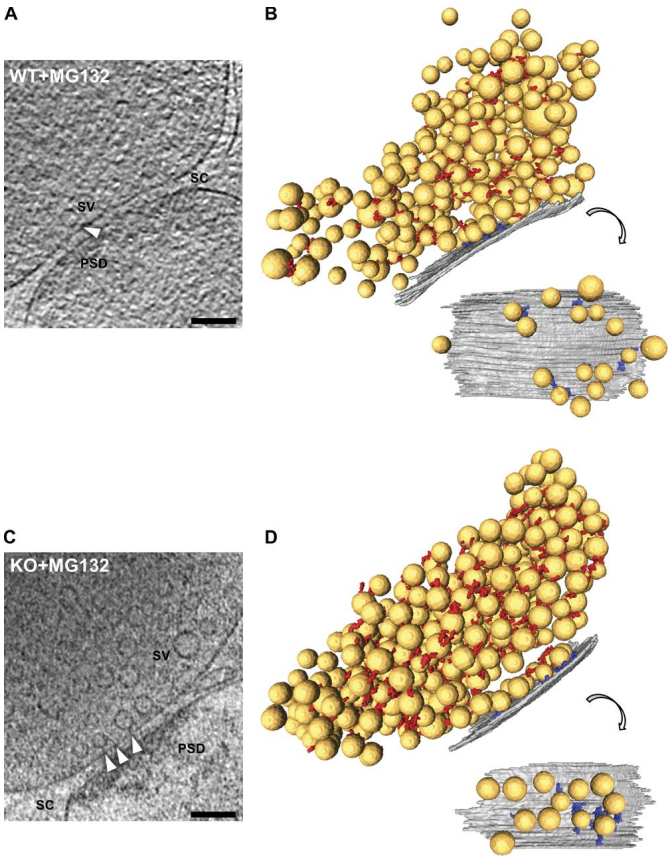

Figure 3.10: Morphology of MG132-treated WT and RIM1α KO synapses by ECT. (A and C) Tomographic slices of MG132-treated WT (A) and RIM1α KO (C) synapses. Postsynaptic density ("PSD"); synaptic cleft ("SC"); synaptic vesicle ("SV"); tethers (white arrowheads). Tomographic slices are 5.4 nm thick. Bars, 100 nm. B and D show corresponding 3D renderings of all vesicles analyzed (left) and of the AZ and proximal vesicles seen from the cytoplasmic side (right). AZ (gray), SVs (yellow), tethers (blue), and connectors (red) are shown. For scale reference, mean vesicle diameter was $40.1 \pm 5.4nm$ (mean ± SD; no scale bars are shown because the image is rendered with 3D perspective). MG132-treated WT and RIM1α KO synapses were comparable in terms of proximal vesicle concentration and vesicle tethering to the AZ.

3.4 Discussion

3.4.1 Abnormalities in RIM1α KO Synapses

In the conducted ECT study, several substantial differences could be seen between WT and RIM1α KO mice synapses. The proximal zone - where the protein RIM1α is located - was especially affected by a significantly disturbed SV concentration and its resulting cytomatrix reorganization.

RIM1α KO synapses demonstrated a severely reduced SV concentration at the proximal zone, directly accounting for the lower proximal SVs number at the AZ (figures 3.4 A, 3.5 A). Combined with the SV tethering defects observed in figure 3.6, we could therefore observe dramatic alterations of at least three important parameters for SV fusion.

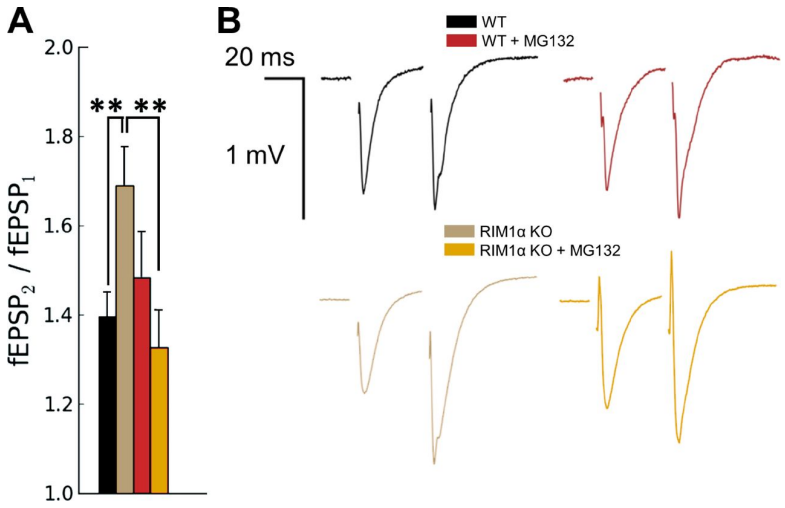

Figure 3.11: (A) PPF ($fEPSP_2/fEPSP_1$) recorded in stratum radiatum of CA1. The graph shows mean values and sem (error bars). Confidence values: $**$,$P < 0.01$. Compared with WT mice, RIM1α KO mice showed an increase in PPF that was reversed by MG132 treatment. (B) Representative traces. Sample sizes are as follows (slices/animals): WT, 14/4; WT + MG132, 16/4; RIM1α KO, 14/4; and RIM1α KO + MG132, 13/4.

The significant tethering defect in RIM1α KO synapses in combination with the reduced number of proximal SVs most likely caused the functional deficit observed in electrophysiology (figure 3.11). Thereby, SVs are rarely tethered but highly connected to other SVs, leading to a low response in the first stimulus, but a much stronger one in the second by pulling its connected SVs partner(s) towards the release site.

A previous report [108] suggested a model where SVs get pulled to the AZ and gain shorter tethers in order to mature and become primed. This is consistent with in vitro observations showing a direct correlation between SV distance to the AZ and its ability to fuse [137, 138]. The correlation shown in table 3.3 indicated that SVs from WT synapses did indeed form more and shorter tethers upon approaching the AZ. However this correlation was lost in RIM1α KO synapses (table 3.3), and together with the tethering defects possibly accounting for the electrophysiological anomaly (figure 3.11) and reduced RRP size observed in RIM1α KO mice [125, 126].

As outlined earlier, RIM1α KO mice exhibited multiple presynaptic defects affecting the overall release kinetics (figure 3.11) and potentially resulting in impaired memory and learning [125]. Interestingly, conventional (chemically-fixed) EM was not able to detect any ultrastructural changes in RIM1α KO synapses [125], most probably due to preparation artifacts occuring during the chemical fixation, dehydration and heavy metal staining steps [4, 128, 129].

3.4.2 MG132 Rescue of RIM1α KO Synapses

WT synapses were mostly unaffected by addition of proteasome inhibitor MG132 in terms of AZ area, proximal SVs number (figures 3.5), and as well as major tethering characteristics (figures 3.6). This is in line with the literature, which did not detect any

major effect on the RRP upon MG132 addition in FM [105].

However, RIM1α KO synapses upon MG132 exposure exhibited a drastic rise in SV concentration near the AZ compared to untreated KO synapses (figure 3.4 A, F). Together with the enhanced formation of shorter tethers (figure 3.6) MG132 treated RIM1α KO synapses appeared to be indistinguishable from WT, effectively rescuing the defects in the proximal area of KO synapses. Subsequently, both correlations between the AZ surface area and the number of SVs (table 3.2), as well as the number of tethers per SV and the SV distance to the AZ (table 3.3) of RIM1α KO synapses were reverted to WT levels upon MG132 addition. This ultrastructural rescue was in agreement with a functional one demonstrated by electrophysiology (figure 3.11).

RIMs, as well as MUNC13 were identified as UPS targets [104, 105, 139–142], which led to moderate increases in RIM1β, RIM2 and MUNC13 levels in KO synapses incubated with MG132, demonstrated by western blotting (figure 3.9), and further verified by means of immunofluorescence (figure 3.7). Since the average difference in tether numbers between WT and KO synapses was small, the slightly higher expression levels of RIMs and MUNC13 might be just enough to form few RIM-MUNC13 priming complexes sufficient to successfully rescue the KO ultrastructure and function.

Therefore the data suggests that the UPS is playing an influential role in the tethering mechanism. This was already observed for the drosophila isoform of MUNC13, which accumulates after proteasomal inhibition [141], and similarly the SV protein synaptophysin [143]. Additionally, the UPS was shown to regulate synaptic strength pre- [144] and postsynaptically [145, 146]. All those lines of evidence affirmed the correlation between the UPS function and the ultrastructural morphological changes observed in our study.

3.4.3 Two RIM1α KO Synapse Groups

We could identify two different subgroups within the RIM1α KO synapses. While KO-aligned synapses demonstrated less severe variations (figures 3.4 A, D and 3.6), the KO-altered showed much more austere alterations compared to WT (figures 3.4 A, C and 3.5 A). Additionally, SVs from RIM1α KO-altered synapses completely failed to form multiple tethers to the AZ (figure 3.6 C), as well as short tethers (figure 3.6F).

Given that synaptosomes were prepared from whole cortices [108, 109, 130], the structural variability in RIM1α KO synapses may reflect the discrepancy in RIM expression levels in synapses from different brain regions or under different activity levels [104, 105, 125, 147]. Thus, a RIM1α KO synapse would be more affected when the RIM1α expression level is usually very high or the level of possibly compensatory other RIMs is very low. Finally, a study found that distribution of RIM1β and MUNC13 is altered in RIM1α KO synapses [133, 148], possibly accounting for the significant difference of those protein levels in our immunostaining experiments (figure 3.7).

Most likely, the heterogenity in the RIM1α KO synapses were not due to differences between inhibitory and excitatory synapses, as most synapses had a prominent postsynaptic density (figure 3.3 A, D, F), and no major differences in synaptic

transmission were measured between inhibitory and excitatory synapses in RIM1α KO mice [133].

3.4.4 Synaptic Vesicle Tether Formation

The exact molecular components of tethers are still unknown [108]. Western blot data presented here (figure 3.9) showed that out of numerous AZ proteins tested, only MUNC13 was downregulated in RIM1α KO synapses. Thus the defect observed in KO synapses could be attributed to these two proteins. However, other AZ proteins not yet analyzed might play a role as well. This gave rise to a tether formation model where RIM1α and/or MUNC13 are important factors, but not solely the only ones, as few tethers still existed in KO synapses.

Another possible candidate for tether formation might be RIM1β, as it was the only synaptic protein found to be upregulated in RIM1α KO [133]; this study (figures 3.9, 3.7). It was shown that overexpression of this protein was able to almost completely rescue the otherwise lethal RIM1/2 KO phenotype [114]. Also, RIM2α and RIM1β are the only other RIM isoforms containing the zinc-finger domain that interacts with MUNC13 [112]. Therefore, the upregulation of RIM1β might be able to partially compensate the missing RIM1α.

3.4.5 Synaptic Vesicle Priming Model

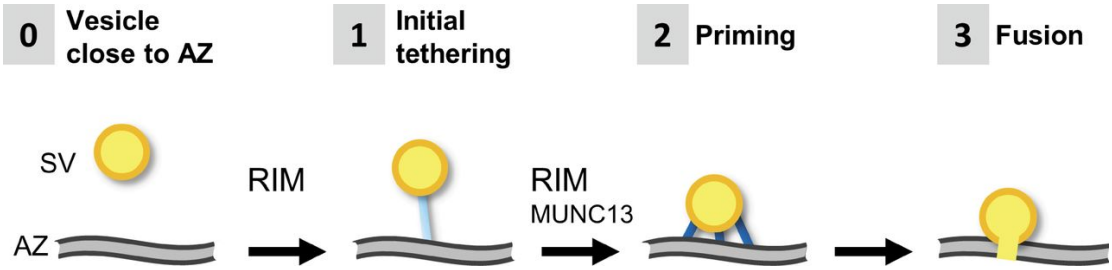

Figure 3.12: In WT terminals, SVs (yellow circles) that are close to the AZ (0) are first linked to the AZ (1) by one or few tethers (blue rods) in a RIM-dependent process. Likely by the action of RIM and MUNC13, vesicles progressively acquire additional shorter tethers, thereby reducing the distance between SV and AZ. SVs with multiple tethers are primed for release (2), and primed SVs can fuse upon Ca^{2+} influx (3).

Our updated model for SV priming proposed in this work is shown in figure 3.12. The first step in the priming process is the formation of the first link between the SV and the AZ. This is very likely dependent on only RIM, as the number of SV within 45nm from the AZ was not reduced in a MUNC13-1/2 DKO study [149], reduced in this RIM1α KO study (figures 3.4 A, 3.5 A), and heavily reduced in RIM1/2 DKO studies [115, 116]. In the next step, the SV approaches the AZ and is getting "structurally primed" by gaining more and shorter tethers. During this step, RIM1α (and maybe other RIMs) are involved, possibly by forming a priming complex with MUNC13. However, we could not exclude that the defects in short tether formation in the RIM1α KO could be exclusively due to the reduction in MUNC13 levels in these mice.

While other proteins, such as synaptotagmin1 or ELKS [150, 151] appear to be interesting candidates for short tethers as well, we did not see any major changes in the protein expression levels in our RIM1α KO sample (figures 3.9, 3.7). Additionally, during the ultrastructural and functional rescue via proteasome inhibition, the UPS regulated targets such as liprins or synaptotagmin1 [104] did not show any significant changes upon MG132 incubation.

All together, the model is proposing a priming mechanism, where the SV first gets its initial tether via a RIM dependent mechanism, and additional shorter tethers probably via RIM and/or MUNC13 dependent processes.

3.5 Summary and Outlook

The data demonstrated the significance of RIM1α in the tethering machinery during SV priming by directly providing the structural correlate to a deranged, SV release impaired RIM1α KO mouse. Based on this comparison, a model was proposed in which RIMs play a major role in the initial tethering of SVs and their approach to the AZ. Interestingly, the UPS was highly involved in presynaptic AZ morphology as well, significantly affecting key parameters, such as SV tethering. Albeit direct evidence of individual 26S proteasomes was missing, the synapses were clearly affected by proteasome inhibition. RIM1α KO synapses were effectively rescued by MG-132 and showed WT like characteristics and PPF signal.

This direct comparison between electrophysiology and ultrastructure allowed us to establish a direct relationship between the reduced number of proximal vesicles and their defects in tether formation with the observed release deficit of RIM1α KO synapses. Furthermore the data suggested an important role of the UPS in both presynaptic cytomatrix and function, both associated with terminal-specific plasticity [104, 105].

For further studies, two major issues are of key interest, which are addressed in later chapters. The first two (chapter 5 with 6) concentrated on the validity of the provided SV exocytosis model in short timeframes of 10-100 ms after stimulation. The second major study (chapter 7) aimed to find direct evidence of 26S proteasome protein complexes within neurons.

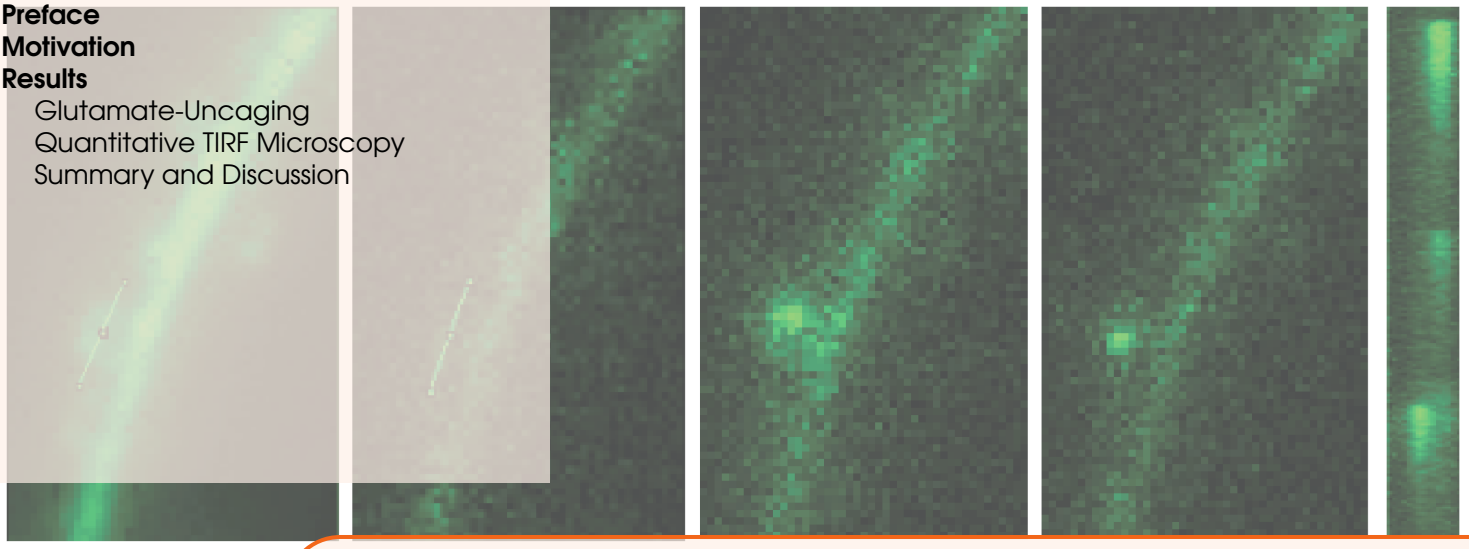

4. Light Microscopy Studies of Cultured Neurons

4.1 Preface

During summer 2012, the author received a JSPS fellowship grant for a two months research stay at the University of Tokyo in the Department of Cellular Neurobiology in the lab of Prof. Shigeo Okabe [1]*. The four major areas of research included:*

1. Preparation and processing of neuronal cell cultures from rats
2. Transfecting neuronal cultures
3. Single spine stimulation with glutamate-uncaging in neuronal cultures
4. Characterizing a novel genetically encoded Ca^{2+}-reporter with TIRFM

The goal of this research project was to acquire the expertise in culturing and transfecting rat hippocampal neurons, in order to use them as a reliable model system for neuronal studies in later ECT projects (chapter 7). Additionally, TIRFM and glutamate uncaging studies on cultured neurons provided invaluable experience in research on time-sensitive, transient biological processes and UV light induced stimulation techniques, necessary for later ECT studies (chapters 5, 6, and 7). The mother animals were generously provided by Prof. Okabe. Training and advice was mainly provided by Dr. Tomoe Urushido and Dr. Ayako Hayashi. All animals, chemicals and equipment were kindly provided by Prof. Shigeo Okabe.

4.2 Motivation

We used synaptosomes as a biological model system to study the ultrastructure underlying synaptic activity. The advantage of synaptosomes lies in their relative

[1] Homepage Department of Cellular Neurobiology, The University of Tokyo: http://synapse.m.u-tokyo.ac.jp

ease of extraction [152, 153] and processing for ECT [108, 109]. On the other hand, disadvantages, such as disrupted membranes and high shear forces during extractions or their limited energy supply [153, 154] require more physiological alternatives. It therefore became cruicial to transition into a less disturbed neuronal model system. Neuronal cultures have been studied for over decades [155], with a significant emphasis on rat hippocampal neuron cultures [156, 157]. To establish a neuronal culture, neurons are isolated by means of mechanical and chemical dissociation from freshly extracted brain tissue, and then cultured in specific media [156, 158]. Advantages of using neuronal cultures are the reduced complexity compared to the pure brain tissue, the possibility for genetic manipulations (transfections), all while still maintaining important cellular functions over a long period of time [156].

Observing neuronal cultures is routinely performed in FM, with latest technical developments encompassing light sensitive channelrhodopsin ion channels [159], highly bleach-resistant quantum dots [160], smart stochastic fluorophore expression mechanisms to identify connectomes [161], and of course the several approaches to superresolution FM, such as PALM [19], STED [17] or STORM [18]. These methods enabled a direct and live view inside neuronal networks and provided extensive knowledge in the molecular interaction and composition of synaptic connections [162]. However, FM cannot visualize ultrastructural details, or the detailed morphology of a synapse, which is necessary for the mechanistic understanding of cellular function.

Ultrastructural studies with conventional EM were first used with slices cut from chemically fixed and resin embedded brain samples [163, 164]. These slices could be prepared thin enough for studying neurons with EM, but were affected by fixation artifacts, such as shrinking membranes, aggregation, or other dehydration effects [33, 165]. In contrast, ECT imaging in frozen-hydrated neurons provide an artifact-free view, but is more challenging to perform, due to difficulties in finding a position with a suitable thickness. Thus, only sparsely seeded neuronal cultures [156] are suitable for artifact-free ECT recording, albeit new FIB methods might be able to lift these restrictions [61]. Notably, a more recent advancement include the combination of the localization capabilities with FM and the ultrastructural resolution in EM in a correlative approach in neurons [166].

Hippocampal Neuronal Cultures

The neuronal cultures were grown from embryonic E18 mouse hippocampal cells, due to the cellular homogeneity within this part of the brain, which consists mainly of pyramidal neurons and some interneurons [167]. Clonal/continuous neuronal cell lines were avoided due to their inability of forming synaptic connections [156]. The protocol used for establishing the neuronal culture was provided by the host department [168]. In essence, a pregnant mouse was anesthetized by ether and then killed by manual cervical dislocation. The belly was cleaned and cut open and 10-12 embryos (embryionic day 18) were carefully taken out of the womb. The brain of each embryo was then extracted and then its hippocampus isolated in ice-cold HBSS. Several rounds of chemical dissociation with physical force (pipetting) was used to separate the cells gently. Additional chemical

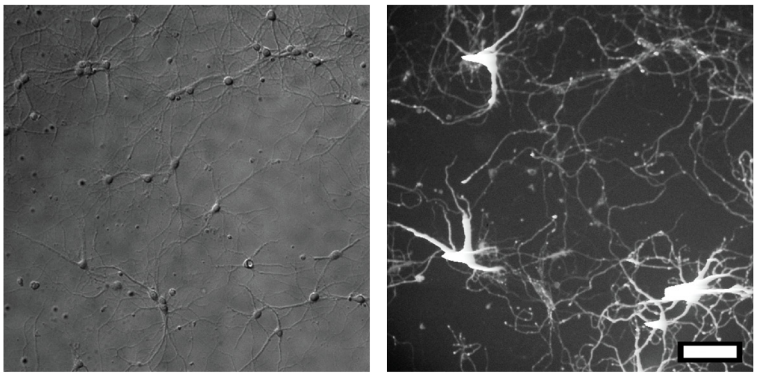

Figure 4.1: 10x magnification images of a healthy hippocampal neuronal culture, transfected with GCaMP7, recorded at DIV18. Left: Bright field image showing several cell bodies. Right: FM image of the transfected cell, clearly showing dendrites and substructures not seen in bright field image. Scalebar: 100 μm

dissociation was done with trypsin supplemented with DNAse to avoid clumping of concentrated and "sticky" DNA. The last step included a mechanical separation with a cell strainer (70μm mesh), before cell counting took place.

High and low density (more suitable for ECT studies) dishes were plated with $2.2 \cdot 10^5$ and $1.8 \cdot 10^5$ cells per 35 mm dish, respectively. After seeding and initial incubation at 37°C and 5% CO_2, 10μM cytosine arabinoside was added two days after plating to stop proliferation of glial cells in culture [169]. Cultured neurons were checked under a light microscope for correct growth and in later experiments, transfection rates verified with FM. An example from a healthy and transfected culture expressing the Ca^2+ reporter GCaMP7 (see section 4.2 below) can be seen in figure 4.1. The main problems of hippocampus extraction arose from severe time restrictions in both taking out the embryos from the womb and cutting out the hippocampus. Extremely precise cutting was required to keep the hippocampi intact and undamaged for further steps. The success rate of the hippocampus removal was around 90%, with the average time of five minutes per hemisphere. All steps were performed in ice-cold buffer to reduce cellular degradation processes.

GCaMP6/7: Genetically Encoded Ca^{2+} Sensors

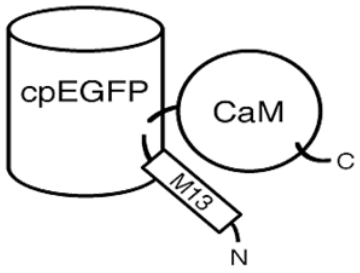

Figure 4.2: The schematic topology of the GCaMP complex. A permutated GFP molecule (cpEGFP) and a calmodulin complex are fused at the C terminus, while the M13 (myosin light chain fragment) is fused on the N terminus. Adapted by permission from Macmillan Publishers Ltd: Nature Biotechnology [170], copyright 2001.

GCaMP6 and GCaMP7 are genetically encoded Calcium indicator dyes that were provided by Prof. Junichi Nakai and Prof. Shigeo Okabe (see figure 4.2 for a schematic topology) [170, 171]. Upon intracellular Ca^{2+} elevation, Ca^{2+} binds to the EGFP fused CaM complex and the Ca-CaM-M13 interaction causes a conformational change in the EGFP molecule, highly improving its fluorescence [2] [170].

The latest generation of genetically encoded Ca^{2+} sensors, GCaMP6, GCaMP7, and GCaMP8 [171] have a high dynamic range (GCaMP6: $F_{max}/F_{min} = 11.4 \pm 0.11$ and GCaMP7: $F_{max}/F_{min} = 36.6 \pm 4.10$, from [171]). Their Ca^{2+} affinity K_d values are inversely related to their dynamic range, with $K_d(GCaMP6) = 158 \pm 4nM$ and $K_d(GCaMP7) = 243 \pm 14nM$ [171]. Signal rise time is 60 ms and the decay time for GCaMP6 and GCaMP8 is 400-450 ms[171].

Neuronal Culture Transfection

The method of choice for transfecting neuronal cultures was the calcium phosphate method [172, 173]. Its ease of use and high reliability (success rate: 38 out of 40 dishes) allowed us to disregard more complicated methods, such as viral infection, DNA-injection or electroporation [174–176]. While some of those alternative methods might be more suitable in other cell systems, they did not provide the same level of reproducibility and/or cell viability [177]. The calcium phosphate transfection method employed was based on the protocol provided by Jiang and Chen [173], with modifications from the laboratory of Prof. Shigeo Okabe. An overview scheme is provided in figure 4.3.

In brief, we prepared 2 mL of Minimum Essential Medium (MEM) medium supplied with 10 μl 100 mM glutamine per 35 mm dish as the transfection medium. After preparation, we first incubated half the medium at 37°C and 5% CO_2, the other half at 10% CO_2 for 20 or more minutes.

[2] Excitation wavelength: 488 nm; Emission wavelength: 509 nm

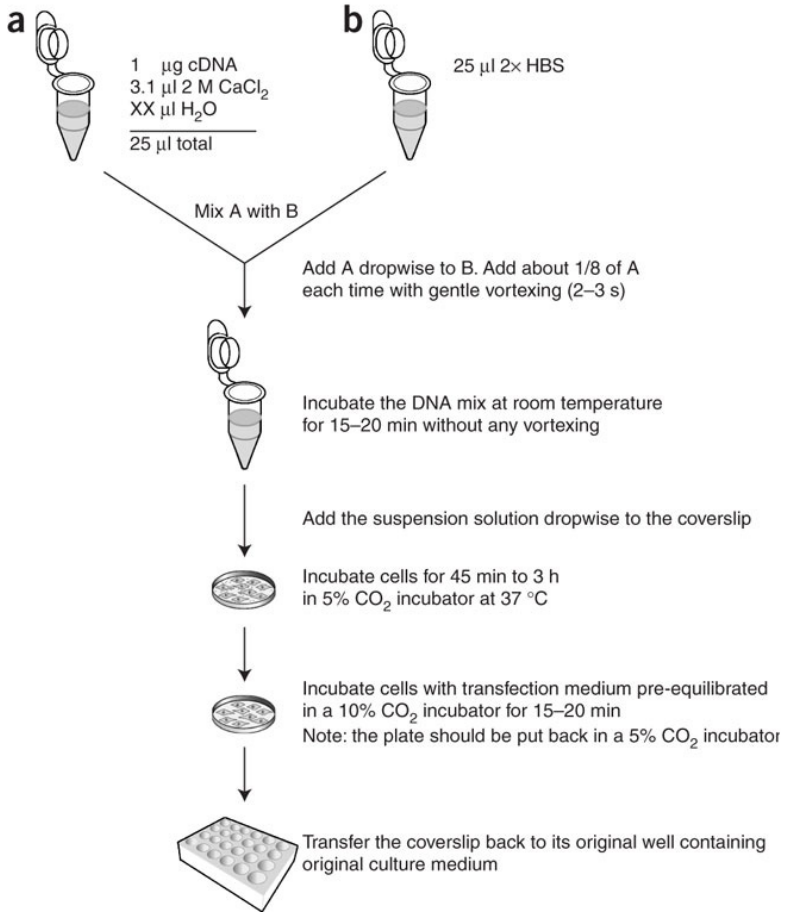

Figure 4.3: A schematic overview of the calcium phosphate method used for transfecting the neuronal culture. Reprinted by permission from Macmillan Publishers Ltd: Nature Protocols [173], copyright 2006.

The medium in the dish was exchanged with the first half of the medium (equilibrated to 5% CO_2) and subsequently stored inside the 37°C and 5% CO_2 incubator. The previous medium was saved in another dish and kept in the 37°C and 5% CO_2 incubator for a later step.

Meanwhile, the transfection solutions (amount per dish) were prepared as following, similar to the values provided by the original protocol [173]:

Solution A:

Transfection DNA	$4\mu g$
2 M $CaCl_2$	$6.25\mu l$
H_2O	fill up to $50\mu l$

Transfections with GCaMP6 and GCaMP7 were done with the concentrations: $4\mu g$ for GCaMP6/7, $1\mu g$ for mRFP, and MCS empty vector to fill up to $8\mu g$ per dish.

Solution B:

2x HBS	$50\mu l$

Solution A was mixed in solution B in eight consecutive steps, by pipetting up and down,

vortexing it gently for 2-3 seconds, and finally leave it to rest for 15-20 minutes. The incubated neurons with the transfection media were then taken out of the incubator and then 100 μl of the mixed transfection solution was pipetted gently over the cells. The dishes were then returned to the 37°C and 5% CO_2 incubator for 1-3 hours. Then the medium was exchanged with the other half of the transfection medium incubated at 10% CO_2 and kept inside the 5% CO_2 incubator for 15-20 minutes. Lastly, we removed the transfection medium completely and resupplemented the culture with the previously saved neuronal medium.

Transfections were done after 6 days in vitro (DIV 6) and mostly observed between DIV 13-20. Neuronal cultures transfected with this method yielded in homogeneously transfected, but also well developed neuronal structures. A qualitative result can be seen in figure 4.1.

Study of excitatory postsynaptic currents (EPSCs) in Transfected Cultured Neurons

In synaptic transmission, neurotransmitter are released into the synaptic cleft and bind to receptors connected to the PSD. Examples of such receptors are the N-Methyl-D-aspartate (NMDA) and α-Amino-3-hydroxy-5-methyl-4-isoxazolepropionic acid (AMPA) ionotropic glutamate receptor classes in excitatory (glutamatergic) synapses. Once the neurotransmitters (glutamate) bind to the receptors, they in turn open ion channels permeable to sodium, which then enters the postsynaptic spine. This depolarization of the postsynaptic membrane potential is called excitatory postsynaptic potential (EPSP), which generates an excitatory postsynaptic current (EPSC). Spontaneous EPSCs are action-potential independent EPSC events, mostly occurring through random SV exocytosis [178].

So called miniature excitatory postsynaptic potentials (mEPSPs) have been described as early as 1951 by Bernard Katz [179], and are considered to be the smallest unit of depolarization by exocytosis of one single SV. Effectively, a bigger EPSP signal is build upon a multitude of these mEPSP "quants". Using glutamate light uncaging and later TIRFM, we were able to induce and image EPSC events. There was no reliable detection of EPSCs with genetically encoded sensors reported, at the time of the experiment [171]. Therefore goal of this study was to characterize basic kinetics of the genetic probes and to check whether they allow for a robust and direct detection of single evoked postsynaptic currents (EPSCs), the precursor for an action potential at the postsynaptic site.

Single Spine Glutamate Light-Uncaging

The microscope used for the glutamate uncaging experiments was an Olympus FV1000 MPE, connected to a MaiTai (Spectra Physics) infrared (2-photon) laser. Due to difficulties in gaining fast switching times between illuminations, we only used the one-photon mode for our experiments.

Glutamate uncaging was performed with caged glutamate (MNI-Glu) on hippocampal cultures transfected with GCaMP6 or GCaMP7 (see section 4.2). The experimental

setup included a micromanipulator with a glass capillary and injection system in order to provide caged glutamate (MNI-Glu, c = 3 mM) close to the area of interest. The correct positioning of the glass capillary closely above the neuron was ensured by visually checking through an Olympus 60x water immersion objective, which was also used for fluorescence imaging. Furthermore, by additional transfection of the cultured neurons with mRFP we were able to visually identify the finer neuronal structures easier, facilitating glass pipette positioning (refer to above section 4.2 for details). Later, instead of microinjection, a bath application of caged glutamate (MNI-Glu, c = 3 mM) was used for uncaging measurements. The programming of the timing of injection and the UV illumination (at 405 nm) were done directly in the Olympus user software.

total internal reflection fluorescence microscopy (TIRFM)

The microscope used for TIRFM was an Olympus IX-81 motorized inverted microscope, with an Olympus 100x TIRFM oil immersion objective. The control of the microscope and the illumination system, as well as the image acquisition was administered by the software Metamorph (Molecular Devices). We used a 488nm Ar-laser setup for the GCaMP6/7 TIRFM recording.

The imaging detector was an Andor Ixon 3 CCD camera with the maximal frame rate of 549 fps, or roughly 1.82 ms resolution. For recording fast responses, we used a field of view of ≤100x100 unbinned pixels (≤13x13 μm), resulting in time resolutions above 3.33 ms. We also used time series with 15ms frames and 40000 frames in total for overviews. The sample stage could be heated, but due to the increase in vibrations, we powered the heating off during image acquisition, eventually limiting the experimental time and the viability of the neurons.

Treatments Used for TIRFM Study of Neuron Culture

Three commonly used channel/receptor blocking agents were utilized for our TIRFM study. The neurotoxin tetrodotoxin (TTX) binds specifically to the extracellular pore opening of voltage-gated sodium channels [180]. This electrostatically blocks the flow of sodium ions inside, effectively inhibiting depolarization and generation of action potentials [181]. The prevalent voltage-gated sodium channel is highly sensitive to TTX, with a $K_D = 6nM$ binding affinity [182] and was used in every buffer (with $c = 1\mu M$) of this study to block neural activity and isolate spontaneous EPSCs, caused by a random SV fusion events at the presynapse [183].

Additionally, $100\mu M$ APV was initially used for blocking N-Methyl-D-aspartate receptor (NMDAR), a glutamate receptor and Ca^{2+} ion channel as control. AP5/APV is a synthetic compound, which blocks NMDA ionotropic glutamate receptors competitively [184] with a K_d of $\approx 50\mu M$. This treatment was used to isolate and evaluate the effect of non-NMDA channels, such as AMPA receptors. By washing the buffer containing the AP5 afterward, we were able to investigate the contributions of NMDAR-dependent processes.

Lastly, in later experiments, $30\mu M$ Bicucullin was additionally used in transfected cultures. Identified in 1932 in plants [185], bicucullin is a competitive γ-aminobutyric

acid (GABA) receptor channel antagonist with a dissociation constant of $k_d \approx 1\mu M$ [186]. The GABA receptor is a Cl^- anion channel, and thus acting inhibitory on action potentials by hyperpolarizing the membrane upon activation. Therefore, by adding bicuculline in micromolar quantities, we induced an epilepsy-like state (of over-excitability), which led to an increased frequency of spontaneous EPSP events [187, 188].

4.3 Results

4.3.1 Glutamate-Uncaging

To first evaluate the diffusion process of the caged glutamate in buffer, we used a fluorescent dye (Rhodamine based Rhod6G) inside the glass pipette. After microinjection of this dye into the buffer, we could observe a fast heterogeneous diffusion of the dye in FM within less than two seconds (figure 4.4). Therefore, to ensure a locally high caged glutamate concentration at the site of stimulation and subsequently uncaging yield, it is required to flash the culture as soon as the compund is microinjected into the neuronal culture.

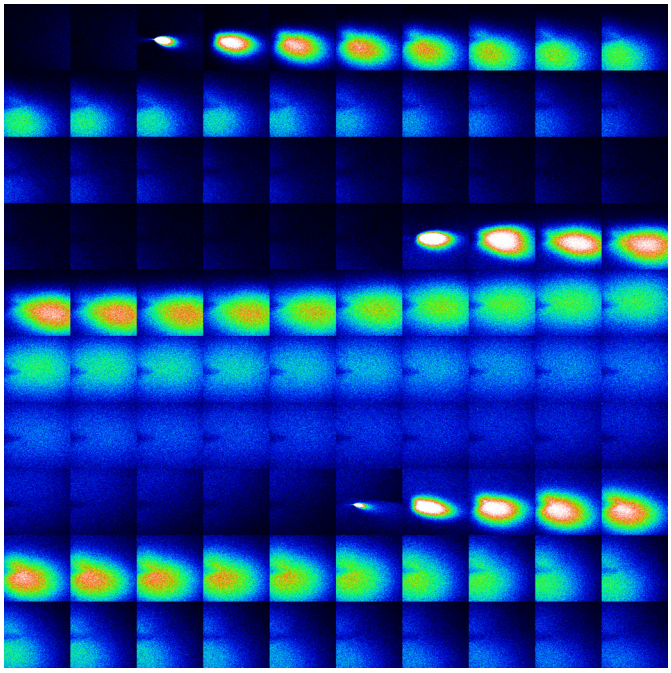

Figure 4.4: Qualitative assessment of dye diffusion with FM. From top left to bottom right: False-color frames of a time series capturing Rhod6G dye diffusion after being microinjected (for a total of three times) in medium. The FM time series was taken with a 60x water immersion objective inside neuronal medium and 430ms intervals between frames.

After checking the microinjection delivery system with dye (figure 4.4), we filled the capillary with caged glutamate (MNI-Glu, $c = 3$ mM) [189, 190]. The regions of interest (ROI) of the UV flash were either single spots or small areas, e.g. a single synaptic spine

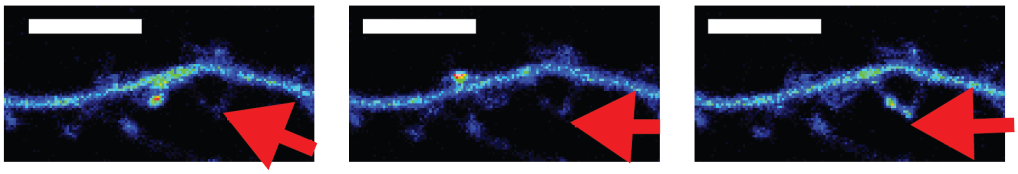

Figure 4.5: Application of a UV flash at a single spot (marked with an red arrow) shortly after spraying MNI-Glu ($c = 3mM$) leads to heterogenous Ca^{2+} response, reported by GCaMP7. Left and center: Stimulation of a remotely located spines. Right: Stimulation at the intended spine. Scalebar: 10 μm

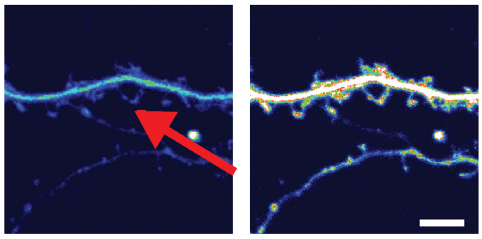

Figure 4.6: Bath application of caged MNI-Glutamate $c = 3mM$ and its inherent localization problem. We stimulated a single spot (red arrow), but most likely due to diffusion of uncaged glutamate, all spines including the dendrite got stimulated (false color representation), and similarly the dendrite below to a lesser extend. Scalebar: 10 μm

(figure 4.5). While it was possible to attain glutamate in high enough levels to generate a postsynaptic response (seen by Ca^{2+}-increase indicated by the Ca^{2+}-reporter), we were not able to reliably induce any single spine responses within the area marked by the ROI (figure 4.5). This was most likely caused by the diffusion of the glutamate (similar to the diffusion observed in figure 4.4), which in turn stimulated remote synapses as well. This problem could be observed more drastically in culture medium supplied with $c = 3$ mM caged glutamate, where one UV flash aimed at a single spine stimulated whole dendrites (figure 4.6).

4.3.2 Quantitative TIRF Microscopy

Initial spontaneous EPSC Detection

TIRFM was performed on hippocampal cultures transfected with GCaMP6 or GCaMP7 (see section 4.2). In both cases, we were able to observe what appeared to be Ca^{2+} transients signals caused by spontaneous EPSCs, as the culture medium (4mM Ca^{2+}) included $1\mu M$ TTX. Delicate structures, such as dendritic spines could be occasionally observed with the GCaMP base fluorescence, but due to low initial signal in some cases they could only be detected during EPSCs (figures 4.7 B, C). This was especially the case in GCaMP7 transfected cultures, where the base fluorescence was very low (compare to figure 4.8 B). However, once a Ca^{2+} transient was reported by the dye, the increase in fluorescence enabled reliable detection of EPSCs (figures 4.7 B, C). Furthermore, we were able to discern highly closely spaced synaptic spines of around 500 nm apart (figures 4.8 C, D, E).

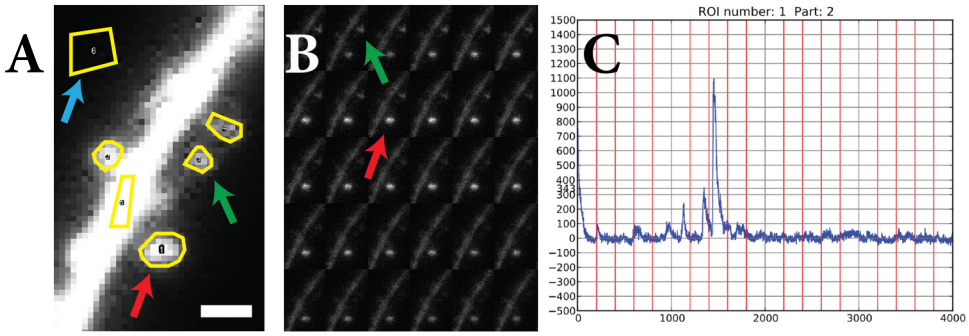

Figure 4.7: Timelapse of an active neuron with several spines. A) Several ROIs marked on a frame (indicated yellow) with the maximum grey value for each pixel of a time series, taken with TIRFM. ROI marked with a blue arrow corresponds to a region used for background and noise calculation measurement. Scalebar: 2 μm. B) Individual frames of the time series showed blinking spines located right of the dendrite, corresponding to ROI 1 and 3 (marked with a red arrow and green arrow in A and B). C) Normalized intensity (a.u.) over frames of ROI 1, showing an EPSC via its sharp peak at around frame 1600.

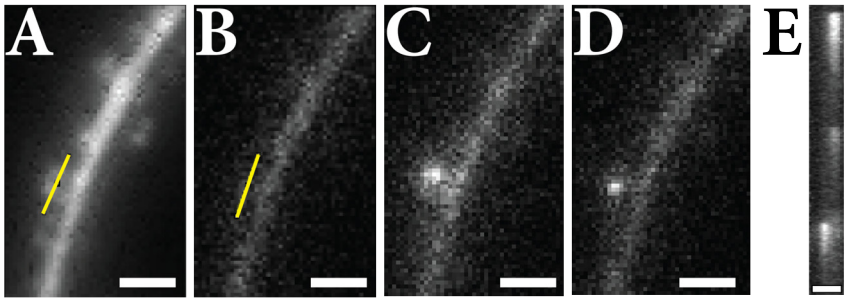

Figure 4.8: Kymograph showing spatially separated synaptic spines. A) A ROI (yellow line) mark displayed on a frame with the maximum grey value for each pixel of a time series, taken with TIRFM 4.3.2. Same area marked on an individual frame (B). Two images, where two separate, but closely spaced spines are blinking (C, D). The spacial distance is clearly visible in a kymograph of the previously marked ROI during the blinking events (E). Scalebars: 2 μm

We were able to observe occasional EPSCs of single spines in the buffer containing no APV (figure 4.7). With addition of Bicuculline and its epilepsy-like effect, we could greatly enhance the frequency of EPSCs in many spines. However, once APV is added to the neuronal culture, we could not any longer detect any Ca^{2+} elevation at spines, suggesting that the frequent spontaneous EPSCs, (observed without APV) are NMDAR-mediated, in line with [191].

EPSCs in Bicuculline treated spines were recorded as a time series and then analyzed with ImageJ and self-written Python programs. The workflow of the quantitative analysis of EPSCs was done semi-automatically:

1) ROIs (e.g. blinking spines) in time series were manually selected in ImageJ (figure 4.7 A), and their average signal per frame imported into the program Microsoft Excel.

2) A self-written python program plotted intensity against frame/time graphs by parsing the excel values. The program furthermore identified putative EPSCs by a standard deviation thresholding algorithm or a value interval based method.

3) Another self-written python program analyzed each event and tried to average them according to user-given criteria (e.g. fluorescence levels). Plots of single traces and averages were returned together with fitting parameters.

Using this workflow, we aimed to characterize the kinetics of GCaMP6/7 and the EPSC frequency in single synaptic spines.

Characterization of GCaMP6/7

Fitting of extracted EPSC intensity curves were performed on normalized data (normalized by peak value) with an exponential fit on both sides of the peak (rise and decay), comparable to methods employed in other studies [192–194].

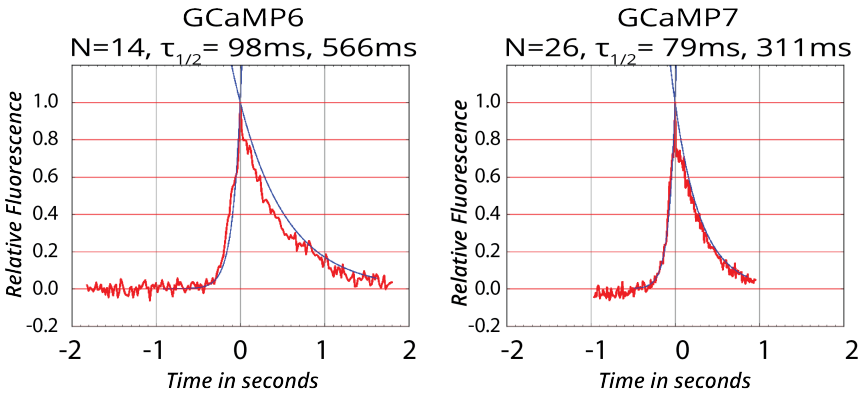

Figure 4.9: Averages of recorded and normalized EPSCs traces for GCaMP6 (left, N=14) and GCaMP7 (right, N=26). X-axis displays time in seconds, and y-axis the normalized fluorescent signal. Fits on both sides by an exponential, with half times of 98 ms and 566 ms (rise and decay times) for GCaMP6 and 79 ms and 311 ms for GCaMP7, respectively.

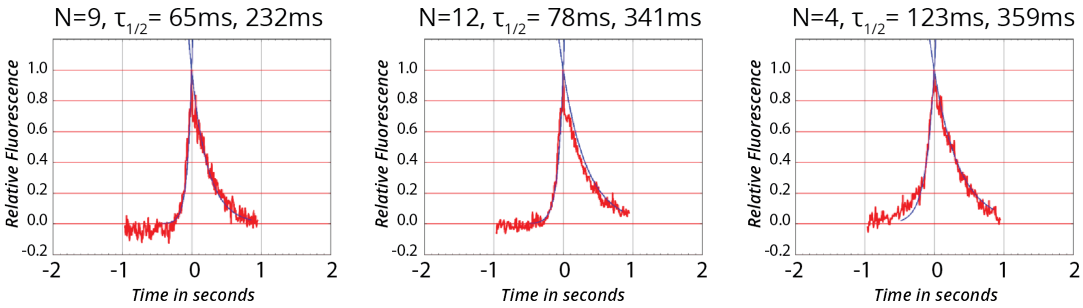

Figure 4.10: Averages of recorded and normalized EPSCs traces for GCaMP7 classified by fluorescence signal strength of the responses of a single spine. X-axis displays time in seconds, and y-axis the normalized fluorescent signal. From left to right: Peak fluorescence level of 90-150 (a.u., N=9), 150-250 (N=12) and 250-600 (N=4). Generally, rise and decay times are higher with higher EPSC signal.

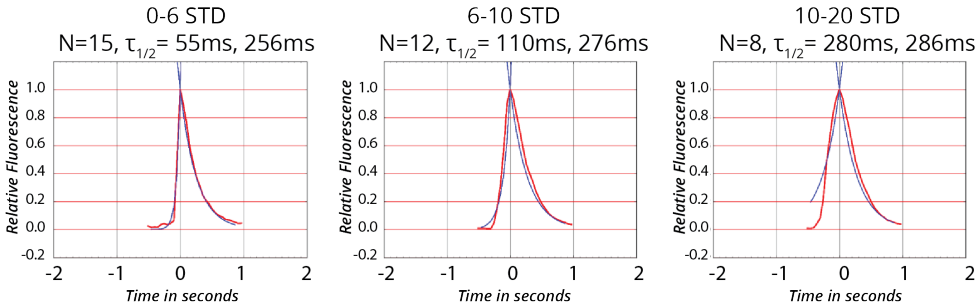

Figure 4.11: Averages of recorded and normalized EPSCs traces for GCaMP7 classified by the peak fluorescence in relation to the std value of its ROI. X-axis displays time in seconds, and y-axis the normalized fluorescent signal. From left to right: 0-6 stds (N=15), 6-10 stds (N=10), 10-30 stds (N=8).

Ca^{2+} elevations upon spontaneous EPSCs could be reliably detected by each of the two GCaMP Ca^{2+} reporters. Comparing the two genetically encoded Ca^{2+} reporters, GCaMP6 appeared to have generally slower kinetics than GCaMP7 (98 ms/566 ms (GCaMP6) vs. 79 ms/311 ms (GCaMP7)), figure 4.9).

Strikingly, it was possible to have different populations (and thus fits) for GCaMP respones of EPSCs. Values of rise and decay times were changing due to EPSC intensity size, with longer times in cases of bigger EPSCs. Therefore, classifications either based on fluorescence intensity intervals in single spines (figure 4.10) or via standard deviation range for a group of different spines (figure 4.11) could be employed [195]. The classification by sorting and comparing the peak fluorescence of EPSCs with the standard deviation of the mean signal is useful, due to its invariance to the total fluorescence value and comparable results over several independent spines.

Putative mEPSC Calculations

Interestingly, we could directly observe an example of a putatively quantized spine response from the extracted fluorescence signals (figure 4.12). Single EPSCs showed fluorescence levels that are double or triple of the smallest (m)EPSC signal. The histogram in figure 4.12 displays the minimum EPSC fluorescence signal to be about 100 - 110 counts in both selected spines (marked with black arrows, figure 4.12), with some events notably being approximately twice, thrice or four times as high at the same synapse (marked with red and cyan arrows, figure 4.12). Due to the fast timescale and apparent random fashion of the strength in these events, this was most likely not due to short term changes in synaptic plasticity [196]. An initial statistical analysis via a χ^2 goodness-of-fit test of the data in figure 4.13 did not reveal a difference to a sample taken from a Poisson distribution at a significance level of 5% [3]. Thus, though the data collected is limited, the statistics hinted towards a Poisson distribution - indicating that all bigger EPSCs observed may be composed of smaller ones [197, 198] (figure 4.13).

[3] MATLAB, *chi2gof* function

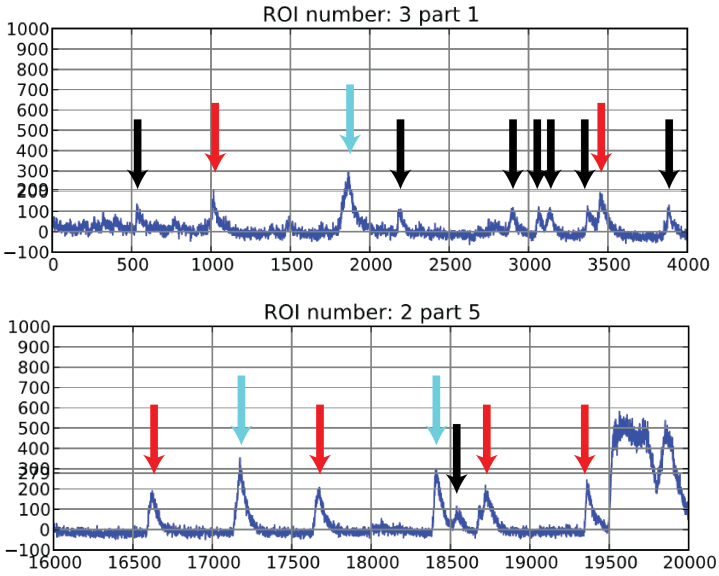

Figure 4.12: Postsynaptic responses from two different spines (top and bottom graph), plotted against the frame (one frame equals to 11ms). The responses appear to be quantal, with multiples of 100 a.u. as a EPSC signal. Hereby, the black arrows are pointing to single "quant" EPSCs (mEPSC), whereas red and cyan arrows are marking EPSCs with fluorescence values of two or three times that of a mEPSC, respectively.

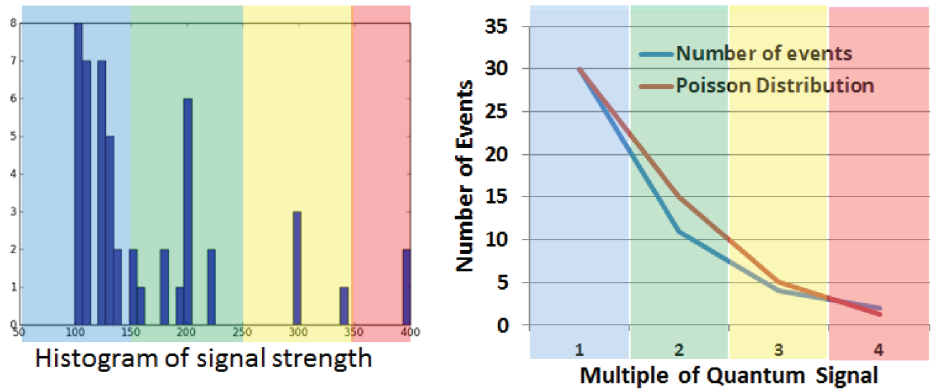

Figure 4.13: Left: Histogram of automatically extracted EPSC intensities (a.u.) of a single spine. Color represent the intervals used for the subsequent histogram bins.
Right: A histogram with reduced bins, now with "1" denoting the smallest quant ("1" $\hat{=}$1 mEPSC, e.g. 120 a.u., blue background) and "2","3","4" multiples thereof (green, yellow, and red background, respectively). The blue line was plotted with the real data and the expected Poisson distribution model for a quantal release of SVs in red for comparison.

4.3.3 Summary and Discussion

The activation of synaptic glutamate receptors produce Ca^{2+} transients with very fast rise and exponential decay times [193]. So far, these postsynaptic responses could not be reliably detected by genetically encoded Ca^{2+} indicators [171], due to the poor signal strength and kinetics compared to synthetic indicators and recording electrodes [199].

However, by using the latest generation of genetically encoded Ca^{2+} indicators GCaMP6 and GCaMP7 [171], we were able to identify single spines and detect individual postsynaptic responses in our transfected neuronal cultures.

First, in our glutamate uncaging study, we were able to demonstrate that we could cause a post-synaptic response upon a UV light flash (figure 4.5). Caged glutamate was thereby either delivered via microinjection close to the neurons, or was supplied with the medium. In both cases, a controlled uncaging of glutamate to invoke a response from single spines proved to be extremely difficult. Both the fast diffusion of the glutamate to other spines, possibly combined with the less confined uncaging volume in one-photon uncaging (compared to the two-photon single spine glutamate uncaging studies [200–202]) could have accounted for the inability to stimulate single spines reliably with UV light.

With TIRFM, we successfully compared and analyzed the two GCaMP Ca^{2+} reporter variants. GCaMP7 provided a lower base fluorescence level, making finer structure more difficult to observe under low Ca^{2+} conditions compared to GCaMP6. This is in agreement with Ohkura *et al.* [171] who reported a lower fluorescence baseline in GCaMP7 compared with GCaMP6, resulting from the higher Ca^{2+} dissociation constant than GCaMP6 (K_d(GCaMP6) = $158 \pm 4nM$ and K_d(GCaMP7) = $243 \pm 14nM$[171]). Rise times measured and calculated were in between 65-100 ms (average 79 ms) for GCaMP7 (figures 4.9, and 4.10), and on average 98 ms for GCaMP6 (figure 4.9). Decay times appeared to be dependent on the response strength and were on average 566 ms for GCaMP6 and 311 ms for GCaMP7 (figure 4.9). Both rise and decay times were in agreement with the literature in our lower temperature conditions [171] (which was published after the research stay). Small deviations of the values from the literature might be due to differences in calculations, as the author only programmed a very rudimentary analysis toolbox during his short stay. Another reason might have been the severe temperature sensitivity of the GCaMP reporters, which caused a 40% increased fluorescence signal in cooler conditions similar to our unheated microscopy stage, and significantly changing the rise and decay times [171].

A first description of the quantal nature of the EPSCs was already done in 1954 by Del Castillo and Katz [197, 198], with numerous confirmations by means of electrophysiology and FM using synthetic dyes [203, 204]. Here, we observed the quantized nature of EPSCs by FM using minimally invasive genetically encoded Ca^{2+} reporters. The results were based on a very preliminary and limited dataset, but already showed promising results.

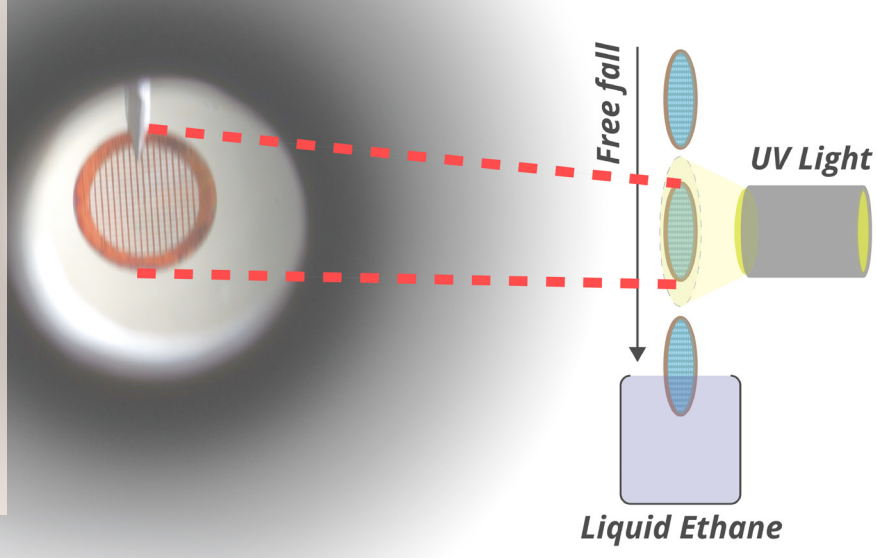

5. Capturing Transient States with electron cryo-tomography

5.1 Means of Synapse Stimulation

The goal of this study was to elucidate the rapid ultrastructural changes upon synaptic stimulation. Depending on the time-regimes of the processes of interest, several means of time-resolved electron microscopy methods are available. With the common manual technique of mechanical mixing of two solutions, the maximum time resolution (fastest time between mixing and plunging) attainable is several seconds [33]. There, at least three processes -mixing, blotting, and plunging- are necessary in this exact order to produce stimulated synapses for cryo-TEM.

This chapter first discusses the viability of implementing a faster time-resolving method into our ECT workflow. We focused on synapse stimulation by UV-light uncaging and checked with simulations and experiments whether the chemical compounds and equipment available meet the requirements. Then, the technical aspects of the integration into our ECT workflow are explained. Lastly, two different cryo-plunger modifications were built and tested for different time regimes and usability.

Imaging rapidly changing structures with cryo-TEM has been performed several times [205–208]. Techniques and instrumentation for cryo-TEM allowing for such experiments were explored as the early as the 1980s, where Heuser et al [209] and Menetret *et al* [210] used electrical pulses or light photolysis followed by immediate vitrification in order to trap and capture highly dynamic events. The rapid mixing method engineered by Berriman and Unwin [211], for example, used a high pressure spray filled with Acetylcholine to capture the Acetylcholine receptor in the open confirmation. By spraying minute amounts of fine droplets on the sample before vitrification in liquid ethane, this allowed for very short timescales of around 5 ms [211]. However, the spray did not cover the whole EM grid area in a reproducible manner and additionally, these liquid droplets increased the ice thickness in sprayed areas [211]. Both of these effects were unacceptable in our cellular ECT workflow, where recording areas are sparse and mostly at the limit in terms of ice thickness.

5.1.1 Light Uncaging

The use of photosensitive or "caged" compounds [205, 206] enabled the light controlled chemical release of a certain compound uniformly over a large area. The duration between the release of the compound and vitrification essentially defines the time resolution attainable in each setup.

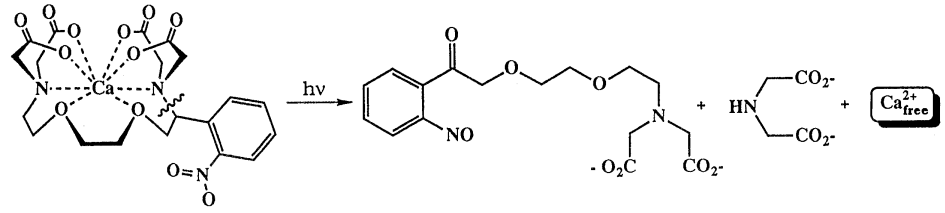

Figure 5.1: Schematic of uncaging DM Nitrophen via UV light to yield free Ca^{2+}. The caging compound (DM Nitrophen) is photo-dissociated by UV light ($h\nu$) and releases two photoproducts and free Ca^{2+} (right). Modified from [212], public domain.

Photosensitive compounds are molecules that either turn (biologically) active or inactive upon light illumination (e.g. releasing Ca^{2+} upon light illumination in figure 5.1). Normally, the compound of choice is covalently bound to an UV sensitive molecule, e.g. "trapping" the compound in an inactive state. Only through UV light illumination, the covalent bond breaks and frees the caged compound - thus the term of "uncaging" the compound. Due to very fast uncaging rates (down to several μs) [213], this technique proved useful in examining fast kinetics in biological systems [214].

There are several possibilities in using caged compounds in stimulation experiments with synapses. For example, caged glutamate enabled the study of postsynaptic responses in the previous study (chapter 4). Usually, in FM studies of cultured neurons, SV exocytosis is invoked by a small Ca^{2+} increase in a very spatially confined area by means of UV light flashing [215, 216]. This time, we incorporated this idea on a bigger scale, by applying a UV flash induced Ca^{2+} increase on the whole EM grid area. The UV-flash device used during the studies was a Rapp JML-C2 Xenon bulb-flash with appropriate filters (UV-1, SP-385), also used in a similar study [205].

Summarized, using UV light uncaging for time-resolved ECT would enable a spatially homogeneous chemical release without increasing the sample thickness. We decided to use Ca^{2+} uncaging, which is already routinely performed in FM studies to elucidate SV exocytosis [215–219]. Since there was no commercial product or setup available to use UV-light flashing combined with cryo-fixation, careful planning and simulations were required before constructing or modifying available equipment.

5.1.2 Integration into ECT Workflow

The strategy of incorporating the UV light uncaging into our EM workflow is shown in figure 5.2. After synaptosome extraction and incubation (refer in detail to section 8.1.1), we supplement the synapses with Ca^{2+}-bound cage, and leaving the synapses

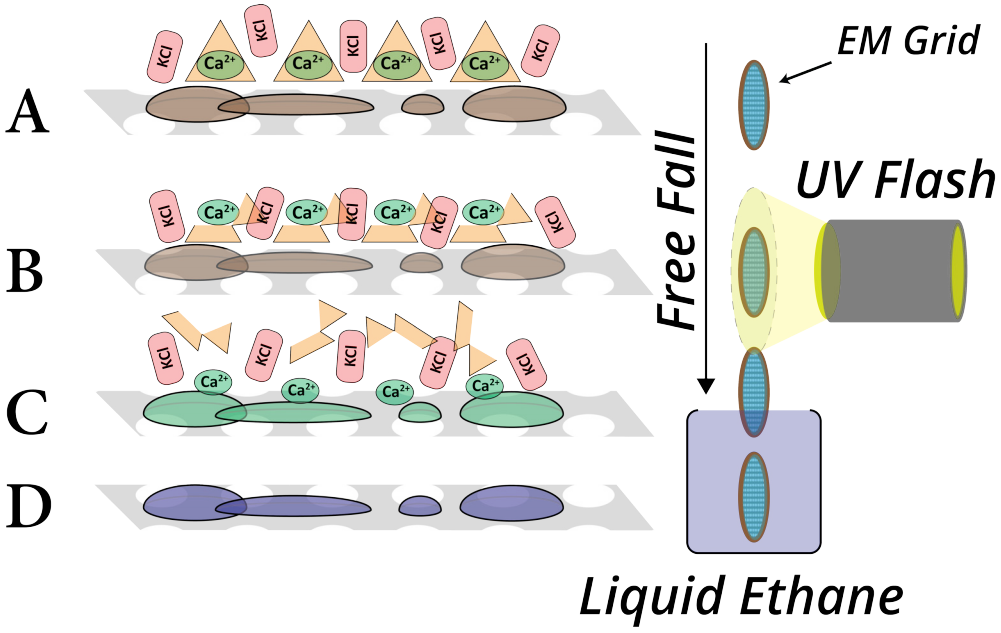

Figure 5.2: Strategy of UV light uncaging in our sample "on-the-fly". From top to bottom: A) Synapse membranes (brown oval shape on grid surface) are depolarized by KCl (red compound). At this stage, the extracellular Ca^{2+} is still caged (Ca^{2+} inside orange triangle) and cannot enter the presynapse (A, left). Upon plunger activation, the UV light (yellow light cone, right) illuminates the sample and releases Ca^{2+} by uncaging (open orange triangles, B, left). The free Ca^{2+} enters the synapses, which leads to SV exocytosis (green synapses, C, left) Shortly after, the stimulated synapses are vitrified in liquid ethane (blue synapses, D, left).

with only nanomolar quantities of free extracellular Ca^{2+}. After application of this synapse suspension on the EM grid, we depolarize the synaptic membrane by adding extracellular KCl. No SV exocytosis takes place at that point, because the extracellular Ca^{2+} necessary for SV exocytosis is bound to the cage [216] (brown synapses in figure 5.2A). We then remove the excess liquid and activate the plunger.

Before vitrification, and optimally during the falling motion, the EM grid is exposed to the UV light flash and free extracellular Ca^{2+} is produced by the dissociation of the caging compound (figure 5.2 (B)). The extracellular Ca^{2+} enters the depolarized synapses via voltage dependent Ca^{2+} channels and induce SV exocytosis (green synapses in figure 5.2 (C)). Shortly afterwards, the stimulated synapses are vitrified in liquid ethane (blue synapses in figure 5.2 (D)).

5.2 Usability of Ca^{2+}-Uncaging Approach

To first assess the applicability of this approach, a glutamate release assay (chapter 8.1.1) was performed (figure 5.3). Depolarizing synaptosomes in normal Ca^{2+} containing buffer showed a typical glutamate release, with increasing glutamate levels indicating SV exocytosis (red trace in figure 5.3). To simulate the uncaging scenario from subsection 5.1.2, we depleted synaptosomes of extracellular Ca^{2+} and added 30 mM

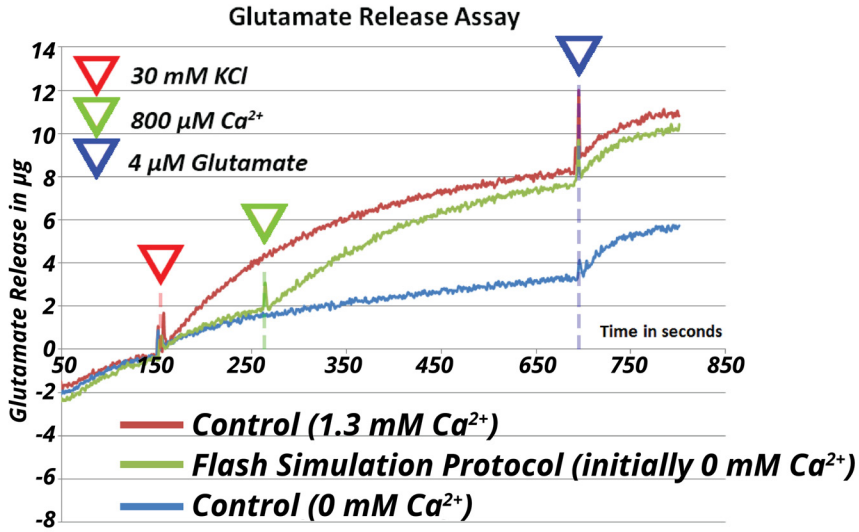

Figure 5.3: Glutamate release assay (see section 8.1.1 for details) simulating a UV uncaging scenario in synaptosomes. The x-axis depict time in seconds, and the y-axis the amount of free glutamate in μg. The green trace depicts our simulation experiment, where the synaptosomes are initially incubated without free extracellular Ca^{2+} and showed no excessive glutamate release upon depolarization with 30 mM KCl (red triangle). Upon adding 800 μM extracellular Ca^{2+} (green triangle), the glutamate level increased due to SV exocytosis. The slow increase after stimulation in the simulation trace before the addition of extracellular Ca^{2+} ($800\mu M$) was most likely caused by residual glutamate leaking from synaptosomal pellets. This could be observed in the negative control synaptosomes without Ca^{2+} (blue trace), where there was no significant difference in slope upon depolarization. The steeper slope observed in the simulation trace after Ca^{2+} addition is indeed caused by SV exocytosis, as a similar slope could be observed in control synaptosomes including extracellular 1.3 mM Ca^{2+} after 30 mM KCl depolarization (red trace). For all three measurements, a fixed amount of 4 μM of glutamate was added at the end (blue triangle), in order to normalize the datasets.

KCl for depolarization (green trace in figure 5.3). Expectedly, we did not observe a significant increase in reported glutamate levels upon depolarization. To mimic the almost instantanous Ca^{2+} increase upon uncaging, we added external Ca^{2+} (in this case, $800\mu M$) to the solution 300 seconds after adding KCl. The slope changed dramatically after this step and indicated that SV exocytosis took place. The glutamate release trace in Ca^{2+} depleted condition (green trace until external Ca^{2+} is added and blue trace in figure 5.3) demonstrated solely the spontaneous SV release, as well as the limited residual glutamate in the buffer [220–222].

Summarized, we demonstrated that synapse membrane depolarization in a Ca^{2+} depleted environment only caused a significant evoked SV exocytosis after additional free extracellular Ca^{2+} was provided. This ideally emulated the uncaging setup with the caged Ca^{2+}, where we keep the synapses depolarized and release free Ca^{2+} by uncaging shortly before vitrification. Subsequently, we were now able to concentrate on the UV uncaging characteristics under experimental conditions.

5.2.1 UV Light Uncaging Simulations

Before utilizing UV light uncaging in biological systems, we approximated the final uncaging yield and decided upon which caging compound to use. Therefore, we divided the photorelease into two separate mechanisms according to this scheme [223]:

$$\text{Compound} \xrightarrow{k_{photo}} \text{Unstable intermediate} \xrightarrow{k_{release}} \text{Product(s) after Uncaging}$$

The compound [C] and product [P] conversion kinetics are [223]:

$$[C] = [C_0] \cdot e^{-k_{photo}t} \tag{5.1}$$

$$[P] = [C_0] \cdot (1 + \frac{k_{photo} \cdot e^{-k_{release}t} - k_{release} \cdot e^{-k_{photo}t}}{k_{release} - k_{photo}}) \tag{5.2}$$

In order to calculate the conversion rates, we first needed to address how the sample thickness changes the overall light intensity. The decrease is given by Beer's law:

$$I = I_0 \cdot 10^{-c\epsilon L} \tag{5.3}$$

where c is concentration, ϵ the extinction coefficient and L the thickness of the sample. By using approximate values for a typical sample layer on an EM grid ($c = 10^{-3}M$, $\epsilon = 10^3 M^{-1}cm^{-1}$ and $L = 10^{-4}cm$), we calculated that the intensity loss is less than 0.03%, and thus insignificant. This enabled us to approximate the absorbed intensity by a Taylor expansion of the first degree:

$$I_{Abs} = I_0 - I = I_0 - I_0 \cdot 10^{-c\epsilon L} = I_0 - (I_0 - I_0 log(10) c\epsilon L) = I_0 log(10) c\epsilon L \tag{5.4}$$

From that amount of light, only a certain fraction actually triggers a photorelease:

$$I_{Abs,Trigger} = I_0 log(10) c\epsilon L \cdot \Phi \tag{5.5}$$

where Φ is the quantum yield, which commonly ranges between 0 and 1:

$$\Phi = \frac{\text{Formation of product}}{\text{Number of photons absorbed}} \tag{5.6}$$

Effectively, we could see that $I_{Abs,Trigger} \propto \epsilon \cdot I_0 \cdot \Phi$, which meant we had to choose a caging compound of high extinction coefficient and quantum yield ($\epsilon \cdot \Phi$ is also termed "uncaging efficiency").

Next, we calculated the photoconversion rate, by using the previous approximation for thin samples (5.5) for the intensity absorbed by the solution [223]:

$$k_{photo} = \frac{1}{\pi \cdot \frac{d}{2}^2} \cdot \frac{log(10) \cdot \Phi \cdot \epsilon}{N_A} \cdot \frac{I_0}{\frac{hc}{\lambda}} \tag{5.7}$$

The first part is a geometric factor that takes the circular illumination area into account. The second factor is the efficiency of the photon absorption, while the third one is $\frac{\text{Intensity}}{\text{Energy per photon}} = \frac{\text{Number of photons}}{\text{Unit time}}$.

The release rate $k_{release}$ compound dependent as well and is approximately between $10^2 s^{-1}$ and $10^7 s^{-1}$. Since the release kinetics are proportional to $e^{-k_{release}t}$, we can also calculate the half-life of the reaction:

$$0.5 = e^{-k_{release}t} \Rightarrow t = \tau_{\frac{1}{2}} = -ln(0.5)k_{release}^{-1} \tag{5.8}$$

We were now ready to tend to the selection of the chemical caging compounds compatible with our ECT study. There are at least eight different caged Ca^{2+} compounds available, with the two most important individual characteristics being the dissociation constant K_d before and after uncaging (change of affinity) and the uncaging efficiency [224]. Since the experiment needed a fast and effective Ca^{2+} release, we were required to choose between NP-EGTA and DM-nitrophen [225] (figure 5.1). With the parameters given by the literature [213], were able to calculate the values for $k_{release}$ and k_{photo} for the two compounds considered in this study (DM-Nitrophen and NP-EGTA):

Parameter	Variable	Value
Wavelength	λ	350 nm
Intensity	I_0	$\frac{24\ mJ}{5\ ms} = 4.8\ W$ from [205]
Quantum yield	$\Phi_{DM-Nitrophen}$	0.18 from [213]
Extinction coefficient	$\epsilon_{DM-Nitrophen}$	4300 $\frac{1}{M \cdot cm}$ from [213]
Quantum yield	$\Phi_{NP-EGTA}$	0.23 from [213]
Extinction coefficient	$\epsilon_{NP-EGTA}$	975 $\frac{1}{M \cdot cm}$ from [213]
Grid diameter	d	3 mm

DM-Nitrophen	$k_{release} \approx 8 \cdot 10^4 s^{-1} \Rightarrow \tau_{\frac{1}{2}} \approx 8.7 \mu s$	$k_{photo} \approx 295.5 s^{-1} \Rightarrow \tau_{\frac{1}{2}} \approx 2.3 ms$
NP-EGTA	$k_{release} \approx 5 \cdot 10^5 s^{-1} \Rightarrow \tau_{\frac{1}{2}} \approx 1.4 \mu s$	$k_{photo} \approx 85.5 s^{-1} \Rightarrow \tau_{\frac{1}{2}} \approx 8.1 ms$

These values clearly showed that the release rate is sufficiently fast. Due to the significantly smaller value of $k_{release}$, the uncaging kinetics in both compounds were governed by k_{photo}. Finally, we used the exact equation (5.1) for simulating the expected photorelease when using UV light.

The simulated photorelease of DM-Nitrophen and NP-EGTA are shown in figure 5.4, and clearly indicated that DM-Nitrophen is superior in terms of attainable dissociation. For a flash duration of roughly 5 ms [205], we calculated a 77% uncaging rate with DM-Nitrophen, under optimal conditions (figure 5.4). However, using experimental conditions [1], reportedly could decrease the uncaging rate down to 40% [205].

UV Flash Duration and Intensity

This experiment was supported by Stefan Prech from the MPIB workshop.

For finding out the exact flashing duration and the total dissipated light energy in our own setup, a very well defined UV sensitive photodiode was attached to a digital oscilloscope

[1] $V = 5\mu l$ of $c = 1mM$ DM-Nitrophen drop on EM grid, flashed from 2 mm distance

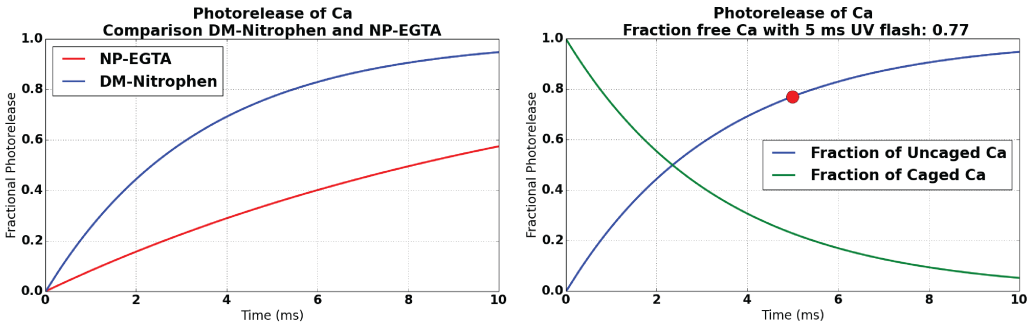

Figure 5.4: Left: Computational simulation of the photorelease of DM-Nitrophen (blue trace) and NP-EGTA (red trace) upon UV light illumination, using the values provided by the literature. X-axis displays the illumination time in ms, whereas the y-axis shows the fraction of compounds photodissociated. It was obvious from the graph, that DM-Nitrophen has a superior Ca^{2+} uncaging yield, compared to NP-EGTA, under the same UV light flashing conditions. Right: Computational simulation of the photorelease of DM-Nitrophen (blue trace) and the remaining, not yet uncaged, DMN-Ca^{2+} complexes (green trace). The red dot indicates the attainable photodissociation of around 77% by our setup with the given values from section 5.2.1.

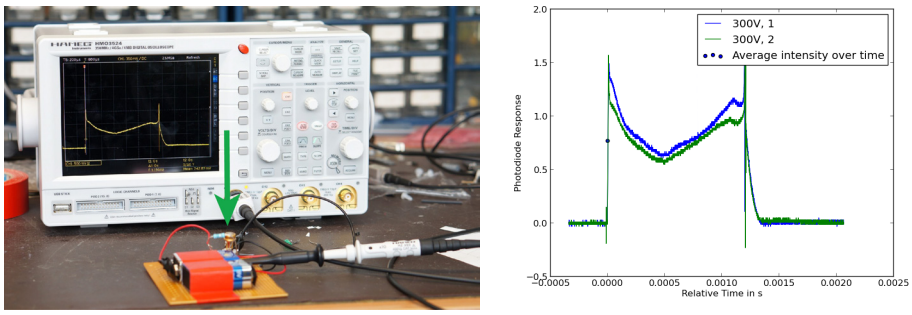

Figure 5.5: Setup using a light sensitive photodiode (green arrow) and an oscilloscope to measure the light intensity and duration of the light flash (left), with two measurements plotted on the right image. X-axis: time in seconds, y-axis: photodiode voltage response (arbitrary units)

capable of voltage triggering (Hameg, HMO3524, figure 5.5, left). UV-light from our high energy flash lamp (Rapp Optoelectronic JML-C2) was directly flashed onto the photodiode and, by a preset voltage trigger, the photodiode voltage spike could be visualized (figure 5.5, right). The total time of one 300V UV-flash was around 1.3 ms (figure 5.5), with the total calculated energy of around $15mJ$. Surprisingly, these values were different than previously reported (t = 5 ms, E = 24 mJ) for the same device at almost identical settings (Voltage: V=300 V (in this study) vs. V=350 V in [205], capacitance: 3000 μF was the same).

We therefore recalculated the yield attainable by our setup. Using the measured values,

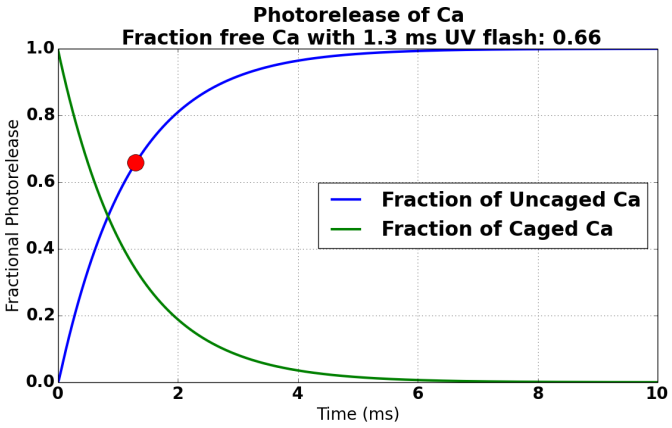

Figure 5.6: Computational simulation of the photorelease of DM-Nitrophen (blue trace) and the remaining, not yet uncaged, DMN-Ca^{2+} complexes (green) with values measured from our device (section 5.2.1). X-axis displays the illumination time in ms, whereas the y-axis shows the fraction of compounds photo-dissociated.

we get a power increase in the UV flash setup:

$$\text{Power(literature values)} = \frac{24mJ}{5ms} = 4.8W$$

$$\text{Power(measured values)} = \frac{15mJ}{1.3ms} = 11.5W$$

Ultimately, however, we got a lower optimal uncaging rate of 66%, due to the overall shorter duration of the UV light flash (figure 5.6).

5.2.2 Photometric Experiments

We could successfully demonstrate Ca^{2+} release upon UV light flashing of Ca^{2+}-DM-Nitrophen complexes, as indicated by the fluorescence of the Ca^{2+}-reporter dye Ca-Green-5N (figure 5.7). The photorelease per single UV flash could be calculated with the formula for a single-wavelength measurement [226]:

$$[Ca^{2+}] = K_D(\text{Ca-Green-5N}) \cdot \frac{F - F_{min}}{F_{max} - F} \tag{5.9}$$

Using this equation (5.9), with the $F_{min} \approx 0$ and $F_{max} \approx 700$ from our experiment in figure 5.7, as well as the dissociation constant K_D(Ca-Green-5N) $\approx 14\ \mu M$, we get an initial photorelease of around 3% per flash at the beginning of the experiment. Using equation 5.3, we calculated an absorption of over 34% for our DM-Nitrophen sample and light path [2]. The sample volume inside the cuvette was 1 ml, therefore not comparable with earlier simulated data using a thin sample approximation (equation 5.7). Thus, due to heavy light absorption within the UV flash light path, we used numerous flashes for almost complete photo-dissociation, as it can be seen in the figure 5.7. For a quantitative validation, we used a much smaller volume, in order to compare it to the thin-film approximation in our calculations.

[2] $c_{DM-Nitrophen} = 21 \cdot 10^{-6}M$, $\epsilon_{DM-Nitrophen} = 4.3 \cdot 10^3 M^{-1}cm^{-1}$ [227] and $L = 2cm$, only taking DM-Nitrophen as a source of absorption into account

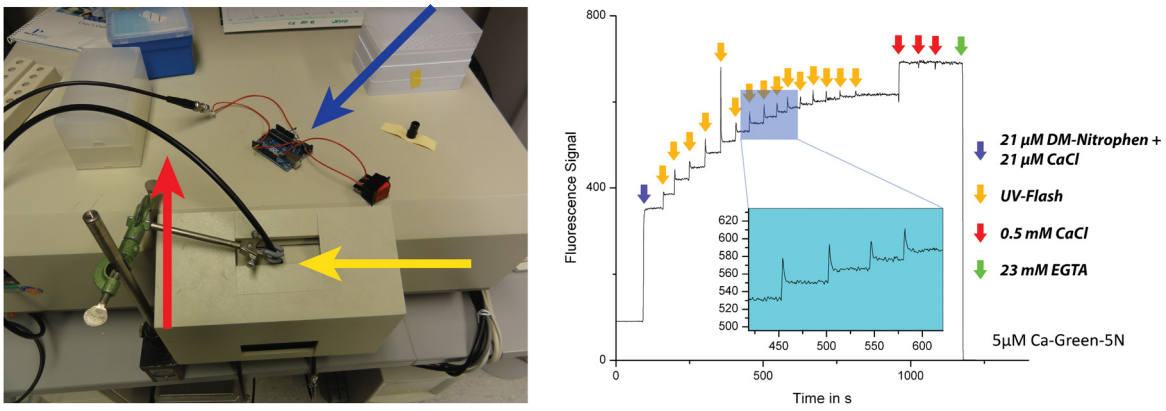

Figure 5.7: Qualitative assessment of Ca^{2+} uncaging capability of the UV light flash. We guided the UV light guide (red arrow) from the flashing device directly inside the sample chamber of the spectrophotometer and into the sample cuvette filled with HBS buffer (left, yellow arrow, cuvette hidden by the light protection hood). A self-written program running on a microcontroller (blue arrow), triggered the UV light every 50 seconds (also see right). The right graph shows a glutamate release assay acquired from the setup shown on the left side. After introducing the DM-Nitrophen and Ca^{2+} in the same concentration into the buffer (violet arrow), we could detect an increase in Ca^{2+} sensor fluorescence (a.u.), most likely due to unbound free Ca^{2+}. Upon flashing the solution with UV light (indicated with yellow arrows), we could see subsequent increases in Ca^{2+} signals, due to photo-released Ca^{2+}. The calcium sensor used was Ca-Green-5N ($5\mu M$), with a Ca^{2+} affinity of $K_d \approx 15\mu M$. After UV flashing did not longer induce any noticeable Ca^{2+} increase, CaCl was added (red arrows) to induce to fully saturate fluorescence ($3 \cdot 0.5mM$). Additionally, Ca^{2+} binding EGTA (green arrow) was added in order to further verify that the observed fluorescence signal is indeed caused by internal Ca^{2+} increase. We arbitrarily set the fluorescence signal after EGTA addition to zero. Both fluorescence signals in high and low free Ca^{2+} environment (F_{max} = 700 (a.u.) and F_{min} = 0 (a.u)) were used to calculate the photorelease.

For observing the light uncaging efficiency in a sample with a short light path/small volume, a spectrophotometer for small volumes was used to evaluate the released Ca^{2+} with a Ca^{2+} reporter dye. Several drops ($3\mu l$ volume) of specified Ca^{2+} concentrations were measured individually with the high K_d Ca^{2+} indicator Rhod-5N (figure 5.8), to establish a calibration curve. Figure 5.9 demonstrates the titration experiment performed to determine the optimal mixing ratio, where almost no free Ca^{2+} is detected. Significant free Ca^{2+} levels in DM-Nitrophen:Ca^{2+} ratios beyond 1.0 are indicating a partial dissociation of DM-Nitrophen, e.g. caused by preexposure of UV light or deterioration of DM-Nitrophen.

The Ca^{2+} levels in solutions containing $333\mu M$ Ca^{2+} and $3.5\mu M$ of the Ca^{2+} reporter dye Rhod-5N were measured before and following one or multiple UV flash(es) (figure 5.10). By comparing the fluorescence between a unflashed and a once flashed sample, we calculated a 21% decrease in fluorescence of the Ca^{2+} reporter upon a single UV flash. This experimental value did not account for the evaporation of liquid either due to the flashes or the additional experiment time, making the measured decrease a conservative

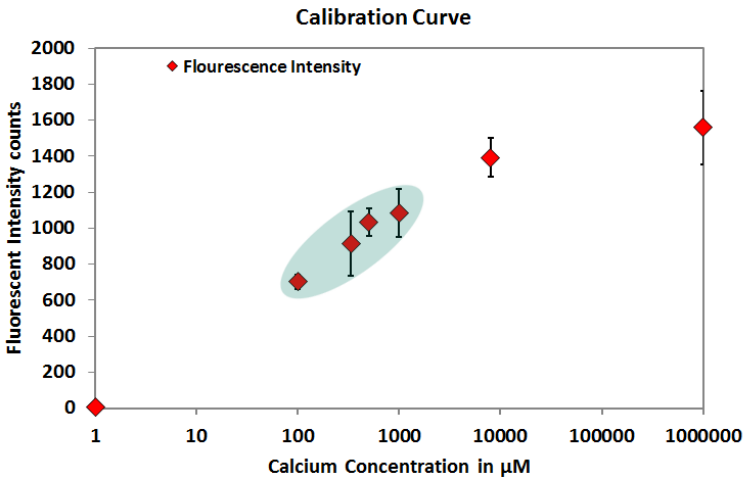

Figure 5.8: Ca^{2+} calibration curve taken with the same spectrophotometer used for glutamate release(refer to section 8.1.1 for details). The dye is reported to be used [228] in the concentration range between 100 μM and 1 mM, marked with a light green overlay. The measurements were done with the Ca^{2+} reporter Rhod-5N ($c = 3.5\ \mu M$, $K_d \approx 320\ \mu M$ [229]). Calibration samples were EGTA ($c = 100\ \mu M$), and Ca^{2+} solutions between 100 μM and 1 M concentration (red diamonds). X-axis shows the Ca^{2+} concentration in logarithmic scale, and the y-axis displays the fluorescence intensity counts (a.u.). For every treatment, at least three measurements were taken, the errorbars are std values.

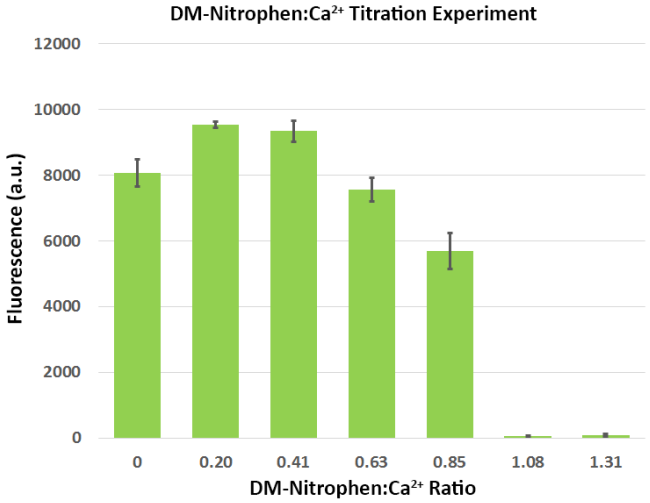

Figure 5.9: Example of a titration experiment to determine the most useful DM-Nitrophen - Ca^{2+} ratio at an initial Ca^{2+} concentration of 0.4 mM. In this example, freshly purchased DM-Nitrophen was used. The very high affinity to Ca^{2+} with a $K_d \approx 5nM$ [227] explains the drop in free Ca^{2+} concentration (green bars) when approaching an 1:1 ratio of DM-Nitrophen and Ca^{2+}. An approximate 1:1 ratio of DM-Nitrophen and Ca^{2+} (both 0.4 mM) in solution would therefore provide both the least amount of free Ca^{2+} and uncomplexed DM-Nitrophen. An additional increase in DM-Nitrophen would not significantly reduce free Ca^{2+}, whereas decreasing DM-Nitrophen would increase uncomplexed free Ca^{2+}. The Ca^{2+} signal was measured with Rhod-5N ($c = 3.5\mu M$, $K_d \approx 320\ \mu M$ [229]). For every titration step, at least three measurements were taken, the errorbars are std values.

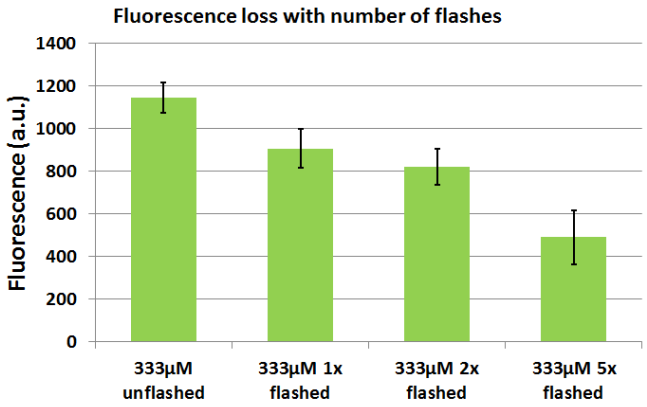

Figure 5.10: Experiment demonstrating photobleaching in Rhod-5N fluorescence with number of UV light flashes. Ca^{2+} calibration samples ($333\mu M$, supplemented with Ca^{2+} indicator Rhod-5N ($c = 3.5\mu M$, $K_d \approx 320\mu M$ [229])) were measured with or without any previous UV flashing (green bars). The photobleaching effect could be observed well, indicating a fluorescence loss of more than 50% after five UV flashes. The first UV flash roughly accounted for a loss of fluorescence signal of around 21%. The settings on the flash device were the same in each experiment and correspond to the settings used for all other photolysis flash experiments (V=300 kV, capacitance: 3000 μF).

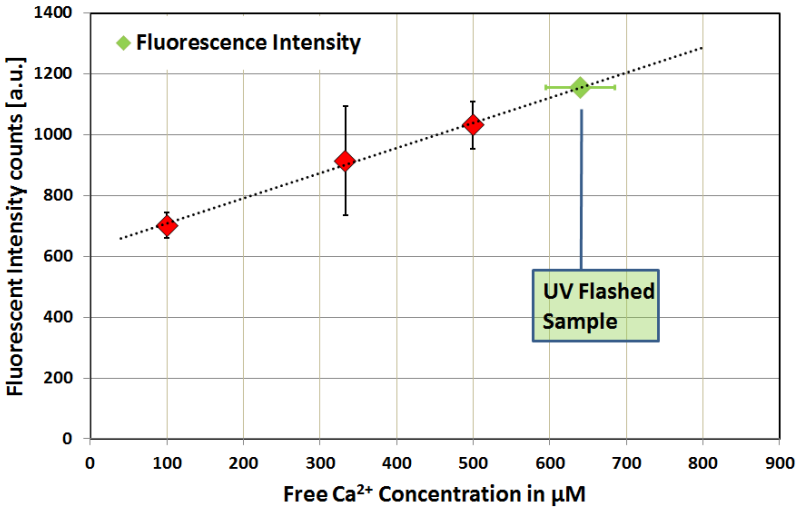

Figure 5.11: The uncaging yield averaged from three UV light flashed solutions, corrected for photobleaching effects from figure 5.10 and using previously collected calibration data from figure 5.8 (red diamonds, with black errorbars depicting std, as well as the linear fit shown as a black dotted line). The green triangle shows the fluorescence signal of the flashed sample. The Ca^{2+} concentration after flashing was roughly 630 μM, at an initial complexed Ca^{2+}-DM-Nitrophen concentration of 2 mM with a DM-Nitrophen:Ca^{2+} ratio of 1.25. Three solutions were flashed and the green error bars in the calculated calcium concentration represent the std. Calcium concentrations were measured as in the previous experiments (figure 5.8) with the Ca^{2+} indicator Rhod-5N ($c = 3.5\ \mu M$, $K_d \approx 320\ \mu M$ [229]).

estimate. Subsequently, we used a correction factor of $\zeta = \frac{1}{1-0.21} \approx 1.27$ to our flashed samples to account for photobleaching:

$$[\text{free } Ca^{2+}]_{\text{Flashed Sample}} = [\text{free } Ca^{2+}]_{\text{Measured}} \cdot \zeta \tag{5.10}$$

Corrected for photobleaching (5.10), the measured free Ca^{2+} upon a UV flash was calculated to be $630\mu M$ or 32% dissociation from the initial complexed $2mM$ Ca^{2+}-DM-Nitrophen solution (figure 5.11). Given that the DM-Nitrophen:Ca^{2+} ratio was around 1.25 in this experiment, this yielded in an effective dissociation rate of $r = \frac{640}{\frac{2000}{1.25}} = 40\%$ of DM-Nitrophen bound Ca^{2+}. This value was identical to the lower limit estimated by UV flashing a droplet on a grid [205], but smaller than the previously calculated 66% dissociation under optimal flashing conditions in figure 5.6. However, in later ECT experiments, additional reflections of the UV light from the sides of the plunging device and the grid itself could aid in improving photolysis yield. Therefore we expected the uncaged free Ca^{2+} under plunging conditions to be in the range of $700 - 800\ \mu M$, where Ca^{2+} induced SV exocytosis was shown to take place (figure 5.3). To keep the chemical stress on synapses to a minimum, we used DM-Nitrophen in our study at a concentration of 2 mM [230] complexed with Ca^{2+} in ratios between 1 and 1.25, depending on the deteriation of the caging agent.

Summarized, we decided to use the method of UV flash uncaging of Ca^{2+} for stimulating synapses in a very fast and controlled fashion. Both simulations and experiments successfully showed the usability of Ca^{2+} UV flash uncaging with synapses.

5.3 First Generation Plunger Modifications

Measuring the Plunger Acceleration

To detect speed variations, as well as faulty mechanics of manual cryo-plungers, the author used a small pinhole strip array and a laser / light sensor setup connected to a microcontroller (figure 5.12). The small pinhole strip was attached to the plunger arm and the laser / light sensor setup aligned horizontally. Once the plunger was activated, the microcontroller (Arduino, figure 5.12 left inside box) registered via a photodiode (figure 5.12, red arrow), when the laser was being blocked by the pinhole strip and displayed the time differences between the consecutive pinholes for each plunge accordingly. It was able to detect subtle variations in speed (figure 5.13 A, and B) and was sensitive enough to even distinguish different lubricants used for the plunging arm. In total, five house-built cryo-plungers with different lubrications were characterized. The cryo-plunger used for the modification and later uncaging experiments was quantified as well, requiring a time of $\approx 108ms$ between plunging signal (rod release) and hitting the liquid ethane.

In order to be able to stimulate synapses shortly before plunging/freezing in liquid ethane, the cryo-plunger needed to be modified. The first modification for a UV-light uncaging and plunging setup included a slight modification of the plunger foot-pedal (figure 5.14). Normally, this foot-pedal is used to trigger the plunging process by releasing the metal rod into the liquid ethane. For the purpose of triggering an UV-flash, the foot-pedal was

Figure 5.12: The plunger speed measurement device was designed by the author. A laser pointer (not shown) was aligned horizontally to illuminate the photodiode sensor (red arrow). This enables detection of the time differences between holes in the metal pinhole strip (right, yellow arrow, built by the workshop) when it is attached to a plunger and dropped.

redesigned. A second switch was installed inside the foot-pedal, which triggered the UV-light shortly before plunger initiation (figure 5.15). Measuring the delay between these two switches was done by recording the typical "clicking" sound of the triggers with a microphone while pressing the foot-pedal. The introduced delay between the UV flashing and the beginning of the plunging process was measured at of $14.6 \pm 1.9ms$ $(mean \pm std)$ (figure 5.15).

With this modification to the manual plunger, the time between the UV flash and sample vitrification was $t_{total} = t_{plunging} + t_{delay} \approx 108ms + 15ms \approx 120ms$.

5.4 Second Generation Plunger Modification

In principle, the delay from our first generation modification could be set virtually to any positive value above the plunging time of $t \geq 108ms$ by using only one trigger and adding a controlled delay loop inbetween the release and the flash signal. However, ultimately, the process was still limited by the duration of the dropping plunging arm, requiring another mechanism to improve the time resolution to $t < 108ms$.

A possible setup included a modification inside the manual plunger (figure 5.16). However, a lens system necessary for proper UV beam collimation, could not be integrated due to very limited space. Furthermore, again spatial limitations restricted the UV fiber to get any closer than $\Delta z \approx 4cm$ above the ethane reservoir (figure 5.16). With the plunging time of around $120ms$ and an approximate speed of $v \approx 1\frac{m}{s}$ at the

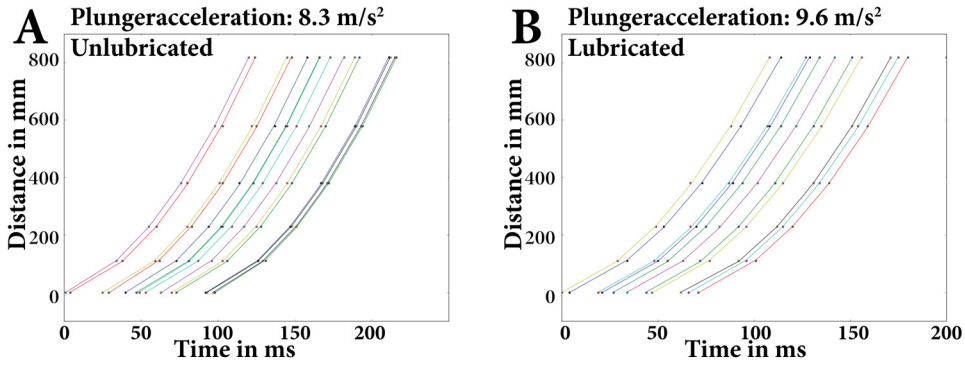

Figure 5.13: Examples of a plunger speed measurement, the left plunger (A) was not lubricated and thus the mounted pinhole only accelerated with 8.3 $\frac{m}{s^2}$, compared to the well lubricated right plunger (B), with an acceleration of 9.6 $\frac{m}{s^2}$, close to the earth gravitational field. X-axis show the time, while y-axis show distance passed by the falling plunger arm. The time offset of the first data point in each experiment is arbitrary. The color indicates separate repetitions of the experiment.

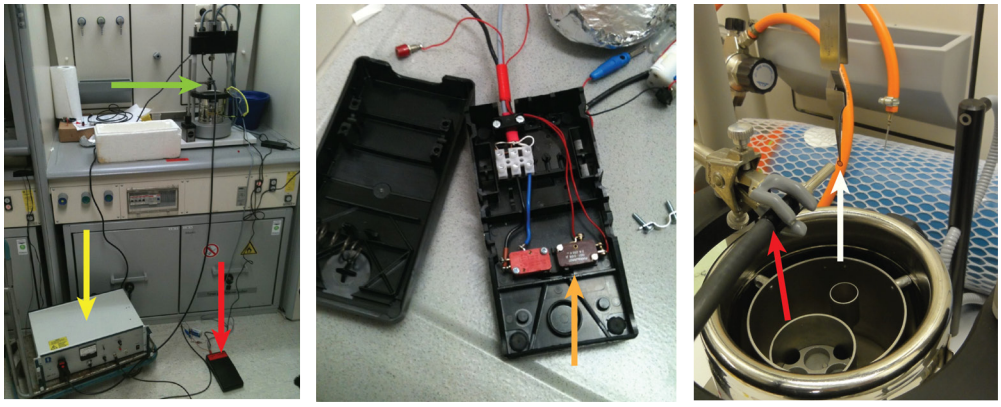

Figure 5.14: First generation plunger modification. The full setup can be viewed on the left, with the modified foot-pedal (red arrow) on the ground, connected via a battery and a coaxial cable to the UV-light source (yellow arrow), which illuminated the EM grid via a fixed liquid light fiber (green arrow). A detailed view of the foot-pedal modification can be seen in the dissembled foot-pedal in the center image, where another switch (brown, indicated with orange arrow) was inserted at a slightly higher position, therefore to be triggered earlier than the metal rod release signal (red switch). Right image: An enlarged view of the light guide (red arrow) fixed almost directly in front of the EM grid (white arrow) during plunging.

time of flashing [3], this setup would have only allowed timescales of up to $\Delta t \approx 40ms$. We therefore decided to move to another setup capable of even shorter timescales.

The Vitrobot (TM) (FEI, Hillsboro, OR, USA) is a commercially available gravity-aided plunging device for electron cryo-microscopy sample preparation. The major advantage of this system over manual plunging is reproducibility. Conditions relevant for plunging grids, e.g. temperature, humidity in the sample chamber and blotting pressure/time can be set manually in the computer attached to the Vitrobot. Here, we modified the FEI

[3] $v = g * t = 9.81 \frac{m}{s^2} * 120ms \approx 1 \frac{m}{s}$

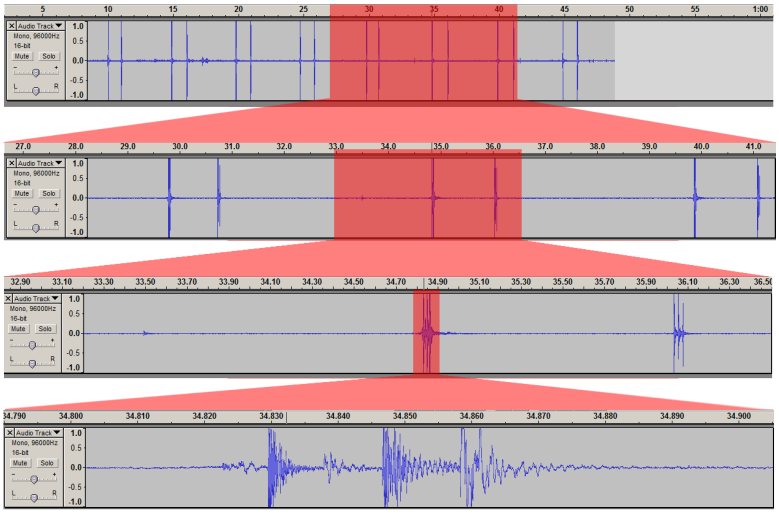

Figure 5.15: Audio recording of the foot-pedal used to estimate the time difference between the two triggers. Continuously expanding the recorded clicking sound revealed the time difference between the two separate triggers. The first two sound waves on the highest time resolution recording (bottom row) represented the clicking sound of the first and the second switch, while the third wave echoed the pedal hitting the ground. The times are shown in seconds.

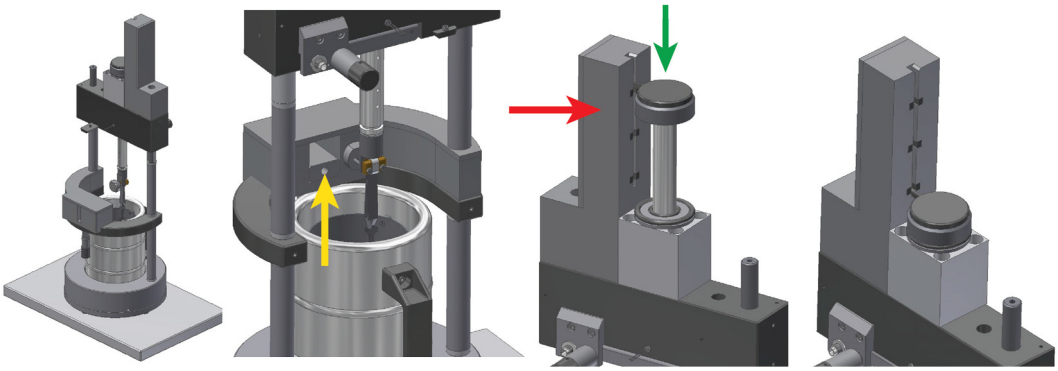

Figure 5.16: The first design of a second generation plunger. The UV light fiber would be fixed at the position indicated by a yellow arrow in the second image. We incorporated a light barrier array (red arrow) for the acceleration measurement and for the UV flash triggering. A sharp blade attached to the top of the plunging rod (green arrow) is passing the light barriers. The initial (top) and "plunged" (bottom) rod positions are shown in the third and fourth image. Due to fabrication difficulties and long timescales, we eventually switched to another type of plunger. 3D model images were provided by Tim Laugks.

Vitrobot Mark III in order to get homogeneous sample quality with additional UV light flashing capabilities.

5.4.1 Vitrobot Disassembly and Electronics

Firing the UV flash during plunging required high precision, as the UV flash (diameter $\approx$ 4 mm) itself is lasting for only 1.3 ms (figure 5.5), whereas the microscopy grid

(diameter 3 mm) is travelling with approximately the speed of $v \approx 1\frac{m}{s}$ [4] (similar as in the manual plunger) psat the UV fiber end (see section 5.3). To ensure the correct light exposure and timing, a microcontroller coupled opto-electrical trigger was assembled (figure 5.18 B). After UV light illumination, the UV fiber could be optionally retracted by a pullback motor activated through the microcontroller (figure 5.17). The circuit diagram is illustrated in figure 5.17.

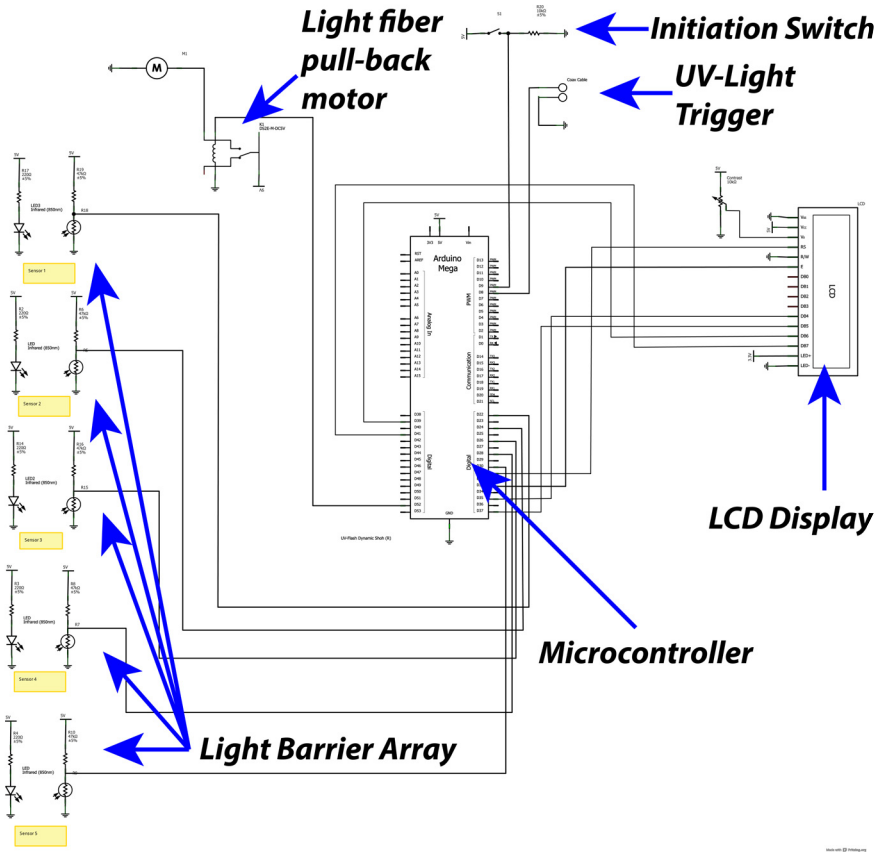

Figure 5.17: Annotated microcontroller setup blueprint showing the light barriers (left) and the display (right). The connection to the flash lamp is implemented by a coaxial cable (top). The initiation switch is located at the top as well, with the optional UV-fiber pull-back motor setup on top left. The microcontroller used is an Arduino MEGA (middle). Since the delay time configuration is only needed to be set once, the electronics for setting the delay is not shown in this blueprint.

First, by disassembling of the Vitrobot (see figure 5.18 A) we obtained the bottom plate of the sample chamber. A hole was drilled into the side of this plate, as well into the middle plunging channel, which connects the preparation chamber and liquid ethane container. Essentially, the UV fiber flashes the EM grid during the falling motion through the tunnel. To further increase UV light illumination onto the sample, we covered the tunnel walls with aluminum foil which has a UV reflectance of about 92.5% in our target wavelength ($\lambda \approx 350nm$) [5].

[4] $v = g * t \approx 15\frac{m}{s^2} * 60ms \approx 1\frac{m}{s}$, see 5.4.2 for values

[5] http:refractiveindex.info?group=METALS&material=Aluminium

Once the plunging sequence was initiated, the liquid ethane chamber is lifted automatically to the bottom plate, thereby shortening the distance between the light guide and the liquid ethane to about 1 cm. For the timing measurements, we designed a light barrier array containing five photodiodes (figure 5.18 B) enclosed in a plastic casing to fit closely to the plunging rod (figure 5.18 C). For triggering these photodiodes, a small copper blade was attached to the plunging rod, which passes the light barriers during the plunging sequence. During the plunging process, the signals from the photodiodes are processed by a microcontroller (Arduino Mega; the setup design is shown in figure 5.18 B). The final setup is displayed in figure 5.18 D.

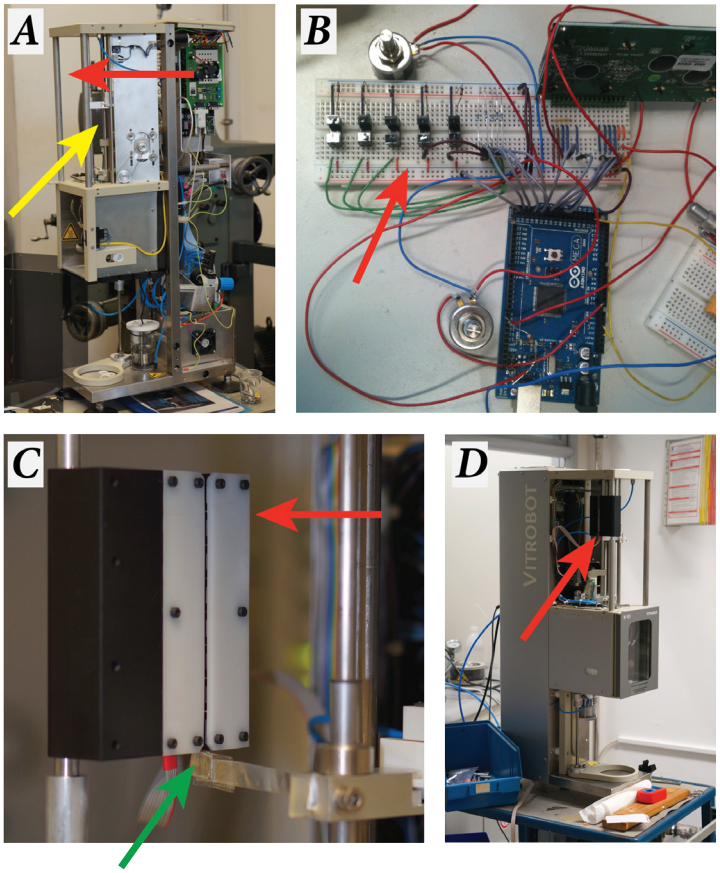

Figure 5.18: (A) The commercial cryo-plunger FEI Vitrobot was disassembled. The indicated position at the left support rod (red arrow) was close to the plunging arm (yellow arrow) and additionally left enough space to install an extension. (B) A light barrier array (red arrow) was connected to a microcontroller. This combination served as a speed measurement device, as well as the trigger for the UV flash. (C) This light barrier array design was incorporated in a small plastic casing by the workshop and attached inside the Vitrobot (red arrow). There, a copper blade attached to the plunging arm (green arrow) slides through the light barrier array slit during plunging. (D) The almost fully re-assembled Vitrobot, with attached light barrier array (red arrow).

Arduino Microcontroller Unit

Online computations and triggering was done with a single-board microcontroller (Arduino Mega2560) based on a surface-mounted ATmega 2560 chip. 54 digital input/output pins and 16 analog inputs allowed us plenty of communication channels, as well as upgrade abilities, while the 16MHz crystal oscillator allowed a time-resolution of four microseconds. Microcontroller programming was done in C/C++ code, and saved on a 256KB flash memory. The whole microcontroller system was powered by a 9V battery. The main function workflow of the microcontroller is illustrated in the flowchart figure 5.19.

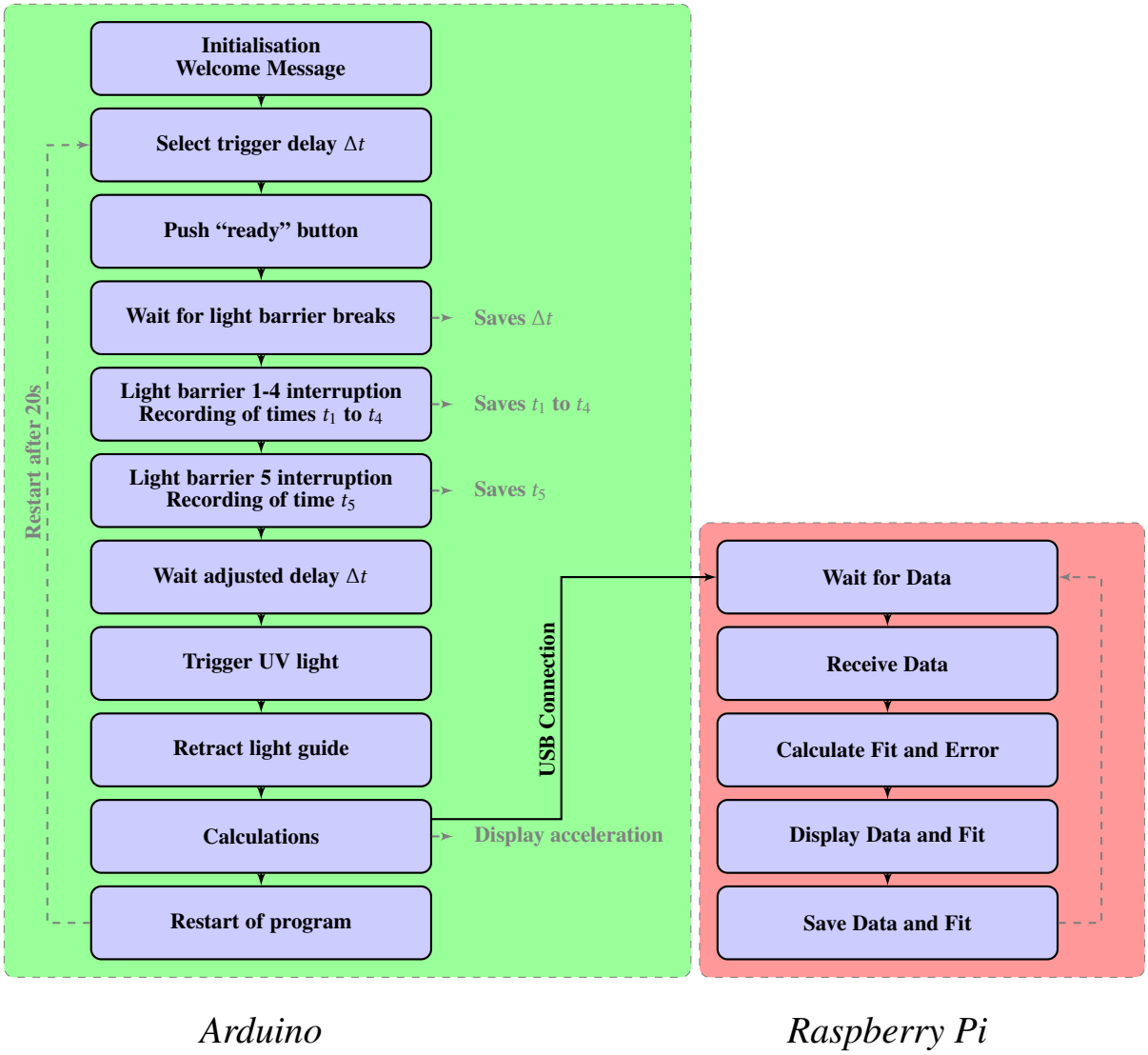

Figure 5.19: Flowchart presenting the overall workflow of the two microcontrollers. Left side, green area: Calculations and actions done by the Arduino. Right side, red: Computations done by the Raspberry Pi. Both are connected to each other by a USB connection (middle arrow, black)

A linear least squared mean regression model was implemented in the microprocessor

(see workflow chart in 5.19), in order to calculate the plunging acceleration by using the interruption times (t_1 to t_5) of the photodiode array. All important information, such as delay times, flash success status, errors, and plunging acceleration, are displayed on a 20x4 LCD display attached to the microcontroller (see blueprint figure 5.17). The delay Δt, the time between the blade passing the last light barrier and triggering the UV light, was initially set *via* a turning potentiometer ($R = 1\ k\Omega$) connected to the microcontroller. A pushbutton was used to fix the delay value and put the device into plunging standby mode. The interruption times are (t_1 to t_5) recorded for each photodiode. After passing the last photodiode, the fixed delay is activated and the UV flash light subsequently triggered by a voltage spike signal (500 ms at 5 V) *via* a coaxial cable. Additionally, after 20 seconds, the device automatically restarts and can be reused again.

5.4.2 Calibration of the Modified Vitrobot

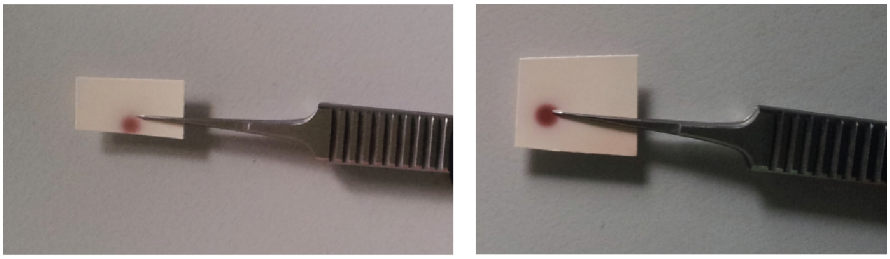

Figure 5.20: Time and position offset estimation by using photosensitive paper. The photosensitive paper was attached to the tweezer and plunged normally inside the modified Vitrobot, with an automatically triggered UV flash. The brown spot on the photopapers indicated light exposure position and therefore was used to correct the positioning of the tweezer. Left image: Incorrect alignment of the tweezer. Right image: Correct tweezer position, where the UV light perfectly covered the approximate area (of $A = \pi \cdot \frac{3\ mm}{2}^2 \approx 7\ mm^2$) of a centered EM grid. The experiment was done in the dark to minimize exposure of the photosensitive paper to ambient light.

To directly assess the timing and tweezer positioning for the correct UV flash, two different photosensitive methods were employed. In both cases, no ambient light was allowed, in order to ensure precise measurements. For all calibrations, we used the fully assembled and modified Vitrobot, with the activation of the UV flash during the falling motion.

A direct observation of the UV flash was done with photographic paper attached to the tweezers. By applying the very strong light burst from the flash lamp, the paper turned brown, revealing the illuminated area. The light pattern displayed the flashed location relative to the tweezer (figure 5.20). Unfortunately, we could see that the UV light fiber was not aligned with the falling axis of the tweezer (figure 5.20, left). Therefore, we used this method to accurately adjust tweezer and grid position by slightly shifting the tweezer towards the side. This way, the grid falls in line with the UV light fiber axis, and with the correct timing, the grid aligned exactly in front of the UV fiber during the falling motion (figure 5.20 right).

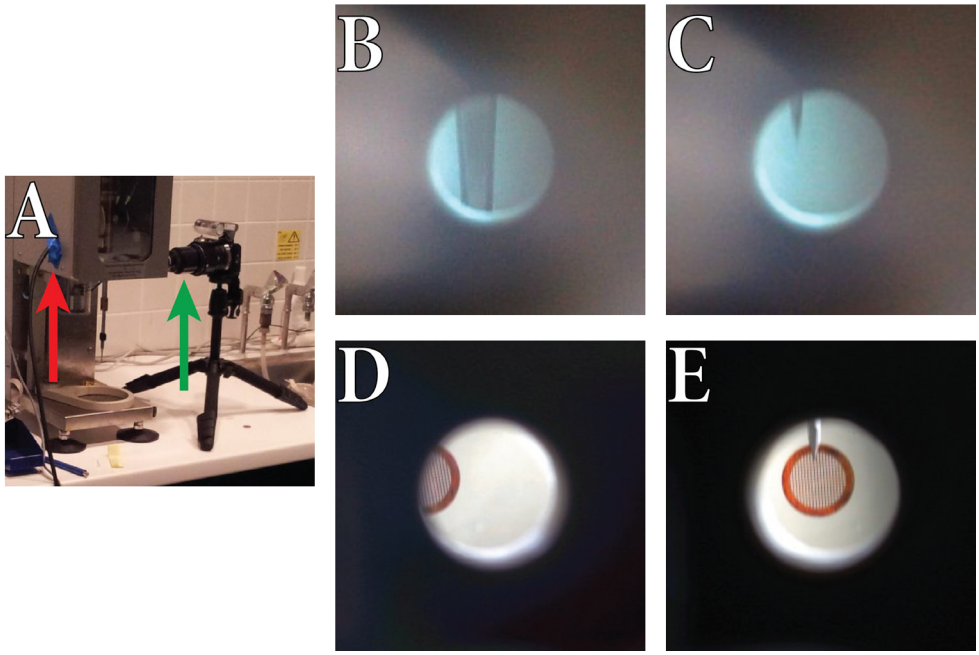

Figure 5.21: A photography based check of the correct flash triggering was used for horizontal and vertical alignments. A) shows the setup, with the digital camera (green arrow) positioned, such as the grid was visible through the light fiber tunnel. The UV light was aimed inside the the chamber and was inserted from the left side (red arrow). B) and C) demonstrate the proper tuning of the delay time (too slow, and EM grid has already passed the UV fiber (B), and the correct timing (C)), by using the UV flash alone as a background illumination. D) and E) show images acquired by using an optically triggered photo flash, and indicated incorrect alignment in the horizontal direction in (D), and after a correct horizontal shift of the tweezer in (E).

The second direct observation method utilized a similar principle. Essentially, we used the UV flash similar to a photographic flash. A camera was installed on the same level as the UV light fiber hole (figure 5.21 A) and the UV fiber inserted in the Vitrobot blotting chamber as a back-illuminating light flash. While the camera was set to long exposure mode of 10 seconds, the digital chip of the camera was only exposed during the automatically triggered short UV flash of 1.3 ms in length (see section 5.2.1). The resulting images, expectedly, showed a slight motion blurring in the falling direction (figure 5.21 B and C). To alleviate this blurring, a photodiode-based optically switched photography flash was triggered additionally to the UV flash. With a rise time in the ns region, the photodiode switch did not lag behind the real UV flash noticeably. Using the more powerful photo-flash, a very sharp, non-blurred image could be taken (figure 5.21 D and E). In both cases the images were used to detect time delay errors (figure 5.21 B and C) or horizontal misalignment (figure 5.21 D and E).

Overall, due to the fixed exit tunnel of the light fiber through the Vitrobot, the alignment in the vertical direction could be fixed within the soft- and hardware by changing the time delay. The offset in x-direction (figure 5.21 D) had to be addressed in subsequent plunging sessions by slightly shifting the tweezers by 2-3 mm to the right side. These settings resulted in stable flashing conditions without recalibrations for at least one year.

Raspberry Pi aided Speed Calculations

For additional analysis of the plunging speed and acceleration, the microcontroller was connected to a Raspberry Pi, an independent Linux computer offering a standard programming environment and far better computational performance. The Raspberry Pi was programmed in Python to receive signals from the Arduino (see section 5.19) and calculate parameters for a second-degree polynomial fit [6]. This offers higher precision than the linear least squared mean algorithm implementation in the Arduino. Additionally, all plunging data, as well as the data points and fit-curves are automatically saved by the Raspberry Pi for later reference. This can be used for checking the lubrication wear-off and/or for indicating mechanical problems inside the plunger.

Discussion of the Microcontroller Setup

The reason for using both an Arduino and a Raspberry Pi lies within the limitations of the devices used. The Arduino microcontroller is a "barebone" microcontroller which offers high precision in timing and receiving/sending, but has its limitations in the lack of computational power. Therefore an "on-line" curve-approximation for a prediction/interpolation-based UV-flashing was not possible. For quickly checking the approximate plunging rod acceleration, a simple linear least mean squared interpolation was used, which ignores the first degree velocity v_0 term. A more exact least mean squared regression could not be integrated due to memory restraints.

The second microcontroller, the Raspberry Pi, was used as an enhanced calculation and plotting device. The computing power is much higher on the Raspberry Pi (load-dependent up to 1GHz), but two main issues were making this device unusable as a replacement for the Arduino:

1. Low precision in timing
2. Limited number and difficulty in accessing input/output pins

Listed by importance, the first point being the low timing precision, which originates from the non-deterministic way signals are being processed. Programming for Raspberry Pi for high time precision would require low level programing, not within the scope of this work. Running Linux adds further delays to (a priori unknown) latency due to prioritizing tasks one after a time. Even without Linux, one would still need to circumvent the fact that the dynamic RAM in conjunction with the GPU leads to delays, same for writing and reading the SD storage card. All these issues together add up to non-deterministic time delays.

The second point raises the issue of the lack of pins accessible. 17 general purpose input/output pins are available with more/less difficulty of accessing them. [7] With currently 15 pins in use for the setup, possible extensions or upgrades would not be feasible without some complications.

To sum up, the Arduino was used for time-sensitive communication and signal

[6] *Numpy.Polyfit* Documentation: http://docs.scipy.org/doc/numpy/reference/generated/numpy.polyfit.html
[7] Low Level RPi: http://elinux.org/RPi_Low-level_peripherals#GPIO_hardware_hacking

transmission, while the more powerful Raspberry Pi was utilized for data vizualisation and as storage system.

Plunging Speed Modifications

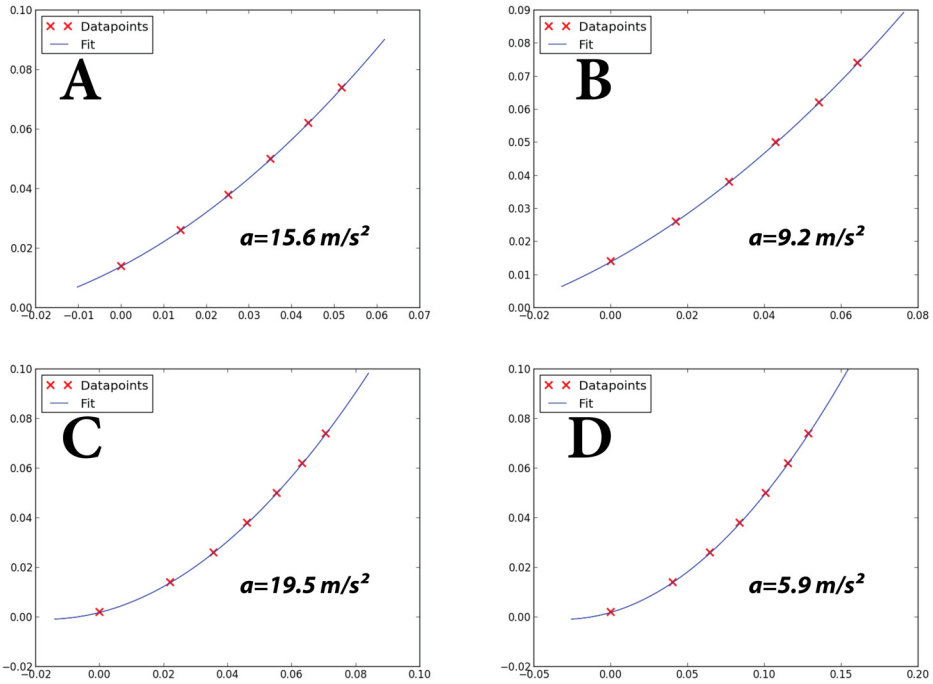

Figure 5.22: The plunging acceleration ("a") was measured by the light barrier array and Raspberry Pi setup introduced above (section 5.4.2 and figure 5.19). A) Normal plunging acceleration, B) after cutting the air pressure, C) after providing the plunger with additional air pressure, and D) after lowering the air pressure by a vacuum cleaner.

The speed measurements implemented inside the Vitrobot yielded plunger accelerations beyond the value of gravity (figure 5.22, A). Unlike the manual plunger, the Vitrobot additionally uses a non-documented air pressure system to accelerate the plunging rod, leading to higher speed and highly accelerated overall plunging. Obviously, once the air pressure was cut off, the acceleration is very close to the ones seen in the manual plungers (and below the gravitation acceleration) (figure 5.22, B).

To extend the capability of the device in terms of achievable timescales, the plunging rod was artificially slowed down or accelerated by either subjecting the rod to under-pressured (with a Miele vacuum-cleaner 1300W [8]), or adding a pressured gas tank to it (beyond $p \geq 6bar$ of pressure). It was possible to finetune the accelerations between 6 $\frac{m}{s^2}$ and 19 $\frac{m}{s^2}$ (figure 5.22 C, D) resulting in time differences of 14 ms down to 9 ms between UV flash and vitrification. A more flexible time resolution would be achievable by subjecting the Vitrobot to even more extreme under- or overpressure.

[8] Average Vacuum Cleaner Suction: http://en.wikipedia.org/wiki/Vacuum_cleanerAverage

5.4.3 UV-Flash Optimizations

To improve UV-uncaging efficiencies, the intensity of the UV-flash required to be optimized. With set parameters, such as charging voltage, capacitance chosen, the typical emission rates in UV from the Xenon flash lamp, or the specifications of the liquid light guide, there were only a few parts to be additionally fine-tuned. Estimated light loss occuring from the total dissipated Xenon flash energy was around 98% in the UV region (see table 5.1), under optimal conditions. Two of the factors reducing the overall yield are demonstrated in figures 5.23 and 5.24. Optical filters can be inserted between the narrow light guide entry and the Xenon light bulb (figure 5.23 A). Due to lack of beam collimation, around 75% of the light is lost here, as we demonstrated by using light sensitive paper and averaging several flash patterns (figure 5.23 B,C,D). On the other hand, the contamination built-up to the Xenon light bulb can be also be a source of the light yield decrease, as demonstrated in figure 5.24.

To optimize the illumination properties, the contaminated flash lamp (figure 5.24) was replaced and the reflector fully checked and realigned. Furthermore, the light guide had be as close as possible to the EM grid in order to minimize energy losses from beam spreading. Due to the flatter geometry of Vitrobot tweezers, we were able to come as close as 2-3 mm to the EM grid.

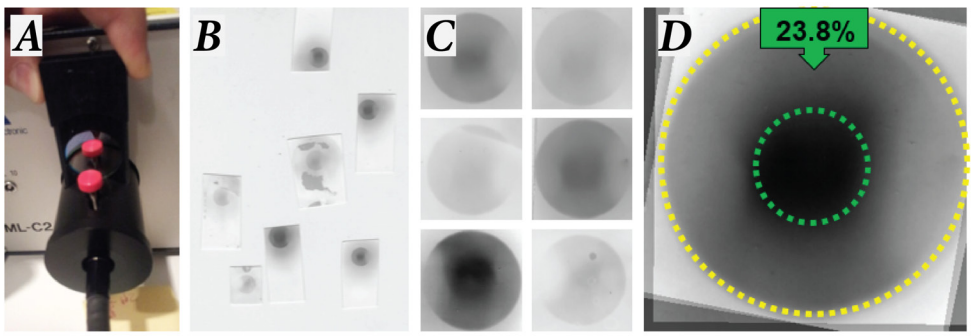

Figure 5.23: Calculating the light loss in the light guide adapter. (A) The light guide adapter is used for inserting up to two optical filters into the light path. (B) Several rounds of flashing were done individually on light sensitive photo-paper, which were subsequently developed. (C) This collage shows a collection of six representative exposures, that were then aligned and averaged (D). The greyvalues were used as an indication of intensity. The yellow dotted circle marks the total amount of light, while the green dotted circle marks the entry of the light fiber. Thus, only 23.8% of the original intensity effectively illuminated the sample.

Figure 5.24: UV flash lamp deterioration by contamination build-up (red arrow) on the glas surface. In the back, part of the parabolic reflector can be seen.

Factor	Relative Light Yield	Explanation	Measurement
Xenon Bulb Deterioration	$\propto 1$	Contamination on the Xenon bulb glass surface	Optimal case, no contamination
Reflector Orientation	$\propto 0.5$	Reflector position affecting light yield	Geometric constraints [a]
Transmission Filter 1	$\propto 0.78$	Transmittance of first filter (UV1)	Transmission filter specs [b]
Transmission Filter 2	$\propto 0.93$	Transmittance of second filter (SP395)	Transmission filter specs [c]
Focus on Fiber	$\propto 0.24$	Light entering entrance pupil of light fiber	Experiment from figure 5.23
Beam spreading	$\propto 0.22$	Loss due to fiber aperture	Geometric calculation [d]
Total	$\propto 0.02$		

Table 5.1: Overview of light losses due to several factors inside the light path. The cumulative light yield of 2% is displayed at the bottom and marked in red.

[a] Assuming that light is emitted in all directions (solid angle $\Omega = 4\pi$) both reflector and lens cover 30°opening angle from both front and back. Solid angle from where light is effectively collected: $\Omega = 2 \cdot (2\pi(1 - cos(2 \cdot 30°))) = 2 \cdot \pi$. Fraction between collected and lost light is 0.5.

[b] Rapp optoelectronic, http://www.rapp-opto.com/optical-filters.html

[c] Rapp optoelectronic, http://www.rapp-opto.com/optical-filters.html

[d] UV fiber of 3mm diameter has opening aperture of 0.5 (opening angle of 60°). The fiber is located on average 3mm from the grid, illuminating an area with a diameter of $2 \cdot (tan(30°) \cdot 3mm) + 3mm = 6.4mm$. The ratio between the illuminated area and the EM grid area is: Ratio $= \frac{(6.4mm)^2}{(3mm)^2} \approx 0.22$

5.5 ECT Imaging Methods

This last section assesses the applicability of dual-axis tomography and the PTEM (in subsections 1.6.2 and 1.6.1), for the tomographic acquisition of samples prepared by the two modified cryo-plungers.

5.5.1 Dual Axis Tomography

Several dual-axis tomograms of synaptosomes were recorded on the Titan Krios microscope, from which an example is shown in figure 5.25. Several problems arised, such as the "bubbling" effect due to high electron dose (see section 1.5 and [59]) and false double membranes from incorrect image alignment (figure 5.25). When looking at a well aligned single SV inside a synaptic terminal in figure 5.26, we could clearly see a more isotropic resolution, where the shape of the SV appeared similarly circular in all three projection planes (XY/YZ/XZ). In comparison with conventional single-axis tomography, we could therefore observe less distortions along the Z-axis (figure 5.26). Nonetheless, the additional time and the uncertainty of a correct image alignment made dual-axis tilt tomography not viable for our purposes, and therefore we decided to use single-axis tomography for all studies in neuronal cellular morphology (chapters 6 and 7).

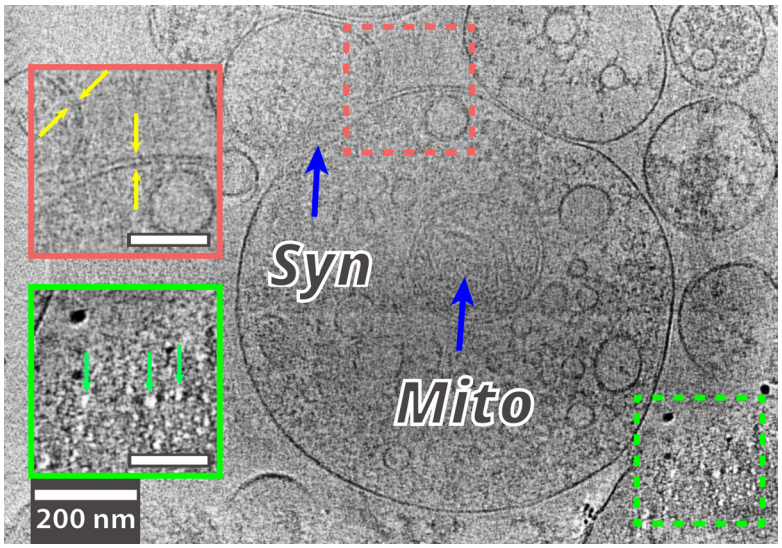

Figure 5.25: Overview of a dual-axis tomogram of a synaptosome taken with a FEI Titan Krios microscope, with attached K2 direct detector camera. The synapse ("Syn", blue arrow) and a mitochondria ("Mito", blue arrow) could be clearly recognized. Problems associated with dual axis tomogram alignment could be observed in the two dotted areas: Double or "ghost" membranes (yellow arrows) were observed due to alignment mismatching of the two separate tilt series (red box). Furthermore, the additional electron dose (green box), induced "bubbling" artifacts (green arrows). Scalebars: Overview: 200 nm, Insets: 100 nm.

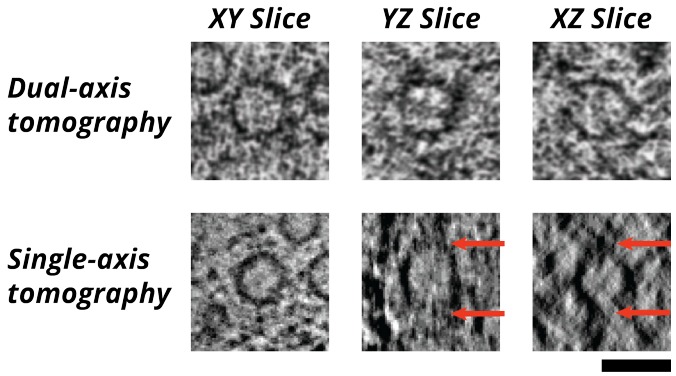

Figure 5.26: Advantage of dual-axis over single-axis tomography. Displayed is a slice through the SV, in three different projections. Dual-axis tomography (top row) showed an almost homogeneous, round SV shape in all projections (from left to right: XY, YZ and XZ), whereas single-axis tomography (bottom row) clearly displayed the more attenuated elongation in Z direction (red arrows). Scalebar: 50nm.

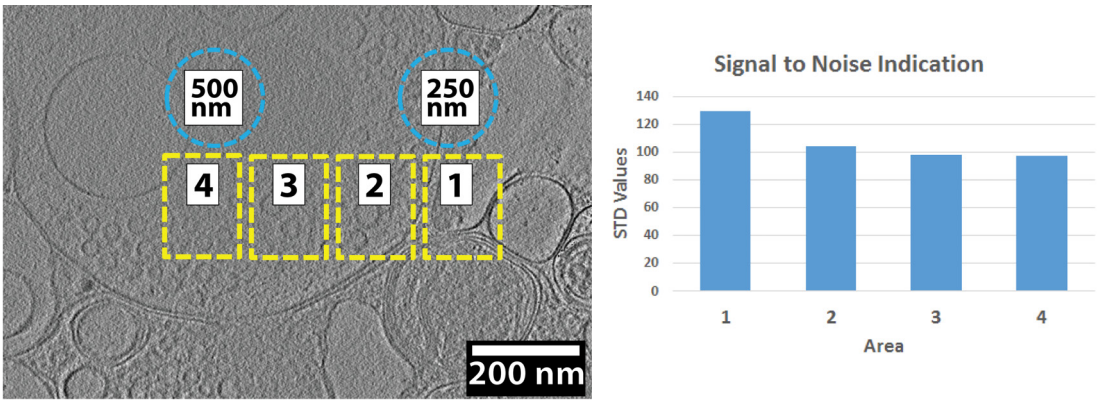

Figure 5.27: Left: Slice from a synaptosome tomogram taken with a 200kV microscope equipped with a VPP. While the right side of the cell was sufficiently thin for reasonable observation (yellow dotted box "1", with a sample thickness of around 250 nm), there was much less contrast at the thicker cell center of about 500 nm in thickness (left, yellow dotted box "4").
Right: Plotted std values in greyscale units for the areas marked in the left slice as an indicator for SNR.

5.6 Phase Plate TEM

The first prototype of the VPP was inserted into a FEI F20 base with modifications for VPP operation. The microscope operated at 200kV acceleration voltage, and had no imaging filter attached. This limited the practicability of this microscope, as observing details from samples beyond 250 nm thickness could not be resolved properly any longer. An example of this can be seen in figure 5.27. Already visually, the 500 nm thick central area of the tomogram appeared less resolved with poor contrast. As a test, we used the standard deviation of the greyvalues as an indicator for SNR. Essentially, in areas of even distribution of structure (e.g. SVs), the std was lower with higher noise contribution and vice versa. The values from the figure 5.27 were agreeing with our observation, that thicker areas appeared with less contrast.

The most recently installed FEI Titan Krios offered a higher acceleration voltage of 300 kV and an image filter, both vital for cellular ECT studies. Together with the Gatan K2 Summit direct detector, the level of contrast (see figure 5.28) can be currently considered state-of-the-art. Therefore, we began to use the VPP during the study of stimulated synapses prepared by the time-resolving cryo-plungers, as well as throughout the localization and characterization of 26S proteasomes in neurons (chapters 6 and 7).

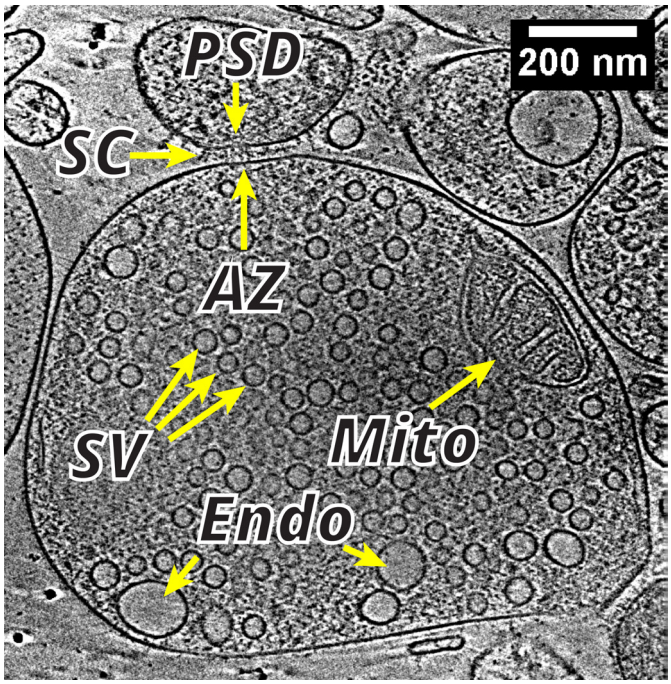

Figure 5.28: Slice from a synaptosome tomogram taken by a 300kV microscope with a VPP. Good contrast could be observed throughout the slice, even in the thicker central area. The synapse with the active zone (yellow arrows, "AZ"), synaptic cleft ("SC") and postsynaptic density ("PSD") was located on top, mitochondria on the right (marked "Mito"), endosomes ("Endo") and synaptic vesicle ("SV") are marked as well. Scalebar: 200nm.

5.7 Summary

This chapter demonstrated the capability and applicability of the UV light uncaging approach for studies of transient events in synapses, such as SV exocytosis. In addition, we described the design and implementation of two cryo-plungers performing time-resolved vitrification, as well as the optimal ECT imaging method.

Briefly, we demonstrated that:

1. Computational simulations showed that the uncaging yield under optimal condition is 66% (figure 5.6) with the parameters collected by direct measurements and the literature [230].
2. Direct observation of Ca^{2+} uncaging in a small volume by means of UV light showed a dissociation rate of 40%, or 630 mM free Ca^{2+} (figure 5.11).

3. This uncaged extracellular Ca^{2+} will likely increase under plunging conditions and is enough to invoke SV exocytosis, as demonstrated by the glutamate release assay in figure 5.3.
4. The first generation manual cryo-plunger is able to resolve times $t \geq 120ms$.
5. The second generation cryo-plunger was augmented with a light barrier array and a microcontroller to trigger the UV light before the sample is vitrified. This advanced design is capable to improve the time resolution down to at least $t \approx 9ms$.
6. The use of single axis tomography yields in less imaging artifacts and faster tomogram acquisition, making it our primary imaging method.
7. VPP in combination with an energy filter and 300 kV acceleration voltage increases SNR significantly and can be exploited for our ECT studies

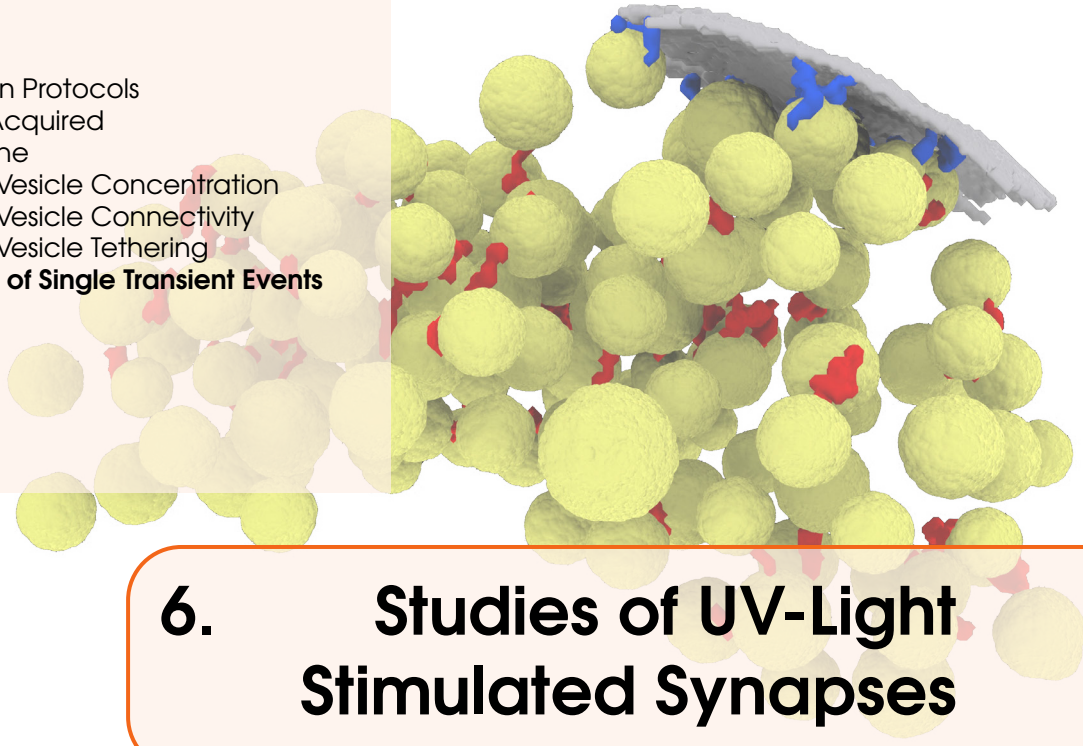

6. Studies of UV-Light Stimulated Synapses

6.1 Preface

We were able to directly observe and characterize fluorescence signals from EPSCs in TIRFM in chapter 4. Though the time resolution of the images were limited by the camera, the maximal image acquisition frequency of $f \approx 250Hz$ for a small ROI was enough to describe EPSCs in the cultured neurons (chapter 4). However, even with speedy and high resolution TIRFM, the XY resolution in live specimen is quite limited to only a couple of tens of nm [231, 232]. To investigate ultrastructural features in synapse morphology, one has to rely on high resolution microscopy methods, such as ECT [33, 233]. Beginning with the RIM studies (chapter 3), we showed ultrastructural deficits near the AZ underlying functional defects upon deletion of the important AZ protein RIM1α. Tethering was implicated in the successful exocytosis of SVs during signal transmission as former studies and chapter 3 showed [109, 234]. The understanding of SV tethering and exocytosis is still incomplete, primarily because direct evidential structural data of exocytosis events are rare [208]. Furthermore, it was already observed that long term stimulation lead to several severe effects in tethering or RRP sizes [109], but changes in these characteristics shortly after stimulation was still missing.

The previous chapter 5 was successful in demonstrating a stimulation protocol and its adaptation for cryo-EM studies, enabling high resolution time-resolved imaging. The technical innovation, combining light uncaging (chapter 4) and compatible cryo-plunger modifications (chapter 5), allowed us to examine the neuro-molecular understanding of SV tethering and exocytosis derived previously (chapter 3) only milliseconds after stimulation. In this chapter, we additionally focused on capturing transient synaptic events, by observing synaptosomes in three different time regimes after stimulation. We described the effects on synaptosomes roughly 10 ms and 120 ms after UV flash based stimulation (plunging sequence in detail in section 8.1.1 and schematically in figure 5.2), as well as after 5 seconds of stimulation with a manual stimulation protocol. The previous chapter 5 was successful in demonstrating a stimulation protocol and its

adaptation for cryo-EM studies, enabling high resolution time-resolved imaging. The technical innovation, combining light uncaging (chapter 4) and compatible cryo-plunger modifications (chapter 5), allowed us to examine the neuro-molecular understanding of SV tethering and exocytosis derived previously (chapter 3) only milliseconds after stimulation. In this chapter, we additionally focused on capturing transient synaptic events, by observing synaptosomes in three different time regimes after stimulation. We described the effects on synaptosomes roughly 10 ms and 120 ms after UV flash based stimulation (plunging sequence in detail in section 8.1.1 and schematically in figure 5.2), as well as after 5 seconds of stimulation with a manual stimulation protocol. The results of the study are outlined in this chapter.

6.2 Results

6.2.1 Stimulation Protocols

Stimulation Studies with UV Light Flash

The previous chapter (chapter 5) already showed the performance of DM-Nitrophen for Ca^{2+} uncaging studies. First, we used 30 mM KCl to depolarize the presynaptic membrane. Then, Ca^{2+} released upon a brief UV light flash enters the presynaptic cell and invoke SV exocytosis (this method is from here on referred to as UV light stimulation). The timing between UV light stimulation and vitrification was roughly 120 ms with the first generation plunger (dataset termed "Uncaged Ca^{2+} 120ms") (see chapter 5). Synapses were also prepared using the latest modified Vitrobot, exhibiting a time difference between flashing and vitrification of only around 10 ms (dataset "Uncaged Ca^{2+} 10ms").

Manual Stimulation with KCl

Prolonged stimulations lasting 1 minute with KCl are causing significant rearrangements of SVs, connectors and tethers in synaptosomes [108], most likely due to exocytosis of SVs. In our KCl stimulation study, the synapses were stimulated with KCl for 5 seconds (in buffer containing extracellular Ca^{2+}) on the EM grid and then frozen immediately (referred to "KCl stimulation" and dataset termed "KCl"). We could therefore describe the the synaptic ultrastructure 5 seconds after stimulation.

Control

Two controls have been measured accordingly: Control (termed "Control") were synapses not treated with DM-Nitrophen, nor subsequently UV flashed. They were kept in Hank's balanced medium (HBM) buffer (refer to section 8.1.1). We used this control for the subsequent statistical analysis and comparison of the different treatments. Additionally, some synapses were exposed to the UV- lightflash (termed "Flash Control") to observe the effect of the intense UV light flash exposure on the synapses. Because of high similarity between the two controls, we subsequently used unflashed control synapses as statistical controls, as they offered a higher sample size (see table 6.1).

6.2.2 Dataset Acquired

Only tomograms with clearly visible PSDs as well as closed presynaptic membranes were kept. The SVs were round and appeared to be of homogeneous size of around 41 nm in diameter. In total, 37 tomograms have been selected for further segmentation and analysis (see table 6.1). In the analysis process, only SVs within 250 nm of the AZ were considered. Confidence tests used were Student's t-test for Gaussian distributed values, Kruskal-Wallis for not normally distributed values and Chi-square for values indiscrete bins. Pearson's coefficient were used for correlation analysis, and its significance determined using t-test. sem was calculated and shown in graphs and confidence values given in the graphs are $p < 0.05$: *, $p < 0.01$: ** and $p < 0.001$: ***. For further details and computation of statistics, refer to section 8.1.4.

Treatment	Animals	N	Vesicles	Connectors	Tethers
Control	4	10	1033	4472	247
Flashed Control	1	6	855	5117	282
Uncaged Ca^{2+}, 10ms ("Flash 10 ms")	3	9	788	3875	135
Uncaged Ca^{2+}, 120ms ("Flash 120 ms")	2	7	686	1890	253
KCl 5 seconds ("KCl")	1	5	333	1029	23
Sum		**37**	**3695**	**16383**	**940**

Table 6.1: Dataset analyzed in this study, where N denotes the number of tomograms taken.

6.2.3 Active Zone

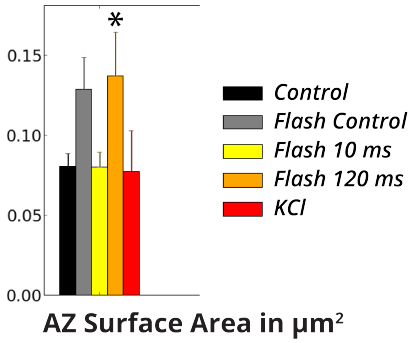

Figure 6.1: AZ surface area in μm^2 demonstrated a slight change upon stimulation in 120 ms stimulated synapses. The AZ surface area was directly extracted and calculated with the manual segmentation provided by the author (refer to section 8.1.4 for details). (Black: control, grey: flashed control, yellow: UV-flash 10ms, yellow: UV-flash 120 ms, red: KCl 5 seconds)

Generally, the AZ surface area did not change significantly upon stimulation, with the exception of 120 ms stimulated synapses. Neither persistent 5 seconds stimulation, nor

shorter 10 ms UV light flashing affected the AZ area significantly, compared to the Control values [1](figure 6.1).

6.2.4 Synaptic Vesicle Concentration

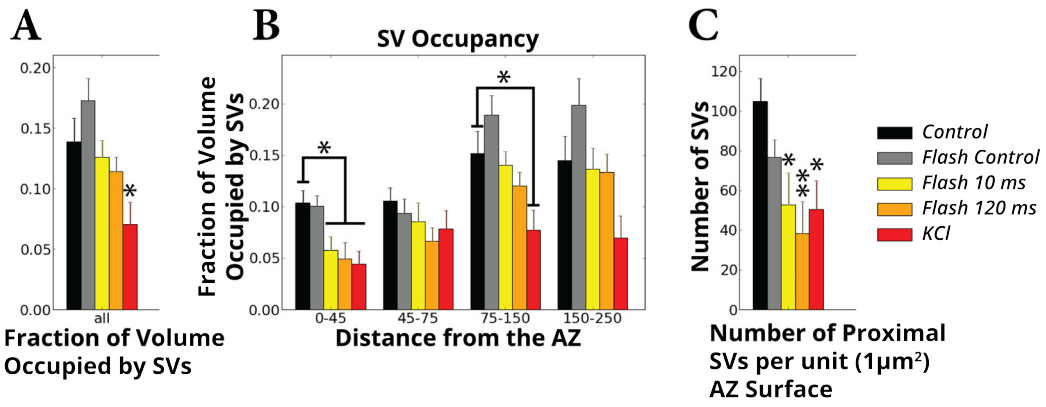

Figure 6.2: A) SV occupancy within 250 nm of the AZ showed decreased concentration with increasing stimulation time. The SV occupancy was calculated by using the fraction of total volume occupied by SVs and the total previously segmented cytoplasmic volume up to 250 nm from the AZ.
B) SV concentration dependance on distance from the AZ was dependent on stimulation. The local occupancy of SVs was calculated by using the fraction of total volume occupied by SVs and the cytoplasmic volume within the given distances. ("Proximal": 0-45 nm from AZ, "intermediate": 45-75 nm, distal regions: 75-150 nm and 150-250 nm) [108, 109]
C) Number of proximal SVs per unit AZ area suggested SV exocytosis after stimulation. By using the AZ surface area from figure 6.1 and the average number of proximal SVs, we were able to calculate the average number of proximal SVs per $1\mu m^2$ AZ area.
(Black: control, grey: flashed control, yellow: UV-flash 10ms, yellow: UV-flash 120 ms, red: KCl 5 seconds)

Next, we will briefly describe the SV concentration within the (manually segmented) cytosol. 5 sec KCl produced a significant reduction of around 50% in overall SV concentration (figure 6.2 A), whereas the two flash protocols displayed non-significant reductions [2].

The SVs concentration with respect to their distances to the AZ (figure 6.2 B) indicated that the SV reduction is most prominently seen in the proximal zone (0-45nm from the AZ), where the significant decrease was around 50% for both flash and KCl stimulation protocols [3]. The distal areas were less affected in UV light stimulated synapses (10ms

[1]Control: 0.08 ± 0.01, Flash Control: 0.13 ± 0.02, Flash 10ms 0.08 ± 0.01 *, Flash 120ms 0.14 ± 0.03 n.s., KCl: 0.08 ± 0.03 n.s.

[2]Control: 0.14 ± 0.02 , Flash Control: 0.17 ± 0.02, Flash 10ms 0.13 ± 0.01 n.s., Flash 120ms 0.11 ± 0.01 *, KCl: 0.07 ± 0.02 *

[3]Control: 0.10 ± 0.01 , Flash Control: 0.10 ± 0.01 , Flash 10ms 0.06 ± 0.01 *, Flash 120ms 0.05 ± 0.02 *, KCl: 0.04 ± 0.01 **

and 120 ms) with a concentration reductions ranging between 36% and 7% [4]. KCl showed an almost stable low SVs concentration throughout all distances compared with Control.

Looking at the number of SVs in the proximal zone normalized by the unit AZ area ($1\mu m^2$) (figure 6.2 C), we saw that stimulation over any timeframe severely and significantly decreased that value compared to the Control [5].

6.2.5 Synaptic Vesicle Connectivity

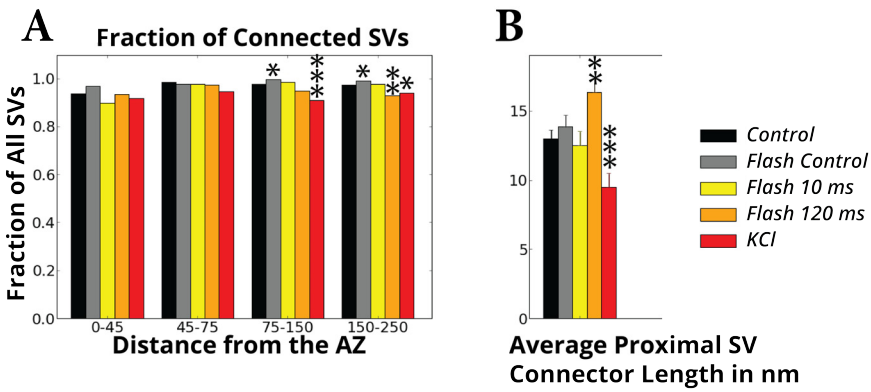

Figure 6.3: A) Fraction of connected SVs depending on distance to the AZ were unaffected by the stimulation protocols in the proximal region. Like figure 6.2 B, the fraction of connected SVs in individual distance bins were calculated.
B) Mean connector length of proximal SVs. The mean connector length is displayed in nm.
(Black: control, grey: flashed control, yellow: UV-flash 10ms, yellow: UV-flash 120 ms, red: KCl 5 seconds).

Even under continuous and prolonged stimulation, the average connectivity rate was above 90% across all distal ares with no significant differences in the proximal and intermediate zone (figure 6.3 A) [6]. In the distal areas, we could observe morphological differences upon the slightly longer stimulated synapses (120 ms and 5 seconds) [7].

If we only look at the proximal zone, these connectors were slightly different in the proximal zone depending on the stimulation (figure 6.3 B), with around 9-16nm in length on average [8].

[4] Control: 0.14 ± 0.02 , Flash Control: 0.20 ± 0.03 , Flash 10ms 0.14 ± 0.02 n.s., Flash 120ms 0.13 ± 0.02 n.s., KCl: 0.07 ± 0.02 n.s.

[5] Control: 104.93 ± 11.42 , Flash Control: 76.73 ± 8.72 , Flash 10ms 52.70 ± 15.98 *, Flash 120ms 38.30 ± 15.94 **, KCl: 50.42 ± 14.37 *

[6] Control: 93.8%, Flash Control: 96.8% , Flash 10ms 89.7% n.s.,Flash 120ms 93.3% n.s., KCl: 91.7% n.s.

[7] Last bin: Control: 97.3%, Flash Control: 99.2% , Flash 10ms 97.8% n.s.,Flash 120ms 92.9% **, KCl: 94.0% *

[8] Control: 12.99 ± 10.43 , Flash Control: 13.85 ± 12.25 , Flash 10ms: 12.53 ± 0.99 n.s., Flash 120ms: 16.35 ± 0.93 ***, KCl: 9.48 ± 1.02 ***

6.2.6 Synaptic Vesicle Tethering

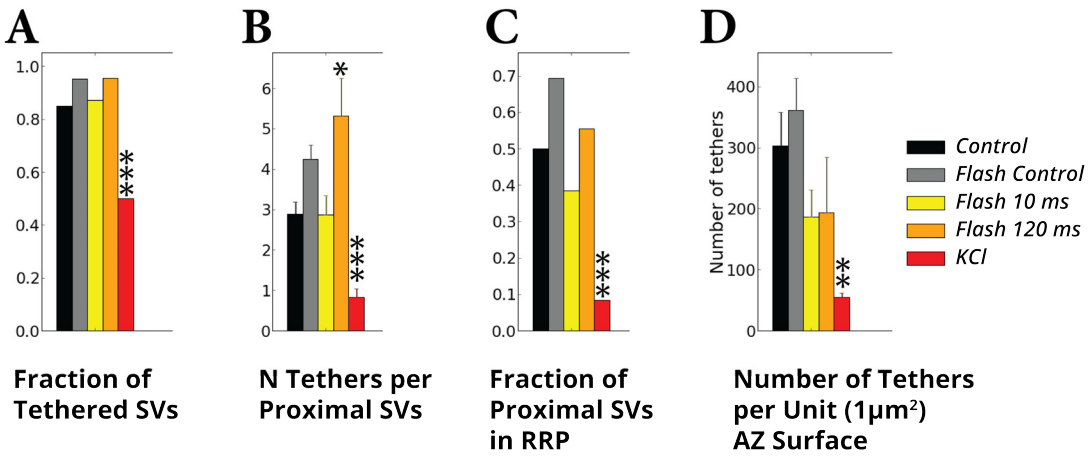

Figure 6.4: A) Fraction of proximal SVs tethered only changed upon strong and prolonged stimulation.
B) Average number of tethers per proximal SV changed upon stimulation.
C) Fraction of proximal SVs that are in the RRP was basically nonexistent after strong and prolonged stimulation. We structurally define SVs as members of the RRP by having more than two tethers.
D) Number of tethers per unit ($1\mu m^2$) AZ area showed decreasing numbers upon the duration of stimulation.
(Black: control, grey: flashed control, yellow: UV-flash 10ms, yellow: UV-flash 120 ms, red: KCl 5 seconds)

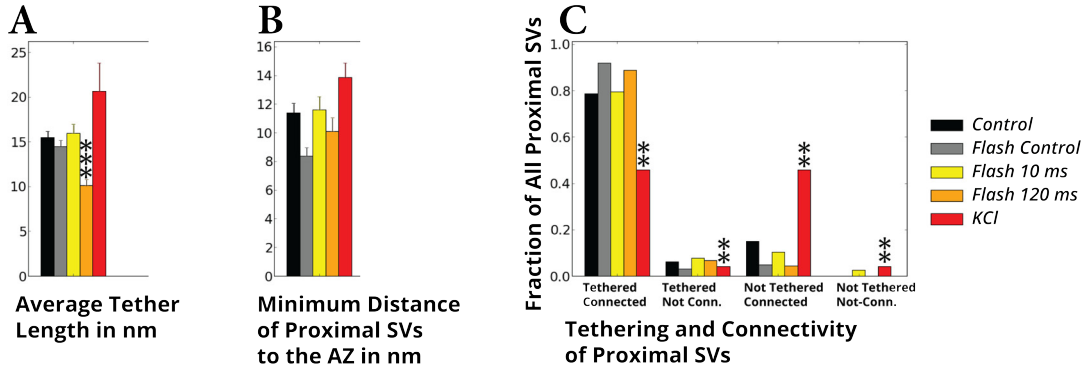

Figure 6.5: A) Mean tether length in nm appeared almost independent of stimulation.
B) Minimum distance of proximal SVs to the AZ in nm was also unaffected by stimulation.
C) Fraction of SVs with their linking status only showed a severe difference upon strong and prolonged KCl stimulation. Here, all proximal SVs were sorted into four different categories (y-axis: tethered and connected, tethered and not connected, not tethered and connected and neither tethered nor connected).
(Black: control, grey: flashed control, yellow: UV-flash 10ms, yellow: UV-flash 120 ms, red: KCl 5 seconds)

Control synapses were highly tethered, however we observed a significant drop in

tethered SVs in KCl stimulated synapses (figure 6.4 A) [9]. Short stimulation, such as the UV flash induced ones, did not induce any significant change in the tethered fraction.

The number of tethers per proximal SV in figure 6.4 B varied from around 3 to 5 tethers in unstimulated and short stimulated SVs, whereas longer KCl stimulation significantly reduced tethers [10].

In KCl, the majority of proximal SVs had no tethers, and only a few are left with more than 2 tethers. We directly used these numbers to calculate the fraction of proximal SVs, that are "structurally primed", i.e. with more than 2 tethers. We denoted them in figure 6.4 C as belonging to RRP. We can clearly see that the RRP was heavily reduced in long KCl stimulation, whereas shorter flash stimulation did not affect the RRP size significantly [11].

Another verification that KCl stimulation significantly depleted tethers, can be seen when we looked at the average tether count normalized per unit AZ surface area ($1\mu m^2$) (figure 6.4 D). Furthermore, due to the overall reduced SVs number, all UV flash stimulated synapses do have lower average tether count per unit AZ surface area as well [12].

The tether length appeared to be mostly independent of stimulation (figure 6.5 A), as there were no significant differences between the treatments, with the exception of 120 ms stimulated synapses [13]. Similarly, the minimal distance of proximal SVs to the AZ was unaffected upon stimulation (figure 6.5 B) [14].

To give a broader overview of the interplay of tethers and connectors in proximal SVs, figure 6.5 C is provided. While the majority of proximal SVs were both connected and tethered the same time (first bin 6.5 C [15]), long KCl stimulation heavily decreased this value from above 80% to only 46%. This significant decrease was due to SVs that are not tethered (but connected), in the third bin 6.5 C [16], suggesting insufficient tether recruitment under long stimulation.

Additionally, table 6.2 lists the correlation between the number of tethers per SV and the SV distance to the AZ. Similar to the RIM study earlier (in section 3.3.2), a higher tether number was correlated to a closer SV proximity to the AZ - independent of the treatment.

[9] Control: 85.0% , Flash Control: 95.2% , Flash 10ms: 87.2% n.s., Flash 120ms: 95.6% n.s., KCl: 50.0% ***

[10] Control: 2.89 ± 0.29 , Flash Control: 4.24 ± 0.36 , Flash 10ms: 2.87 ± 0.47 n.s., Flash 120ms: 5.31 ± 0.94 *, KCl: 0.83 ± 0.21 ***

[11] Control: 50.0% , Flash Control: 69.4% , Flash 10ms: 38.5% n.s., Flash 120ms: 55.6% n.s., KCl: 8.3% ***

[12] Control: 303.05 ± 54.88 , Flash Control: 361.80 ± 52.10 , Flash 10ms: 186.60 ± 44.63 n.s., Flash 120ms: 193.81 ± 90.66 n.s., KCl: 54.28 ± 7.69 **

[13] Control: $15.50 \pm 0.68nm$, Flash Control: $14.49 \pm 0.67nm$, Flash 10ms: $15.94 \pm 1.00nm$ n.s., Flash 120ms: $10.10 \pm 0.69nm$ ***, KCl: $20.62 \pm 3.18nm$ n.s.

[14] Control: $11.38 \pm 0.67nm$, Flash Control: $8.39 \pm 0.57nm$, Flash 10ms: $11.58 \pm 0.94nm$, Flash 120ms: $10.11 \pm 0.92nm$, KCl: $13.84 \pm 1.03nm$

[15] Control: 78.7% , Flash Control: 88.9%, Flash 10ms: 79.5% n.s., Flash 120ms: 88.9% n.s., KCl: 45.8% **

[16] Control: 15.0% , Flash Control: 4.8% , Flash 10ms: 10.3% n.s., Flash 120ms: 4.4% n.s., KCl: 45.8% **

Condition	Pearson Correlation Coefficient	P (t-test)
Control	-0.51	< 0.001
Flash Control	-0.54	< 0.001
Flash 10 ms	-0.66	< 0.001
Flash 120 ms	-0.61	< 0.001
KCl	-0.58	< 0.001

Table 6.2: Correlation between number of tethers per vesicle and vesicle distance to the AZ. Statistical significance (P values) was determined by t-test.

6.3 Observation of Single Transient Events

Exocytosis Events

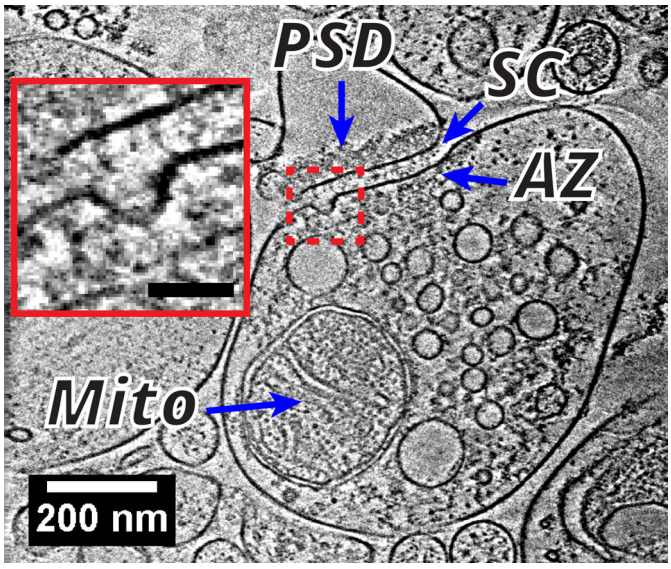

Figure 6.6: Slice of a tomogram showing a membrane invagination. AZ membrane ("AZ"), synaptic cleft ("SC"), PSD, and mitochondria ("Mito") are marked with blue arrows. At the AZ (red dotted rectangle), a membrane invagination is visible (enlarged view top left). Scalebars: 200 nm for the overview and 50 nm in inset.

Figures 6.6, 6.7, 6.8, 6.9, and 6.10 show some examples of single events extracted from 10 ms UV light stimulated tomograms. Generally, putative exocytosis events, such as in figures 6.6, 6.7 and 6.8 were rare, and almost non-existent.

The figure 6.6 displays a well resolved membrane invagination of a diameter of around 50 nm, without any obvious additional membrane coating, which might hint towards exocytosis, rather than a membrane retrieval aided by Clathrin.

For the two invaginations in figure 6.7, the surface area was measured to be 10140 nm^2 and 6450 nm^2 with an average diameter of around 70 nm and 40 nm, respectively. Compared with the average surface area of around 5300 nm^2 (by using our average SV diameter of 41 nm), we could assign the smaller invagination most likely to a single exocytosed SV, whereas the larger one either poses a bigger SV (such as the one

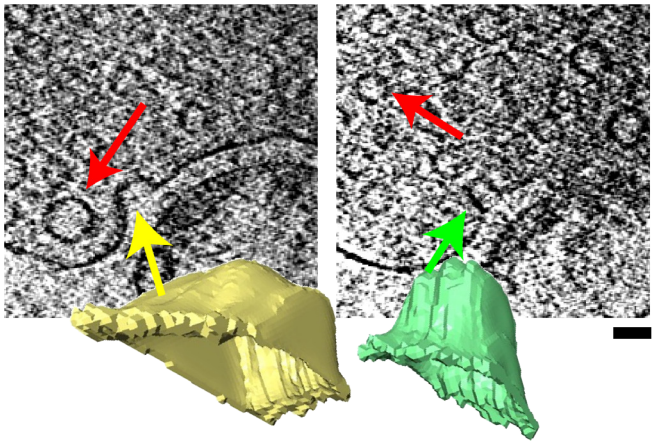

Figure 6.7: Two different membrane invaginations from the same synapse are displayed with their respective enlarged segmentations. Both of them were segmented and the isosurfaces displayed slightly tilted below for visualization. The yellow and green arrow indicate the location of the invaginations. The surface areas of these invaginations were calculated as 10140 nm^2 and 6450 nm^2 with the manual segmentation. The red arrows indicate neighboring SVs with the surface area matching the invagination in the same frame (diameter left SV: 58 nm (surface: 10568 nm^2), right SV: 46 nm (surface: 6647 nm^2)). Scalebar: 50 nm

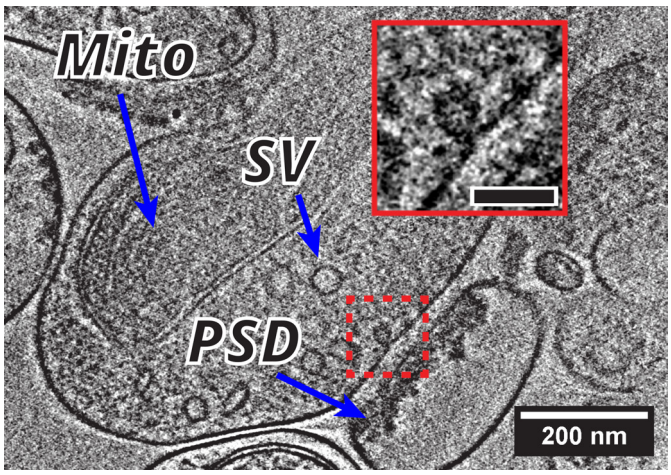

Figure 6.8: A putative SV exocytosis event is taking place at the AZ (red dotted square). A membrane contact forming a presumably open SV neck is visible in the enlarged view, where the AZ membrane is clearly interrupted at the contact point. PSD ("PSD") and mitochondria ("Mito") are marked with blue arrows. Scalebars: 200 nm in the overview and 50 nm in the inset.

indicated on the same frame with a red arrow in figure 6.7), compound exocytosis, or instead a (ultrafast) bulk endocytosis mechanism.

Figure 6.8 demonstrated a more delicate structure, which might be an exocytotic fusion pore [235], where the SV is fused to the AZ. In the case of an exocytosis event, it was unclear from this snapshot alone, whether it showed the beginning of the full-collapse model or a "kiss-and-run" scenario [236], where an open channel between SV and the AZ is used for neurotransmitter discharge into the synaptic cleft. However, figure 6.8

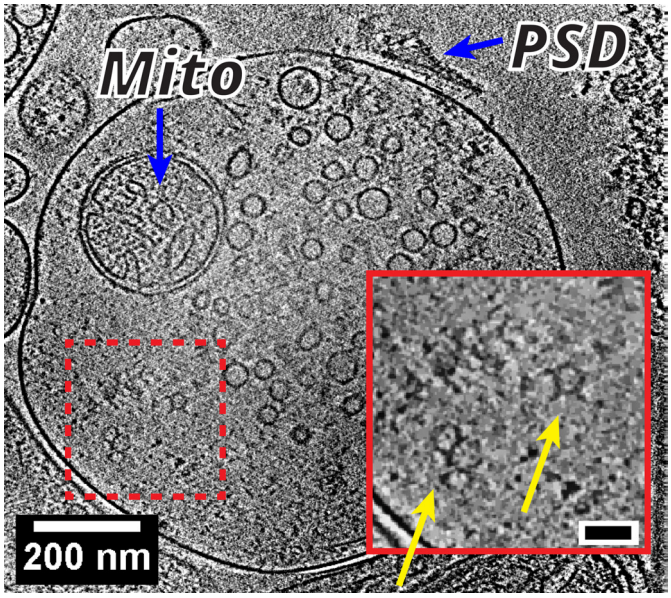

Figure 6.9: Slice of a tomogram showing clathrin coats. PSD and mitochondria ("Mito") are marked with blue arrows. Remotely, in the back part of the synapse (red dotted rectangle), several clathrin coats were visible (yellow arrows in enlarged view top left). Scalebars: 200 nm for the overview and 50 nm in inset.

could be also interpreted as a membrane point contact, possibly hinting towards a single SV exocytosis, or a single SV retrieval from the AZ membrane (single SV endocytosis).

The previously described appearance of hemi-fused SVs [237] was most likely due to fixatives and crosslinking artifacts employed in that study and was shown to produce data of limited accuracy [238]. In our samples, only SVs with very short tethers could be detected, where the SV membrane can still be clearly distinguished from the AZ membrane 6.11.

Endocytosis Events

Endocytosis is important in replenishing the SVs "lost" after or during prolonged stimulation [81]. The retrieval of single SVs upon stimulation is supported by CME [239]. While the CME requiring several seconds ($\approx 11sec$) to complete, there are also fast modes ($\approx 1sec$) without any clathrin interaction, most likely linked to the "kiss-and-run" exocytosis models [91, 240]. Due to the relatively long time constant in CME, clathrin coats were readily visible in several tomograms such as in figures 6.9 and 6.10, easily recognizable with its characteristic penta- and hexagonal lattice, where even single triskelions of clathrin could be detected (figure 6.10). In the some of the cases (such as in figure 6.9), clathrin coats could be identified close to the membrane, and possibly to early endosomes. The clathrin structure observed is in good agreement with those obtained in ECT *ex situ* studies from isolated or reassembled coats [241, 242].

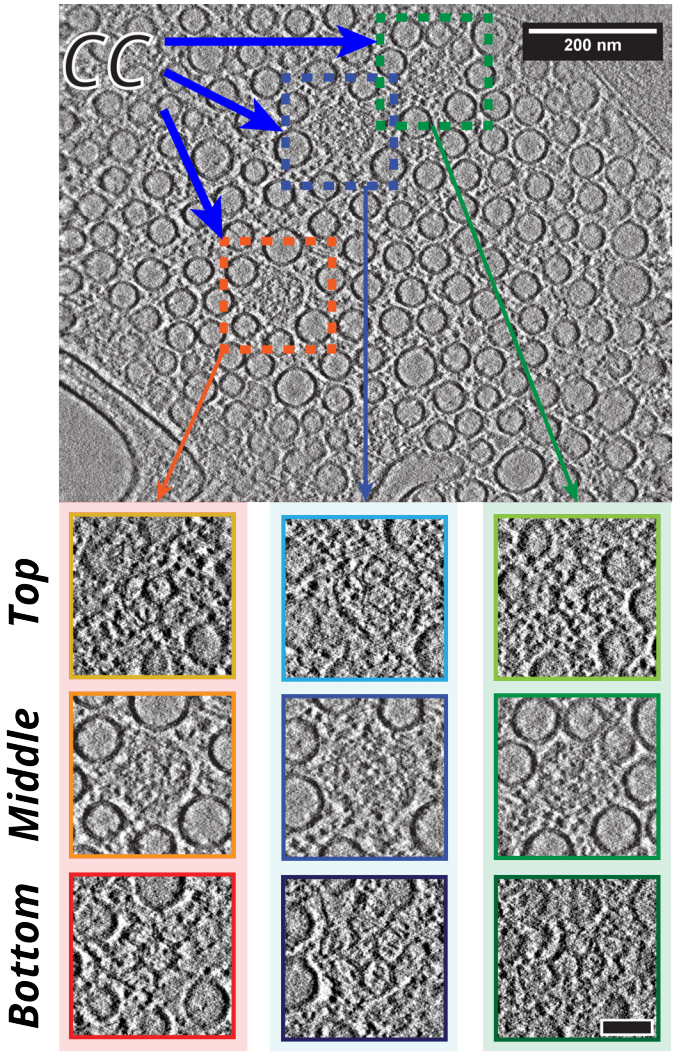

Figure 6.10: Well visible clathrin coats in isolated SVs. Clathrin coats ("CC") in this tomogram were empty, i.e. without any SV inside. The locations of the clathrin coats are indicated by blue arrows and are marked with a red/blue/green rectangle. Each rectangle area (represented by three columns) was then divided into three different Z levels and displayed below the overview (top, middle, bottom row). Both the top and bottom view clearly shows the typical clathrin coat hexa- and pentameric latticestructure. Scalebars: 200 nm for the overview (top) and 50 nm in the enlarged slices (bottom).

6.4 Discussion

Three different time regimes after synaptic stimulation (10ms, 120ms and 5 seconds) were probed in our setup. Our group already applied KCl stimulation over a comparatively long period of time (1 minute) and observed its effect on synapses [108]. This study revealed major changes in SV concentration and tethering characteristics similar in nature as the previous study [109] upon a 5 seconds stimulation duration and, to a lesser extend, in synapses of 10 ms and 120 ms stimulated synapse.

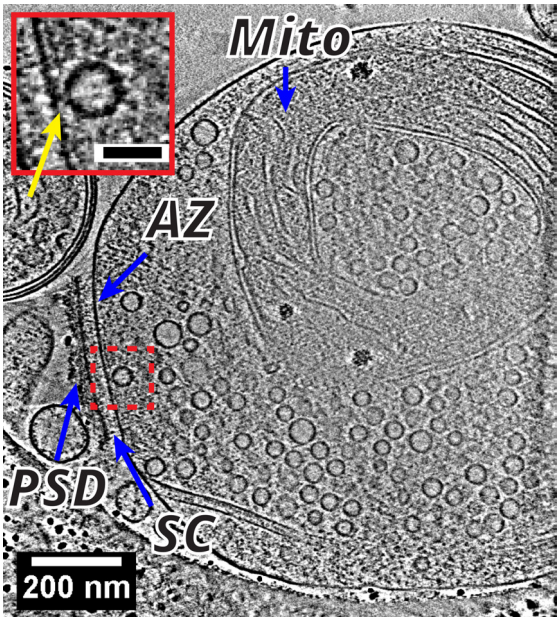

Figure 6.11: Overview slice of a representative synaptosome with a SV very close and attached to the AZ membrane with a tether. Postsynaptic density ("PSD"), AZ ("AZ"), mitochondria ("mito"), and synaptic cleft ("SC") are denoted with black arrows. The red dotted rectangle is enlarged top left to show the short tether (yellow arrow) connecting the SV with the AZ membrane. Scalebars: 200 nm in the overview, 50 nm in the inset.

Effect of Stimulation on Synaptic Morphology

The KCl stimulation invoked a strong decrease in SV concentration (figure 6.2 A), which is plausible and in good agreement with longer stimulation times of the previous study [108]. We observed that less severe and shorter stimulation with UV flash changed the SV concentration profile only slightly (figure 6.2 A). Nonetheless, the decrease in SVs under every stimulation protocol was evident in the proximal distance (figure 6.2 B), strongly suggesting that this effect was caused by exocytosed SVs near the AZ [108, 208].

Prolonged 5 seconds KCl stimulation led to a highly significant reduction in overall tethering (figures 6.4A, B, D and 6.5 C). Combined with its stark decline of the RRP in this treatment (figures 6.4C), we could clearly observe the aftermath of excessive SV exocytosis over the time course of 5 seconds. These results are well in line with the literature, which proposed extremely fast exocytosis mechanisms [243–245]. Most likely tether recruitment was the limiting factor of SV exocytosis in 5 second stimulated synapses, as there were still enough SVs in the proximal zone (figure 6.2B), but an overall low number of tethers per tethered SV, thus highly limiting the RRP (figures 6.4 B and 6.4 C).

Contrary to the strong phenotype after 5 seconds of KCl stimulation, a far less severe morphological reorganization near the AZ was observed with the UV flashed synapses. They were virtually not affected in SV tethering (figures 6.4 A, B) or RRP size (figure 6.4 C). Within a time scale of 15 ms after stimulation, it was shown that the AZ membrane is essentially in an equilibrium [208], also shown by the similar values in AZ surface

in figure 6.1. Thus overall, compensatory mechanisms were likely the cause in the similarity of two flashed synapses to the control group in overall tethering and SV concentration characteristics.

In general, the tethering mechanics seemed to work appropriately, also under strong and prolonged KCl stimulation, as the intact correlation between the number of tethers and the distance to the AZ showed (table 6.2). Combining the reduced SVs concentration with the high decrease in tethering, we could see that exocytosis effectively removed more tethers than SVs in stimulated synapses, in accordance with the model proposed in the earlier work [109]. Overall, we observed a more prevalent tethering compared to previous studies [108, 109]. We assumed this to be based on the higher detection rate of those filaments due to the increased quality of tomograms. This was also seen in the tether length (figures 6.5 A), where the Control and KCl values demonstrated a much higher value (factor of two to three) compared to the old data [108].

As anticipated, our control group was very similar to earlier studies [108, 109] using synaptosomes extracted from rodent brain. This included the typical SV concentration profile and high (inter-)connectivity. Expectedly, the "Flash Control" treatment showed similar values to control. Several studies using setups with the same UV flash device with an illumination area three orders of magnitude smaller ($0.008 - 0.015 mm^2$ instead of $\approx 30 mm^2$) did not report any obvious UV phototoxicity [246, 247], ruling out any serious phototoxic effects in our sample. The temperature jump recorded by another study using a UV light flash [205] might have had a small-scale effect, which could not be ruled out completely. This temperature jump however, would have only affecting the synapse morphology during the plunging drop of less than 120 ms, most likely not causing any observable major changes.

Transient Events

The putative SV exocytosis events recorded, such as in figures 6.6, 6.7 and 6.8, are most likely in fact of exocytotic nature. The invaginations formed were not located to the sides of the AZ and therefore did not correlate at all with the endocytic intermediates observed 50 ms - 100 ms after stimulation [208]. The almost non-existent endocytotic pit formation described 15 ms - 30 ms after stimulation [208], strongly suggested against the recorded events being categorized as endocytosis related. The two invaginations in figure 6.7 might stem from two different processes. The invagination with the smaller surface area was within 20% of the average SV surface area, making it likely a single SV exocytosis event. The other invagination with the surface area of roughly two times the average SV surface area might be either a bigger SV during exocytosis, a compound exocytosis event, or a bulk endocytosis event. Compared with the literature, the smaller SV with its diameter of around 40 nm corresponded well to SV exocytosis pits observed in mouse hippocampal synapses in size [208], whereas the bigger invagination could not be clearly assigned to one specific process.

Single SVs endocytosis in form of CME were sometimes observed (figure 6.9), and clathrin coated SVs were most likely pinched off from endosomes as proposed by the literature [90]. The empty clathrin coat structure acquired from isolated SVs and depicted in figure 6.10 were in good agreement with those observed in the literature

[242]. The clathrin coat buildup in isolated SVs in figure 6.10 was possibly caused by a lack of activity in ATP-dependent uncoating agents, such as Hsc70 [248]. Fast bulk endocytosis reported earlier [88, 91] should be readily visible [208], but could not be identified in any of our stimulated synapses.

6.5 Summary

Stimulated synapses were observed using ECT and compared with earlier high resolution studies [91, 109, 208]. We revealed major changes in SV concentration and tethering characteristics upon only 5 seconds of stimulation, demonstrating severe morphological alterations comparable with the previous study [108] in a significantly shorter time. Additionally, we were able to describe the morphological landscape of synapses after even shorter stimulation. Interestingly, both 10 ms and 120 ms UV light uncaging based stimulations were successful in introducing changes at the proximal zone close to the AZ, highly suggesting working SV exocytosis. However, the overall morphological alterations in the ms time regime after UV light stimulation were small compared to the control synapses, in agreement with the literature [208]. Several snapshots of transient events (see section 6.3) were taken from 10 ms stimulated tomograms and provided visual evidence of working SV exo- and endocytosis in synaptosomes at a short timescale (figures 6.6, 6.7 and 6.8), demonstrating the capabilities of time-resolved vitrification and ECT.

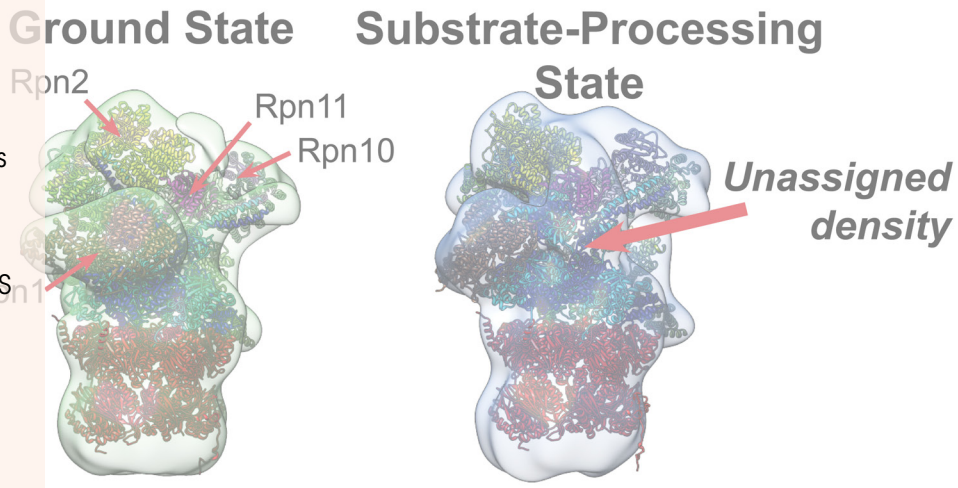

7. 26S Proteasome *in Situ* in Intact Neurons

7.1 Preface

This study has been conducted with Dr. Yoshiyuki Fukuda and this section is a modified version of the manuscript ("A molecular census of 26S Proteasomes in Intact Neurons" by Shoh Asano*, Yoshiyuki Fukuda*, Florian Beck, Antje Aufderheide, Friedrich Förster, Radostin Danev, and Wolfgang Baumeister; * Equal contribution). This study has been published in *Science* [32].

The contributions for the work were as following:

Shoh Asano	Tomogram and data analysis
Dr. Yoshiyuki Fukuda	Preparation and data acquisition
Florian Beck	Computer and scripting support
Antje Aufderheide	Rigid body fitting
Dr. Friedrich Förster	Group leader, computational structural biology
Dr. Radostin Danev	Group leader, phase plate electron microscopy
Prof. Wolfgang Baumeister	Department director

All authors contributed in the discussion and S.A., F.F. and W.B. wrote the manuscript. Figures were prepared by S.A.. Senior authors were all participating in the analyses steps.

7.2 Introduction

The UPS plays an integral role in neurons, with its function ranging from neuronal morphogenesis [249] or regulating presynaptic processes [104, 109] (see section 2.3).

In brief, the 26S proteasome is a 2.5 MDa multi-subunit protein, which is responsible

for degradation of most proteins inside the cells [30]. The proteolytic sites are located within the barrel shaped 20S core particle, which is capped on either or both ends by the 19S RP, as indicated in figure 7.1, left.

Proteins to be degraded are tagged with several ubiquitin molecules, which in return are recognized by the RP. The tagged protein is bound to the RP and then unfolded and guided into the 20S core particle, where it is digested [250] (figure 7.1 right). Hereby, the ubiquitin chain is removed and can be reused.

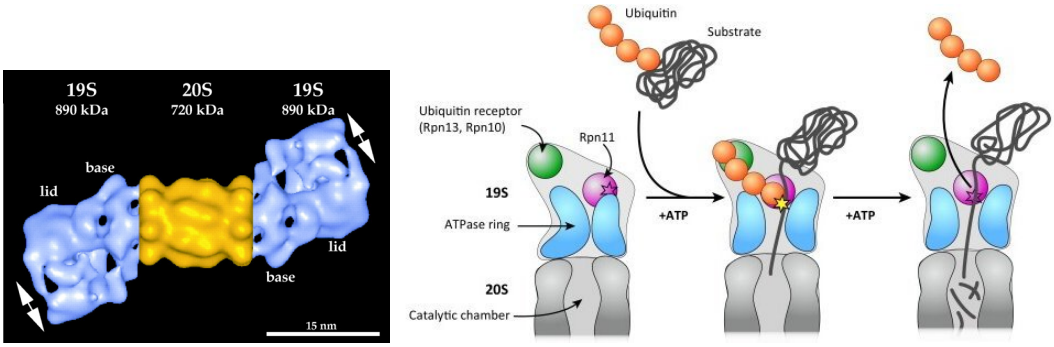

Figure 7.1: Left: The structure of a double-capped 26S proteasome from *Drosophila Melanogaster*. The 20S core particle containing the proteolytic sites with the size of 720 kDa is shown here in yellow, whereas the two RPs are shown in light blue. From [30] with permission.
Right: Proposed model demonstrating the substrate degration procedure in a 26S proteasome. ubiquinated substrate (orange spheres attached to the string-like substrate) is bound by ubiquitin receptors (green sphere). Upon unfolding of the substrate and guiding the substrate into the catalytic chamber of the 20S core particle, deubiquitination sites (purple sphere) cleave the ubiquitin-chains. From [251] with permission.

Already more than 20 years ago, it was shown that isolated and purified 26S proteasomes exist in different assembly forms [252, 253]. Examples are the single- and double-capped 26S proteasomes, with one or two RPs attached to the core particle (CP), or only the 20S CP without any RP [254, 255]. Due to their complexity consisting of 33 different canonical subunits, (dis-)assembly intermediates are very common as well [28].

Several studies of our laboratory tried to elucidate the ultrastructure of this protein *ex situ* and successfully described it to Angstrom levels via EM SPA [25, 28, 29]. Furthermore, first steps into describing the 26S proteasome function within synapses were made comparing the synaptic morphology with and without proteasome inhibition (section 3 and [109]), demonstrating a putative interaction of the proteasome and the synaptic morphology. On an ultrastructural level, several laboratories [256–258] independently focused on localization of single RP subunits within the complex, with very similar results. This was largely possible due to the high resolution EM structures, which e.g. allowed integrative approaches combining datasets from different techniques to be used [258].

Most recently, our laboratory was able to extract three major conformations of the 26S proteasome within their SPA dataset with high fidelity and resolution [29]. These three conformations were termed s1, s2 and s3, and were shown to represent the

"substrate-accepting", "commitment" and "translocating" states [29]. This study proposed a model, in which the substrate-accepting 26S proteasome (s1 conformation) is considered a non-substrate bound ground state, while the commitment and translocating states are substrate bound conformations with distinct structural features. Together with the work from Matyskiela *et al.* [259], who was able to demonstrate a substrate-bound 26S proteasome, first insights into the mechanistic workings of the 19S RP during substrate binding were shown. In that study, isolated 26S proteasomes from *Saccharomyces cerevisiae* were incubated with an excess of model substrate to facilitate substrate bound particles. A low resolution density accounting for the model substrate could be identified near the pore opening of the 26S proteasome AAA+ ring and the Rpn11 subunit.

While these cryo-TEM SPA studies posed a tremendous advancement in our understanding of the 26S proteasome, they were all based on extracted and purified 26S proteasomes outside their native environment. Furthermore, while cell lysis and isolation steps in previous studies became less lengthy and aggressive over time, they were still not completely able to recover all 26S proteasomes without at least partial disassembly [25, 28]. Thus, the total or relative abundances of 26S proteasomes and their assembly states inside cells remained unclear.

The next step was therefore to directly take a look inside the cell, observing and describing 26S proteasomes in their native environment. This approach eliminated damaging this highly fragile protein complex during an otherwise necessary purification process and allowed us furthermore to address important other questions, like orientation, localization and conformation of complexes *in situ*. Previous attempts of locating the 26S proteasome *in situ* inside synaptosomes failed, though their existence was shown indirectly [109, 260] (see chapter 3).

This study aimed for finding and describing 26S proteasome complexes within their native environment inside cultured neuronal cells. Identifying protein complexes inside conventional defocus phase contrast tomograms was both tedious and prone to high noise and false positives. With the advent of new imaging technologies, such as the VPP [62], and the direct electron detector [42], we tried to overcome these difficulties.

7.3 Results

7.4 Detection of 26S Proteasomes

Overall, co-author Dr. Yoshiyuki Fukuda recorded 70 tomograms of neuronal cells, grown on EM grids (see section 8.2.1 for details), which were subsequently used for analysis. All tomograms were between 200 and 450 nm in thickness and showed compartment(s) of neuronal processes, partly with some cell organelles, such as mitochondria or endosomes. Due to the strong contrast invoked by the VPP [62], it was possible for the first time, to precisely identify and locate the 26S proteasomes inside a cell. Examples of readily identifiable 26S proteasomes can be observed in figures 7.2 and 7.3. As seen in these figures, the 26S proteasome in the cell remained in different assembly states, usually with either one or two RPs attached. Rarely we

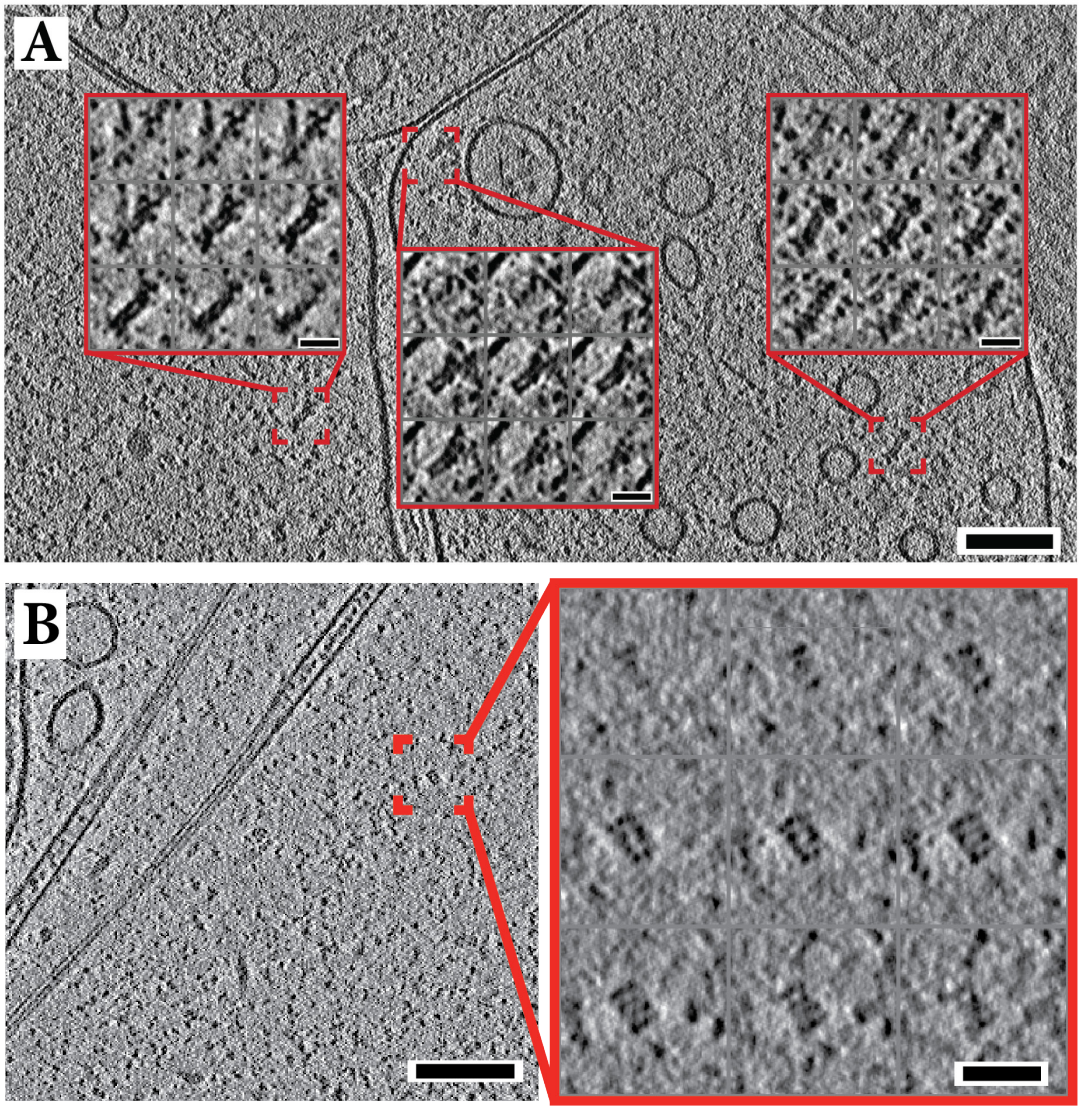

Figure 7.2: Raw images displaying readily identifiable 26S proteasomes.
A) Cropped slice from a representative cryotomogram of a cultured hippocampal neuronal cell on a electron microscopy grid. One single-capped (center) and two double-capped 26S proteasomes (left and right) are indicated by a red frame. The insets display magnified 1.7 nm thick Z-slices through each proteasome volume. Scale bars: Overview: 100 nm; Insets: 25 nm
B) Cropped slice from another cryotomogram, displaying a 20S core particle (red frame). The inset shows the automatically extracted 20S core particle inside a cultured neuron. The Z-slices inside the inset are 1.3 nm in thickness. Scale bars: Overview: 100 nm; Inset: 25 nm;
Modified from [32]. Reprinted with permission from AAAS.

could observe a 20S proteasome lacking a RP, such as in figure 7.2. Generally, 26S proteasomes were isotropically oriented (figure 7.3), as expected from within a cellular environment.

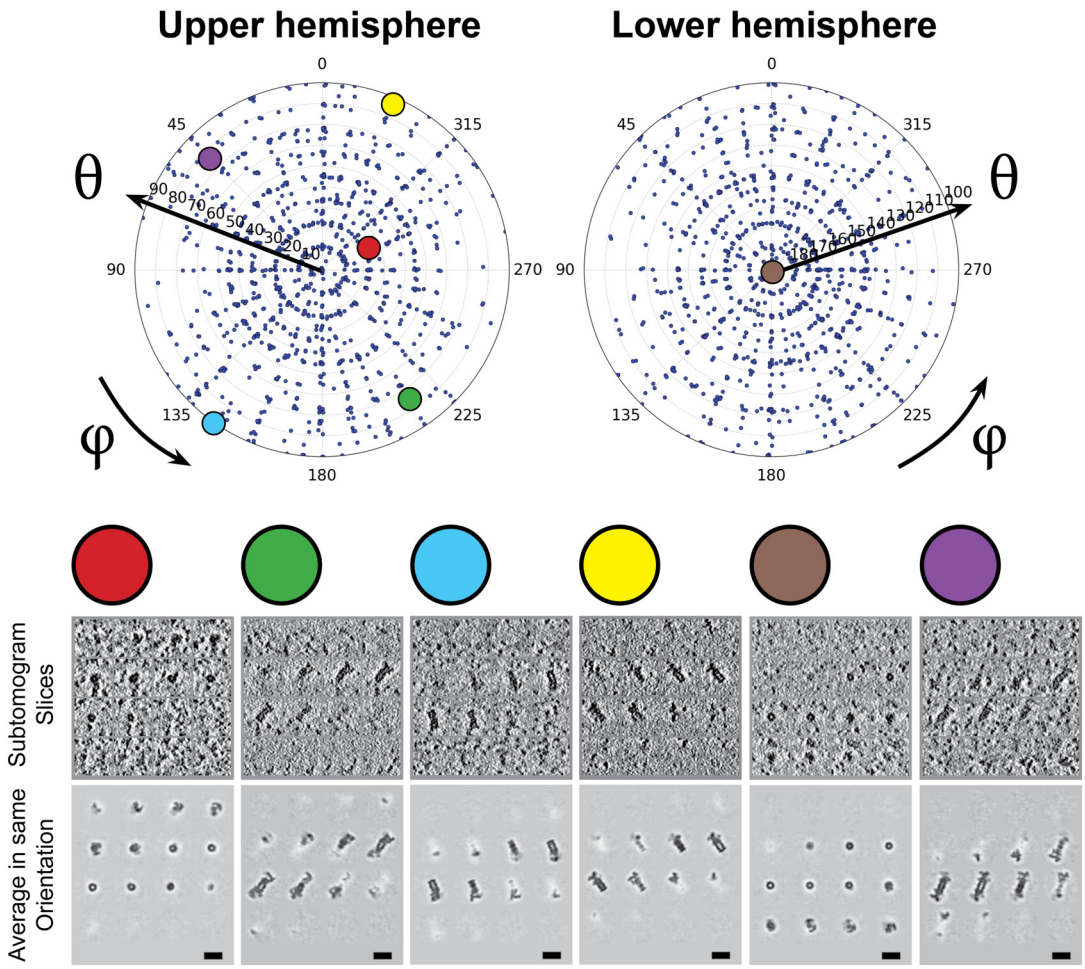

Figure 7.3: 26S proteasomes were found in different orientations, as expected from an *in situ* sample. Here, the orientation extracted from the initial template matching of the two relevant Euler angles θ and ϕ is shown. Long axis rotation (Euler angle ψ) was not plotted. The resulting graph is a spherical surface plot, which can be flattened and displayed (upper hemisphere (top left) with θ = [0°-90°] as well as the lower hemisphere (top right) with θ = [90°-180°]). Overall, the distribution of the particles was isotropic, with 26S proteasomes covering both the upper and the lower hemisphere.
We selected six representative subtomograms of different directions (marked with color dots on the top graphs) and displayed the original subtomogram dataset, as well as their corresponding group average (single and double capped 26S proteasomes) in the same orientation for comparison (bottom row). Scalebars: 25 nm
From [32]. Reprinted with permission from AAAS.

For a more objective and comprehensive analysis of the 26S proteasomes inside the neurons, we performed an automatic template matching approach of all tomograms. As a template, we computationally removed one RP from a double-capped 26S proteasome

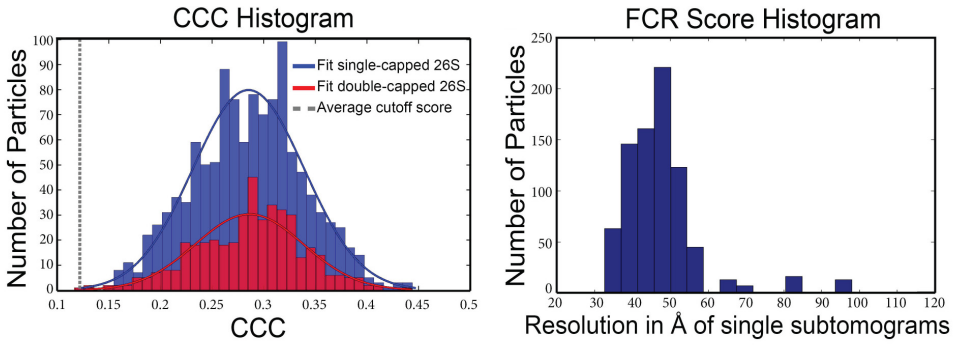

Figure 7.4: Quality assessment of extracted particles.
Left side: Histogram depicting the cross-correlation coefficients (CCC) of all single-capped (blue bars) and double-capped (red bars) 26S proteasomes. The histograms were fitted with a Gaussian distribution (blue: single-capped 26S proteasomes, mean CCC 0.28; red: double-capped 26S proteasomes, mean CCC 0.28). The dashed grey line illustrates the average cut-off threshold of 0.12, below which template matching results have been discarded.
Right side: Histogram showing the FCR (at 0.3 cutoff frequency, see section 8.2.5 for details) of each single-capped 26S proteasome and the atomic model of the *S. cerevisiae* single-capped 26S proteasome (PDB: 4cr2). The mean cross resolution is at 47 Å. Modified from [32]. Reprinted with permission from AAAS.

model (EMDB: 2165, [25]) and low-pass filtered the resolution to 40Å. This way, we were successful to detect both single- and double-capped 26S proteasomes reliably. (For a more detailed description of the methodology, please refer to section 8.2.3).

Template matching was done on the whole tomogram with PyTOM [73, 261] (refer in detail to 8.2.3), yielding a cross-correlation coefficient (CCC) volume indicating putative particles. To disregard high intensity scores resulting from fiducial markers or membranes, only the previously segmented cytoplasmic region was taken into account. After identifying putative particles by their CCC, we visually examined them to confirm their presence. The false positives rate was high, with more than 90% of the initial particles disregarded manually by visual inspection.

A histogram depicting the CCC of single- and double-capped 26S proteasomes can be seen in figure 7.4. Interestingly, the mean CCC for both populations was fairly similar (CCC $\approx$ 0.28, figure 7.4), and almost 35% higher than the values we obtained from non-phase plate tomograms (CCC $\approx$ 0.21, not shown). Generally, the CCC values followed roughly a Gaussian distribution. Only CCCs above a generous cut-off value were considered for our subsequent analysis. This cut-off value is indicated in figure 7.4 with a dashed gray line and included more than 3 σ of all putative proteasomes, thereby suggesting that we detected and extracted almost all 26S proteasomes in our tomograms.

To complement these first results, we similarly performed a search with a 20S-Cdc48 complex [262, 263], according to section 8.2.3. Unfortunately. we were unable to detect a significant class populated by such a complex in the neurons we searched.

Next, we assessed the signal quality of the particles we found by comparing our

detected single-capped 26S proteasomes to a high-resolution map obtained by electron cryo-microscopy SPA (PDB: 4cr2) [29] by FCR (refer in detail to section 8.2.5). According to this criterion, the individual resolution of the majority of the subtomograms ranged from 35 Å to 50 Å (figure 7.4).

7.4.1 26S Proteasomes with One or Two RPs

Next, we subjected all particles to subtomogram averaging. This was done without any external starting model to avoid reference bias [261] (figure 7.5). After 20 iterations, the subtomogram average clearly showed a 26S proteasome with a single RP. However, under more careful inspection, a density at the second RP location became visible upon either adjusting the density level, or by observing the variance map (figure 7.6 A). To separate subtomograms by this heterogeneity, a newly developed 3D autofocus classification algorithm [264] was used (refer to section 8.2.3 for details).

This led us to three main classes, out of which two were of high homogeneity. The third one was considered as a hypervariable background bin (figure 7.8), which consisted of 20S core particles, (dis-) assembly intermediates, and possibly a few remaining false positives. Since the various molecular species contained in this bin were too few to yield meaningful averages, we discarded this class in our subsequent analysis. The other two classes were clearly showing a single- and double-capped 26S proteasome population (figure 7.6, second row). This clear distinction could be seen in the difference map between the two classes, which expectedly showed the second RP as the difference.

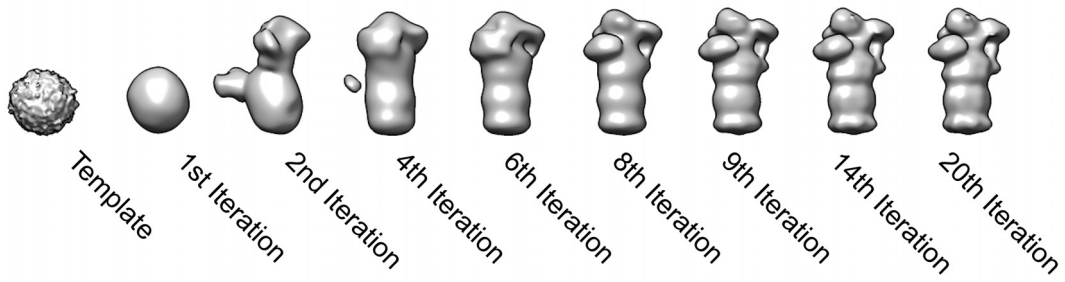

Figure 7.5: In subtomogram averaging, the initial template was generated by averaging all particles in a random orientation, giving an almost sphere-like structure (“Template”, left). Then, several iterations were selected to show the converging structure until the 20th (final) iteration (right). All models were displayed with the same greyscale threshold. Modified from [32]. Reprinted with permission from AAAS.

The quantitative analysis showed that only 27 % of the viable 26S proteasomes were double-capped, while the population of 26S proteasomes with only a single RP was almost triple that size (73%). The averages were calculated at 34Å and 37Å resolution (measured with FSC 0.3 criterion, see section 8.2.5), and, as anticipated, better than the individual FCR resolution of around 48Å calculated earlier (figure 7.4). With the “cleaned” classes and their abundances, as well as the segmented cytosol (see section 8.2.3), we were able to directly calculate the mean cytosolic concentration of 26S proteasomes inside the neurons. The calculated concentration was approximately 190 nM ± 14 nm (sem), albeit with high variablilty due to the varying quality (and thus

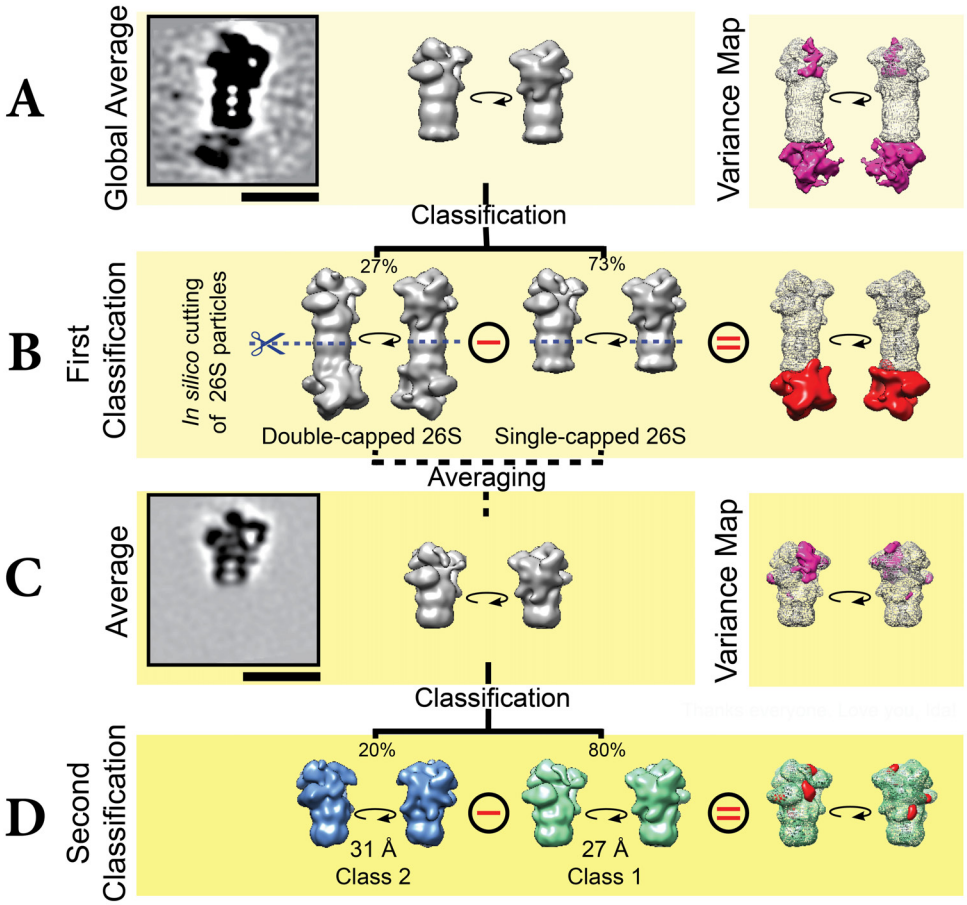

Figure 7.6: Subtomogram workflow and classification procedure
The global average isosurface view (A center) shows a single-capped 26S proteasome. Both the center slice through the raw 3D data (A left), as well as the variance map (A right, variance shown in violet) clearly showed contribution of double-capped 26S proteasomes. The first round of classification yielded the single-capped and double-capped 26S proteasomes (B). The difference map between the two classes (B right, difference shown in red) showed the additional RP. The *in silico* cutting was performed along the blue dashed line indicated (between the two β-rings in the 20S core particle) in double-capped and single-capped 26S proteasomes. The resulting average slice (left) and isosurface (center) are displayed in C. The variance map (C right) still showed some inhomogeneity in the sample, which is resolved by a second classification step (D). This classification divided the dataset into two classes: Class 2 (D left, light blue isosurface) and Class 1 (D center, light green isosurface), with the difference map showing the main density differences at the Rpn1, Rpn6 and substrate entry location. Scale bars for the slices: 25 nm.
From [32]. Reprinted with permission from AAAS.

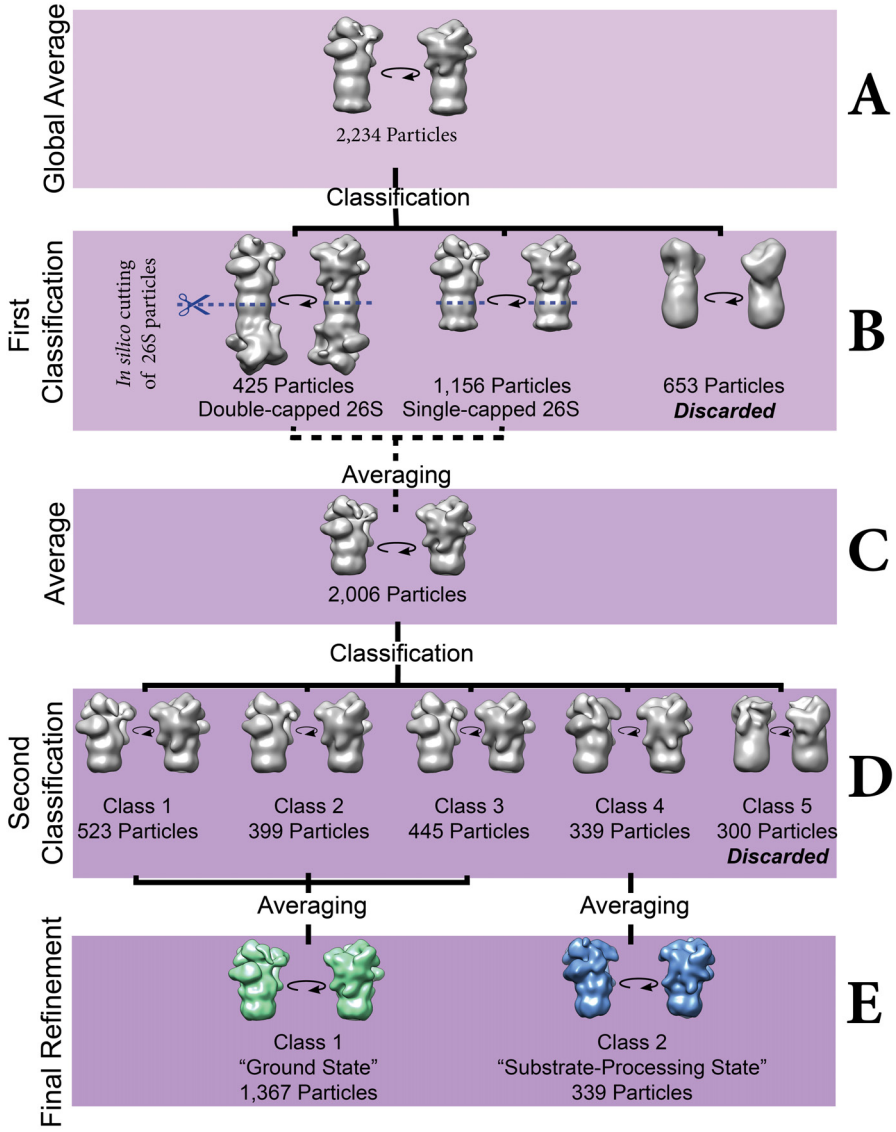

Figure 7.7: Overview of the total number of particles acquired in each step.
From top to bottom:
A) Global average, with 2234 particles contributing (top row).
B) First classification into three classes (double-capped 26S (425 particles), single-capped 26S (1156) and background bin (653)) (second row)
C) Subsequent *in silico* cutting doubles particles from double-capped 26S, yielding an average comprised of (2x425+1156=) 2006 particles (third row).
D) Second classification into five classes (Class 1 (523), Class 2 (399), Class 3 (445), Class 4 (339), and Class 5 (300)). Class 5 was discarded as a hypervariable class (forth row).
E) Final averaging yielded Class 1 (1367, "Ground State") by combining the previous classes 1-3 and Class 2 (339, "Substrate-Processing State") by refining the previous Class 4 (bottom row).
Modified from [32]. Reprinted with permission from AAAS.

detection rate) of the data set. This value was within the cytoplasmic 26S proteasome subunit concentration range previously reported for *Saccharomyces cerevisiae* (140-200 nM) [260]. If we only included tomograms of higher visual quality and thus more reliable particle detection, we get 26S proteasome concentrations beyond 220 nM.

Summarized, as evident from the previous tomographic slice overview (figure 7.2), we were able to detect both single- and double-capped 26S proteasomes and could quantitatively describe the abundances of those inside the neuron.

7.4.2 Two Conformations of the RP

Once we already distinguished double- and single-capped 26S proteasomes, we decided to use the same 3D classification approach to elucidate the conformation(s) of the highly variable RP. First, to increase the effective particle number, as well to better implement the alignment procedures, we cut each individual particle between the two β-rings of the 20S core particle *in silico*. Thereby, the double-capped 26S proteasomes produced two separate subtomograms for the subsequent analysis. The resolution of the first average (figure 7.6, C) produced by the truncated particles was at 31 Å.

Interestingly, the variance map indicated high variability for distinct RP subunits, such as Rpn6, and Rpn1 (figure 7.6, C). Moreover, the variance was high in an area surrounded by Rpn1, Rpn2, Rpn10, and Rpn11, where there is no density in single particle reconstructions of purified 26S proteasomes [25, 29, 256–258, 265]. This led us to use another classification round, where we separated the data into two homogeneous classes (figure 7.6 D) and another discarded hypervariable bin (figure 7.7 D).

Class 1 accounted for roughly 80% of all RPs (1367 particles), while class 2 only for 20% (339 particles). The difference map between those two classes can be seen in figure 7.6 D. Major differences include a tilted Rpn5/6 pair as well as the Rpn1 subunit, which changes orientation between the classes. Class 2 displayed an exclusive big density at the area enclosed by Rpn1, Rpn2, Rpn10 and Rpn11.

7.4.3 Template and Reference Bias

Template and reference bias can both heavily influence the resulting structures [266]. This occurs when a (high resolution) structure is used for template matching and/or as a reference structure for subsequent subtomogram averaging. In this case, even with data entirely obtained from noise, a well resolved structure can be reproduced, provided a high amount of “particles” and lack of attention [267].

In order to address this technical issue, we carefully adjusted our procedures and provided several lines of evidence suggesting that neither template, nor reference bias was affecting our results:

1. If template bias would influence our result, we would not be able to extract numerous double capped 26S proteasomes from a search of single capped 26S proteasome (see figure 7.6).

2. Template matching with a 25% computationally reduced 26S proteasome still produced an intact 26S proteasome as an average (see figure 7.8), therefore excluding template bias.
3. The first subtomogram averaging was done with a neutral starting model, essentially a sphere, therefore removing any initial reference bias (see figure 7.5).
4. Finally, the reference bias is typical for low SNR datasets, e.g. low defocus EM with no phase plate. Fortunately, the use of the phase plate allowed for much better contrast, where the SNR was much higher and the particles can be clearly distinguished, such as in figures 7.2 or 7.3.

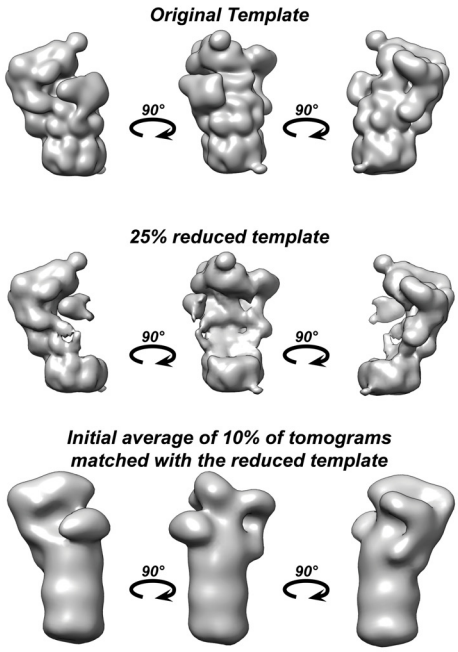

Figure 7.8: To address template bias, we performed template matching of a highly reduced template (middle row) on 10% of the dataset (7 tomograms). To produce this template, we computationally removed a sphere from the RP of the original template (top row). After particle picking and subtomogram alignment (all steps were done exactly the same as in the study), the subtomogram average (bottom row) did not have any missing densities previously produced in the initial template, therefore indicating that template bias is negligible.
From [32]. Reprinted with permission from AAAS.

7.4.4 Rigid Body Fitting

Rigid body fitting was performed by co-author Antje Aufderheide.

Previous cryo-TEM single particle studies of isolated *S. cerevisiae* 26S proteasomes revealed three coexisting conformations of the RP, namely s1, s2 and s3 [29] (also refer to section 8.2.4 for details). While s1 is the abundant substrate-accepting state without any substrates bound, s2 mediates their tighter binding (commitment state) and activates

the Rpn11 deubiquitylating module, and s3 enables translocation of substrates into the CP.

In order to compare our new mammalian *in situ* models to the previously described models, we used rigid body fitting [268]. Therefore, we placed the atomic *in vitro* models of s1, s2 and s3 inside the class 1 and class 2 densities and the positions and orientations of the subunits were optimized (figure 7.9 A). The comparison of the fits to the initial models suggested that class 1 is most similar to the s1 (substrate accepting) state (Root-mean-square deviation, RMSD $\approx$ 8.9Å), whereas class 2 most closely resembles the s3 (translocating) state (RMSD $\approx$ 7.4Å).

When we crosscompared the fits of other conformations into a "wrong" class, we saw a higher RMSD value, indicating a worse (and thus very likely an incorrect) fit. An overview showcasing the different *in vitro* and *in situ* models of the 26S proteasome with their RMSD values after fitting can be seen in figure 7.10.

Interestingly, another study recently described a model substrate attached to a 26S proteasome with high resolution in cryo-TEM [259] with a very high similarity to the s3 state [29]. Accordingly, we refer to the major conformational states represented in class 1 and class 2 as "ground state" (GS) and "substrate-processing state" (SPS), respectively. A visual representation of the different states inside the neuron can be seen in figure 7.9B, where the models of GS and SPS 26S proteasomes were pasted into the tomogram under the correct orientation.

A quantitative analysis disclosed that GS represented a majority of 80% of the analyzed RPs, compared to the 20% in the SPS conformation. Using these numbers, we calculated the expected abundances of individual and uncorrelated RPs of double-capped 26S proteasomes (GS-GS, SPS-GS, SPS-SPS). The analysis yielded an excellent agreement with our data (GS-GS: 64% (acquired from real data) vs. 63% (predicted by calculations), GS-SPS: 32% vs. 33%, and SPS-SPS: 4% vs. 4%) (figure 7.9C), therefore like previous studies [29, 259] favoring a model of independent activity of both RPs.

The proteasome distribution appeared almost random with a few undefined "hotspots" of higher concentration in figure 7.9 B. To test for randomness of this distribution, we applied a k-means clustering with different clustersizes on our data and a simulated dataset and used the Calinski Harabasz criterion of MATLAB (function *evalcluster*) to estimate the optimal clustersize (figure 7.11). Summarized, significant accumulations of 26S proteasomes close to cellular membranes or organelles could not be detected, but interestingly, the data suggested that the proteasomal distribution slightly differs from computationally generated random distributions.

7.4.5 Classification of RPs in the GS and SPS

In the GS, there was still heterogeneity in regions, such as the vicinity of Rpn1 or Rpn13 subunits. To estimate the number of classes to generate, we first classified the SPS and estimated the minimum population per class. Then, we classified the GS into classes of a similar population size (figure 7.12). Finally, we combined and reduced this number by hierarchical clustering. The final number of meaningful classes in GS was

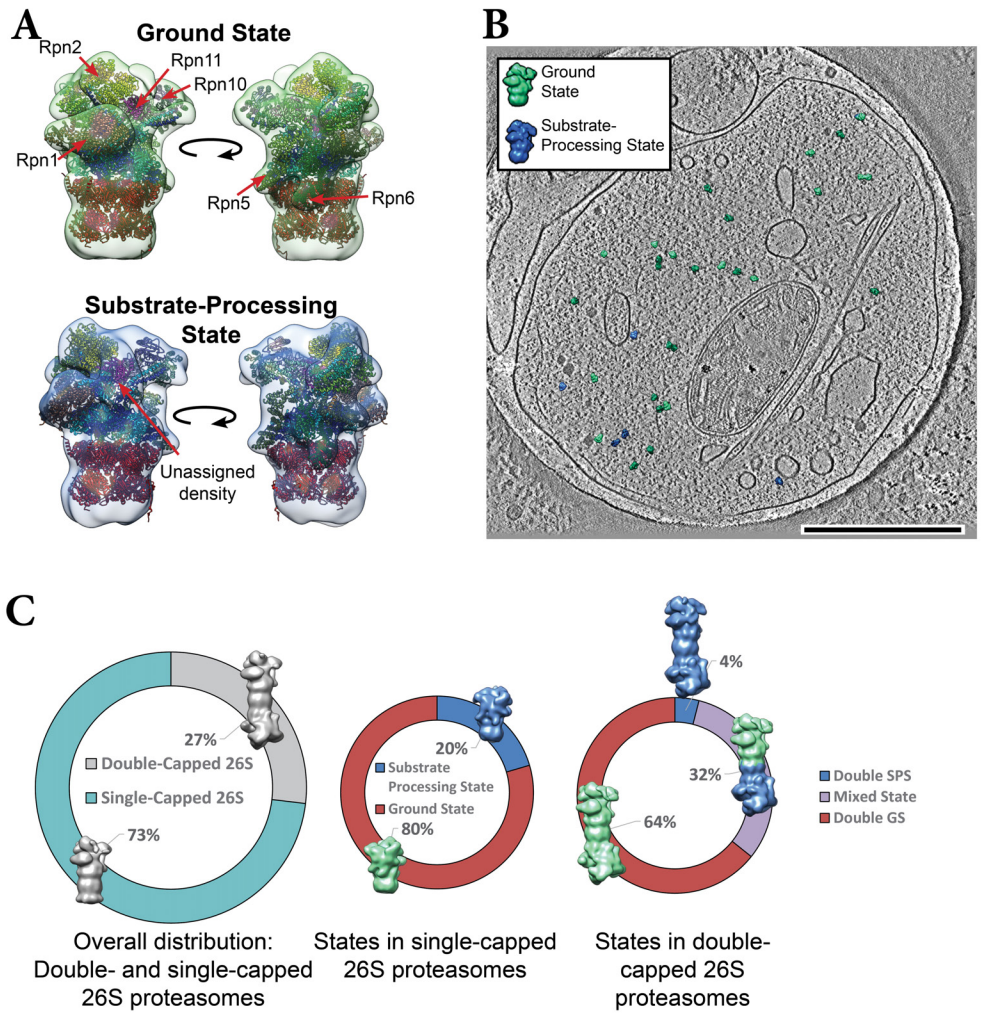

Figure 7.9: Rigid body fitting of atomic subunit models into EM densities.
A) Fitted atomic models of the *S. cerevisiae* 26S proteasome (PDB: 4cr2, 4cr4) provided by coauthor Antje Aufderheide were placed into the EM densities (ground state top in semitransparent green, substrate-processing state below in semitransparent blue) produced by the second classification step (see figure 7.6 D). In the atomic models, the subunits Rpn9/5/6/7/3/12 are colored in different shades of green, Rpn8 in light and Rpn11 in dark magenta, the ubiquitin receptors Rpn10 and Rpn13 in purple, Rpn1 in brown, Rpn2 in yellow, the AAA-ATPase hexamer in blue, and the CP in red [29]. Some of the Rpns, as well as the unassigned density in the substrate-processing state are indicated with a red arrow.
B) Single-capped and double-capped 26S proteasomes in their individual orientation, assembly, and RP state are displayed as green (GS) and blue (SPS) isosurfaces on top of a tomographic slice of a representative tomogram. Scale bar: 500 nm
C) Chart showing the overall distribution of single-capped and double-capped 26S proteasomes in our dataset. The distribution of the different states within single-capped and double-capped 26S proteasomes are shown to the center and right.
From [32]. Reprinted with permission from AAAS.

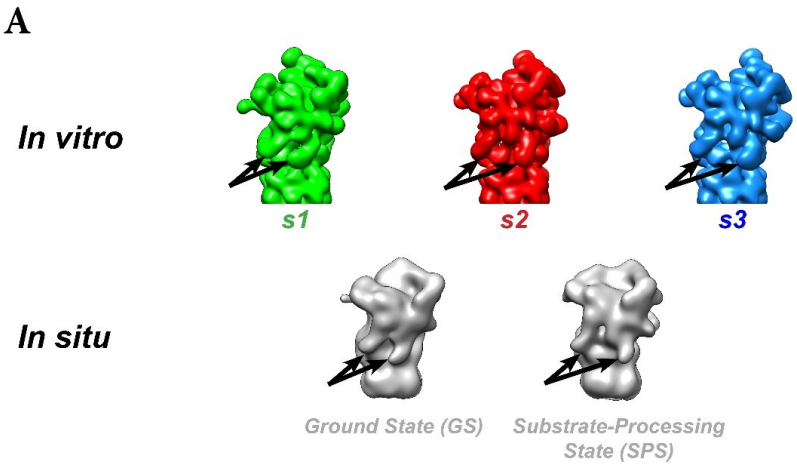

B

GS — Fit result from … compared to	seed s1	seed s2	seed s3
s1	8.87	9.21	9.80
s2	24.08	23.60	23.84
s3	22.49	22.18	21.53

Best result: GS fitted with seed s1

GS → s1

SPS — Fit result from … compared to	seed s1	seed s2	seed s3
s1	15.18	15.67	16.26
s2	12.26	11.53	12.41
s3	8.99	8.80	7.43

Best result: SPS fitted with seed s3

SPS → s3

Figure 7.10: We compared the 26S proteasome *in situ* with the *in vitro* structure by rigid body fitting (see section 8.2.4 for details).
A) The three in vitro structures (s1, s2 and s3; filtered down to 28 Å) [29] are shown with the two *in situ* states (GS and SPS). The arrows point to the Rpn 5 and Rpn 6 subunits, already suggesting that GS is similar to s1, whereas SPS is closer to s2/s3.
B) We compared the resulting pseudo atomic model fits by RMSD. We used s1/s2/s3 as seeds for the rigid body fitting in GS (left) and SPS (right) and compare these to the original s1/s2/s3 models. The table clearly shows that the GS is fitted best with s1 with its lowest RMSD value (underlined), while SPS is most likely s3.
From [32]. Reprinted with permission from AAAS.

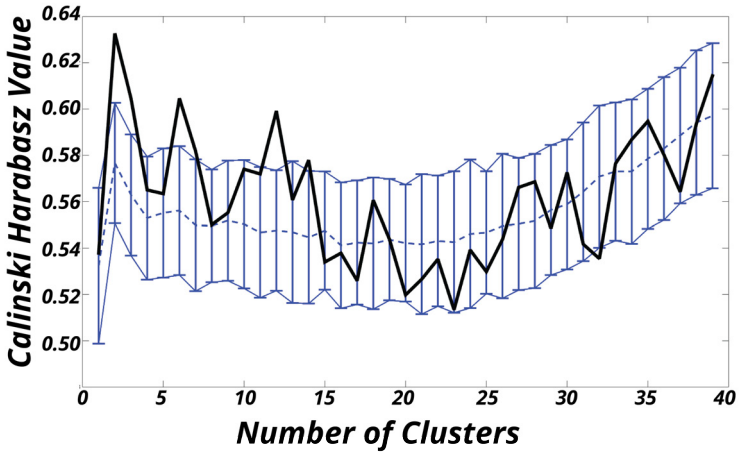

Figure 7.11: A set of 100 datasets of each containing 87 randomly distributed particles was generated. The clustersize is displayed on the x-axis and its calculated Calinski Harabasz value on the y-axis. This dataset (dashed blue line) was compared to the original dataset (solid black line). The x/y errorbars shows the std (solid blue line). On several clustersizes, the Calinski Harabasz value of the original dataset was beyond 1 std from the randomly generated dataset, hinting towards a weak clustering within the cytoplasmic volume.

four, all showing structural distinct features (figure 7.12), all with similar populations between 18% and 34% (figure 7.13A). GS1 with a abundance of 24% showed almost no additional density compared to the down-filtered atomic structure, which lacked the Rpn13 density (figure 7.13 A bottom left). GS2 (18%) on the other hand showed a very defined density attached to Rpn1. GS3 (34%) is defined by smaller densities at the Rpn13 and Rpn10 ubiquitylation sites, whereas GS4 (24%) had an even more pronounced density at the Rpn13 site.

We classified SPS into three subclasses (figure 7.13B). The differences of all three classes, when compared to the atomic model, located to a region comprising the groove above Rpn11 and an area enclosed by Rpn13 and Rpn10 at the top, and above the "mouth" of the proteasomal AAA-ATPase module at the bottom. In the three classes this difference density adopted a higher position in SPS1 (38%) and a lower position SPS2 (35%) and SPS3 (27%). In addition, the density of the last class occupied a larger volume than SPS1 and SPS2. If we calculate the additional masses for these classes (refer to section 8.2.5), we get values between 150kDa and 250kDa.

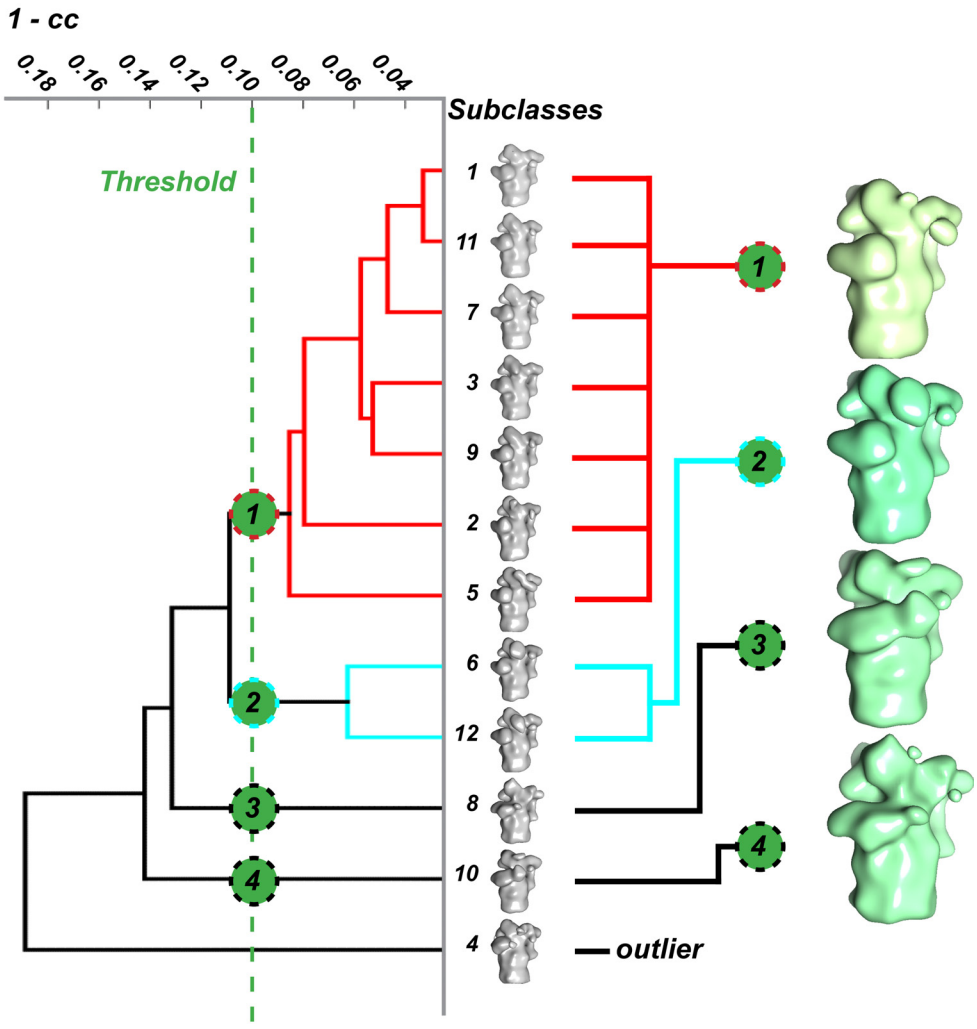

Figure 7.12: To approximate the class size of the GS dataset, we initially used the minimum particle size given by the SPS classification. This resulted in 12 subclasses (middle row), each of them similarly populated with particles. The last class average was classified as an outlier, most likely due to underpopulation of that particular class and was discarded. We used hierarchical clustering, based on pairwise cross correlation, as an indicator of similarity (left). When we thresholded the tree at the indicated linkage level (green dotted line), we got the four major conformations with distinct features (right), identical to those of our initial GS classification in figure 7.13.
From [32]. Reprinted with permission from AAAS.

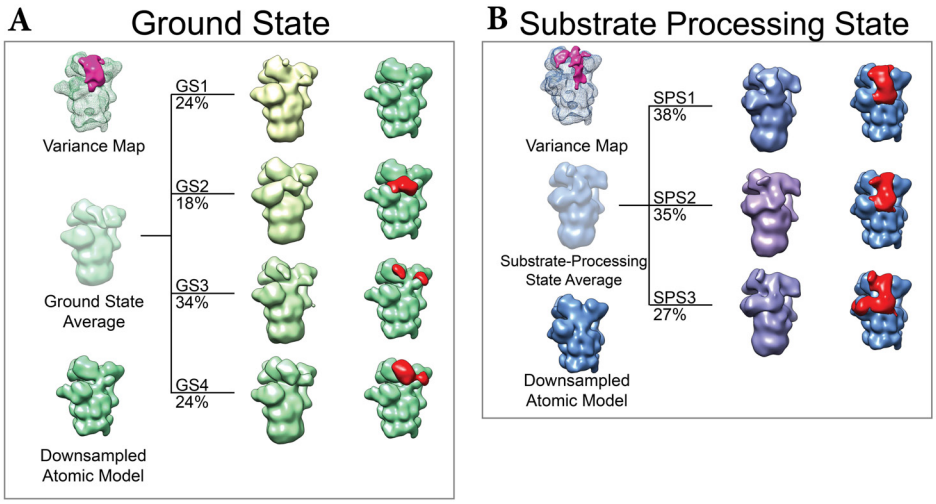

Figure 7.13: Subclassification within GS and SPS demonstated the heterogeneity in each state.
A) GS class has been classified into four subclasses. Left side: Variance map (top), the GSaverage (middle) and corresponding downsampled atomic model (bottom). Subclasses with their respective abbreviations and abundances are shown with the "front view" isosurface (different shades of green) in the middle. On the right, the difference between the individual subclass and the downsampled atomic model is shown in red.
B) SPS class has been classified into three subclasses. Left side: Variance map (top), the GS average (middle) and corresponding downsampled atomic model (bottom). Subclasses with their respective abbreviations and abundances are shown with the "front view" isosurface (different shades of blue) in the middle. On the right, the difference between the individual subclass and the downsampled atomic model is shown in red.
From [32]. Reprinted with permission from AAAS.

7.5 Discussion

7.5.1 RP Assembly in 26S Proteasomes

This study was the first *in situ* structural study of 26S proteasomes inside cells. To analyze the structural heterogeneity of our particle ensemble inside neurons, we subjected it to statistical analysis by subtomogram averaging and classification. Both visual and automatic detection of 26S proteasomes inside the tomograms proved the existence of double- and single-capped 26S proteasomes *in situ* (figures 7.2 A and 7.3), agreeing with the previous *in vitro* studies [25, 28, 29, 257]. However, in this study, we were able to count each occurrence of assembly states inside the neuron and additionally could infer from it the regional concentration - without any genetic modification or other invasive methods.

Earlier studies involving lyzation and purification steps showed that "dumbbell-shaped" [255] (double-capped) 26S proteasomes (in *Xenopus* oocytes) appear to be the predominant form and subsequently thought that to be the native and substrate-degrading proteasome complex [28]. With our *in situ* study, we were able to conclude that the opposite holds true for our cultured neurons, where the single-capped 26S population (73%) was almost three times as abundant than the double-capped one (27%). In addition, these values are remarkably close to the ratio observed in native gel densitometry of rat cortex in another study [269]. We were able to calculate a mean cytoplasmic concentration of around 190 nM, similar to the Rpn1 subunit concentration in *S. cerevisiae* assessed by single-particle FCS [260].

7.5.2 RPs Resemble s1 and s3 States

Cutting the particles between the two β-rings of the CP enabled us to boost our particle number to 2006 particles, by effectively doubling the RPs from the double-capped 26S proteasome. The improvement to 31 Å, as well as visibly better definition of subunits in the new average was due to this larger sample size. As expected, the subtomogram averaging worked flawlessly and arranged the newly cut particles very precisely, as there was no density on the other side of the CP (figure 7.6). Additionally, the average was clearly smaller than a single-capped 26S proteasome, as we cut away one α- and β-ring from each particle. As the variance was still indicating high structural inhomogeneity, we initially performed another classification into 5 classes.

The classification clearly managed to divide the whole dataset into the structurally more homogeneous groups (figure 7.7 forth row). One group (Class 5) turned out to be comprised of either badly aligned or incomplete/(dis-)assembled RPs and was discarded. The others were visibly similar to the conformation models obtained earlier [29]. Most interestingly, Class 4 had a prominent big density placed on top of the substrate entry pore of the 26S proteasome. This location has been previously located in SPA of isolated substrate-bound 26S proteasomes [259]. We successfully demonstrated the structural similarity of Class 4 and the s3 (substrate-translocating) conformation [29] by means of rigid body fitting.

As a measure of similarity, we used the Root-mean-square deviation (RMSD) between

the fitted map and the original s1/s2/s3 conformation [29] (figure 7.10). Expectedly, our abundant Class 1 was most similar to the s1 conformation described earlier, and was therefore named "Ground State" (GS). Class 2 was almost identical to the s3 conformation, and therefore termed "Substrate-Processing State" (SPS).

Previous studies already focused on the conformational states in the RPs of the isolated 26S proteasomes [29, 259]. However, these structural studies were only possible because of the recent advancements in camera and microscopy technology, as well as highly automated procedures. Both major works were based on SPA approaches of isolated and purified 26S proteasomes, with datasets spanning between 90000 [259] up to 3 million particles [29]. Deconvoluting the dataset into three states shown in [29] was only possible because of the size of the dataset and through intense computational efforts. Most likely due to the inherent 3D information contained in subtomograms in comparison to 2D data in SPA images, the classification into the GS and SPS conformations could be reproduced with a significantly smaller sample size.

Interestingly, despite the high degradation turnover for most proteins [98, 270, 271], we found that only 20% of the 26S proteasomes we detected are in the SPS, leaving plenty of room for situations of enhanced activity, such as during proteolytic stress. So far, earlier measurements addressing this problem *ex situ* commonly used fluorogenic peptide substrates, but these showed quite variable results, most likely due to different preparation steps [250, 272].

We were able to show 26S proteasomes *in situ* during substrate-processing, but unfortunately, we could not yet identify any specific substrate or detect any additional density inside the active sites of the 20S core particle within the SPS class. This is most likely resulting from our lower resolution reconstructions (30 Å), caused by a smaller set of particles, as well as the higher pixel size used in our approach, compared to the previous SPA studies (see above).

Subclassifications of RP states

Classification by means of 3D autofocused classification (for details and parameters refer to section 8.2.3) was able to split the dataset of GS and SPS RPs into four and three distinct subclasses (figure 7.13).

Rpn 13 was localized in an earlier study by means of cryo-TEM single particle studies of Rpn 13 deletion mutants in *S. cerevisiae* [273]. It has been well known that some RPs, such as Rpn13 are binding the 26S proteasome in a substochiometric manner [28, 274]. Thus it was very likely to observe classes within the GS population either with (58%) or without Rpn13 (42%).

For the other densities attaching to either Rpn1 (GS2) or Rpn13 (GS4), proteasome-interacting particles (PIPs) were our major candidates. The most abundant and highest affinity PIPs binding to Rpn1 are the deubiquitylating enzyme (DUB) Usp14, and the shuttling receptor Rad23 [275–277], possibly accounting for the attached density in GS2. It seems that Rpn13 bound 26S proteasome could be seen in both GS3 and GS4, with an extra density attached to it in GS4. This extra density might be the DUB Uchl5, which is know to be a ligand of Rpn13 [278–280].

The classifications of the SPS dataset showed less defined differences (figure 7.13 B).

A big density covering the entry pore of the proteasomal AAA-ATPase module was seen in every SPS subclass, and most likely contained a substrate. In between subclasses, it appeared that this density shifted position from a higher (SPS1) to a lower one (SPS2, SPS3), possibly hinting towards the degradation stage. In all cases we saw a direct link of this density to the Rpn11 deubiquitylation site. Interestingly, this density corresponded to 150kDa -250kDa in size for the three subclasses - significantly bigger than the average protein size of around 60kDa. We therefore assumed that the additional density might be composed of other proteasome-associated densities, such as DUBs and E3 ubiquitin ligases, which are frequently found in association with 26S proteasomes [281, 282].

Due to the high protein heterogeneity in the cell and thus the endless combinations of substrates and PIPs with the 26S proteasome, it was impossible to pinpoint any additional electron densities to a known protein. The lack of resolution at our current stage and the low particle number were limiting the interpretabiliy. Ultimately, the exact description of the extra densities is still in the early stages, but might be overcome with genetically modified or inducible cell lines.

7.6 Conclusion

For the first time, we were able to reliably observe 26S proteasomes *in situ* inside intact cells. With new advances in technology, such as direct detectors and the contrast-enhancing VPP, we pinpointed individual 26S proteasomes in nanometer precision, correct orientation and conformational state inside neurons, embedded in their native and cellular environment. This also led us to provide vital information regarding 26S population and their states *in situ*, some of them even opposing prior studies or models.

Summarized, we investigated the 26S proteasome in its native environment by means of ECT and were able to successfully address and clarify several issues:

1. Technological advances enabled *in situ* localization of 26S proteasomal complexes both visually and computationally by template matching
2. 26S proteasomes were present in both assembly states (double and single-capped) inside the cell
3. Single-capped were far more abundant than double-capped 26S proteasomes.
4. We were able to identify two different conformations of the RP and could link them to previously described *in vitro* models. These two conformations showed 26S proteasomes in a GS and a substrate-bound SPS.
5. A big majority (80%) of the RPs were idle (GS) and only 20% in the substrate-processing state.
6. Both of these conformations were observed in both assembly states. This demonstrated that both assembly states were therefore capable and used for substrate degradation *in situ*.

7. This study showed the first time a cellular map of 26S proteasomes with their assembly states and structural conformations within their native environment.
8. RPs of double-capped 26S proteasomes were working independently from each other, with no detectable cooperativity.
9. Globally, the UPS in neurons in our study had a big buffer capacity, which is likely to be utilized during proteolytic stress.

8. Materials and Methods

8.1 Synaptosome Studies

This section covers the materials and methods used in the synaptosome studies investigated in chapters 3 and 6.

8.1.1 Synaptosomes

Synaptosome Extraction

A slightly modified protocol from Dunkley et al. [152] was used to extract cerebrotical synaptosomes from rodents [109, 234]. All procedures described here are in accordance with those accepted by the Max Planck Institute for Biochemistry.

For synaptosomes used in the RIM experiments (chapter 3), we used six to eight weeks old male RIM1α +/+ (wildtype, "WT")and -/- (knock-out, "KO") mice [125]. The animals were sacrificed by cervical dislocation and decapitated. The cerebral cortex was extracted and placed into ice-cold homogenization buffer (HB: 0.32 M sucrose, 50 mM EDTA, pH 7.4). As the protease inhibitor commonly used in the preparation blocks chymotrypsin like activity (such as in the 26S proteasome) [1], no such inhibitors were used in the HB, to ensure proper proteolysis activity of the UPS. For all other experiments (chapter 6), six to eight weeks old Wiskar rats were anesthetized with 2 ml chloroform and decapitated. The cerebral cortex was extracted and placed in HB with protease inhibitors (cOmplete Mini EDTA-free, Roche; 7 tablets in 70 ml HB).

In general, white matter and blood vessels were removed and the remaining cortex was immersed in HB (mice: 3 ml; rats: 9 ml per cortex). Homogenization was done at up to 700 rpm in a glass-teflon homogenizer with around six to seven strokes to ensure that no big chunks of biomaterial is left. This homogenate was centrifuged at 2000 g for

[1] Protease inhibitor data sheet: https://cssportal.roche.com/LFR_PublicDocs/ras/11836170001_en_09.pdf

two minutes (two times) to remove unbroken cells, nuclei and other large components. Supernatants of both runs were combined and centrifuged at 9500 g for twelve minutes. The newly formed pellet contained crude synaptosomes [152]. To further purify this pellet, we resuspended it carefully and loaded it onto a Percoll (GE Healthcare) gradient (3%, 10%, 23%) in HB for a six minutes centrifugation at 25000 g. We collected the fraction formed between the 10% and 23% Percoll solution interface and diluted it in Ca^{2+}-free Hepes-buffered medium (Ca^{2+}-free HBM: 140 mM NaCl, 5 mM KCl, 5 mM $NaHCO_3$, 1.2 mM Na_2HPO_4, 1 mM $MgCl_2$, 10 mM glucose, 10 mM Hepes, pH 7.4). Percoll was removed by centrifugation at 22000 g for 10 minutes. The remaining pellet was resuspended in HBM supplemented with 1.2 mM $CaCl_2$ and was used immediately for measuring protein concentration, or incubation prior to plunging or glutamate release assay. The sample had to be kept at around 4°C to avoid protease degradation activity throughout the whole extraction and purification procedure.

Protein Density Measurements and Incubation of Sample

Protein density was measured with a spectrophotometer (IMPLEN NanoPhotometer) using the Christian/Warburg method [283]. This takes the absorbance values of the sample at λ =280 nm and λ =260 nm and calculates the protein density according to:

$$\text{Concentration}(\frac{mg}{ml}) = 1.55 \cdot A_{280nm} - 0.76 \cdot A_{260nm}$$

Synaptosomes were diluted to $c \approx 0.8 - 1 \frac{mg}{ml}$ final protein concentration and incubated at 37°C for 60 minutes. For the RIM studies covered in chapter 3, we added compounds during this incubation time according to table 8.1.

Compound	Concentration	Incubation Time
DMSO	$10\mu M$	30 min
MG132	$10\mu M$	30 min

Table 8.1: Incubation with compounds during the RIM1α-KO studies in chapter 3

Glutamate-Release Assay

Measuring glutamate release in synaptosomes was done according to the enzymatic assay proposed by Nicholls and Sihra [220, 221] with slight modifications. Briefly, after 60 minutes incubation of synaptosomes supplemented in Ca^{2+} free HBM with $16\mu M$ BSA, a 1 ml aliquot was transferred together with a stirrer into a quartz or plastic cuvette already containing 1mM $NADP^+$ and (depending on experiment) supplemented with 1.33 mM $CaCl_2$. Excitation and emission wavelengths were 340 nm and 460 nm, respectively. After starting the measurement, 40 μL of glutamate-dehydrogenase (Sigma) was added. After t =100 s, 10 μL of 3 M KCl for depolarization (30 mM final concentration) and after t =500 s, 4 μL of 1mM glutamate (4 μM final concentration) was added as a reference.

For experiments simulating uncaging conditions, $CaCl_2$ was added after depolarization, to observe synaptic response from the transition of a Ca^{2+}-free environment to an environment with extracellular Ca^{2+} upon UV light uncaging (chapter 5).

The on-line fluorimetry was done in an Elmer-Perkin LS-55 spectrophotometer with the temperature kept constant at 37°C and the stirrer speed set at "low". Traces were collected and exported in CSV files and imported into Origin (OriginLab, Massachusetts, USA) using a custom-made filter. First, background fluorescence was subtracted and the baseline set to the first datapoint after KCl depolarization for all traces. The calibration was done individually in each trace by measuring the response to the pure 4 μM glutamate reference.

Plunging Preparation

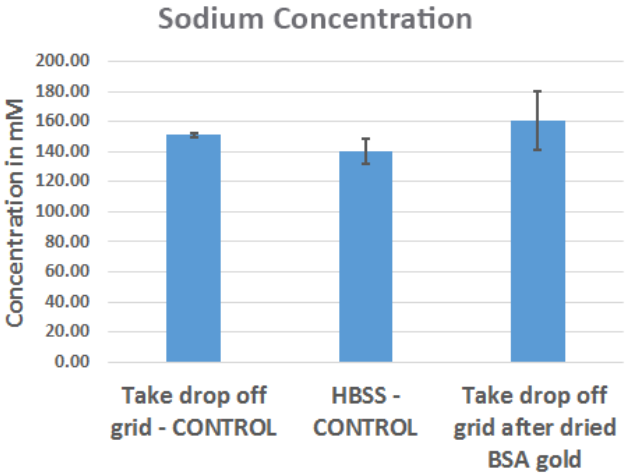

Figure 8.1: Fluorescence measurement with a sodium indicator (CoRoNa Dye, $c = 10\ \mu M$) showed no major difference in sodium concentration upon using BSA coated gold with or without previous centrifugation. In all cases the same amount of liquid was measured. The first bar (from left to right) shows HBM applied to the EM grid and then taken for measurement. The second bar is HBSS without EM grid contact. The third bar is a drop of HBM retrieved from a grid, where 4 μl BSA coated gold was previously applied and subsequently dried out. Errorbars show the std.

We used molybdenum or copper 200 mesh grids with a Quantifoil R 2/1 holey carbon support film (Quantifoil, Jena, Germany) for synaptosomes. The grids were glow discharged for 30 seconds to render them hydrophilic (negatively charged) [284], as well as to clean them thoughroughly from organic contaminants. A 3-4 μl drop of 10 nm colloidal gold was applied on the grid. Later, we switched to 10 nm BSA coated gold (Aurion, Netherlands), which provided a more homogeneous distribution of fiducials. The BSA coated gold solution needed to be centrifuged prior (14000 RPM, 60 min, 2 times) and resuspended in MilliQ Water to mainly remove the NaN_3 (Sodiumazide), which is used as a preservative. However, even when applying the drop without prior centrifugation, neither significant change in ionic concentration (figure 8.1), nor any obvious negative effect on biomaterial could be observed [109]. The solvent liquid evaporated and only the fiducial gold is left dispersed over the carbon support film.

Plunging of Sample

A self-closing tweezer (Dumont negative action tweezer) in the case of the in-house plunger and a costom made tweezer for the Vitrobot fixed the EM grid at the plunger. After incubation, 4 μl synaptosomes were applied onto the grid. The excess liquid is then blotted away and after a foot-pedal activation, the grid is immediately plunged into liquid propane/ethane mixture and transferred into a gridbox kept in the liquid nitrogen conditions.

The first generation UV flash plunger was an in-house manual plunger with slight modifications. For stimulation protocols, 2 μL of synaptosomeal solution were supplemented on the grid with 2μL of KCl (30 mM final concentration) and complexed DM-Nitrophen (final concentration 2mM) in the case of UV light stimulation. After blotting, the foot-pedal first initiated the UV-light to trigger before dropping the sample into the liquid propane/ethane mixture. The second generation UV flash plunger used the FEI Vitrobot as a base, and flashed the sample "on-the-fly" between the time points of rod release and vitrification. Parameters for plunging were set to 37°C temperature and 95% humidity. The blotting waiting time was 0 seconds, with 10 seconds overall blot time. After the plunging process, the gridboxes were collected and stored in liquid nitrogen dewars. Degradation of the vitrified sample quality over time (several months) could not be seen in our experiments.

Immunofluorescence Imaging for RIM1α Study

Preparation and Imaging was done by Ana-Maria Oprisoreanu, analyses by the author.

As outlined in [109], synaptosomes from WT and RIM1α KO mice were treated with DMSO or MG132 and processed as described [285]. In brief, synaptosomes were plated on poly-L-Lys-coated coverslips and allowed to attach for 30 min, followed by 30 min incubation with DMSO or MG132. Synaptosomes were fixed for 5 min in PBS containing 4% paraformaldehyde and blocked with PBS containing 1% BSA, 10% normal goat serum and 0.1% Triton X-100. After several washes, synaptosomes were incubated with primary antibodies for 12-14h (antibodies for RIM1 and RIM2 were a kind gift from Frank Schmitz (Hamburg University); MUNC13 (126102), VAMP2 (104211) and ELKS (143003) antibodies were purchased from Synaptic Systems; Bassoon (SAP7F407) antibody was purchased from Enzo Life Science). 25 Synaptosomes were washed and further incubated with secondary antibodies for 40 min at room temperature (goat anti-mouse FITC and goat anti-rabbit Cy3 purchased from Jackson Immunoresearch). Coverslips were washed extensively in PBS and mounted in Mowiol (Sigma-Aldrich).

Images were acquired in a laser scanning Nikon A1 confocal microscope using a CFI Plan APO IR 60x WI objective (NA 1.27) and Nikon NIS-Elements 4.0 acquisition software. The fraction of AZ protein staining (ELKS, MUNC13, RIM1, RIM2) colocalizing with presynaptic marker staining (VAMP2, Bassoon) was quantified using thresholded Manders coefficients as implemented in the JACoP plug-in [286] of ImageJ [287]. Sample size was five pairs of WT and RIM1α KO littermates, with 15-20 images per condition.

8.1.2 Electron Microscope

The main electron microscopes used in the earlier experiments were two Tecnai G2 Polara (FEI, Hillsboro, OR, USA), both capable of sample observation at liquid nitrogen temperature. Both microscopes used a FEG as an electron source and operated at 300 kV acceleration voltage. A multispecimen holder stored up to six cartridges (samples). An insertion rod pushed the cartridges inside the microscope column and fixed it to the sample stage by a screw-mechanism. The stage can be tilted up to ±70°and could be moved freely and with high precision in three directions. Both microscopes were equipped with an in column CCD camera (Gatan UltraScan 4k) for thin specimen, a retractable TV camera in the Gatan imaging filter (GIF) column and the 2k CCD after the GIF (refer to section 1.4). Two other microscopes were used in later stages of the project. A modified F20 TEM equipped with a VPP [62], used an acceleration voltage of 200 kV and did not have an energy filter installed. The images were taken on a FEI 4k Eagle CCD camera. A FEI Titan Krios was used as well, using 300 kV acceleration voltage, equipped with a VPP, an energy filter and a K2 Summit 4k direct detector.

8.1.3 Software

Electron microscopy software

The Tecnai G2 and Titan Krios both used Digital Micrograph in addition to its own tomographic acquisition software package from FEI. The object pixelsize in our experiments were ≈ 0.55 nm (RIM1α data) and ≈0.47 nm (all the others) and the defocus $\Delta z = -9\ \mu m$ and $\Delta z = -5\ \mu m$, respectively. Later, with the use the phase plate, the defocus was kept at $\Delta z = -1\ \mu m$ at a pixelsize of ≈ 0.42 nm. The tilting increment was 2°(RIM1α data) and 1.5°, with the total range of at least from -60 - +60°. The objective aperture was set to 3 in studies with the Tecnai G2, to ensure a balance between filtering out highly scattered electrons and still having a viable image at higher tilts. Additionally, we set the thickness value in the FEI tomography software to around 2.0 - 2.8. This undocumented value in the software has been investigated by the author to understand its effect on the electron distribution. The software takes this value (here referred to as "Factor") in its calculation of the exposure on each tilt angle (α):

$$\text{Exposure} = \text{Exposure}(0^o) \cdot \text{Factor}^{\frac{1}{cos(\alpha)}-1}$$

leading to exposing the sample with 2.0 - 2.8 times the electron dose at 60°compared to the 0°image. If we assume the ice as a homogeneous sheet with thickness d, rotating it by an angle α increase the optical path the beam has to penetrate ($d^* = \frac{d}{cos(\alpha)}$). Therefore we have to apply a weighting factor ($\text{Factor}^{\frac{1}{cos(\alpha)}-1}$) to the exposure time, such as the electron dose scales with the increase in thickness.

After a feature of interest was found, we checked the area around for contamination, thick ice or grid bars to make sure that these do not disturb our recording at higher tilt angles. The electron dose in the first image at zero degree was measured in order to fine-tune the appropriate exposure time for the whole series.

The total electron dose received by the sample was about 100 $\frac{e}{A^2}$, but less than 150 $\frac{e}{A^2}$. Depending on the sample/ice thickness this resulted in a total electron dose present in

the (energy filtered) tomographic series of about 20-50 $\frac{e}{A^2}$. Angle range and acquisition scheme therefore dictated a necessity of a filtered dose of less than 1 $\frac{e}{A^2}$ per projection. For the exact dose calculation a self written program in Python and PHP was used.

Later studies utilized the subframe capabilities of the K2 direct detector, in order to correct for sample movement/diffusion during image acquisition. We used subframes with a set exposure time, so that the first zero-degree image is composed of 10 subframes.

The micrographs were taken automatically with user interruptions when necessary. The eucentric height had to be set roughly manually and was automatically adjusted more carefully with the aid of the software. The software on both microscopes allowed to define a defocus value for the tilt series, which was subsequently checked before every acquisition. Due to the electron dose sensitivity of the sample, we were using a low-dose acquisition scheme in our setup [12]. In this setup, only the actual image recording took place at the spot of interest. Any other auxiliary steps, e.g. focussing and tracking, were done at a spatially close spot on the tilt axis to ensure eucentricity. Before acquiring an image, the current and previous tracking image were compared by cross-correlation and if necessary, the beam shifted to ensure the feature of interest stays in the field of view.

Reconstruction in TOM

The resulting tomographic projection images from earlier studies were stored in EM image format [288]. We used the TOM toolbox for alignment and reconstruction of tomograms [289]. With the use of 10 nm colloidal gold as fiducial markers, we tried to keep the average marker error as low as possible, ideally below a value of 1.5.

A weighted back projection model was used for analytical reconstruction of the tomogram from given micrographs. For making the segmentation easier, exact reconstruction model was used with the thickness parameter of 800 pixels, where low frequencies such as SVs or membranes were enhanced and high frequencies attenuated. Since both methods yielded similar tomograms, manual segmentation was done on exact, while analyses were performed on the (denoised) analytical reconstructions. We binned the images twice to decrease computational time and configured the low-pass filter to the Nyquist frequency of the final (binned) image. The final image dimensions were 512^3 pixels and the pixel size 1.87 nm (= 4 x 0.468 nm) and 2.64 nm (= 4 x 0.661 nm) for the RIM studies. Cropping the tomogram was necessary to speed up later filtering steps and was done within the TOM software framework.

Denoising

Analytically reconstructed tomograms still appeared very noisy. To get a higher SNR, an advanced denoising algorithm was used. The AND algorithm has already been used on tomograms of cells or compartments and showed promising results [290]. An improved version of this algorithm with automated parameter tuning (TOMOAND) [234] was used for our experiments. Denoising parameters were chosen to produce "mild" denoising, where features of interest detected in the original tomogram also remained in the denoised tomogram. To reduce computing time, only the part of a tomogram containing the synapse was denoised.

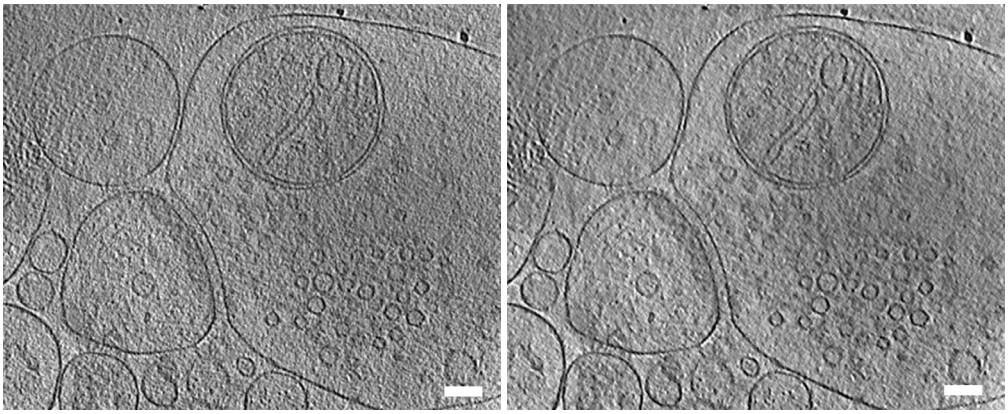

Figure 8.2: The effect of AND denoising. On the left side the original slice of the tomogram is shown. Lipid membranes inside the mitochondria could be hardly identified. SVs could be seen, but the contrast was suboptimal.
The right side shows the same slice from the AND denoised tomogram. The contrast in most areas was slightly enhanced while still preserving the fine structure. (Scalebars: 100 nm)

Reconstruction in IMOD

For the latest K2 direct detector based datasets, Digital Micrograph performed the subframe alignment and averaging. Subsequently, tomograms were reconstructed in the IMOD package [291], as TOM suffered from memory allocation errors in bigger imagesizes. Furthermore, a dual-tilt reconstruction was at that time only feasible in IMOD. The reconstruction procedure was slightly different in IMOD, as the software guided the user through all necessary steps. First, the X-rays were automatically removed in the image stack. After a brief cross correlation procedure, which acts as a rough pre-alignment step, one was able to choose between four different options for a fine alignment. Depending on the quality of the tilt images, as well as the number of fiducial markers visible, the user could solely rely on a cross correlation method or a marker-based alignment. With this information, IMOD corrected for tilt angle, magnification and/or rotational errors. A preliminary reconstruction aided in positioning the tomogram for the final reconstruction. The reconstruction algorithm used in some of the presented figures was SIRT (simultaneous iterative reconstruction technique). Iteration number variied between 20 and 25, depending on the tomogram. Additional (IMOD internal) AND filtering was performed on selected tomograms for better visualization.

8.1.4 Segmentation and Computation

While automatic segmentation showed some very promising results in some samples provided by the author [292], manual segmentation still appeared to be the most robust and reliable way in the noisy data we obtained. Therefore, we followed the semi-automatic segmentation procedure established [108, 109]:

- Manual segmentation of membranes (AZ, SVs) and cytoplasm in Amira (Visage Imaging, Richmond, Australia)

- Python program to form spheres out of a segmented central slice of a SV (pyto software package)
- Gray-scale based automatic segmentation of membrane attached protein complexes, such as SV connectors and SV tethers (pyto software package)
- Analysis for each tomogram in respect to morphological properties of SVs, connectors and tethers (pyto software package)
- Statistical analysis of the above results between different treatments (pyto software package)

Examples of bad tomograms not fitting the criteria for further analysis can be observed in figures 8.3 and 8.4. These included multiple synapses (e.g. figure 8.3), overall bad morphology (e.g. figure 8.4) or bad alignment (not shown).

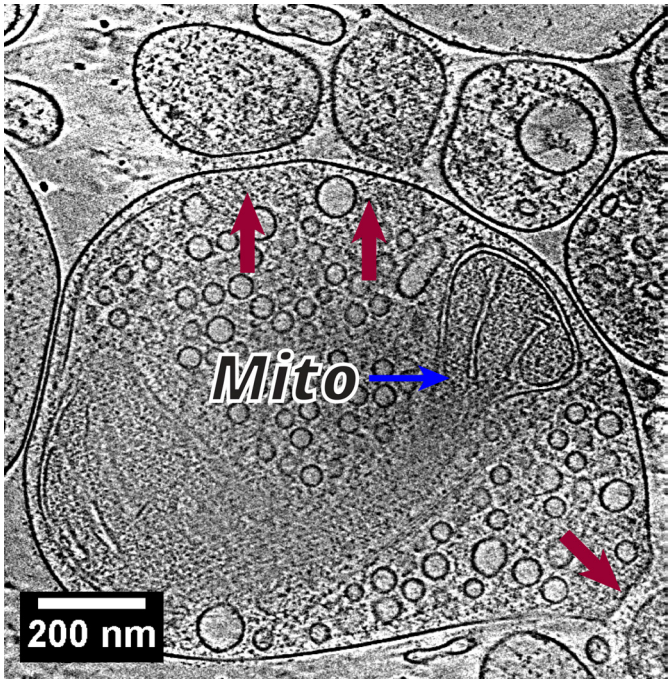

Figure 8.3: Overview slice of a synaptosome with three synapses (red arrows). The SVs could not be assigned unambiguously to each synapse separately, which made this tomogram unusable for analysis. Mitochondria ("Mito") is marked with another blue arrow. Scalebar: 200nm.

The pyto software package for analyzing 3D images was written by Dr. Vladan Lucic in Python (utilizing Numpy and Scipy packages) with small additions and customizations from the author. The sem was calculated and shown in graphs. Confidence tests used were Student's t-test for Gaussian distributed values, Kruskal-Wallis for not normally distributed values and Chi-square for values in discrete bins. Pearson's coefficient for used for correlation analysis, and its significance was determined using t-test. Confidence values given in the graphs were $p < 0.05$: *, $p < 0.01$: ** and $p < 0.001$: ***.

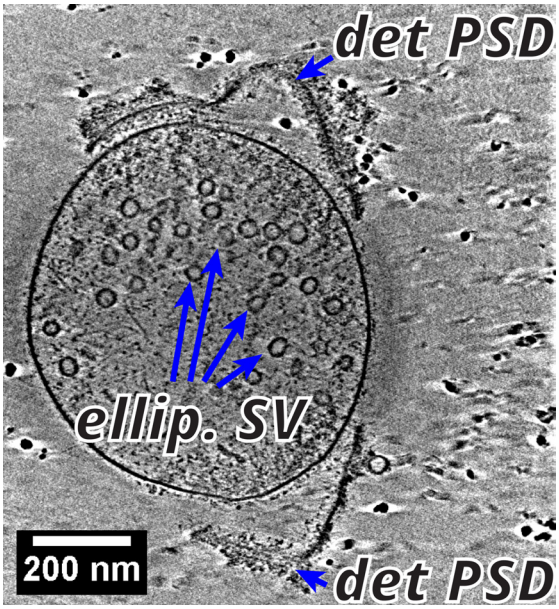

Figure 8.4: Overview slice of a synaptosome with several ellipsoid SVs ("ellip. SV", blue arrows). Additionally, there is no mitochondria, and two detached PSDs ("det PSD", blue arrows, top and bottom) rendering precise segmentation impossible. Scalebar: 200nm.

Workflow

A typical example of the whole computational workflow for synaptosomal analysis can be seen in figure 8.5. The main procedures used and their function in our workflow are described below.

Preparation Procedures

Drift_combine.py (self-written):
(Only for IMOD datasets:) Uses mdoc documentation files provided by the microscopy software to build one coherent big image stack according to tilt angle information. The stack can be cropped or flipped for further processing.

Sort_series.py (pyto package):
This program sorted the files in order of ascending angle (minus to plus side), removes extremely bright pixels (caused by X-rays) and calculated the (filtered) electron dose on the sample.

Discs_to_balls.py (pyto package):
This program converted the single slices of user-defined segmentations into perfect spheres by calculating the center point and expanding the disc in Z-dimension.

Blank.py (pyto package):
To make segmentation easier, this program was able to "blank-out" and set all vesicular (or other user-defined) segmentations to a certain grey level, e.g. white. This improved visibility of already segmented volumes and reduces user errors.

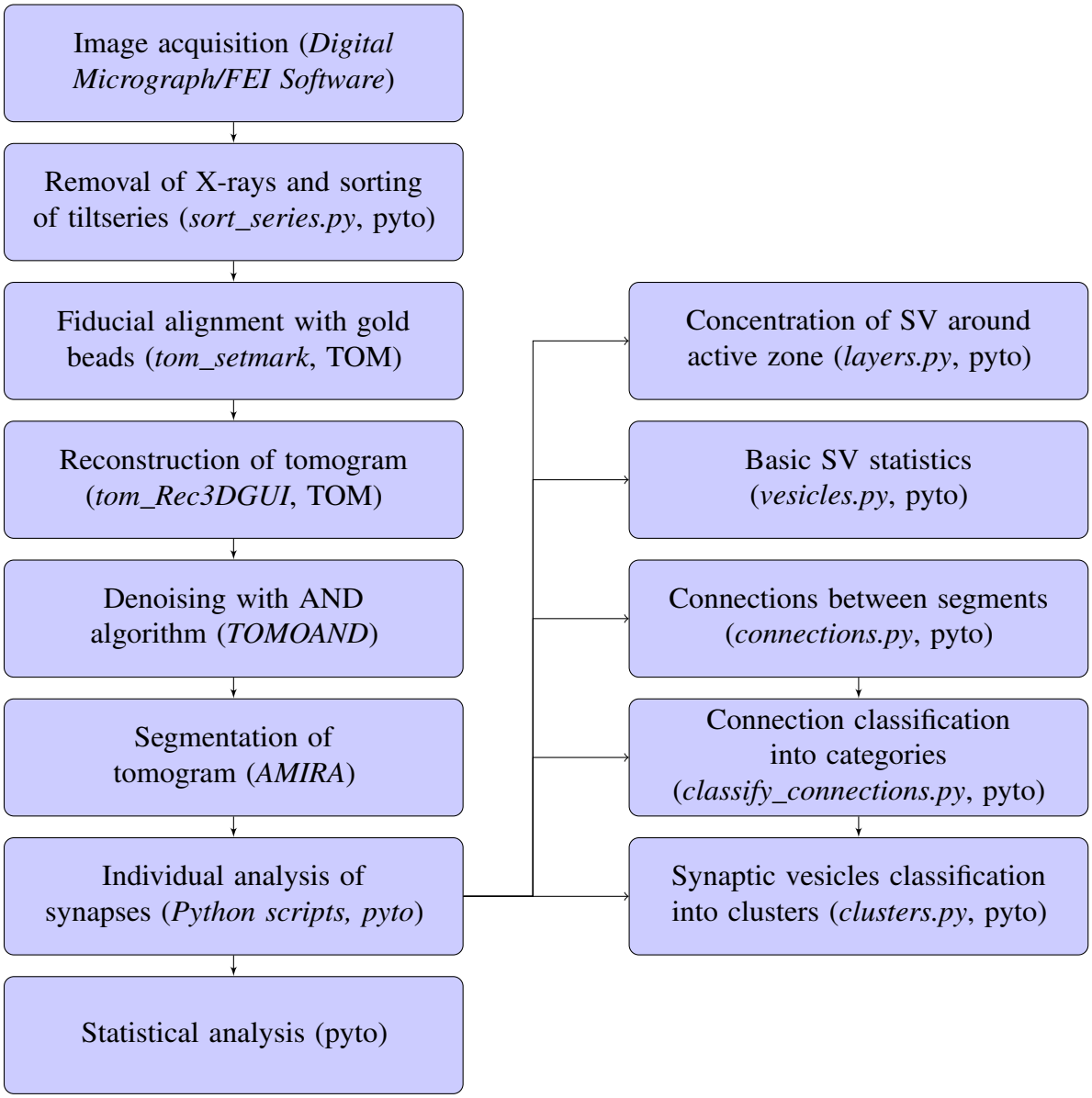

Figure 8.5: This workflow shows the computational steps after the image acquisition.

Analysis Pyto Procedures

Vesicles.py (pyto package):
A program used for calculating everything related to single SVs. The calculaton included lumen density, exact center position in X/Y/Z or distance from the AZ, amongst other things.

Layers.py (pyto package):
This program analyzed the SV distribution by forming one voxel thick layers from the AZ into the cytoplasm and calculated the ratio of cytoplasm occupied by SVs.

Connectors.py (pyto package):
This program detected connections between materials (SVs and AZ) by using a connectivity and thresholding approach (related to watershed transformation). In our

studies, only connections between two materials were analyzed, such as connectors (between SVs) and tethers (between SV and AZ).

Classify_connections.py (pyto package):
This program sorted the results from connectors.py by a given criteria. In our case, we separated the SV-AZ connections into the "tethers", while keeping all other ones (SV-SV) in the "connectors" group.

Work.py (pyto package):
This program was used for the statistical analysis between different treatment groups. All graphs, correlations and statistics demonstrated in chapters 3 and 6 were produced by this program.

8.2 26S Proteasomes in Situ Study

This section covers the materials and methods employed in the *in situ* study of 26S proteasomes in intact neurons in chapter 7.

8.2.1 Cell Culture and Sample Preparation

Cell culture and sample preparation were performed by co-author Dr. Yoshiyuki Fukuda.

Gold Quantifoil grids (R1/4, Au 200 mesh, Quantifoil Micro Tools, Jena, Germany) were chosen as the substrate for neuronal cell cultivation due to their inertness. After cleaning the grids with acetone and adding an additional carbon deposition ($\approx$ 25 nm, with a MED 020, BAL-TEC) on top of the grids, they were sterilized by UV irradiation for 30 min. To aid in cellular attachment, the grids were immersed in 1 mg/ml poly-L-lysine/0.1 M borate buffer (pH 8.5) in the dark overnight and then washed with autoclaved distilled water and were kept in plating medium for later use. Primary neuron cultures were prepared as described by Kaech and Banker [156] with some modifications and in accordance with the animal guidelines of the Max-Planck Society.

In brief, 2-day-old postnatal rat pups were anesthetized by CO_2 and then decapitated with a scissor. The brain was removed and submerged in ice-cold CMF-HBSS (calcium-, magnesium-, and bicarbonate-free Hank's balanced salt solution). For all subsequent steps, the brain was kept at 4°C to slow down/stop any cellular processes, including cellular denaturation. Under a dissecting microscope, the meninges membrane layers on top of the brain hemispheres were removed carefully. This was done to avoid any fibroblasts contained in the layers that may otherwise overgrow the hippocampal neurons. Once the meninges was removed, the hippocampus was extracted, minced and collected.

The pooled hippocampi were digested by 2.5% Trypsin and incubated for 15 minutes at 37°C. After removing Trypsin, the hippocampi were dissociated manually by pipetting the tissue through a Pasteur pipette, until a homogeneous solution was reached. This solution was then filtered with a cell strainer (Becton Dickinson and company, Franklin Lakes, NJ, USA) to remove remaining debris. The cellular density was measured via a light microscopy cell counter and then the proper concentration of $4.0x10^5$ cells

per dish was seeded on top of our EM grids. The cells were then incubated in CO_2 for approximately 4 hours and then transferred to another culture dish containing pre-conditioned Neurobasal-A/B27 medium and glial feeder cell layer. In order to stop any glial proliferation, additional cytosine arabinoside was added three days later. One third of the culture medium was exchanged once per week.

After 18 days of culturing, the neurons on the grids were plunge-frozen in a liquid ethane/propane mixture at close to liquid nitrogen temperature using a Vitrobot (FEI, Eindhoven, The Netherlands). 4 μl of 4 times up-concentrated BSA coated gold nano particle solution (Aurion 10 nm BSA coated gold) were dropped on the back side of the grid to aid in subsequent image alignments. Settings of the Vitrobot were as follows: Temperature was set to 37°C and 90% humidity, blotting waiting time to 5 seconds, and 10 seconds overall blot time. After plunging, excess ethane/propane mixture was blotted from the grid using a small piece of filter paper within liquid nitrogen conditions. Gridboxes containing four grids were stored in liquid nitrogen until usage.

8.2.2 Electron Cryotomography

ECT acquisition was done by co-author Dr. Yoshiyuki Fukuda.

The prepared EM grids were fitted into a clip ring and then mounted inside a gridholder for up to 10 grids. The gridholder was inserted into the cryo-electron microscope, the Titan Krios (FEI, Eindhoven, The Netherlands), which was equipped with a FEG, a Gatan post-column energy filter connected to a K2 Summit direct detector (Gatan, Pleasanton, CA, USA), and a FEI phase plate [62]. We used 300 kV acceleration voltage, commonly used in the cellular ECT workflow.

The K2 direct detector was operated in counting mode, allowing us to use frame-alignment procedures in order to avoid smearing or blurring due to sample and/or stage movements during acquisition. The tilt range was ±60°, with an increment of 2°. The total dose applied to the sample was around 110 $\frac{e}{A^2}$, which was tested beforehand to not influence the sample ultrastructurally. The magnification was 33000x, resulting in a pixel size of 4.21 Å at the specimen level, and the defocus value set at $\Delta z \approx -1\ \mu m$. Tilt series were collected with SerialEM [293].

8.2.3 Image Processing

After tomographic acquisition, the raw counting mode subframes were first aligned with Digital Micrograph (Gatan, Pleasanton, CA, USA), using cross-correlation and then averaged to yield one final frame. This procedure was done for every tilt angle (61 in total), and then all final images converted into a stack by a self-written program in python. To discard intensity outliers from the micrographs of the tilt series, high intensity pixels beyond 10 standard deviations were replaced by their neighborhood values. The tilt series were aligned based on fiducial gold, localized using the IMOD package [291]. Marker position optimization, image alignment (4 degrees of freedom per image: shifts, rotation, magnification) as well as weighted backprojection of the 3D volume were done in MATLAB using the AV3 [294] and TOM [295] toolboxes.

The micrographs were low-pass filtered at the Nyquist frequency of the three-dimensional reconstruction, i.e., depending on the binning of the volume. Two times binned tomograms (924 x 924 x 600 pixel volume, 16.84$Å^3$ per voxel) were reconstructed for initial template matching in PyTom [73, 261]. This size was chosen as the optimal compromise between speed of the template matching algorithm and the validity of particle detection.

Template Matching

A double capped 26S proteasome (EMDB: 2165) [25] with one RP removed, was filtered down to 40 Å and used as a template. The mask used for template matching was an enlarged, heavily downfiltered single-capped 26S proteasome. Additionally, the missing wedge was set to 30°, appropriate for the tilt scheme used (-60°to +60°). The rotational sampling included 7112 orientations.

The cytoplasmic regions of the tomograms were segmented manually in Amira (FEI, Eindhoven) and constrained correlation peaks [294] were extracted within this segmented volume, in order to remove high-intensity values caused by gold markers outside the cytoplasm. For each tomogram, 300 peaks were inspected manually in an author-modified procedure in TOM and true positives were retained. Both single- and double-capped 26S proteasomes had similar high CCC values (figure 7.2B). Subtomograms of 128^3 pixel volume and 4.21 Å pixelsize corresponding to the positive hits were reconstructed from unbinned projections and used for subsequent analysis. In total, 2234 subtomograms were reconstructed from 70 tomograms (figure 7.8).

Template matching for the 20S-Cdc48 complex was done identically with a filtered model of mouse Cdc48 (PDB: 3CF1) fused to a *S. cerevisiae* 20S proteasome (PDB: 1RYP).

Subtomogram Averaging and Classification

Initial subtomogram averaging over 20 iterations was performed using fast rotational matching implemented in PyTom [261], with a sum of all particles in randomized (neutral) orientations as the initial reference and a spherical mask (figure 7.3). The remaining parameters are given below [2]. This procedure divided the dataset into two halves that are aligned independently and hence allowed resolution determination according to the "gold standard" Fourier shell correlation (FSC) [296]. The resolution of the first average after 20 iterations containing single, double, (dis-) assembled 26S proteasome particles, as well as false positives was measured using FSC at approximately 34Å (37Å). As a resolution criterion we used $FSC = 0.3$ and additionally determined the resolution for $FSC = 0.5$ (stated in brackets), both stricter than $FSC = 0.143$, which is commonly applied in the SPA field for "gold standard FSC" [296]. We used a neutral spherical mask encompassing the full 26S proteasome for FSC calculations.

After computing the initial particle alignment, 3D auto-focus classification [264], with a spherical mask encompassing the full double-capped 26S proteasome, was applied to

[2] Range of frequency (in pixels) used for alignment: [4, 64]; Frequency in pixels used for resolution determination: 10; Maximum offset of the particle: 5; Adaptive resolution setting: 0.2

divide the aligned dataset into three distinct classes, with the additional parameters [3].

The first two classes were single (1165 particles, or 52%, 31 Å (33 Å) resolution) and double-capped 26S proteasomes (425 particles or 19%, 39 Å (44 Å) resolution), while the third one (653 particles or 29%) included (dis-) assembled 26S, 20S particles and false positives (figure 7.8). The first two classes were cut *in silico* between the β-rings in the 20S CP, thus allowing to treat the double-capped 26S as two independent particles. Truncated particles were first aligned and then subsequently classified into two main classes with 3D auto-focus classification [4], the GS (1339 particles, or 67%, 27 Å (29 Å) resolution) and SPS (667 particles, or 33%, 31 Å (33 Å) resolution), as well as an uncategorizable background class (300 particles). Subsequently, the GS class was classified into four classes, and the SPS class into three classes [5] (figure 7.13). The classes were chosen to best reflect and represent the variance in the initial class averages (figure 7.13). The resolutions of the subclasses were similar, ranging from 30 to 35 Å.

8.2.4 Fitting of Atomic Models

The work involved in this section was done by co-author Antje Aufderheide.

Atomic models for the GS and the SPS were obtained by molecular dynamics flexible fitting (MDFF) [268]. To prevent overfitting into the low-resolution maps, strong elastic network restraints, which essentially enforced rigidity of the subunits, were applied as described previously [29, 265]. To evaluate the bias of the starting model, we used all three of the previously published s1, s2 and s3 structures (PDB: 4cr2, 4cr3 and 4cr4) as initial configurations. Prior to fitting, the three starting models were aligned with respect to the 20S core particle using Visual Molecular Dynamics (VMD) [297]. Analogously, the maps of the GS and SPS were aligned to the core particle of the s1 structure applying the "fit-in-map" and "matrixcopy" functions of UCSF Chimera [298, 299]. Thereafter, the β-ring subunits were kept fixed throughout the fitting procedure. For both maps, the fit results using all three initial configurations were compared to the s1, s2 and s3 structures based on the root-mean-squared deviation (RMSD) of their atomic coordinates, which were calculated using VMD.

8.2.5 Miscellaneous Methods

A total of 20000 averaged bootstrap volumes each consisting of 50 random subtomograms, were used for each variance map calculation in PyTom.

Difference maps were calculated by first adjusting the threshold of the pair of filtered subtomogram averages to the same volume and then subtracting them.

Molecular weights of segments of EM maps were estimated in UCSF Chimera by comparing the volume of the maps and using the protein density value of 1.21 $Å^3$ per

[3] Frequency in pixels used for score calculation: 12; Binning: 1; Potential offset of the particle: 5; Iterations: 10; Cluster dispersion value: 10; Particle density threshold for difference map: -2; Threshold for difference map: 0.2

[4] Using the same parameters as the initial classification, but a smaller mask covering the full RP

[5] Using the same parameters as the previous classification

Da [300].

FCR measurements were performed with the atomic model of s1 (GS) single-capped 26S proteasome (PDB: 4cr2) against each of the 805 single-capped, GS subtomograms with a neutral spherical mask. For each operation, the subtomogram was aligned to the atomic model volume. The missing wedge was subsequently applied to the atomic model volume and both volumes were subjected to FSC [301]. The resolution indicated for each particle was calculated at a cutoff of 0.3.

For visualization, positions as well as orientation of the 26S proteasome taken from the results given by the subtomogram averaging. Visualization of the subtomogram averages was performed in UCSF Chimera [298].

Acronyms

2D	two-dimensional
3D	three-dimensional
AMPA	α-Amino-3-hydroxy-5-methyl-4-isoxazolepropionic acid
AND	anisotropic nonlinear diffusion
ATP	adenosine triphosphate
AZ	active zone
CCD	charged coupled device
ECT	electron cryo-tomography
CME	clathrin mediated endocytosis
cryo-TEM	transmission electron cryo-microscopy
CTF	contrast transfer function
EM	electron microscopy
EPSC	excitatory postsynaptic current
EPSP	excitatory postsynaptic potential
FEG	field emission gun
FIB	focussed ion beam
FM	fluorescent microscopy
FSC	Fourier shell correlation
GABA	γ-aminobutyric acid
GIF	Gatan imaging filter
GS	ground state
HBM	Hank's balanced medium
mEPSP	miniature excitatory postsynaptic potential
MTF	modulation transfer function
NMDA	N-Methyl-D-aspartate
NMDAR	N-Methyl-D-aspartate receptor
PALM	photo activated localization microscopy
ROI	regions of interest
RRP	readily releasable pool
SNARE	soluble NSF-attachment protein receptor
SNR	signal-to-noise ratio
SPA	single particle analysis
SPS	substrate-processing state
STED	stimulated emission depletion
STORM	stochastic optical reconstruction microscopy
SV	synaptic vesicle
TEM	transmission electron microscopy
TIRFM	total internal reflection fluorescence microscopy
TTX	tetrodotoxin
UPS	ubiquitin-proteasome system
UV	ultraviolet
VPP	Volta phase plate
Z	atomic number

Document Information

The template used for the design of this thesis was modified by the author from a template provided by the website latextemplates.com. This thesis was written in LaTeXunder Linux and Windows.

All figures have been produced by the author (Shoh Asano) except mentioned otherwise. The author obtained a permission for each published figure from the individual publisher. Arrows, letters as well as colored frames were done in Adobe Photoshop CS6, Adobe Illustrator CS6, Adobe Indesign CS6 or ImageJ. All plots were generated in either Python with pyto, SciPy/NumPy or Matlab.

The blueprint of the electrical circuit was created with Fritzing, the workflows with the package TikZ within Latex. 3D rendered images for the titles were done in 3DSMax with self-written scripts and other title images were used from photographs/images by the author or freely available images (Cajal neurons background in chapter 2).

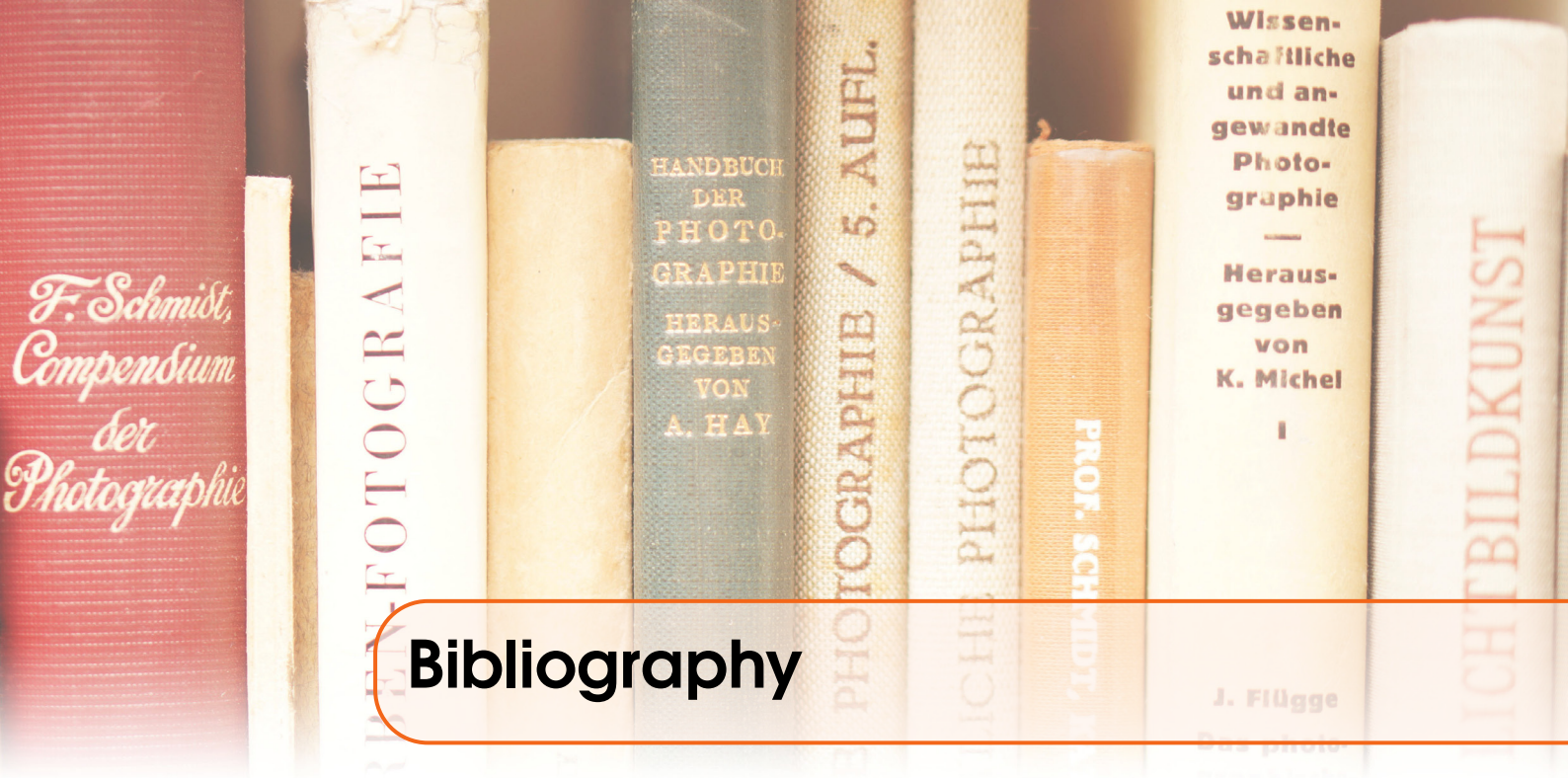

Bibliography

[1] P. Garcia-Lopez, V. Garcia-Marin, and M. Freire. "The histological slides and drawings of Cajal". *Frontiers in Neuroanatomy* 4 (2010).

[2] E. G. Gray. "Electron microscopy of synaptic contacts on dendrite spines of the cerebral cortex". *Nature* 183 (4675) (1959), page 1592.

[3] E. D. P. De Robertis and H. S. Bennett. "Some features of the submicroscopic morphology of synapses in frog and earthworm". *The Journal of Biophysical and Biochemical Cytology* 1 (1) (1955), pages 47–58.

[4] M. Adrian *et al.* "Cryo-electron microscopy of viruses". *Nature* 308 (5954) (1984), pages 32–36.

[5] D. J. De Rosier and A. Klug. "Reconstruction of three dimensional structures from electron micrographs." *Nature* 217 (5124) (1968), pages 130–134.

[6] User:Hat'nCoat. *Electron energy loss spectroscopy - Wikipedia, the free encyclopedia*.

[7] L. Reimer and H. Kohl. *Transmission Electron Microscopy: Physics of Image Formation*. Springer, 2008.

[8] R. Grimm *et al.* "Determination of the inelastic mean free path in ice by examination of tilted vesicles and automated most probable loss imaging". *Ultramicroscopy* 63 (3) (1996), pages 169–179.

[9] B. Feja and U. Aebi. "Determination of the inelastic mean free path of electrons in vitrified ice layers for on-line thickness measurements by zero-loss imaging". *Journal of Microscopy* 193 (1) (1999), pages 15–19.

[10] A. Meents *et al.* "Origin and temperature dependence of radiation damage in biological samples at cryogenic temperatures". *Proceedings of the National Academy of Sciences of the United States of America* (2009).

[11] J. C. H. Spence. *High-resolution electron microscopy*. Oxford University Press, 2013.

[12] A. J. Koster *et al.* "Perspectives of Molecular and Cellular Electron Tomography". *Journal of Structural Biology* 120 (3) (1997), pages 276–308.

[13] J. Wall, J. Langmore, and M. S. Isaacson. "The collection of scattered electrons in the dark field electron microscopy - II. Inelastic scattering". *Scanning electron microscopy: systems and applications 1973: Proceedings of a Conference*. 1973, page 136.

[14] D. B. Williams and C. B. Carter. *Transmission electron microscopy: A textbook for materials science*. Springer Verlag, 2009.

[15] S. J. Pennycook and P. D. Nellist. *Scanning transmission electron microscopy: imaging and analysis*. Springer Science & Business Media, 2011.

[16] J. Frank. *Electron tomography*. Springer, 1992.

[17] T. A. Klar *et al.* "Fluorescence microscopy with diffraction resolution barrier broken by stimulated emission". *Proceedings of the National Academy of Sciences of the United States of America* 97 (15) (2000), pages 8206–8210.

[18] B. Huang *et al.* "Three-dimensional super-resolution imaging by stochastic optical reconstruction microscopy". *Science* 319 (5864) (2008), pages 810–813.

[19] E. Betzig *et al.* "Imaging intracellular fluorescent proteins at nanometer resolution". *Science* 313 (5793) (2006), pages 1642–1645.

[20] B. Rupp and J. Wang. "Predictive models for protein crystallization". *Methods* 34 (3) (2004), pages 390–407.

[21] M. Von Ardenne. "Das Elektronen-Rastermikroskop". *Zeitschrift für Physik* 109 (9-10) (1938), pages 553–572.

[22] M. Knoll and E. Ruska. "Das Elektronenmikroskop". *Zeitschrift für Physik A Hadrons and Nuclei* 78 (5) (1932), pages 318–339.

[23] P. D. Nellist *et al.* "Direct sub-angstrom imaging of a crystal lattice". *Science* 305 (5691) (2004), pages 1741–1741.

[24] R. Erni *et al.* "Atomic-Resolution Imaging with a Sub-50-pm Electron Probe". *Physical Review Letters* 102 (9 2009), page 096101.

[25] F. Beck *et al.* "Near-atomic resolution structural model of the yeast 26S proteasome". *Proceedings of the National Academy of Sciences of the United States of America* 109 (37) (2012), pages 14870–14875.

[26] N. Grigorieff and S. C. Harrison. "Near-atomic resolution reconstructions of icosahedral viruses from electron cryo-microscopy". *Current Opinion in Structural Biology* 21 (2) (2011), pages 265–273.

[27] X.-c. Bai *et al.* "Ribosome structures to near-atomic resolution from thirty thousand cryo-EM particles". *ELife* 2 (2013), e00461.

[28] S. Bohn *et al.* "Structure of the 26S proteasome from Schizosaccharomyces pombe at subnanometer resolution". *Proceedings of the National Academy of Sciences of the United States of America* 107 (49) (2010), pages 20992–20997.

[29] P. Unverdorben *et al.* "Deep classification of a large cryo-EM dataset defines the conformational landscape of the 26S proteasome". *Proceedings of the National Academy of Sciences of the United States of America* 111 (15) (2014), pages 5544–5549.

[30] D. Voges, P. Zwickl, and W. Baumeister. "The 26S proteasome: a molecular machine designed for controlled proteolysis". *Annual Review of Biochemistry* 68 (1) (1999), pages 1015–1068.

[31] J. Walz *et al.* "26S proteasome structure revealed by three-dimensional electron microscopy". *Journal of Structural Biology* 121 (1) (1998), pages 19–29.

[32] S. Asano *et al.* "A molecular census of 26S proteasomes in intact neurons". *Science* 347 (6220) (2015), pages 439–442.

[33] V. Lucic, F. Förster, and W. Baumeister. "Structural studies by electron tomography: From cells to molecules". *Annual Review of Biochemistry* 74 (2005), pages 833–865.

[34] R. Fernandez-Busnadiego *et al.* "Insights into the molecular organization of the neuron by cryo-electron tomography". *Journal of Electron Microscopy* 60 (2011), S137–S148.

[35] D. Vanhecke *et al.* "Cryo-electron tomography: methodology, developments and biological applications". *Journal of Microscopy* 242 (3) (2011), pages 221–227.

[36] Z. Kochovski. "Image analysis of molecular complexes present in cryo-tomograms of neuronal synapses". PhD thesis. Technische Universität München, Dissertation, 2014.

[37] P. W. Hawkes and J. C. H. Spence. "Science of microscopy" (2007).

[38] M. E. Mochel and J. M. Mochel. "A CCD imaging and analysis system for the VG HB5 STEM". *Proc. of the 44 th Ann. Meet. EMSA* (1986), pages 616–617.

[39] O. L. Krivanek and P. E. Mooney. "Applications of slow-scan CCD cameras in transmission electron microscopy". *Ultramicroscopy* 49 (1) (1993), pages 95–108.

[40] B. E. Bammes *et al.* "Direct electron detection yields cryo-EM reconstructions at resolutions beyond 3/4 Nyquist frequency". *Journal of Structural Biology* 177 (3) (2012), pages 589–601.

[41] P. Lu *et al.* "Three-dimensional structure of human [ggr]-secretase". *Nature* 512 (7513) (2014), pages 166–170.

[42] X. Li *et al.* "Electron counting and beam-induced motion correction enable near-atomic-resolution single-particle cryo-EM". *Nature Methods* 10 (6) (2013), pages 584–590.

[43] R. S. Ruskin, Z. Yu, and N. Grigorieff. "Quantitative characterization of electron detectors for transmission electron microscopy". *Journal of Structural Biology* 184 (3) (2013), pages 385–393.

[44] P. Grob *et al.* "Ranking TEM cameras by their response to electron shot noise". *Ultramicroscopy* 133 (2013), pages 1–7.

[45] A. R. Faruqi and R. Henderson. “Electronic detectors for electron microscopy”. *Current Opinion in Structural Biology* 17 (5) (2007), pages 549–555.

[46] J. Radon. “Über die Bestimmung von Funktionen durch ihre Integralwerte längs gewisser Mannigfaltigkeiten”. *Berichte Sächsische Akademie der Wissenschaften* 69 (1917), pages 262–277.

[47] R. N. Bracewell. “Strip integration in radio astronomy”. *Australian Journal of Physics* 9 (2) (1956), pages 198–217.

[48] P. Unverdorben. “Pseudo-atomare Interpretation von Konformationsänderungen des 26S Proteasoms nach Klassifizierung von Kryo-Elektronenmikroskopie-Daten”. PhD thesis. Technische Universität München, Dissertation, 2014.

[49] R. A. Crowther. “Procedures for Three-Dimensional Reconstruction of Spherical Viruses by Fourier Synthesis from Electron Micrographs”. *Philosophical Transactions of the Royal Society of London. Series B, Biological Sciences* 261 (837) (1971), pages 221–228.

[50] R. Hegerl and W. Hoppe. “Influence of electron noise on three-dimensional image reconstruction”. *Zeitschrift Naturforschung Teil A* 31 (1976), pages 1717–1721.

[51] J. Dubochet *et al.* “Electron microscopy of frozen water and aqueous solutions”. *The Journal of Microscopy* 128 (1982), pages 219–237.

[52] O. B. Reite. “Mechanical Forces as a Cause of Cellular Damage by Freezing and Thawing”. *Biological Bulletin* 131 (1) (1966), pages 197–203.

[53] M. J. Costello. “Cryo-Electron Microscopy of Biological Samples”. *Ultrastructural Pathology* 30 (5) (2006), pages 361–371.

[54] J. Dubochet *et al.* “Cryo-electron microscopy of vitrified specimens”. *Quarterly Reviews of Biophysics* 21 (2) (1988), pages 129–228.

[55] S. B. Hayward and R. M. Glaeser. “Radiation damage of purple membrane at low temperature”. *Ultramicroscopy* 4 (2) (1979), pages 201–210.

[56] E. Knapek and J. Dubochet. “Beam damage to organic material is considerably reduced in cryo-electron microscopy”. *Journal of Molecular Biology* 141 (2) (1980), pages 147–161.

[57] A. C. M. Young *et al.* “Enhancement in resolution and lack of radiation damage in a rapidly frozen lysozyme crystal subjected to high-intensity synchrotron radiation”. *Journal of Applied Crystallography* 23 (3) (1990), pages 215–218.

[58] J. Dubochet *et al.* “Low temperature electron microscopy”. *Annual Review of Biophysics and Bioengineering* 10 (1) (1981), pages 133–149.

[59] L. R. Comolli and K. H. Downing. “Dose tolerance at helium and nitrogen temperatures for whole cell electron tomography”. *Journal of Structural Biology* 152 (3) (2005), pages 149–156.

[60] A. McDowall *et al.* “Electron microscopy of frozen hydrated sections of vitreous ice and vitrified biological samples”. *Journal of Microscopy* 131 (1) (1983), pages 1–9.

[61] A. Rigort *et al.* "Focused ion beam micromachining of eukaryotic cells for cryoelectron tomography". *Proceedings of the National Academy of Sciences of the United States of America* 109 (12) (2012), pages 4449–4454.

[62] R. Danev *et al.* "Volta potential phase plate for in-focus phase contrast transmission electron microscopy". *Proceedings of the National Academy of Sciences of the United States of America* 111 (44) (2014), pages 15635–15640.

[63] I. Arslan, J. R. Tong, and P. A. Midgley. "Reducing the missing wedge: high-resolution dual axis tomography of inorganic materials". *Ultramicroscopy* 106 (11) (2006), pages 994–1000.

[64] K. A. Taylor *et al.* "Three-dimensional reconstruction of rigor insect flight muscle from tilted thin sections." *Nature* 310 (5975) (1983), pages 285–291.

[65] D. N. Mastronarde. "Dual-axis tomography: an approach with alignment methods that preserve resolution". *Journal of Structural Biology* 120 (3) (1997), pages 343–352.

[66] P. Penczek *et al.* "Double-tilt electron tomography". *Ultramicroscopy* 60 (3) (1995), pages 393–410.

[67] M. Karuppasamy *et al.* "Radiation damage in single-particle cryo-electron microscopy: effects of dose and dose rate". *Journal of Synchrotron Radiation* 18 (3) (2011), pages 398–412.

[68] J. Z. Chen *et al.* "A dose-rate effect in single-particle electron microscopy". *Journal of Structural Biology* 161 (1) (2008), pages 92–100.

[69] R. Danev and K. Nagayama. "Transmission electron microscopy with Zernike phase plate". *Ultramicroscopy* 88 (4) (2001), pages 243–252.

[70] V. Knauer, R. Hegerl, and W. Hoppe. "Three-dimensional reconstruction and averaging of 30 S ribosomal subunits of Escherichia coli from electron micrographs". *Journal of Molecular Biology* 163 (3) (1983), pages 409–430.

[71] H. Oettl, R. Hegerl, and W. Hoppe. "Three-dimensional reconstruction and averaging of 50 S ribosomal subunits of Escherichia coli from electron micrographs". *Journal of Molecular Biology* 163 (3) (1983), pages 431–450.

[72] J. A. G. Briggs. "Structural biology *in situ*-the potential of subtomogram averaging". *Current Opinion in Structural Biology* 23 (2) (2013), pages 261–267.

[73] T. Hrabe *et al.* "PyTom: A python-based toolbox for localization of macromolecules in cryo-electron tomograms and subtomogram analysis". *Journal of Structural Biology* 178 (2) (2012), pages 177–188.

[74] User:LadyofHats. *Neuron - Wikipedia, the free encyclopedia*.

[75] N. Arimura and K. Kaibuchi. "Neuronal polarity: from extracellular signals to intracellular mechanisms". *Nature Reviews Neuroscience* 8 (3) (2007), pages 194–205.

[76] E. De Robertis and H. S. Bennett. "Submicroscopic vesicular component in the synapse". *Federation Proceedings*. Volume 13. 35. 1954, page 1954.

[77] V. P. Whittaker and M. N. Sheridan. “The morphology and acetylcholine content of isolated cerebral cortical synaptic vesicles”. *Journal of Neurochemistry* 12 (5) (1965), pages 363–372.

[78] V. Lučić *et al.* “Morphological Characterization of Molecular Complexes Present in the Synaptic Cleft”. *Structure* 13 (3) (2005), pages 423–434.

[79] J. E. Heuser and T. S. Reese. “Evidence for recycling of synaptic vesicle membrane during transmitter release at the frog neuromuscular junction”. *The Journal of Cell Biology* 57 (2) (1973), pages 315–344.

[80] S. Sankaranarayanan and T. A. Ryan. “Real-time measurements of vesicle-SNARE recycling in synapses of the central nervous system”. *Nature Cell Biology* 2 (4) (2000), pages 197–204.

[81] B. Ceccarelli, W. P. Hurlbut, and A. Mauro. “Turnover of transmitter and synaptic vesicles at the frog neuromuscular junction”. *The Journal of Cell Biology* 57 (2) (1973), pages 499–524.

[82] X.-S. Wu and L.-G. Wu. “Rapid endocytosis does not recycle vesicles within the readily releasable pool”. *The Journal of Neuroscience* 29 (35) (2009), pages 11038–11042.

[83] R. Fesce *et al.* “Neurotransmitter release: fusion or kiss-and-run?” *Trends in Cell Biology* 4 (1) (1994), pages 1–4.

[84] C. F. Stevens and J. H. Williams. “Kiss and run exocytosis at hippocampal synapses”. *Proceedings of the National Academy of Sciences of the United States of America* 97 (23) (2000), pages 12828–12833.

[85] S. M. Smith, R. Renden, and H. von Gersdorff. “Synaptic vesicle endocytosis: fast and slow modes of membrane retrieval”. *Trends in Neurosciences* 31 (11) (2008), pages 559–568.

[86] S. A. Mousavi *et al.* “Clathrin-dependent endocytosis.” *Biochemical Journal* 377 (1) (2004), pages 1–16.

[87] M. G. J. Ford *et al.* “Simultaneous binding of PtdIns (4, 5) P2 and clathrin by AP180 in the nucleation of clathrin lattices on membranes”. *Science* 291 (5506) (2001), pages 1051–1055.

[88] W. Wu and L.-G. Wu. “Rapid bulk endocytosis and its kinetics of fission pore closure at a central synapse”. *Proceedings of the National Academy of Sciences of the United States of America* 104 (24) (2007), pages 10234–10239.

[89] O. Cremona and P. De Camilli. “Synaptic vesicle endocytosis”. *Current Opinion in Neurobiology* 7 (3) (1997), pages 323–330.

[90] S. Watanabe *et al.* “Clathrin regenerates synaptic vesicles from endosomes”. *Nature* 515 (7526) (2014), pages 228–233.

[91] S. Watanabe *et al.* “Ultrafast endocytosis at Caenorhabditis elegans neuromuscular junctions”. *eLife* 2 (2013).

[92] S. O. Rizzoli. “Synaptic vesicle recycling: steps and principles”. *The EMBO journal* 33 (8) (2014), pages 788–822.

[93] Y. Moriyama, M. Maeda, and M. Futai. "The role of V-ATPase in neuronal and endocrine systems." *The Journal of Experimental Biology* 172 (1992), page 171.

[94] R. H. Edwards. "The neurotransmitter cycle and quantal size". *Neuron* 55 (6) (2007), pages 835–858.

[95] B. Granseth *et al.* "Clathrin-mediated endocytosis is the dominant mechanism of vesicle retrieval at hippocampal synapses". *Neuron* 51 (6) (2006), pages 773–786.

[96] J. Balaji and T. A. Ryan. "Single-vesicle imaging reveals that synaptic vesicle exocytosis and endocytosis are coupled by a single stochastic mode". *Proceedings of the National Academy of Sciences* 104 (51) (2007), pages 20576–20581.

[97] A. Ciechanover. "The ubiquitin-proteasome proteolytic pathway". *Cell* 79 (1) (1994), pages 13–21.

[98] M. H. Glickman and A. Ciechanover. "The ubiquitin-proteasome proteolytic pathway: destruction for the sake of construction". *Physiological Reviews* 82 (2) (2002), pages 373–428.

[99] A. Hershko, A. Ciechanover, and A. Varshavsky. "The ubiquitin system". *Nature Medicine* 6 (10) (2000), pages 1073–1081.

[100] A. G. Eldridge and T. O'Brien. "Therapeutic strategies within the ubiquitin proteasome system". *Cell Death & Differentiation* 17 (1) (2009), pages 4–13.

[101] J. Maupin-Furlow. "Proteasomes and protein conjugation across domains of life". *Nature Reviews Microbiology* 10 (2) (2012), pages 100–111.

[102] D. Finley. "Recognition and Processing of Ubiquitin-Protein Conjugates by the Proteasome". *Annual Review of Biochemistry* 78 (2009), pages 477–513.

[103] B. Bingol and M. Shang. "Deconstruction for Reconstruction: The Role of Proteolysis in Neural Plasticity and Disease". *Neuron* 69 (1) (2011), pages 22–32.

[104] V. Lazarevic *et al.* "Extensive Remodeling of the Presynaptic Cytomatrix upon Homeostatic Adaptation to Network Activity Silencing". *Journal of Neuroscience* 31 (28) (2011), pages 10189–10200.

[105] X. Jiang *et al.* "A Role for the Ubiquitin-Proteasome System in Activity-Dependent Presynaptic Silencing". *Journal of Neuroscience* 30 (5) (2010), pages 1798–1809.

[106] J. N. Keller, K. B. Hanni, and W. R. Markesbery. "Impaired proteasome function in Alzheimer's disease". *Journal of Neurochemistry* 75 (1) (2000), pages 436–439.

[107] E. Leroy *et al.* "The ubiquitin pathway in Parkinson's disease". *Nature* 395 (6701) (1998), pages 451–452.

[108] R. Fernández-Busnadiego *et al.* "Quantitative analysis of the native presynaptic cytomatrix by cryoelectron tomography". *The Journal of Cell Biology* 188 (1) (2010), pages 145–156.

[109] R. Fernandez-Busnadiego *et al.* "Cryo-electron tomography reveals a critical role of RIM1α in synaptic vesicle tethering". *The Journal of Cell Biology* 201 (5) (2013), pages 725–740.

[110] T. Dresbach *et al.* "The presynaptic cytomatrix of brain synapses". *Cellular and Molecular Life Sciences* 58 (1) (2001), pages 94–116.

[111] S. Schoch and E. D. Gundelfinger. "Molecular organization of the presynaptic active zone". *Cell and Tissue Research* 326 (2) (2006), pages 379–391.

[112] T. Mittelstaedt, E. Alvarez-Baron, and S. Schoch. "RIM proteins and their role in synapse function". *Biological Chemistry* 391 (6) (2010), pages 599–606.

[113] J. Lu *et al.* "Structural basis for a Munc13–1 homodimer to Munc13–1/RIM heterodimer switch". *PLoS Biology* 4 (7) (2006), e192.

[114] L. Deng *et al.* "RIM Proteins Activate Vesicle Priming by Reversing Autoinhibitory Homodimerization of Munc13". *Neuron* 69 (2) (2011), pages 317–331.

[115] Y. Han *et al.* "RIM Determines Ca^{2+} Channel Density and Vesicle Docking at the Presynaptic Active Zone". *Neuron* 69 (2) (2011), pages 304–316.

[116] P. S. Kaeser *et al.* "RIM Proteins Tether Ca^{2+} Channels to Presynaptic Active Zones via a Direct PDZ-Domain Interaction". *Cell* 144 (2) (2011), pages 282–295.

[117] P. S. Kaeser *et al.* "RIM genes differentially contribute to organizing presynaptic release sites". *Proceedings of the National Academy of Sciences of the United States of America* 109 (29) (2012), pages 11830–11835.

[118] User:Curtis Neveu. *Active Zone - Wikipedia, the free encyclopedia*.

[119] T. C. Südhof. "A molecular machine for neurotransmitter release: synaptotagmin and beyond". *Nature Medicine* 19 (10) (2013), pages 1227–1231.

[120] Y. Wang and T. C. Südhof. "Genomic definition of RIM proteins: evolutionary amplification of a family of synaptic regulatory proteins". *Genomics* 81 (2) (2003), pages 126–137.

[121] Y. Wang, S. Sugita, and T. C. Südhof. "The RIM/NIM Family of Neuronal C2 Domain Proteins Interactions with Rab3 and a new class of Src homology 3 domain proteins". *Journal of Biological Chemistry* 275 (26) (2000), pages 20033–20044.

[122] E. O. Gracheva *et al.* "Direct interactions between C. elegans RAB-3 and Rim provide a mechanism to target vesicles to the presynaptic density". *Neuroscience Letters* 444 (2) (2008), pages 137–142.

[123] S. P. Koushika *et al.* "A post-docking role for active zone protein Rim". *Nature Neuroscience* 4 (10) (2001), pages 997–1005.

[124] E. Fourcaudot *et al.* "cAMP / PKA signaling and RIM1α mediate presynaptic LTP in the lateral amygdala". en. *Proceedings of the National Academy of Sciences of the United States of America* 105 (39) (2008), pages 15130–15135.

[125] S. Schoch *et al.* "RIM1α forms a protein scaffold for regulating neurotransmitter release at the active zone". *Nature* 415 (6869) (2002), pages 321–326.

[126] N. Calakos *et al.* "Multiple roles for the active zone protein RIM1α in late stages of neurotransmitter release". *Neuron* 42 (6) (2004), pages 889–896.

[127] C. M. Powell *et al.* "The presynaptic active zone protein RIM1α is critical for normal learning and memory". *Neuron* 42 (1) (2004), pages 143–153.

[128] J. L. A. N. Murk *et al.* "Influence of aldehyde fixation on the morphology of endosomes and lysosomes: quantitative analysis and electron tomography". *Journal of Microscopy* 212 (1) (2003), pages 81–90.

[129] P. J. Szczesny, P. Walther, and M. Müller. "Light damage in rod outer segments: the effects of fixation on ultrastructural alterations". *Current Eye Research* 15 (8) (1996), pages 807–814.

[130] V. P. Whittaker, I. A. Michaelson, and R. J. Kirkland. "The separation of synaptic vesicles from nerve-ending particles (synaptosomes)". *The Biochemical Journal* 90 (2) (1964), pages 293–303.

[131] V. P. Whittaker. "Thirty years of synaptosome research". *Journal of Neurocytology* 22 (9) (1993), pages 735–742.

[132] D. H. Lee and A. L. Goldberg. "Proteasome inhibitors: valuable new tools for cell biologists". *Trends in Cell Biology* 8 (10) (1998), pages 397–403.

[133] P. S. Kaeser *et al.* "RIM1α and RIM1β Are Synthesized from Distinct Promoters of the RIM1 Gene to Mediate Differential But Overlapping Synaptic Functions". *Journal of Neuroscience* 28 (50) (2008), pages 13435–13447.

[134] H.-C. Tai *et al.* "Characterization of the brain 26S proteasome and its interacting proteins". *Frontiers in Molecular Neuroscience* 3 (2010), page 12.

[135] S. C. Upadhya *et al.* "Differential regulation of proteasome activity in the nucleus and the synaptic terminals". *Neurochemistry International* 48 (4) (2006), pages 296–305.

[136] A. M. Thomson. "Facilitation, augmentation and potentiation at central synapses". *Trends in Neurosciences* 23 (7) (2000), pages 305–312.

[137] T. F. Liu *et al.* "Inhibitory effects of 12-O-tetradecanoylphorbol-13-acetate on dye leakage from single Novikoff cells and on dye transfer between reaggregated cell pairs". *Methods and Findings in Experimental and Clinical Pharmacolgy* 19 (9) (1997), pages 573–7.

[138] G. van den Bogaart *et al.* "Synaptotagmin-1 may be a distance regulator acting upstream of SNARE nucleation". *Nature Structural & Molecular Biology* 18 (7) (2011), 805–U82.

[139] I. Yao *et al.* "SCRAPPER-dependent ubiquitination of active zone protein RIM1 regulates synaptic vesicle release". *Cell* 130 (5) (2007), pages 943–957.

[140] B. Aravamudan and K. Broadie. "Synaptic Drosophila UNC-13 is regulated by antagonistic G-protein pathways via a proteasome-dependent degradation mechanism". *Journal of Neurobiology* 54 (3) (2003), pages 417–438.

[141] S. D. Speese *et al.* "The ubiquitin proteasome system acutely regulates presynaptic protein turnover and synaptic efficacy". *Current Biology* 13 (11) (2003), pages 899–910.

[142] H. Tada *et al.* "Fbxo45, a Novel Ubiquitin Ligase, Regulates Synaptic Activity". *Journal of Biological Chemistry* 285 (6) (2010), pages 3840–3849.

[143] T. C. Wheeler *et al.* "Regulation of synaptophysin degradation by mammalian homologues of seven in absentia". *Journal of Biological Chemistry* 277 (12) (2002), pages 10273–10282.

[144] G. V. Rinetti and F. E. Schweizer. "Ubiquitination Acutely Regulates Presynaptic Neurotransmitter Release in Mammalian Neurons". *Journal of Neuroscience* 30 (9) (2010), pages 3157–3166.

[145] M. Burbea *et al.* "Ubiquitin and AP180 regulate the abundance of GLR-1 glutamate receptors at postsynaptic elements in C. elegans". *Neuron* 35 (1) (2002), pages 107–120.

[146] M. D. Ehlers. "Activity level controls postsynaptic composition and signaling via the ubiquitin-proteasome system". *Nature Neuroscience* 6 (3) (2003), pages 231–242.

[147] P. E. Castillo *et al.* "RIM1α is required for presynaptic long-term potentiation". *Nature* 415 (6869) (2002), pages 327–330.

[148] Y. S. Andrews-Zwilling *et al.* "Binding to Rab3A-interacting molecule RIM regulates the presynaptic recruitment of Munc13-1 and ubMunc13-2". *Journal of Biological Chemistry* 281 (28) (2006), pages 19720–19731.

[149] L. Siksou *et al.* "A common molecular basis for membrane docking and functional priming of synaptic vesicles". *European Journal of Neuroscience* 30 (1) (2009), pages 49–56.

[150] S. Hallermann *et al.* "Naked Dense Bodies Provoke Depression". *Journal of Neuroscience* 30 (43) (2010), pages 14340–14345.

[151] T. C. Südhof. "The Presynaptic Active Zone". *Neuron* 75 (1) (2012), pages 11–25.

[152] P. R. Dunkley, P. E. Jarvie, and P. J. Robinson. "A rapid Percoll gradient procedure for preparation of synaptosomes". *Nature Protocols* 3 (11) (2008), pages 1718–1728.

[153] P. R. Dunkley *et al.* "A rapid percoll gradient procedure for isolation of synaptosomes directly from an S1 fraction - Homogeneity and morphology of subcellular fractions". *Brain Research* 441 (1-2) (1988), pages 59–71.

[154] M. Erecińska, D. Nelson, and I. A. Silver. "Metabolic and energetic properties of isolated nerve ending particles (synaptosomes)". *Biochimica et Biophysica Acta (BBA)-Bioenergetics* 1277 (1) (1996), pages 13–34.

[155] L. J. Millet and M. U. Gillette. "Over a century of neuron culture: from the hanging drop to microfluidic devices". *The Yale Journal of Biology and Medicine* 85 (4) (2012), page 501.

[156] S. Kaech and G. Banker. "Culturing hippocampal neurons". *Nature Protocols* 1 (5) (2006), pages 2406–2415.

[157] G. A. Banker and W. M. Cowan. "Rat hippocampal neurons in dispersed cell culture". *Brain Research* 126 (3) (1977), pages 397–425.

[158] G. J. Brewer. "Isolation and culture of adult rat hippocampal neurons". *Journal of Neuroscience Methods* 71 (2) (1997), pages 143–155.

[159] F. Zhang *et al.* "Channelrhodopsin-2 and optical control of excitable cells". *Nature Methods* 3 (10) (2006), pages 785–792.

[160] X. Michalet *et al.* "Quantum dots for live cells, in vivo imaging, and diagnostics". *Science* 307 (5709) (2005), pages 538–544.

[161] J. Livet *et al.* "Transgenic strategies for combinatorial expression of fluorescent proteins in the nervous system". *Nature* 450 (7166) (2007), pages 56–62.

[162] S. Ebrahimi and S. Okabe. "Structural dynamics of dendritic spines: Molecular composition, geometry and functional regulation". *Biochimica et Biophysica Acta - Biomembranes* 1838 (10) (2014), pages 2391–2398.

[163] S. L. Palay *et al.* "Fixation of neural tissues for electron microscopy by perfusion with solutions of osmium tetroxide". *The Journal of Cell Biology* 12 (2) (1962), pages 385–410.

[164] T. S. Reese and M. J. Karnovsky. "Fine structural localization of a blood-brain barrier to exogenous peroxidase". *The Journal of Cell Biology* 34 (1) (1967), pages 207–217.

[165] J. J. Bozzola and L. D. Russell. *Electron microscopy: principles and techniques for biologists*. Jones & Bartlett Learning, 1999.

[166] Y. Fukuda *et al.* "Coordinate transformation based cryo-correlative methods for electron tomography and focused ion beam milling". *Ultramicroscopy* 143 (2014), pages 15–23.

[167] D. L. Benson *et al.* "Characterization of GABAergic neurons in hippocampal cell cultures". *Journal of Neurocytology* 23 (5) (1994), pages 279–295.

[168] S. Okabe *et al.* "Continual remodeling of postsynaptic density and its regulation by synaptic activity". *Nature Neuroscience* 2 (9) (1999), pages 804–811.

[169] A. Suzumura *et al.* "The isolation and long-term culture of oligodendrocytes from newborn mouse brain". *Brain Research* 324 (2) (1984), pages 379–383.

[170] J. Nakai, M. Ohkura, and K. Imoto. "A high signal-to-noise Ca^{2+} probe composed of a single green fluorescent protein". *Nature Biotechnology* 19 (2) (2001), pages 137–141.

[171] M. Ohkura *et al.* "Genetically encoded green fluorescent Ca^{2+} indicators with improved detectability for neuronal Ca^{2+} signals". *PLoS One* 7 (12) (2012), e51286.

[172] R. E. Kingston, C. A. Chen, and J. K. Rose. "Calcium phosphate transfection". *Current Protocols in Molecular Biology* (2003), pages 9–1.

[173] M. Jiang and G. Chen. "High Ca^{2+}-phosphate transfection efficiency in low-density neuronal cultures". *Nature Protocols* 1 (2) (2006), pages 695–700.

[174] H. Nakamura and J.-I. Funahashi. "Introduction of DNA into Chick Embryos by *in Ovo* Electroporation". *Methods* 24 (1) (2001), pages 43–48.

[175] D. Luo and W. M. Saltzman. "Synthetic DNA delivery systems". *Nature Biotechnology* 18 (1) (2000), pages 33–37.

[176] A. Pfeifer *et al.* "Transgenesis by lentiviral vectors: lack of gene silencing in mammalian embryonic stem cells and preimplantation embryos". *Proceedings of the National Academy of Sciences of the United States of America* 99 (4) (2002), pages 2140–2145.

[177] T. K. Kim and J. H. Eberwine. "Mammalian cell transfection: the present and the future". *Analytical and Bioanalytical Chemistry* 397 (8) (2010), pages 3173–3178.

[178] O. Paulsen and P. Heggelund. "Quantal properties of spontaneous EPSCs in neurones of the guinea-pig dorsal lateral geniculate nucleus." *The Journal of Physiology* 496 (3) (1996), pages 759–772.

[179] P. Fatt and B. Katz. "An analysis of the end-plate potential recorded with an intra-cellular electrode". *The Journal of Physiology* 115 (3) (1951), pages 320–370.

[180] T. Yasumoto and M. Murata. "Marine toxins". *Chemical Reviews* 93 (5) (1993), pages 1897–1909.

[181] G. M. Lipkind and H. A. Fozzard. "A structural model of the tetrodotoxin and saxitoxin binding site of the Na^+ channel". *Biophysical Journal* 66 (1) (1994), pages 1–13.

[182] J. J. Clare *et al.* "Voltage-gated sodium channels as therapeutic targets". *Drug Discovery Today* 5 (11) (2000), pages 506–520.

[183] J. M. Bekkers, G. B. Richerson, and C. F. Stevens. "Origin of variability in quantal size in cultured hippocampal neurons and hippocampal slices." *Proceedings of the National Academy of Sciences of the United States of America* 87 (14) (1990), pages 5359–5362.

[184] R. Morris. "Synaptic plasticity and learning: selective impairment of learning rats and blockade of long-term potentiation in vivo by the N-methyl-D-aspartate receptor antagonist AP5". *The Journal of Neuroscience* 9 (9) (1989), pages 3040–3057.

[185] R. H. F. Manske. "The Alkaloids of Fumeraceous Plants: II. Dicentra Cucullaria". *Canadian Journal of Research* 7 (3) (1932), pages 265–269.

[186] R. Schneggenburger, J. López-Barneo, and A. Konnerth. "Excitatory and inhibitory synaptic currents and receptors in rat medial septal neurones." *The Journal of Physiology* 445 (1) (1992), pages 261–276.

[187] T. Z. Baram and O. C. Snead III. "Bicuculline induced seizures in infant rats: ontogeny of behavioral and electrocortical phenomena". *Developmental Brain Research* 57 (2) (1990), pages 291–295.

[188] A. M. Hamilton *et al.* "Activity-dependent growth of new dendritic spines is regulated by the proteasome". *Neuron* 74 (6) (2012), pages 1023–1030.

[189] M. Canepari *et al.* "Photochemical and pharmacological evaluation of 7-nitroindolinyl-and 4-methoxy-7-nitroindolinyl-amino acids as novel, fast caged neurotransmitters". *Journal of Neuroscience Methods* 112 (1) (2001), pages 29–42.

[190] M. Matsuzaki *et al.* "Dendritic spine geometry is critical for AMPA receptor expression in hippocampal CA1 pyramidal neurons". *Nature Neuroscience* 4 (11) (2001), pages 1086–1092.

[191] I. Mody, J. D. C. Lambert, and U. Heinemann. "Low extracellular magnesium induces epileptiform activity and spreading depression in rat hippocampal slices". *Journal of Neurophysiology* 57 (3) (1987), pages 869–888.

[192] M. Ohkura *et al.* "An improved genetically encoded red fluorescent Ca^{2+} indicator for detecting optically evoked action potentials". *PLoS One* 7 (7) (2012), e39933.

[193] E. Yaksi and R. W. Friedrich. "Reconstruction of firing rate changes across neuronal populations by temporally deconvolved Ca^{2+} imaging". *Nature Methods* 3 (5) (2006), pages 377–383.

[194] F. Helmchen, K. Imoto, and B. Sakmann. "Ca^{2+} buffering and action potential-evoked Ca^{2+} signaling in dendrites of pyramidal neurons". *Biophysical Journal* 70 (2) (1996), pages 1069–1081.

[195] A. C. Meyer, E. Neher, and R. Schneggenburger. "Estimation of quantal size and number of functional active zones at the calyx of held synapse by nonstationary EPSC variance analysis". *The Journal of Neuroscience* 21 (20) (2001), pages 7889–7900.

[196] R. S. Zucker and W. G. Regehr. "Short-term synaptic plasticity". *Annual Review of Physiology* 64 (1) (2002), pages 355–405.

[197] J. Del Castillo and B. Katz. "Quantal components of the end-plate potential". *The Journal of Physiology* 124 (3) (1954), pages 560–573.

[198] I. A. Boyd and A. R. Martin. "The end-plate potential in mammalian muscle". *The Journal of Physiology* 132 (1) (1956), pages 74–91.

[199] L. Tian *et al.* "Imaging neural activity in worms, flies and mice with improved GCaMP calcium indicators". *Nature Methods* 6 (12) (2009), pages 875–881.

[200] R. Araya *et al.* "The spine neck filters membrane potentials". *Proceedings of the National Academy of Sciences* 103 (47) (2006), pages 17961–17966.

[201] A. G. Carter and B. L. Sabatini. "State-dependent calcium signaling in dendritic spines of striatal medium spiny neurons". *Neuron* 44 (3) (2004), pages 483–493.

[202] M. Matsuzaki *et al.* "Structural basis of long-term potentiation in single dendritic spines". *Nature* 429 (6993) (2004), pages 761–766.

[203] J. S. Isaacson and B. Walmsley. "Counting quanta: direct measurements of transmitter release at a central synapse". *Neuron* 15 (4) (1995), pages 875–884.

[204] A. M. Aravanis, J. L. Pyle, and R. W. Tsien. "Single synaptic vesicles fusing transiently and successively without loss of identity". *Nature* 423 (6940) (2003), pages 643–647.

[205] T. R. Shaikh *et al.* "Implementation of a flash-photolysis system for time-resolved cryo-electron microscopy". *Journal of Structural Biology* 165 (3) (2009), pages 184–189.

[206] J. Ménétret *et al.* "Time-resolved cryo-electron microscopic study of the dissociation of actomyosin induced by photolysis of photolabile nucleotides". *Journal of Molecular Biology* 219 (2) (1991), pages 139–144.

[207] K. Moffat and R. Henderson. "Freeze trapping of reaction intermediates". *Current Opinion in Structural Biology* 5 (5) (1995), pages 656–663.

[208] S. Watanabe *et al.* "Ultrafast endocytosis at mouse hippocampal synapses". *Nature* 504 (7479) (2013), pages 242–247.

[209] J. Heuser *et al.* "Synaptic vesicle exocytosis captured by quick freezing and correlated with quantal transmitter release." *The Journal of Cell Biology* 81 (2) (1979), pages 275–300.

[210] J.-F. Menetret, W. Hofmann, and J. Lepault. "Cryo-electron microscopy of insect flight muscle thick filaments: An approach to dynamic electron microscope studies". *Journal of Molecular Biology* 202 (1) (1988), pages 175–178.

[211] J. Berriman and N. Unwin. "Analysis of transient structures by cryo-microscopy combined with rapid mixing of spray droplets". *Ultramicroscopy* 56 (4) (1994), pages 241–252.

[212] G. Ellis-Davies and J. Kaplan. *Structure and synthesis of nitrophenyl-EGTA, a caged calcium, intermediates thereof and a method of producing a high photochemical yield of liberated calcium*. 1995.

[213] G. C. R. Ellis-Davies. "Caged compounds: photorelease technology for control of cellular chemistry and physiology". *Nature Methods* 4 (8) (2007), pages 619–628.

[214] S. R. Adams and R. Y. Tsien. "Controlling cell chemistry with caged compounds". *Annual Review of Physiology* 55 (1) (1993), pages 755–784.

[215] K. R. Delaney and R. S. Zucker. "Calcium released by photolysis of DM-nitrophen stimulates transmitter release at squid giant synapse." *The Journal of Physiology* 426 (1) (1990), pages 473–498.

[216] R. Heidelberger *et al.* "Calcium dependence of the rate of exocytosis in a synaptic terminal." *Nature* 371 (6497) (1994), page 513.

[217] T. D. Parsons *et al.* "Docked granules, the exocytic burst, and the need for ATP hydrolysis in endocrine cells". *Neuron* 15 (5) (1995), pages 1085–1096.

[218] E. Neher and R. S. Zucker. "Multiple calcium-dependent processes related to secretion in bovine chromaffin cells". *Neuron* 10 (1) (1993), pages 21–30.

[219] A. F. Oberhauser, I. M. Robinson, and J. M. Fernandez. "Simultaneous capacitance and amperometric measurements of exocytosis: a comparison." *Biophysical Journal* 71 (2) (1996), page 1131.

[220] D. G. Nicholls, T. S. Sihra, and J. Sanchez-Prieto. "Calcium-Dependent and-Independent Release of Glutamate from Synaptosomes Monitored by Continuous Fluorometry". *Journal of Neurochemistry* 49 (1) (1987), pages 50–57.

[221] D. G. Nicholls and T. S. Sihra. "Synaptosomes possess an exocytotic pool of glutamate". *Nature* 321 (6072) (1986), pages 772–773.

[222] A. P. Barrie *et al.* "An ion channel locus for the protein kinase C potentiation of transmitter glutamate release from guinea pig cerebrocortical synaptosomes". *Journal of Neurochemistry* 57 (4) (1991), pages 1398–1404.

[223] J. P. Y. Kao. "Caged molecules: principles and practical considerations". *Current Protocols in Neuroscience* (2006), pages 6–20.

[224] G. C. R. Ellis-Davies. "Neurobiology with Caged Calcium". *Chemical Reviews* 108 (5) (2008), pages 1603–1613.

[225] G. C. R. Ellis-Davies and J. H. Kaplan. "A new class of photolabile chelators for the rapid release of divalent cations: generation of caged calcium and caged magnesium". *The Journal of Organic Chemistry* 53 (9) (1988), pages 1966–1969.

[226] A. Takahashi *et al.* "Measurement of intracellular calcium". *Physiological Reviews* 79 (4) (1999), pages 1089–1125.

[227] J. H. Kaplan and G. C. Ellis-Davies. "Photolabile chelators for the rapid photorelease of divalent cations". *Proceedings of the National Academy of Sciences of the United States of America* 85 (17) (1988), pages 6571–6575.

[228] M. Soibinet *et al.* "Rhod-5N as a fluorescent molecular sensor of cadmium (II) ion". *Journal of Fluorescence* 18 (6) (2008), pages 1077–1082.

[229] G. David, J. Talbot, and E. F. Barrett. "Quantitative estimate of mitochondrial Ca in stimulated motor nerve terminals". *Cell Calcium* 33 (3) (2003), pages 197–206.

[230] G. C. Ellis-Davies and J. H. Kaplan. "Nitrophenyl-EGTA, a photolabile chelator that selectively binds Ca^{2+} with high affinity and releases it rapidly upon photolysis". *Proceedings of the National Academy of Sciences of the United States of America* 91 (1) (1994), pages 187–191.

[231] P. Kner *et al.* "Super-resolution video microscopy of live cells by structured illumination". *Nature Methods* 6 (5) (2009), pages 339–342.

[232] H. Shroff *et al.* "Live-cell photoactivated localization microscopy of nanoscale adhesion dynamics". *Nature Methods* 5 (5) (2008), pages 417–423.

[233] V. Lučić, A. Rigort, and W. Baumeister. "Cryo-electron tomography: the challenge of doing structural biology *in situ*". *The Journal of Cell Biology* 202 (3) (2013), pages 407–419.

[234] J. Fernández, S. Li, and V. Lucic. "Three-Dimensional Anisotropic Noise Reduction with Automated Parameter Tuning: Application to Electron Cryotomography". *Current Topics in Artificial Intelligence*. 2007, pages 60–69.

[235] M. B. Jackson and E. R. Chapman. "The fusion pores of Ca^{2+}-triggered exocytosis". *Nature Structural & Molecular Biology* 15 (7) (2008), pages 684–689.

[236] A. A. Alabi and R. W. Tsien. "Perspectives on kiss-and-run: role in exocytosis, endocytosis, and neurotransmission". *Annual Review of Physiology* 75 (2013), pages 393–422.

[237] G. A. Zampighi *et al.* "Conical electron tomography of a chemical synapse: vesicles docked to the active zone are hemi-fused". *Biophysical journal* 91 (8) (2006), pages 2910–2918.

[238] L. Siksou *et al.* "A common molecular basis for membrane docking and functional priming of synaptic vesicles". *European Journal of Neuroscience* 30 (1) (2009), pages 49–56.

[239] H. T. McMahon and E. Boucrot. "Molecular mechanism and physiological functions of clathrin-mediated endocytosis". *Nature Reviews Molecular Cell Biology* 12 (8) (2011), pages 517–533.

[240] W. J. Jockusch *et al.* "Clathrin-dependent and clathrin-independent retrieval of synaptic vesicles in retinal bipolar cells". *Neuron* 46 (6) (2005), pages 869–878.

[241] Y. Cheng *et al.* "Cryo-electron tomography of clathrin-coated vesicles: structural implications for coat assembly". *Journal of Molecular Biology* 365 (3) (2007), pages 892–899.

[242] A. Fotin *et al.* "Molecular model for a complete clathrin lattice from electron cryomicroscopy". *Nature* 432 (7017) (2004), pages 573–579.

[243] T. F. J. Martin. "Tuning exocytosis for speed: fast and slow modes". *Biochimica et Biophysica Acta - Molecular Cell Research* 1641 (2) (2003), pages 157–165.

[244] T. Moser and D. Beutner. "Kinetics of exocytosis and endocytosis at the cochlear inner hair cell afferent synapse of the mouse". *Proceedings of the National Academy of Sciences of the United States of America* 97 (2) (2000), pages 883–888.

[245] J. Sun *et al.* "Synapsins regulate use-dependent synaptic plasticity in the calyx of Held by a Ca^{2+}/calmodulin-dependent pathway". *Proceedings of the National Academy of Sciences of the United States of America* 103 (8) (2006), pages 2880–2885.

[246] K. Parthasarathi *et al.* "Connexin 43 mediates spread of Ca^{2+}-dependent proinflammatory responses in lung capillaries". *The Journal of Clinical Investigation* 116 (8) (2006), page 2193.

[247] H. Ichimura *et al.* "Lung surfactant secretion by interalveolar Ca^{2+} signaling". *American Journal of Physiology-Lung Cellular and Molecular Physiology* 291 (4) (2006), pages L596–L601.

[248] T. G. Chappell *et al.* "Uncoating ATPase is a member of the 70 kilodalton family of stress proteins". *Cell* 45 (1) (1986), pages 3–13.

[249] A. M. Hamilton and K. Zito. "Breaking it down: the ubiquitin proteasome system in neuronal morphogenesis". *Neural Plasticity* 2013 (2013).

[250] O. Coux, K. Tanaka, and A. L. Goldberg. “Structure and functions of the 20S and 26S proteasomes”. *Annual Review of Biochemistry* 65 (1) (1996), pages 801–847.

[251] G. Kleiger and T. Mayor. “Perilous journey: a tour of the ubiquitin–proteasome system”. *Trends in Cell Biology* 24 (6) (2014), pages 352–359.

[252] R. Hough, G. Pratt, and M. Rechsteiner. “Purification of 2 High-Molecular-Weight Proteases from Rabbit Reticulocyte Lysate”. *Journal of Biological Chemistry* 262 (17) (1987), pages 8303–8313.

[253] E. Shelton *et al.* “Cytoplasmic Particles and Aminoacyl Transferase-I Activity”. *The Journal of Cell Biology* 45 (1) (1970), pages 1–8.

[254] T. Yoshimura *et al.* “Molecular characterization of the "26S" proteasome complex from rat liver”. *Journal of Structural Biology* 111 (3) (1993), pages 200–11.

[255] J. M. Peters *et al.* “Structural Features of the 26-S Proteasome Complex”. *Journal of Molecular Biology* 234 (4) (1993), pages 932–937.

[256] P. C. A. da Fonseca, J. He, and E. P. Morris. “Molecular Model of the Human 26S Proteasome”. *Molecular Cell* 46 (1) (2012), pages 54–66.

[257] G. C. Lander *et al.* “Complete subunit architecture of the proteasome regulatory particle”. *Nature* 482 (7384) (2012), 186–U75.

[258] K. Lasker *et al.* “Molecular architecture of the 26S proteasome holocomplex determined by an integrative approach”. *Proceedings of the National Academy of Sciences of the United States of America* 109 (5) (2012), pages 1380–1387.

[259] M. E. Matyskiela, G. C. Lander, and A. Martin. “Conformational switching of the 26S proteasome enables substrate degradation”. *Nature Structural & Molecular Biology* 20 (7) (2013), pages 781–+.

[260] C. G. Pack *et al.* “Quantitative live-cell imaging reveals spatio-temporal dynamics and cytoplasmic assembly of the 26S proteasome”. *Nature Communications* 5 (2014).

[261] Y. X. Chen *et al.* “Fast and accurate reference-free alignment of subtomograms”. *Journal of Structural Biology* 182 (3) (2013), pages 235–245.

[262] D. Barthelme *et al.* “Architecture and assembly of the archaeal Cdc48*20S proteasome”. *Proceedings of the National Academy of Sciences of the United States of America* 111 (17) (2014), E1687–94.

[263] D. Barthelme and R. T. Sauer. “Bipartite determinants mediate an evolutionarily conserved interaction between Cdc48 and the 20S peptidase”. *Proceedings of the National Academy of Sciences of the United States of America* 110 (9) (2013), pages 3327–32.

[264] Y. X. Chen *et al.* “Autofocused 3D Classification of Cryo-electron Subtomograms”. *Structure* (2014).

[265] P. Sledz *et al.* “Structure of the 26S proteasome with ATP-gamma S bound provides insights into the mechanism of nucleotide-dependent substrate translocation”. *Proceedings of the National Academy of Sciences of the United States of America* 110 (18) (2013), pages 7264–7269.

[266] Z. Yu and A. S. Frangakis. "M-free: Scoring the reference bias in sub-tomogram averaging and template matching". *Journal of Structural Biology* 187 (1) (2014), pages 10–19.

[267] J. Cohen. "Is High-Tech View of HIV Too Good to Be True?" *Science* 341 (6145) (2013), pages 443–444.

[268] L. G. Trabuco *et al.* "Flexible fitting of atomic structures into electron microscopy maps using molecular dynamics". *Structure* 16 (5) (2008), pages 673–683.

[269] H.-C. Tai *et al.* "Characterization of the brain 26S proteasome and its interacting proteins". *Frontiers in Molecular Neuroscience* 3 (2010).

[270] U. Schubert *et al.* "Rapid degradation of a large fraction of newly synthesized proteins by proteasomes". *Nature* 404 (6779) (2000), pages 770–774.

[271] R. M. Gronostajski, A. B. Pardee, and A. L. Goldberg. "The ATP dependence of the degradation of short-and long-lived proteins in growing fibroblasts." *Journal of Biological Chemistry* 260 (6) (1985), pages 3344–3349.

[272] A. F. Kisselev and A. L. Goldberg. "Monitoring activity and inhibition of 26S proteasomes with fluorogenic peptide substrates". *Methods in Enzymology* 398 (2005), pages 364–378.

[273] E. Sakata *et al.* "Localization of the proteasomal ubiquitin receptors Rpn10 and Rpn13 by electron cryomicroscopy". *Proceedings of the National Academy of Sciences of the United States of America* 109 (5) (2012), pages 1479–1484.

[274] X. R. Wang and L. Huang. "Identifying dynamic interactors of protein complexes by quantitative mass spectrometry". *Molecular and Cellular Proteomics* 7 (1) (2008), pages 46–57.

[275] S. Elsasser *et al.* "Proteasome subunit Rpn1 binds ubiquitin-like protein domains". *Nature Cell Biology* 4 (9) (2002), pages 725–730.

[276] J. X. You and C. M. Pickart. "A HECT domain E3 enzyme assembles novel polyubiquitin chains". *Journal of Biological Chemistry* 276 (23) (2001), pages 19871–19878.

[277] D. S. Leggett *et al.* "Multiple associated proteins regulate proteasome structure and function". *Molecular Cell* 10 (3) (2002), pages 495–507.

[278] H. Holzl *et al.* "The regulatory complex of Drosophila melanogaster 26S proteasomes: Subunit composition and localization of a deubiquitylating enzyme". *The Journal of Cell Biology* 150 (1) (2000), pages 119–129.

[279] X. B. Qiu *et al.* "hRpn13/ADRM1/GP110 is a novel proteasome subunit that binds the deubiquitinating enzyme, UCH37". *The EMBO Journal* 25 (24) (2006), pages 5742–5753.

[280] J. Hamazaki *et al.* "A novel proteasome interacting protein recruits the deubiquitinating enzyme UCH37 to 26S proteasomes". *The EMBO Journal* 25 (19) (2006), pages 4524–4536.

[281] A. D. Jacobson *et al.* "Autoregulation of the 26S proteasome by *in situ* ubiquitination". *Mol Biol Cell* 25 (12) (2014), pages 1824–35.

[282] H. C. Besche *et al.* "Autoubiquitination of the 26S Proteasome on Rpn13 Regulates Breakdown of Ubiquitin Conjugates". *The EMBO Journal* 33 (10) (2014), pages 1159–1176.

[283] C. Warburg and W. Christian. "Determination of DNA content". *Biochemische Zeitschriften* 310 (1941), page 384.

[284] U. Aebi and T. D. Pollard. "A glow discharge unit to render electron microscope grids and other surfaces hydrophilic". *Journal of Electron Microscopy Technique* 7 (1) (1987), pages 29–33.

[285] R. Martin, M. Torres, and J. Sanchez-Prieto. "mGluR7 inhibits glutamate release through a PKC-independent decrease in the activity of P/Q-type Ca^{2+} channels and by diminishing cAMP in hippocampal nerve terminals". *European Journal of Neuroscience* 26 (2) (2007), pages 312–322.

[286] S. Bolte and F. P. Cordelieres. "A guided tour into subcellular colocalization analysis in light microscopy". *Journal of Microscopy* 224 (2006), pages 213–232.

[287] C. A. Schneider, W. S. Rasband, and K. W. Eliceiri. "NIH Image to ImageJ: 25 years of image analysis". *Nature Methods* 9 (7) (2012), pages 671–675.

[288] R. Hegerl. "The EM Program Package: A Platform for Image Processing in Biological Electron Microscopy". *Journal of Structural Biology* 116 (1) (1996), pages 30–34.

[289] S. Nickell *et al.* "TOM software toolbox: acquisition and analysis for electron tomography". *Journal of Structural Biology* 149 (3) (2005), pages 227–234.

[290] A. S. Frangakis and R. Hegerl. "Noise Reduction in Electron Tomographic Reconstructions Using Nonlinear Anisotropic Diffusion". *Journal of Structural Biology* 135 (3) (2001), pages 239–250.

[291] J. R. Kremer, D. N. Mastronarde, and J. R. McIntosh. "Computer visualization of three-dimensional image data using IMOD". *Journal of Structural Biology* 116 (1) (1996), pages 71–76.

[292] A. Martinez-Sanchez *et al.* "Robust membrane detection based on tensor voting for electron tomography". *Journal of Structural Biology* 186 (1) (2014), pages 49–61.

[293] D. N. Mastronarde. "Automated electron microscope tomography using robust prediction of specimen movements". *Journal of Structural Biology* 152 (1) (2005), pages 36–51.

[294] F. Förster *et al.* "Retrovirus envelope protein complex structure *in situ* studied by cryo-electron tomography". *Proceedings of the National Academy of Sciences of the United States of America* 102 (13) (2005), pages 4729–4734.

[295] S. Nickell *et al.* "TOM software toolbox: acquisition and analysis for electron tomography". *Journal of Structural Biology* 149 (3) (2005), pages 227–234.

[296] S. H. W. Scheres and S. X. Chen. "Prevention of overfitting in cryo-EM structure determination". *Nature Methods* 9 (9) (2012), pages 853–854.

[297] W. Humphrey, A. Dalke, and K. Schulten. "VMD: Visual molecular dynamics". *Journal of Molecular Graphics and Modelling* 14 (1) (1996), pages 33–38.

[298] E. F. Pettersen *et al.* "UCSF chimera - A visualization system for exploratory research and analysis". *Journal of Computational Chemistry* 25 (13) (2004), pages 1605–1612.

[299] T. D. Goddard, C. C. Huang, and T. E. Ferrin. "Visualizing density maps with UCSF Chimera". *Journal of Structural Biology* 157 (1) (2007), pages 281–287.

[300] Y. Harpaz, M. Gerstein, and C. Chothia. "Volume Changes on Protein-Folding". *Structure* 2 (7) (1994), pages 641–649.

[301] M. van Heel and M. Schatz. "Fourier shell correlation threshold criteria". *Journal of Structural Biology* 151 (3) (2005), pages 250–62.

Scientific publications of Shoh Asano during his PhD candidacy time (in chronological order)

Title:	**Cryo-electron tomography: methodology, developments and biological applications**
Authors:	Vanhecke, D., **Asano, S.**, Kochovski, Z., Fernandez-Busnadiego, R., Schrod, N., Baumeister, W., and Lucic, V.
Journal:	*Journal of Microscopy*
Volume:	242(3)
Pages:	221-227
Year:	2011

Title:	**Insights into the molecular organization of the neuron by cryo-electron tomography**
Authors:	Fernandez-Busnadiego, R., Schrod, N., Kochovski, Z., **Asano, S.**, Vanhecke, D., Baumeister, W., and Lucic, V.
Journal:	*Journal of Electron Microscopy*
Volume:	60(suppl 1)
Pages:	S137-S148
Year:	2011

Title:	**Cryo-electron tomography reveals a critical role of RIM1α in synaptic vesicle tethering**
Authors:	Fernandez-Busnadiego, R.*, **Asano, S.***, Oprisoreanu, A. M., Sakata, E., Doengi, M., Kochovski, Z., Zürner, M., Stein, V., Schoch, S., Baumeister, W., and Lucic, V. * These authors contributed equally.
Journal:	*Journal of Cell Biology*
Volume:	201(5)
Pages:	725-740
Year:	2013

Title:	**Three-dimensional architecture of actin filaments in Listeria monocytogenes comet tails**
Authors:	Jasnin, M., **Asano, S.**, Gouin, E., Hegerl, R., Plitzko, J. M., Villa, E., Cossard, P., and Baumeister, W.
Journal:	*Proceedings of the National Academy of Sciences of the United States of America*
Volume:	110(51)
Pages:	20521-20526
Year:	2013

Title:	**Robust membrane detection based on tensor voting for electron tomography**
Authors:	Martinez-Sanchez, A., Garcia, I., **Asano, S.**, Lucic, V., and Fernandez, J. J.
Journal:	*Journal of Structural Biology*
Volume:	186(1)
Pages:	49-61
Year:	2014

Title:	**A molecular census of 26S Proteasomes in Intact Neurons**
Authors:	**Asano, S.***, Fukuda, Y.*, Beck, F., Aufderheide, A., Förster, F., Danev, R., and Baumeister, W. * These authors contributed equally.
Journal:	*Science*
Volume:	347
Pages:	439-442
Year:	2015

Acknowledgements

I like to thank Prof. Wolfgang Baumeister for giving me the opportunity to work in his department during my Diploma and PhD time. His experience and guidance was great and his support for my future was extraordinary. Both professionally, and personally, this department were the right choice.

From the TU Munich side, I want to thank Prof. Matthias Rief and Prof. Andreas Bausch, who helped me to decide in which direction I should go. Especially I am grateful to Prof. Erich Sackmann for his initial advice on joining the lab and many interesting conversations.

My direct PhD advisor and group leader Dr. Vladan Lucic deserves special thanks. The years I spend with him and the group were delightful. During my PhD candidacy time I explored many different subjects of my interest and thank him for his understanding and his full support throughout.

I would like to thank in particular my colleagues in our synapse group. Especially Zdravko, Niko and Ulrike- thank you for making everyday life great and helping me consistently. Fuku-chan for enduring my horrible Japanese and his great work he did and shared with us. Ruben, with whom I had the joy of passing a paper together through the most difficult revisions so far.

Tim, you not only helped me out with the tools necessary to my research, you also did a very, very fine job during my wedding. Thank you, I will not forget these days!

A special thanks go to Friedrich, Florian, Antje, Pia and Yuxiang for their help and input for the 26S story, as well as Radostin and Maryam for the help with the phase plate.

My sincere gratitude to the other people in the department, which whom I enjoyed my time, especially Felix, Daniel, Marion, Andreas, Marc, Thomas, and Luca. I always appreciated and thank for the encouraging words and everlasting help from Birgit and Nathalie.

Lots of things are going smoothly in our department thanks to a lot of people who should be named here: Jürgen and Günter for microscopes, Inga for computers, and Harald for virtually anything else. Thank you to all the other technicians and people who made the lab life much easier, such as the workshop team, Silvia, and Herbert. As the landlords of my temporary second home, I would like to thank the library team for their understanding.

Outside of the department I want to thank Prof. Shigeo Okabe for the great time at the University of Tokyo, and the “usual suspects” from the IMPRS-LS program -Cardin, Amit, Dhawal, and Vlad - for coming together even in stressful times, and all my friends outside of work who accepted my limited free time in later years.

The biggest appreciation goes to my family. My mother Carmen to whom I owe a life of joy and happiness, who supported me in good and the bad times (if there were any). Ultimately, she is the reason to what I am now. To my father Akihiro, whose calm and wise character is exemplary and who never ceases to amaze me in other different aspects of life. To my grandfather Lothar, who sadly passed away during the PhD

candidacy time, but infused me with the love to science. To my grandmother Irmgard, who reminded all of us to live life by the simple rule of “carpe diem”. To my brother Yuki, who I deeply respect and congratulate for what he has accomplished so far. I am very sure you will continue to amaze all of us [hopefully positively ◡̈]. To my families outside Munich: Nadine and Dima from Russia, as well as Val, Tanja and Mark from US: Thank you for welcoming me so wholeheartedly into your families. Having such an international family all over the world is fantastic.

Last, but not least, to my wife Ida: Thank you for the wonderful time together here in Munich and all the places we visited. Our PhD journey brought us early together and we swore our oaths in the most stressful of times. I am still in awe how we did all that during the last phases in each of our PhD candidacy time. Thank you for your inspiration, your patience, your endless help and your unconditional love. Above all the joy and successes I was allowed to take part in and experience, being close to you were by far the one I am the most proud of. Let us begin our next step in life, with new challenges that we will rise up to - together.

Thank you for reading.